NANOSTRUCTURED PROMOTED TITANIA PHOTOCATALYSTS

RIMA TROFIMOVAITE
Doctor of Philosophy

Aston University
European Bioenergy Research Institute (EBRI)
September 2017

ASTON UNIVERSITY

Nanostructured promoted titania photocatalysts

Rima Trofimovaite

Doctor of Philosophy

September 2017

Thesis Summary

Concern over the economics of accessing fossil fuel and widespread acceptance of the anthropogenic origin of rising CO_2 emissions and associated climate change is driving academic and commercial research into new routes to sustainable fuels, to meet the demands of a rapidly rising global population and reduce an impact on the environment. The titania oxide semiconductor has attracted a great interest as a photocatalyst for wide-ranging applications including wastewater depollution, solar fuels via both H_2 production and CO_2 reduction. Tailoring the physicochemical properties of titania photocatalysts, and their resulting reactivity, in a predictable fashion remains challenging.

The thesis explores the impact of thermal processing, macroporosity and metal deposition on the surfactant-templated mesoporous TiO_2 and dual soft-hard templated macro-mesoporous TiO_2 series and resulting activity in aqueous phase photocatalytic dye degradation, H_2 production and CO_2 reduction reactions. Control over the structural and photophysical properties of mesoporous titania enables systematic tuning of Methyl Orange photocatalytic depollution and H_2 evolution. Hierarchical macro-mesoporous titanias exhibit uniform mesopores with macropore diameters that can be systematically tuned between 140-310 nm, resulting in a close-packed, ordered macropore framework. Hierarchically-structured TiO_2 display two fold increase in photoactivity relative to mesoporous counterparts in the H_2 production. Ultra-low concentrations (0.02-0.1 wt%) of copper introduced into the mesoporous and macro-mesoporous titania surfaces by wet-impregnation enhance activity for dye degradation by six fold, and for H_2 production four fold, through the genesis of isolated Cu (I) species which suppress charge recombination. Furthermore, promotion with Pt increases photocatalytic activity in Methyl Orange degradation by eleven fold, H_2 production 16-26 times and are the only series which display activity in the CO_2 reduction reaction. Moreover, the impact of the macropore diameter on the activity of the Methyl Orange degradation is observed for Cu and Pt promoted macro-mesoporous TiO_2 series.

Nanostructured promoted titanias offer an insight into the relative importance of physicochemical and electronic properties upon their associated activity together with significantly enhanced photocatalytic performance.

Keywords: hydrogen, carbon dioxide, Methyl Orange, mesoporous, macroporous.

Acknowledgements

I am very grateful and thankful to:

Prof A. F. Lee and Dr M. Granollers-Mesa for the supervision.
Prof K. Wilson and Dr W. Lee for the co-supervision.
Dr C. M. A. Parlett and Dr M. A. Isaacs for the TEM, XPS and Synchrotron assistance.
Dr S. Kumar and Ms B. Barbero for the discussions about the photocatalysis projects.
Dr R. E. Douthwaite and Mr B. Coulson for the photoluminescence measurements.
Ms L. Frattini for assisting at Synchrotron.
My colleagues at the SMAC group and EBRI institute for the stimulating discussions and relaxing tea breaks.
EPSRC (EP/K021796/1 and EP/K029525/2) for the financial support.

I am especially grateful to my mum Asta Zemliene for always believing and supporting me. She has been a constant reminder that there is a light on the horizon and no matter how hard the situation is, I must feel good and enjoy my life because it never stops being beautiful. My grandparents Aldona and Jurgis Kalinauskai for developing my interest in science and technology since childhood. My precious friends for the help, encouragement and all the endless proofreading.

List of Contents

List of Abbreviations

AOP – advanced oxidation process
BET - Brunauer, Emmett and Teller adsorption theory
BJH - Barrett, Joyner and Halenda pore size distribution method
CB – conductance band
EXAFS - extended X-ray absorption fine structure
FWHM – full width half maximum
HOMO – highest occupied molecular orbital
ICP-OES - inductively coupled plasma optical emission spectroscopy
KM – Kubelka-Munk function
LA – low angle
LUMO – lowest unoccupied molecular orbital
MO – Methyl Orange
NHE – normal hydrogen electrode
ppm - parts per million
PS – polystyrene
Redox – reduction and oxidation
ROC – reactive organic compounds
RT – room temperature
SEM - scanning electron microscope
SPR – surface plasmon resonance
HRSTEM – high resolution scanning transmission electron microscope
TEM - transmission electron microscope
TGA – thermogravimetric analysis
TPO – temperature programmed oxidation
TRPL – time-resolved photoluminescence
UV - ultraviolet
VB – valence band
Vis – visible
WA – wide angle
WS – water splitting
XANES - X-ray absorption near edge structure
XAS - X-ray absorption spectroscopy
XPS - X-ray photoelectron spectroscopy
XRD - X-ray diffraction

List of Figures

List of Tables

List of Equations

Chapter 1

Introduction

1 Introduction

Concern over the economics of accessing fossil fuel reserves and widespread acceptance of the anthropogenic origin of rising CO_2 emissions and associated climate change is driving research into new routes to sustainable fuels via both H_2 production and CO_2 reduction to meet the demands of a rapidly rising global population and ensure future energy security.[1-3] In addition, the lack of clean safe drinking water or having little or no sanitation are affecting millions of people around the world. Photocatalysts have attracted great interest in both academic and commercial research for wide-ranging applications including environmental waste water remediation,[4] non-disruptive technology for solar fuels production[5, 6] and as a source of renewable hydrogen.[7]

1.1 Principles of photocatalysis

Based on International Union of Pure and Applied Chemistry (IUPAC) photocatalysis corresponds to a change of a chemical reaction rate or its initiation under the action of light radiation in the presence of a substance (the photocatalyst/semiconductor) that absorbs light and facilitates the chemical transformation of the reactants. Semiconductors are commonly used for light harvesting because of their band gap capable of absorbing solar light and producing charge carriers for the oxidation-reduction reactions.[8] Usually, metals do not have any band gap or it is lower than 0.05 eV, while for insulators the band gap is usually greater than 3.5 eV and requires an extensive amount of energy. The energy states of the valence band are filled with electrons while the conductance band states are empty. In a photocatalytic process (**Figure 1.1**), solar (light) radiation ($h\vartheta$) having energy equal or greater than the band gap energy (E_g) of a semiconductor (photocatalyst) irradiates its surface and excites electrons (−) from filled valence band (VB) to empty conductance band (CB) leaving behind holes (+). The lifetime of charge carrier (+ and −) is just a few nanoseconds, thus many of them recombine immediately (Volume/Bulk recombination) releasing heat as wasteful energy. Electrons (−) and holes (+) which manage to escape from the excitation regions migrate to the surface of the CB and VB respectively and are trapped by adsorbed reactants. They participate in various reduction (acceptor) and oxidation (donor) processes to produce final products. However, if the charge carriers fail to meet species on the surface or/if their energy is too small to carry out reactions, they recombine producing heat (Surface recombination) (**Equation 1.1**). For the efficient photocatalytic process, it is crucial to have enough photon energy, suppress recombination of electrons and holes and contain pre-adsorbed surface species.[9]

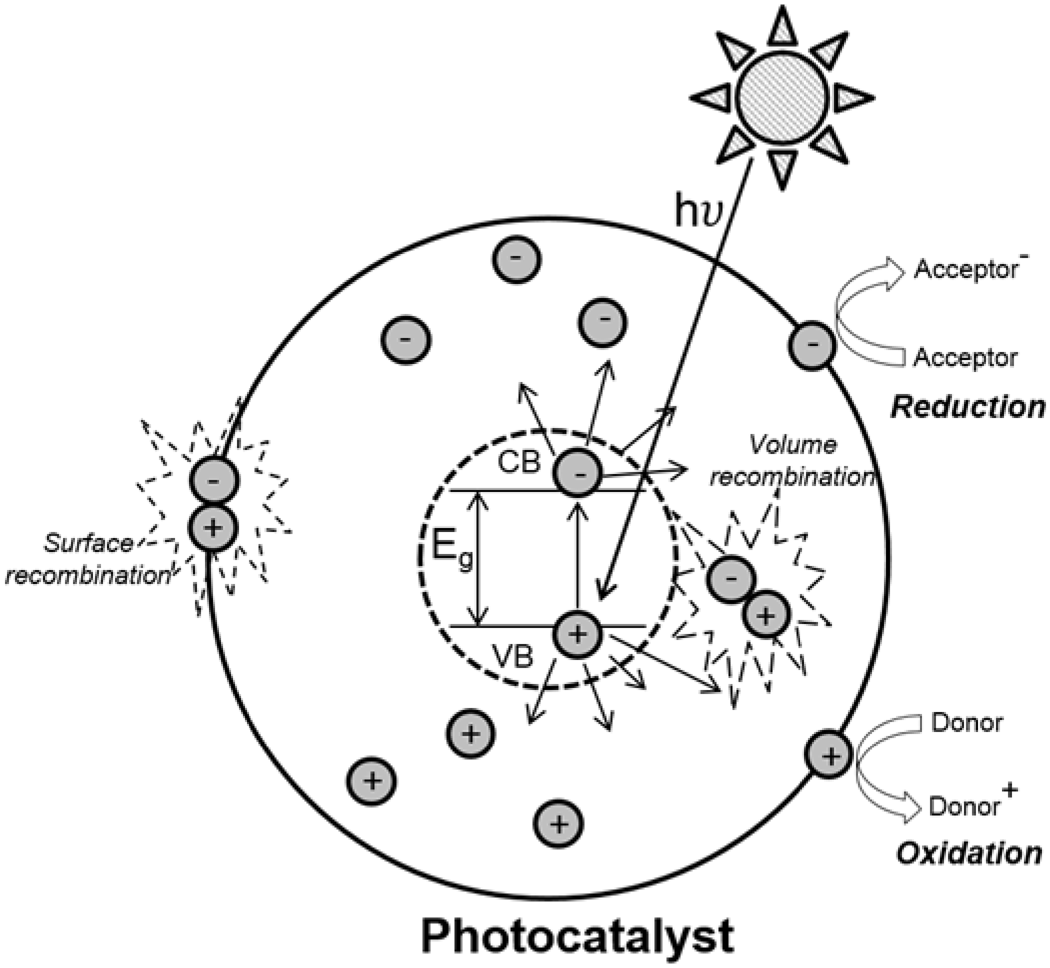

Figure 1.1 A schematic representation of photocatalytic process on a heterogeneous photocatalyst.

Light absorption	Photocatalyst + $h\nu \rightarrow h_{VB}^+$ & e_{CB}^-
Recombination	$h_{VB}^+ + e_{CB}^- \rightarrow$ heat
Reduction reaction	$A + e_{CB}^- \rightarrow A^-$
Oxidation reaction	$D + h_{VB}^+ \rightarrow D^+$

Equation 1.1 Processes occurring in semiconductor upon light irradiation.

The ability of adsorbed species to participate in oxidation-reduction reactions depends on redox potentials of adsorbates. The redox potential measures the capability of chemical species to acquire electrons. More positive (lower) reduction potential gives greater affinity for electrons and drives oxidation reaction. The more negative (higher) the redox potential, the higher the tendency to lose electrons which drives reduction reaction on the photocatalyst surface. The electron and hole transfer is controlled by alignment of quasi-Fermi levels of the photocatalyst semiconductor and the redox potentials of the adsorbates.[10] For n-type semiconductors, these quasi-Fermi levels are located very close to conductance and valence band edges thus reaction conditions are commonly expressed in terms of the position of band edges of semiconductor and redox potentials. For the reduction to occur the conductance band should be higher than lowest unoccupied molecular orbital (LUMO) of the acceptor. Considering that the scale goes from positive to negative redox potentials when energy increases, the conductance band needs to be more negative than the reduction potential of the molecule. For the oxidation to take place the valence band of the photocatalyst should be lower than the highest occupied molecular orbital (HOMO) of the adsorbate. In other words, HOMO has to be more negative than the potential of the VB. Taking into account these thermodynamic requirements, the optimum photocatalyst is a compromise between a small band gap materials able to absorb visible light and a wide enough band gaps covering a range of redox potentials relevant to the photocatalytic reaction. From the kinetic side of the reaction, not only a range of potentials but also significant kinetic overpotential (energy difference between the band edges and redox potentials) is required. Small overpotential leads to a low reaction rate, therefore, for kinetics, the band gap should be as wide as possible. To conclude, not only the band gap width but its edges play a key role in determining compatibility and maximum efficiency for the desired photocatalytic reaction.

1.2 Photocatalysts

The large group of light-sensitive materials that have been investigated as photocatalysts includes semiconductors, more commonly metal oxides but non-metals are also applied. The summary of different types of photocatalysts are presented below (**Figure 1.2**).[7, 11] Catalysts can be divided into two major groups as being UV or visible light sensitive. This depends on the energy associated with the band gap of the material. In other words, a small band gap requires less energy and higher wavelengths thus gives visible light sensitivity and opposite – larger band gap needs more energy and leads to UV light absorption. UV light catalysts are less economically efficient since UV radiation is only 3-4% of solar light spectrum[12] and electron-hole pair recombination rate is fast[13] which results in lower activity and selectivity. UV-light catalysts could be split into two subgroups - single oxide: usually different metal oxides with the most popular being TiO_2, and mixed oxides: combination of metal and non-metal oxides with the best-known TiO_2 – zeolite.[14]

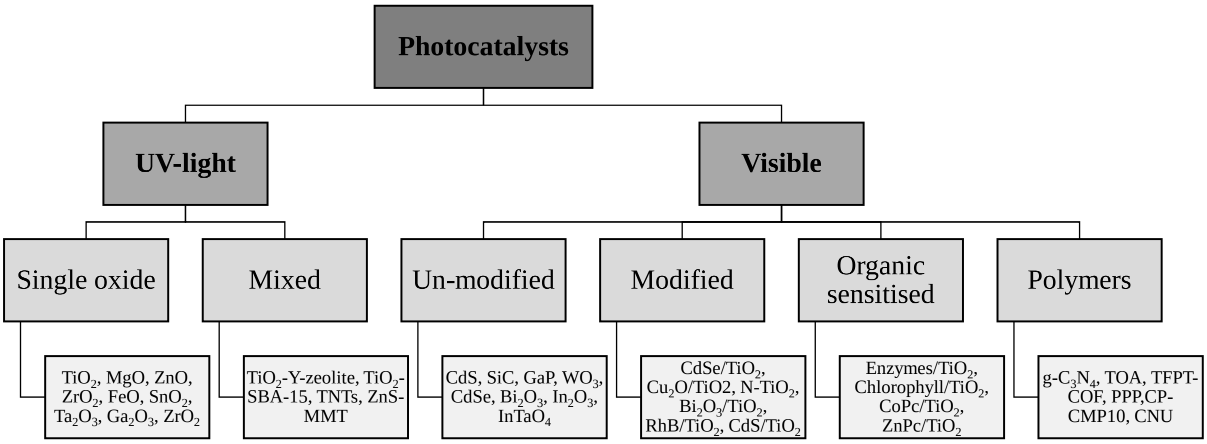

Figure 1.2 Examples of the variety of photocatalysts available.

The other group of photocatalysts are visible light sensitive catalysts, for example, Bi_2O_3. They utilise solar light more effectively since visible light is 45% of sun radiation[12]. Most popular visible light photocatalysts are UV catalysts that were surface modified by sensitisation or doping.[15, 16] Promotion with metals or non-metals with more negative conductance edge increases visible light response leading to higher activity and better charge separation and also an ability to tune selectivity (**1.4 Promotion of titania photocatalysts**). The two newest sub-groups of visible light catalysts are polymers and organic sensitised semiconductors, which employ new approaches of engineering photocatalysts by using enzymes etc.[17]

1.3 Titania photocatalysts

Titania has been one of the most widely used semiconductor photocatalysts due to its abundance, low cost, thermochemical stability, low toxicity and suitable optical properties.[18] Titania photoactivity is predominantly influenced by structural and electronic properties,[19, 20] which may be tuned via structure engineering.[21]

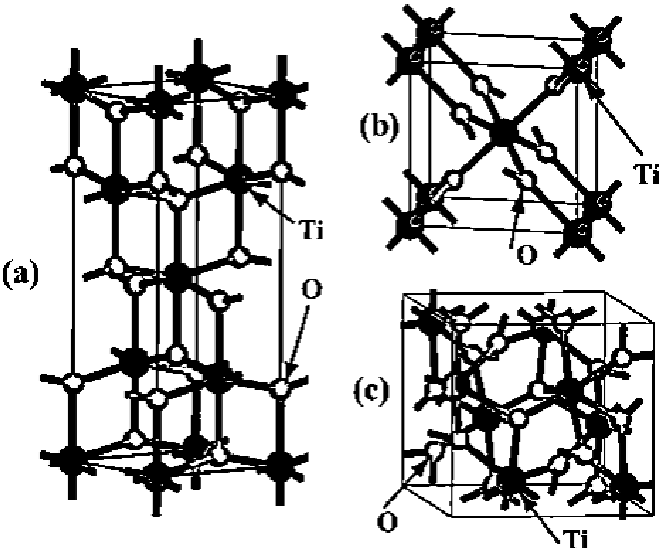

Figure 1.3 Unit cell diagrams of (a) anatase (b) rutile (c) brookite crystalline phases. Adapted from ref. 22.

Titania possesses three principal crystalline forms: anatase (tetragonal), rutile (tetragonal) and brookite (orthorhombic) (**Figure 1.3**).[22] The most commonly studied are the metastable anatase and the most stable rutile. The former presents chains of elongated TiO_6 octahedra with each Ti^{4+} ion surrounded by six O^{2-} ions, whereas the second shows only small orthorhombic distortion and higher symmetry.[9, 23] The distortion of anatase octahedron is more pronounced thus it shows lower symmetry. In addition, the anatase phase is considered to be more reactive than rutile due to tenfold improvement in the hole trapping arising from higher Fermi level and predominant indirect band gap.[24] Moreover, a mixture of majority anatase phase with small amounts of rutile is the proposed optimum for photoactivity due to charge separation across their interface (electron transfer from anatase to rutile).[25, 26] There are two proposed mechanisms of superior performance of mixed-phase anatase and rutile titania (**Figure 1.4**): A – the offset of 0.2 eV between higher anatase and lower rutile conduction bands improves the separation of the charge carriers through electron transfer from anatase to rutile; B – trap states located 0.8 eV below the CB of anatase are populated by electrons from rutile.[27] In this context, commercial P25 titania, comprising anatase and rutile crystallites (which appear to exhibit synergistic photocatalysis due to heterojunction formation) is typically the first port of call for academic and industrial applications.[28-30] Lastly, the interface region between anatase and rutile itself may act as a trap site aiding charge separation.[31] Higher crystallinity (over amorphous) increases the lifetime of the charge carriers.[32] Improved crystallinity demonstrated greater efficiency in electron transfer between orbitals of adsorbed dyes and conductance band of titania[33] because of less loose bonds and lattice distortions which can act as trapping and recombination sites.[34]

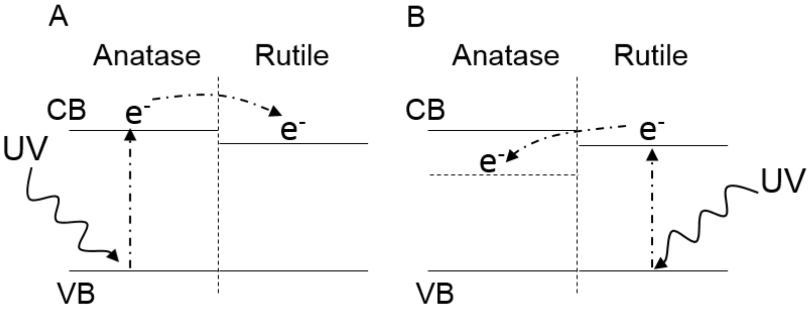

Figure 1.4 Two possible mechanisms of high performance of mixed anatase-rutile phase TiO_2.

TiO_2 is an n-type semiconductor due to a few oxygen vacancies which are compensated by the presence of Ti^{3+} centres. N-type semiconductors are a type of extrinsic semiconductors where the dopant atoms or vacancies are capable of providing extra conduction electrons to the host material and this creates an excess of negative electron charge carriers. On the other hand, in p-type semiconductors, holes are in excess and p-type semiconductors are created by doping an intrinsic semiconductor with acceptor impurities.[35] Anatase and rutile both exhibit wide band gaps in UV region of 3.2 eV (387 nm) and 3.0 eV (413 nm) respectively due to variation in the crystal structure.[36] The difference in the band gap values arises because anatase has a 0.2 eV higher conductance band than rutile.[37] 2p orbitals of the oxygen atoms form the valence band while 3d states of the Ti^{4+} with t_{2g} symmetry form the lower part of the conduction band. Anatase only exhibits indirect allowed transitions.[18] On the other hand, rutile can feature both indirect and direct allowed transitions. Indirect transition requires addition of an additional photon to conserve the momentum and thus leads to decrease in photonic efficiency. The rate of recombination of charge carriers reach 90% within 10 ns.[38]

Not only photocatalyst phase but also particle size greatly influence the activity via multiple surface phenomena and a particle confinement effect - decrease particle size in nanoscale increases the band gap of the material.[39, 40] For smaller semiconductor particles there is more surface atoms present leading to the increase in surface area to volume ratio.[18] As a result, more surface active sites are available and interfacial charge transfer is improved. The optimum 25-40 nm nanocrystallites of TiO_2 are established due to competition between light harvesting efficiency, scattering, bulk/surface recombination and specific surface area.[41] Koci et al. studied the effect of TiO_2 particle size on photocatalytic reduction of carbon dioxide with the optimum particle size of 14 nm corresponding to the highest yields of methane and methanol.[42]

Surface defects such as oxygen vacancies (V_o) and Ti^{3+} sites also enhance TiO_2 photoactivity.[43] Oxygen vacancies not Ti interstitials defects is dominant contributors to the band gap states of TiO_2 surface based on electron bombardment data.[44] Furthermore, oxygen vacancies affect the absorption of water, CO_2 and other molecules on TiO_2 surfaces in the photocatalytic processes.[45] Oxygen vacancies most often form at the surface region of TiO_2 so the surface defects are more important than bulk ones.[46, 47]

Density functional calculations have also highlighted the importance of crystal facets for anatase, with surface energies and photoactivity of decreasing from (001) 0.90 J m^{-2} > (100) 0.53 J m^{-2} > (101) 0.44 J m^{-2}.[48, 49] As a result, research has been focused on synthesising preferably (001) facets or mixture of (001) and (101)[50] for water splitting and dye degradation reactions. [51-54]

1.3.1 Nanostructured titania

The morphology of the material plays an important role in the activity and in technical aspects of the application and reactor design. For a structure to be considered as nanostructured its dimensions have to be between 0.1 to 100 nm. Heterogeneous nanostructured materials can be classified based on their structure: zero-dimensional (0D) e.g. nanoparticles, one-dimensional (1D) e.g. nanotubes, two-dimensional (2D) e.g. nanosheets and three-dimensional (3D) e.g. mesoporous structures (**Figure 1.5**).[55] Nano in comparison with the bulk materials exhibit distinct physical and electronic properties. Nanostructures expose more surface atoms which contribute to the change in the free energy and affects thermodynamic properties such as thermal stability.[56] The electronic properties of nanocrystals can be altered by quantum size effect – dependence of optical characteristics on the particle size due to variation in the density of electronic energy levels.[39] Moreover, a broad range of nanostructures can facilitate the integration of multiple diverse components to create materials with multiple functionalities. Many kinds of TiO_2 morphologies have been investigated including films, spheres, hollow spheres, nanotubes, nanorods, nanosheets etc.

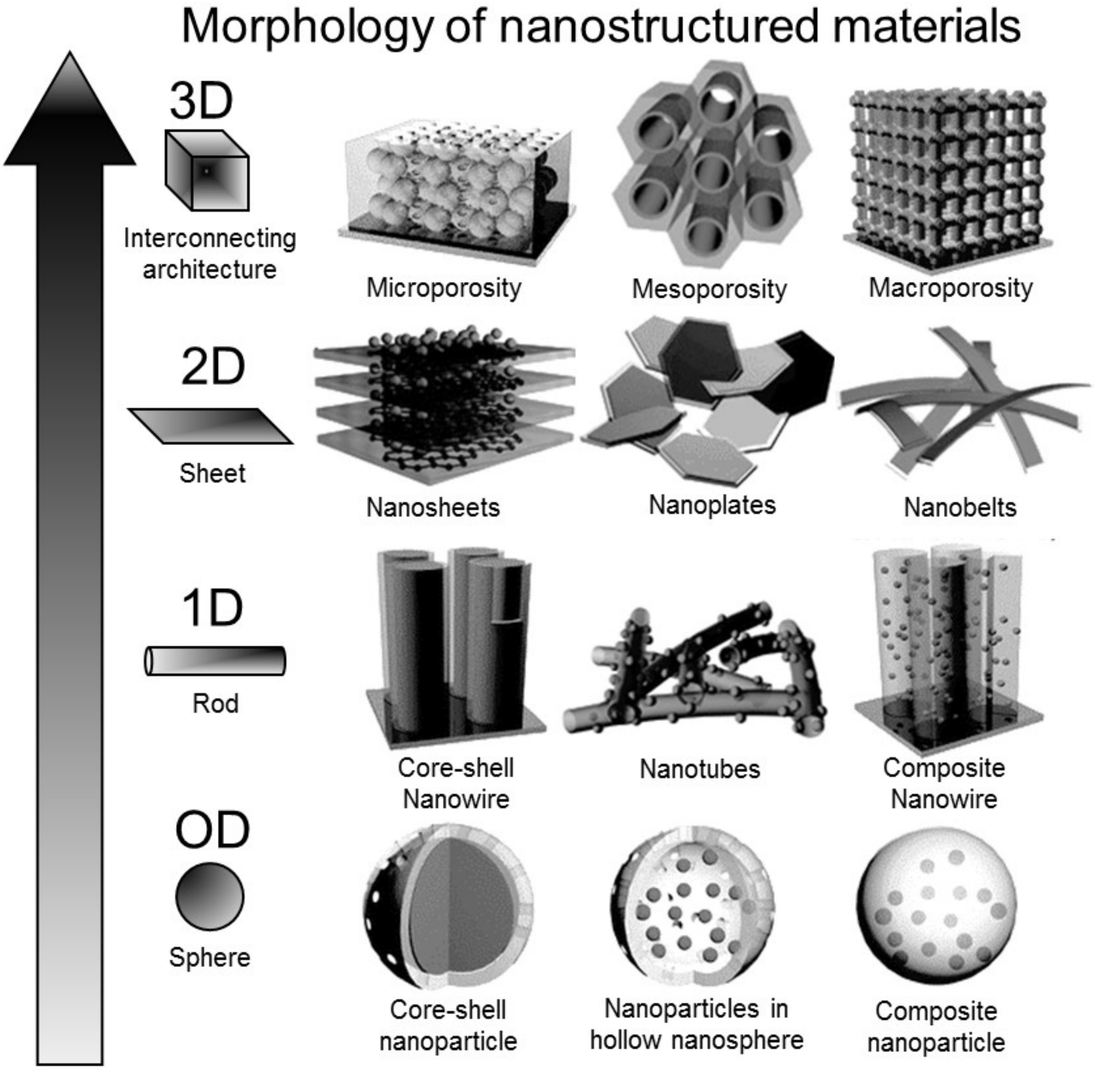

Figure 1.5 Morphology of nanostructured materials. Adapted from ref 55.

Thin films are commonly used in dye-sensitised solar cells or fabrication of devices as a coating.[57-59] TiO_2 with 1-D structure such as rods, wires, fibres and tubes display diverse electrical and optical properties that depend on size and shape.[60-62] TiO_2 nanotubes and nanorods are the popular choice due to their increased surface area, reduced grain boundaries and enhanced charge transportation due to the 1-D structure.[63] Spheres and hollow spheres are also promising materials in energy conversion, environmental and biotechnology applications.[64, 65] The presence of porosity in nanostructured materials can greatly enhance their chemical and physical properties. Mesoporous TiO_2 gained increased attention for multiple applications including energy storage and conversion, catalysis and separation because of their tunable structural properties like pore diameter, shape and volume, surface area and nanocrystallinity.[66] In comparison to bulk TiO_2, mesoporous TiO_2 with uniform channels increase the density of the active sites, improve accessibility, enhance adsorption of reactant molecules, assists rapid transport of photoexcited carriers to the catalyst surface resulting in suppressing recombination processes .[67] Addition of the mesoporosity enhance charge separation and decrease bulk recombination of charge carriers.[68] Macropore incorporation into mesoporous architectures leads to formation of three-dimensional hierarchical materials with improved properties arising from their unique morphology and complex architectures, which typically possess high surface areas and diverse pore-interconnectivities.[69] Such materials offer enhanced catalytic activity *via* increased light scattering and faster in-pore mass transport of sterically hindered reagents, in particular for the photodegradation of organic dyes, relative to their bulk, nanoparticulate or monomodal nanoporous counterparts. [70-72] The unique surface and structural characteristics of these architectures increase photon absorption, leading to enhanced quantum efficiency.[73-75] In general, titania materials exhibit a wide band gap, which absorbs only the UV light, consisting just 3 – 4% of overall solar radiation[12] and thus has limited activity. The efficient use of solar energy requires the photocatalysts with a small band gap to absorb all wavelengths of the spectrum. For the titania materials to fulfil this requirement, they need to be promoted.

1.4 Promotion of titania photocatalysts

The wide band gap materials like TiO_2 allow a wide range of redox reactions, with significant available overpotential, making them desirable photocatalysts. Surface trapping,[76] doping, [77] sensitisation[78] are promising approaches to overcome the limitations of pure titania through modifying the quantum efficiency, band gap/energies, charge carrier mobility, surface structure, and adsorption properties (**Figure 1.6**).[26, 77-82] A red shift from 400 nm to visible light region can be achieved by forming a heterojunction or engineering a band gap of the semiconductor while activity can be improved via better charge separation and prolonged lifetime of the charge carriers.[83, 84]

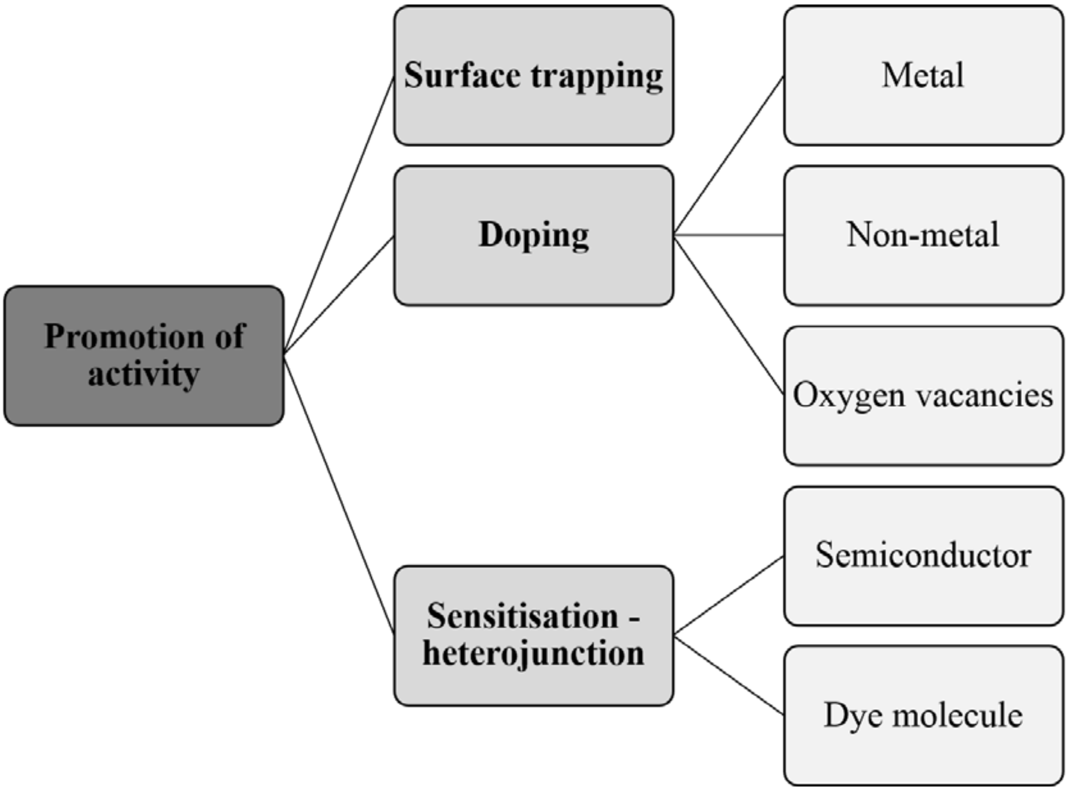

Figure 1.6 Multiple ways of promoting photocatalyst activity.

Functionalising by earth-abundant metals such as copper is especially appealing with a wide range of promoter formats employed, including Cu metal,[85] Cu_xO clusters,[86] nano-Cu_2O,[78] Cu doped sol-gels,[87, 88] $Cu(OH)_2$ clusters,[89] and Cu_2O shells[90] to extend light absorption and improve charge carrier mobility, and in turn quantum efficiencies for photocatalytic pollutant degradation[78, 85-87] and solar fuels production.[89, 90] Another extensively used promotion method is modification with noble metals such as Pt.[91, 92] Platinum is often used to modify the TiO_2 surfaces because among the common metals it has the highest work function and the smallest H_2 evolution over-potential.[93] The Pt(0), Pt(II) and Pt(IV) species can exist on the surface TiO_2 but most commonly observed is Pt metal formation.[92, 94]

1.4.1 Surface trapping

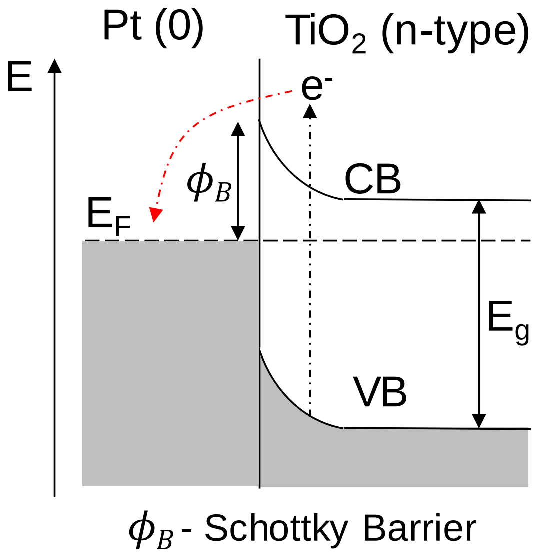

Figure 1.7 Schematic illustration of the Schottky barrier.

Deposition of elements such as Pt, Au, Ag on the surface of semiconductor catalysts significantly improves the photocatalytic activity by acting as an electron trap, promoting interfacial charge transfer and therefore inhibiting recombination of the electron-hole pair.[95, 96] Charge separation via transfer is achieved by the Schottky barrier (**Figure 1.7**) which arises when metal is in contact with n-type semiconductor and electrons populate on metal species if the Fermi level of the metal is lower than conductance band of the semiconductor. Thus, the electron reaches the adsorbate faster, thus the composite is more reductive. The metallic components of the metal/semiconductor system could also enhance the light absorption through the surface plasmon resonance (SPR) induced effect.[97, 98] Noble metal nanoparticles exhibiting SPR display a broad absorption band in the UV or visible light range which arises due to collective resonant oscillation of the free electrons of the conduction band of the metal. Strong SPR absorption in the visible region of, for example, supported Au or Ag nanoparticles significantly improve photoactivity by injecting hot electrons from the excited SPR states of Au or Ag to the conduction band of TiO_2. Unlike the widely studied Au and Ag nanostructures, which have distinct and well-defined SPR absorption peaks, small (<10 nm) Pt nanoparticles always exhibit broad extinction from the ultraviolet to short wavelengths of visible light, without observable peaks.[99]

1.4.2 Doping

The already weakly reductive conductance band of titania is restricting major minimisation of the band gap via lowering conductance band energy. Nevertheless, the absorption energy can be reduced and shifted towards higher wavelengths (like visible light) by "raising" the valence band via band gap engineering. There are three main approaches (**Figure 1.8**)[27]: A – raising the valence band by hybridisation with other orbitals of a metal; B - doping with a non-metal to create intraband states above the valence band; C – creation of intraband impurity states such as oxygen vacancies, below the Fermi level or additional states arising from the collection of semiconductor nanoparticles.[100, 101]

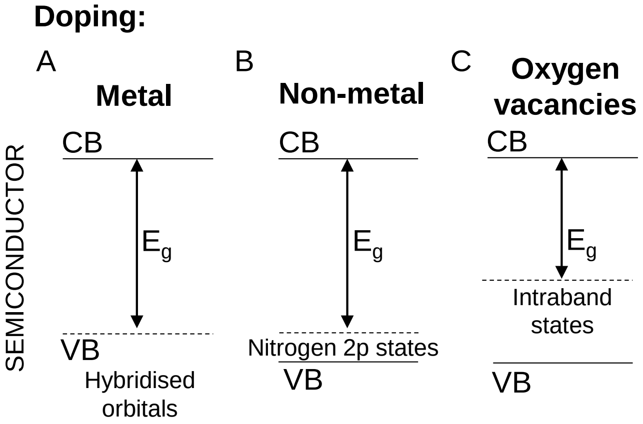

Figure 1.8 Doping of semiconductor with a wide band gap.

Metal ion doping includes transition metal ions such as copper, chromium, iron, nickel, cobalt, niobium and rare-earth metal ions like lanthanum, cerium as potential dopants for visible light activity.[102] However, metal ion dopants can also serve as recombination centres, resulting in decreased photocatalytic activity. Non-metal ion doping commonly involves elements like nitrogen, sulphur, and carbon.[103] For example, in nitrogen doped TiO_2 case, N species result in localized 2p states above the valence band of titania and the visible light electronic transitions occur from a localized N 2p state to the conductance band.[104] In contrast to metal ion doping, non-metallic dopants replace lattice oxygen. More recently, a co-doping with metal and non-metal is explored to combine best qualities from both effects.[105, 106]

1.4.3 Sensitisation – heterojunction

As discussed above, doping of the photocatalysts is less flexible in altering the electronic structure and display only small charge separation. Another way of lowering energy and shifting semiconductor photoresponse to visible range region is by sensitising it via formation of the heterojunction. In this technique, a secondary material with a smaller (narrower) band gap able to absorb visible light is introduced via a type II heterojunction.[84] The type II staggered band gap heterostructure forms an interface where charges are separated and electrons are channelled to one size and holes to the other. There are two types of sensitiser materials (**Figure 1.9**): A - narrow band gap semiconductors with aligned conduction band minima such as quantum dots, and B - visible light active molecules like dyes.[107] Semiconductor sensitisers enhance activity through electron transfer to another semiconductor with the lower conductance band edge (e.g. TiO_2) while the holes travel in the opposite direction to the sensitiser, which has the higher valence band edge. Dye sensitisers work based on a similar principle, the electron is excited from HOMO to LUMO of the dye and then is transferred from LUMO of the dye, which is higher, to conductance band of the semiconductor.[108] However, in this case, there are additional requirements such as orientation and distance of the dye to the surface as well as size and flexibility of the molecule.[109, 110] In both cases, sensitisers extended absorption range and improve charge carrier separation leading to reduced recombination and promoted activity. Most commonly used semiconductor sensitisers are CdS (on TiO_2), CdSe (on ZnO).[111]

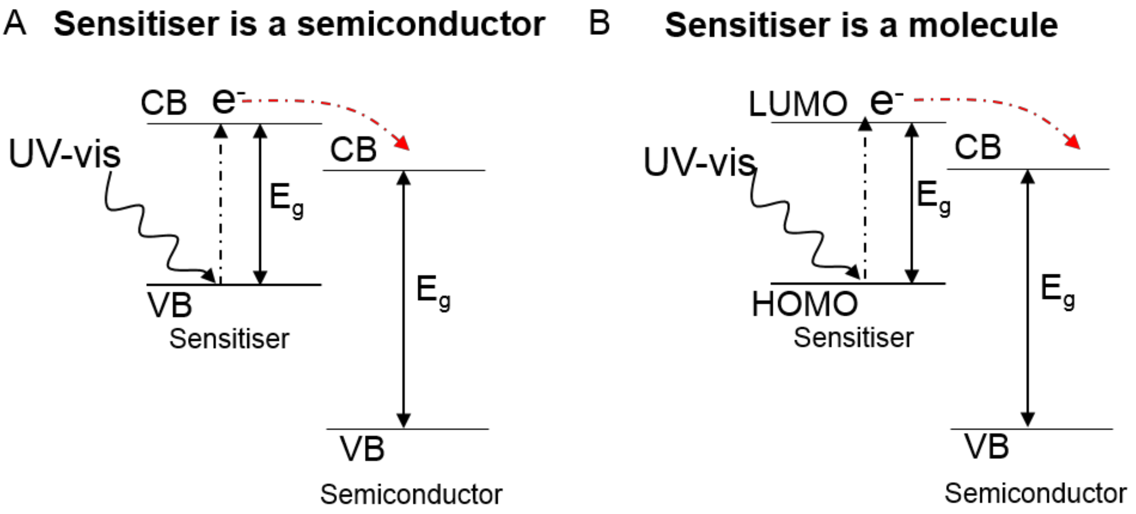

Figure 1.9 Heterojunction of wide band gap semiconductor with A – another semiconductor sensitiser; B – a dye molecule sensitiser.

The majority of dyes can inject an electron into the conduction band of a semiconductor when photoexcited. Dye sensitisers such as ruthenium based inorganic or organic dyes are more popular in dye-sensitized solar cells (DSSC).[112, 113] In dye-sensitized solar cells, the sensitized dye degradation, which could follow the electron injection by the photoexcited dye into the conduction band of the photocatalyst, is prevented by the design of the device, but this is not the case for aqueous suspensions.[114] Due to this phenomena, using dye degradation in the assessment of photocatalytic activity is problematic, because, in the irradiated aqueous suspension, degradation could be either a photocatalytic process, what one is after, or a dye sensitization, or even both.

1.5 Photocatalytic reactions

The efficiency of photocatalytic reactions depends on light absorption of the photocatalyst, charge carrier formation, and the lifetime and utilisation of those charge carriers. It involves three steps (**1.1 Principles of photocatalysis)**:

1. Photon absorption and charge carrier generation – photophysical process.
   Electron and hole formation is dictated by the optical properties of the photocatalyst and can be tuned (**1.3 Titania photocatalysts**).
2. Charge carrier diffusion – photophysical process.
   For the successful diffusion of electrons and holes to the surface, the recombination of the charge carriers needs to be suppressed, normally by the catalyst modification (**1.4 Promotion of titania photocatalysts**).
3. Charge carrier transfer to the reactants – electrochemical reaction.
   Successful redox reaction depends on the position of band edges of semiconductor and redox potentials of the products. The charge carrier transfer process is more efficient if reactants are already pre-adsorbed on the surface.

The rate of the photocatalytic reaction mainly depends on the photocatalyst properties and the wavelengths of the light irradiation but other factors can, to some extent, influence the activity. Higher reaction temperatures lead to more frequent collisions between the semiconductor and the substrate; pH can shift redox potential and band edges; oversupply of light accelerates recombination; pressure can improve solubility of gases.

1.5.1 Methyl Orange decomposition

Water pollution and its associated impact on human health account for >840,000 fatalities annually worldwide.[115] Around 80% of contaminants in wastewater arise from the unregulated discharge of toxic, recalcitrant organic compounds by the textile, paper, petrochemical, food, energy and mineral processing sectors into aquatic ecosystems, and their depollution represents a significant challenge particularly for emerging countries.[116-119] Recalcitrant organic compounds, which include organic azo dyes such as Methyl Orange, cannot be treated by conventional biological and/or physicochemical processing (e.g. microorganisms, flocculation or chlorination).[120, 121] Advanced oxidation processes, including Fenton oxidation,[122] photocatalytic oxidation,[123] photo-Fenton oxidation,[124] catalytic wet air oxidation,[125] electrocatalytic oxidation,[126] electro-Fenton oxidation[127-129] are promising solutions for the oxidative removal of persistent organic compounds from wastewater. However, while Fenton-type AOPs exhibit high removal efficiencies (100 mg L^{-1})[130] for diverse ROCs including cyanotoxins, they share a common high demand for H_2O_2 (~2.1 kg per kg of biological/chemical oxygen demand depending on the water to treat).[131] Furthermore, heterogeneous

Fenton analogues are susceptible to transition metal leaching.[132] Hence, photocatalytic solutions to wastewater depollution are highly sought after.[4, 16, 133]

It is important to recognise that Azo-dyes (exemplified by MO) are integral to the textile industry, and major sources of waste water contamination,[134] and hence their removal from aquatic environments is critical to improve human health. In the present work, dye degradation was investigated to target the removal of a specific Azo-dye commonly discharged to waste water in developing countries, and not simply to assay the general photocatalytic performance of our materials (Rochkind and co-workers published a recent critical review on this distinction [135]).

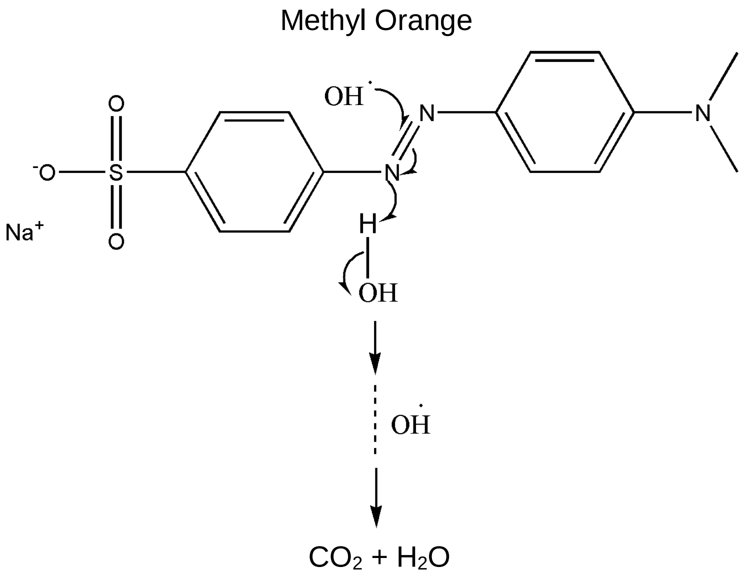

Figure 1.10 Exemplar Methyl Orange degradation by hydroxyl radical.

Methyl Orange decomposition over the semiconductor photocatalyst is strongly driven by the holes in the valence band via direct oxidation or hole reaction with water to produce the primary hydroxyl radical ($OH^{\cdot}$), which is very powerful oxidant having the oxidation potential of +2.32 eV (NHE).[136] Hydroxyl radicals break down Methyl Orange into carbon dioxide and water on the photocatalyst surface and in the solution (**Figure 1.10**). In addition, there is an electron induced decomposition pathways. Four distinct mechanisms are proposed for the Methyl Orange photocatalytic degradation; a direct hole oxidation process[137] (**Equation 1.2 A**), hydroxyl radical oxidation[138, 139] (**Equation 1.2 B-D**) and superoxide radical formation[140] (**Equation 1.2 E-K**):

$h_{VB}^{+} + dye \rightarrow dye^{\bullet+} \rightarrow$ dye oxidation products (A)

$h_{VB}^{+} + H_2O \rightarrow H^{+} + OH^{\cdot}$ (B)

$h_{VB}^{+} + OH^{-} \rightarrow OH^{\cdot}$ (C)

$OH^{\cdot} + dye \rightarrow$ dye oxidation products (D)

$e_{CB}^{-} + O_2 \rightarrow O_2^{\cdot-}$ (E)

$O_2^{\cdot-} + H_2O \rightarrow HO_2^{\cdot} + OH^{-}$ (F)

$HO_2^{\cdot} + HO_2^{\cdot} \rightarrow H_2O_2 + O_2$ (G)

$H_2O_2 + h\nu \rightarrow 2OH^{\cdot}$ (H)

$H_2O_2 + O_2^{\cdot-} \rightarrow OH^{\cdot} + OH^{-} + O_2$ (I)

$e_{CB}^{-} + H_2O_2 \rightarrow OH^{\cdot} + OH^{-}$ (J)

$OH^{\cdot} + dye \rightarrow$ oxidation of the dye (K)

Equation 1.2 Methyl Orange decomposition.

Based on thermodynamics, for these reactions to occur, previously discussed conductance and valence band edges (**1.1 Principles of photocatalysis**) should be positioned in the way that, the oxidation potential of the hydroxyl radicals (+2.32 V (vs NHE)) and the reduction potential of superoxide radicals (-0.3 V (vs NHE)) would lie well within the band gap of a semiconductor photocatalyst like in titania (+2.7 to -0.5 V (NHE)) (**Figure 1.11**).

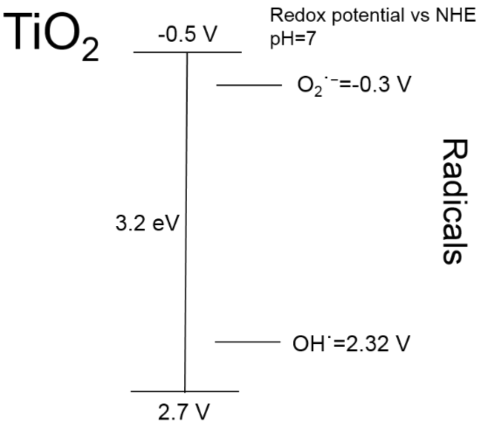

Figure 1.11 Energy diagram and redox potentials of radical formation for MO degradation.

1.5.2 Water splitting

The photocatalytic water splitting offers a clean economically efficient sustainable technology for hydrogen production.[141] It provides an advantage of abundant resources of solar energy and water to produce fuel or hydrogen for the chemical industry. Currently, the majority of the hydrogen is produced by steam reforming from natural gas.[142] Water splitting by the photocatalysts is considered to be an artificial photosynthesis where products have higher energy than reactants thus energetically is more challenging.[143] In contrast, photo-oxidation of organic compounds products possess lower energy than reactants thus these type of reactions occur more readily.[11] There are three main methods of water splitting involving light: photoelectrolysis using a semiconductor electrode,[144] photobiological water splitting involving algae[145] and heterogeneous photocatalysis where semiconductor catalysts are suspended in water, alcohol/water or water/hole scavenger mixes.[7]

In water splitting reactions, electrons are key charge carriers that reduce water to hydrogen (**Equation 1.3 A-B**). The direct splitting of water has a very low efficiency[143] because of the rapid recombination of photo-generated electrons and holes and backwards to reaction to water. It is challenging to achieve water splitting for hydrogen production using solely TiO_2 photocatalyst in pure water. In order to reduce recombination and increase hydrogen production rate sacrificial electron donors - hole scavenger like Na_2SO_3 can be employed.[146] Adding electron donors or sacrificial reagents to react with the photo-generated holes is an effective measure to enhance the electron-hole separation. The hole scavengers trap holes and reduce recombination allowing more electrons participate in the reaction (**Equation 1.3 C-D**). Sodium sulphite donates electrons and together with holes form side products. However, the drawback of this method is the need to continuously add hole scavengers in order to sustain the reaction since they are consumed during the reaction. Normally, H_2 and O_2 evolution should proceed in a stoichiometric 2:1 ratio and if this is not the case, there is an issue with experimental setup and reverse reaction is favoured.[147]

$$2H_2O + 4\,h_{VB}^{+} \rightarrow 4\,H^{+} + O_2 \qquad \text{(A)}$$
$$4H^{+} + 4\,e_{CB}^{-} \rightarrow 2H_2 \qquad \text{(B)}$$

$$H_2O \rightleftharpoons H^{+} + OH^{-} \qquad \text{(C)}$$
$$SO_3^{2-} + 2h_{VB}^{+} + 2OH^{-} \rightarrow SO_4^{2-} \qquad \text{(D)}$$

Equation 1.3 Water splitting.

In order to form hydrogen, the conduction band edge needs to be more negative than the hydrogen production level (0V (vs NHE)) and valence band edge more positive than water oxidation (+1.23V (vs NHE) e.g. in TiO_2 case (+2.7 to -0.5 V vs (NHE)) (**Figure 1.12**). The redox potential for the overall reaction at pH=7 is −1.23 V vs (NHE).

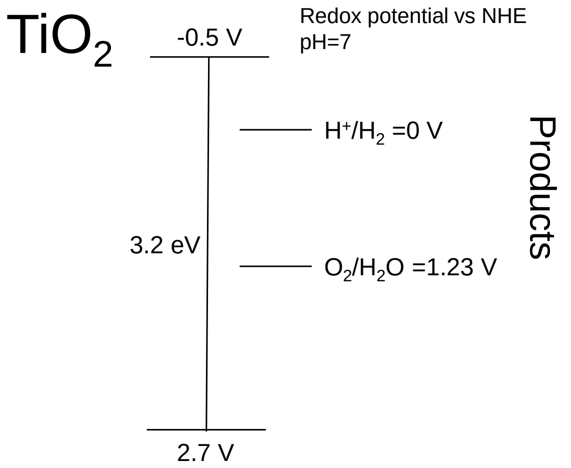

Figure 1.12 Energy diagram and redox potentials of water splitting on the TiO_2 photocatalyst.

1.5.3 Carbon dioxide reduction

CO_2 reduction to hydrocarbons (fuels or valuable chemicals) is a significantly more challenging procedure than water splitting because CO_2 is kinetically and thermodynamically very stable thus the process requires a large input of energy.[148] Photocatalytic CO_2 reduction involves electron transfer to the adsorbed molecules leading to a cascade of the multi-step reduction reactions. Up to 8 electrons can participate in these reactions where C-O bonds are broken and new C-H are formed resulting in numerous products depending on semiconductor and redox potentials. [149] Negative redox potential corresponds to CO_2 reduction while positive ones - to water oxidation by holes.

In this project, water was chosen as a reducing agent and hydrogen source since it is very cheap, non-toxic, readily available, and a source of protons. Nevertheless, the use of water as a hydrogen source is challenging compared to other possibilities. During CO_2 reduction with H_2O, it is more favourable to reduce water (E_{redox}=0 V) than carbon dioxide (E_{redox}= -1.9 V).[149] Thus in addition to CO_2 reduction products, H_2 can be detected. If large amounts of H_2 is generated it indicates that water splitting is competing with CO_2 reduction and operating conditions need to be optimised to improve selectivity and suppression of hydrogen generation.

Reaction routes are not specific and strongly depend on the reaction conditions. Up to today, there are several variations of the CO_2 photoreduction pathways under debate. First of all, CO_2 reduction to an anion radical $CO_2^{\bullet -}$ using a single-electron process (**Equation 1.4 A**) has a strongly negative -1.9 V redox potential, therefore, essentially no semiconductor can facilitate this electron transfer.[150] Most common theory of photocatalytic CO_2 reduction using water as reductant is as below (**Equation 1.4 A-J**)[149, 151] which involves the proton-assisted transfer of multiple electrons that have more positive reduction potentials and are less negative than conductance band potentials of common semiconductors. In other words, multi electronic processes require less energy per electron transfer compared to single electron transfer. This leads to formation of formic acid, CO, formaldehyde, methanol and methane products (**Equation 1.4 B-J**).[149, 152] The values are comparable to proton reduction, which involves only one electron (**Equation 1.4 G**). The holes oxidise water on the surface of the photocatalyst and provide protons for CO_2 reduction (**Equation 1.4 H-J**). However, literature does not provide strong evidence to support this reaction pathway. This leaves with the series of single electron reactions with the first electron transfer as a liming step.[153]

	E_{Redox} / V	
$CO_2 + e_{CB}^{-} \rightarrow CO_2^{\cdot-}$ Further electronation/protonation → hydrocarbon	-1.90	(A)
$CO_2 + 2H^+ + 2\,e_{CB}^{-} \rightarrow HCOOH$	-0.61	(B)
$CO_2 + 2H^+ + 2\,e_{CB}^{-} \rightarrow CO + H_2O$	-0.53	(C)
$CO_2 + 4H^+ + 4\,e_{CB}^{-} \rightarrow HCHO + H_2O$	-0.48	(D)
$CO_2 + 6H^+ + 6\,e_{CB}^{-} \rightarrow CH_3OH + H_2O$	-0.38	(E)
$CO_2 + 8H^+ + 8\,e_{CB}^{-} \rightarrow CH_4 + 2H_2O$	-0.24	(F)
$2H^+ + 2\,e_{CB}^{-} \rightarrow H_2$	-0.41	(G)
$H_2O + h_{VB}^{+} \rightarrow OH^{\cdot} + H^+$	+2.32	(H)
$2H_2O + 2\,h_{VB}^{+} \rightarrow H_2O_2 + 2H^+$	-	(I)
$2H_2O + 4\,h_{VB}^{+} \rightarrow 4H^+ + O_2$	+0.82	(J)

Equation 1.4 CO_2 reduction pathway 1 and associated redox potentials pH=7.

Secondly, the adsorption of carbon dioxide to the surface of semiconductor provides an attractive solution to overcome an inert carbon dioxide molecule. When CO_2 adsorbs to the surface it forms partially charged $CO_2^{\bullet-}$ anion radical through interaction with surface atoms.[154] The activation barrier is lower in an aqueous dispersion of photocatalyst because dipolar interaction with water stabilise $CO_2^{\bullet-}$.[152] Formation of carbon dioxide anion radical and hydrogen radical further results in production of hydrocarbon materials (**Equation 1.5 A-G**).[155]

$CO_2 + e_{CB}^{-} \rightarrow CO_2^{\bullet-}$ (A)

$H^+ + e_{CB}^{-} \rightarrow H^{\bullet}$ (B)

$CO_2^{\bullet-} + 2\,H^{\bullet} + 2\,h_{VB}^{+} \rightarrow HCOOH$ (C)

$CO_2^{\bullet-} + 2\,H^{\bullet} + 2\,h_{VB}^{+} \rightarrow CO + H_2O$ (D)

$CO_2^{\bullet-} + 4\,H^{\bullet} + 4\,h_{VB}^{+} \rightarrow HCHO + H_2O$ (E)

$CO_2^{\bullet-} + 6\,H^{\bullet} + 6\,h_{VB}^{+} \rightarrow CH_3OH + H_2O$ (F)

$CO_2^{\bullet-} + 8\,H^{\bullet} + 8\,h_{VB}^{+} \rightarrow CH_4 + 2H_2O$ (G)

Equation 1.5 CO_2 reduction pathway 2 via $CO_2^{\bullet-}$ radical.

Thirdly, carbon dioxide has low solubility in water (0.033 mol/L at 25 ºC, 1 atm)[156] which strongly depends on the pH. The theory states that in water CO_2 partially hydrates to carbonic acid which can dissociate into bicarbonate and carbonate ions (**Equation 1.6 A-B**).[153] Theoretical photocatalytic reduction pathways for carbonic acid and carbonate ion presented in **Equation 1.6 A-J**.[17]

		E_{Redox} / V	
$CO_2 + H_2O \rightleftharpoons H_2CO_3 \rightleftharpoons H^+ + HCO_3^-$	pK_a=6.4	n/a	(A)
$HCO_3^- \rightleftharpoons H^+ + CO_3^{2-}$	pK_a=10.3	n/a	(B)
$H_2CO_3 + 2H^+ + 2\ e_{CB}^- \rightarrow HCOOH + H_2O$		-0.166	(C)
$H_2CO_3 + 4H^+ + 4\ e_{CB}^- \rightarrow HCHO + 2H_2O$		-0.05	(D)
$H_2CO_3 + 6H^+ + 6\ e_{CB}^- \rightarrow CH_3OH + 2H_2O$		+0.044	(E)
$2CO_3^{2-} + 8H^+ + 6\ e_{CB}^- \rightarrow CH_3OH + 2H_2O$		+0.209	(F)
$2CO_3^{2-} + 3H^+ + 2\ e_{CB}^- \rightarrow HCOO^- + 2H_2O$		+0.311	(G)
$2CO_3^{2-} + 4H^+ + 2\ e_{CB}^- \rightarrow C_2O_4^{2-} + 2H_2O$		+0.478	(H)
$2C_2O_4^{2-}\ 2H^+ + 2\ e_{CB}^- \rightarrow 2HCOO^-$		+0.145	(I)
$HCOO^- + 5H^+ + 4\ e_{CB}^- \rightarrow CH_3OH + 2H_2O$		+0.157	(J)

Equation 1.6 CO_2 reduction pathway 3 via carbonic acid and carbonate ion.

As previously discussed (**1.1 Principles of photocatalysis**), edges of conductance and valence bands can be used to evaluate potential reactions and their products. Reactions (acceptors as adsorbed species) with reduction potential lower (more positive) than conductance band of the semiconductor are more favourable due to more efficient use of energy of photoexcited electrons to be transferred toward adsorbed species. For example, Anpo et al. tested TiO_2 catalysts with conductance band edge of -0.5 V and observed that they are more likely to produce methanol and methane than any other products.[157] In general, the most common products observed in CO_2 photoreduction on TiO_2 are CO, CH_4, HCOOH, HCHO, CH_3OH (**Figure 1.13**). Large band gap materials are more desired because they provide a variety of reactions and have more energy (greater overpotential) but also require higher input.[9] Titania is a suitable photocatalyst to provide sufficiently negative and positive redox potentials.

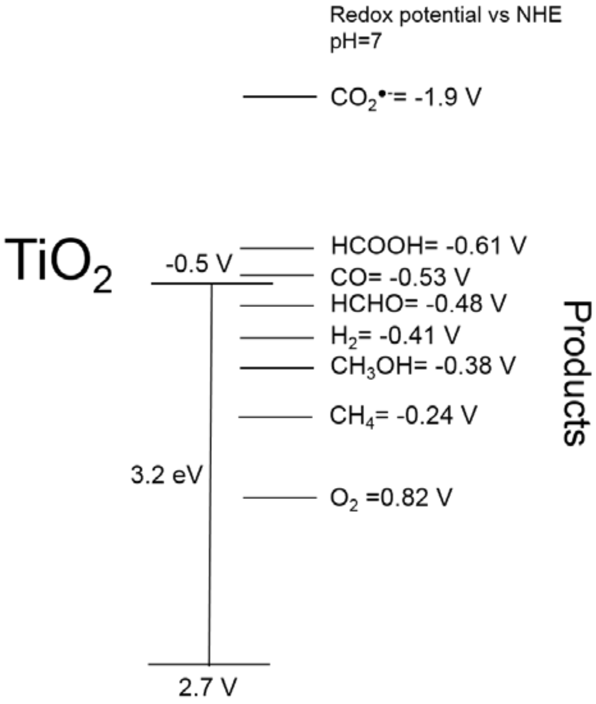

Figure 1.13 Energy diagram and redox potentials of CO_2 photoreduction on the TiO_2 photocatalyst.

The exact order and mechanistic details of CO_2 reduction are not fully examined and a number of pathways can result in the same product. Three main alternatives to form methane product are presented in literature: formaldehyde, carbene and glyoxal routes (**Figure 1.14**) based on their intermediates.[27] The route of methane formation depends on the binding mode of $CO_2^{\bullet -}$ to the surface of TiO_2. Formaldehyde pathway is favoured when radical bonds via its oxygen atom, usually in reaction solutions with high dielectric constant like water.[158, 159] However, computational and experimental data could not definitely confirm this pathway.[160] On the other hand, carbene route is assisted by $CO_2^{\bullet -}$ attachment to a carbon atom. Combined methane and methanol formation has been observed on multiple occasions and the results match with computational studies, therefore, carbene route appears to be more possible.[157, 160-163] An EPR study showed that CO_2 reduction pathways cannot pass either through formaldehyde or methanol and new glyoxal pathway was postulated.[164] The new approach avoids intermediates that could block the process before reaching methane product.

Operating parameters of the reaction such as pressure, temperature, light source, intensity and especially pH have a major impact on the activity and selectivity of the reaction. Change of atmospheric pressure and room temperature are not desired because these would require additional energy input, which leads to less economic and benign to nature conditions. The light source is expected to be natural solar light. The main optimisation that is performed is pH of the reaction medium. Under basic pH, the conduction band of the photocatalyst becomes more reductive[37] and CO_2 photoreduction is more favourable. However, at the same time carbonates, bicarbonates are produced more often which are good quenchers of holes and are more stable than CO_2 thus harder to reduce. Under acidic conditions, a lower CO_2 reduction potential is observed leading to a water splitting reaction competing with CO_2 reduction and producing hydrogen gas as a product. However, an acidic pH could shift the conductance band towards to be more positive and it would become more favourable to reduce carbon dioxide to methanol.[17]

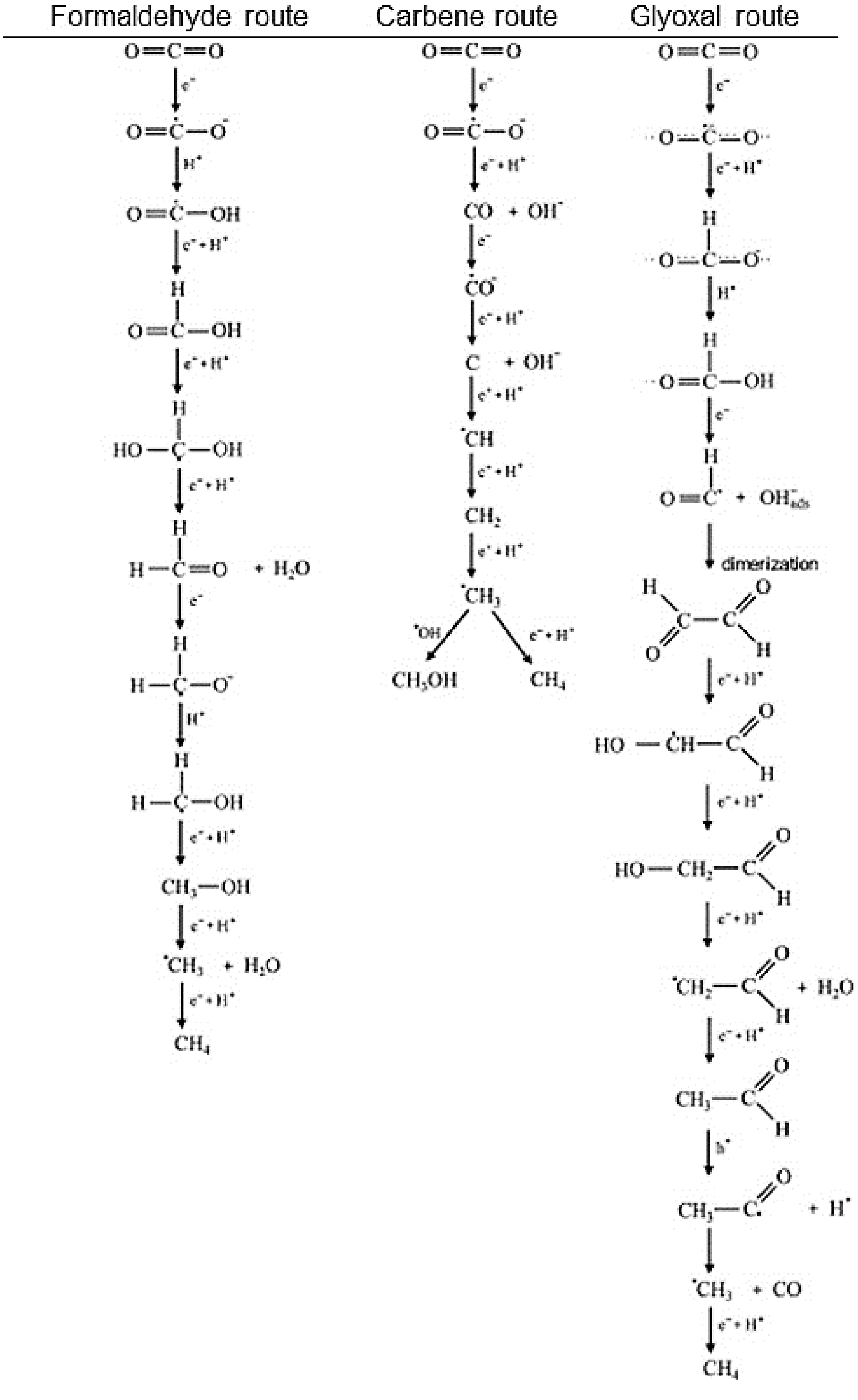

Figure 1.14 Three proposed mechanism of CO_2 reduction to methane: formaldehyde, carbene and glyoxal. Adapted from ref 27.

1.6 The aim of the thesis

Despite significant advances in our mechanistic understanding of the heterogeneous photocatalytic processes, notably in water depollution and splitting as well as CO_2 photoreduction, the development of high activity photocatalysts has progressed in large part through empirical approaches to materials discovery. Numerous examples of the exotic photocatalyst architectures have appeared in the recent literature; however, most employ complex multi-step syntheses, non-recyclable templates, and/or earth scarce or toxic components, and hence are neither scalable nor sustainable.[165-167] Control over the structural and photophysical properties of catalysts is critical to understanding their impact on photocatalysis and hence progress the rational design of improved functional materials. Effect of pore framework in terms of mesopores and macropores provides an important step towards understanding the synergy between catalyst architecture, the impact on its promoter species and the resulting photocatalytic activity. Considering all of these aspects, the aims of this research are focused on the following objectives:

- Explore a facile route to control the porosity and photophysical properties of the high area, mesoporous TiO_2 via thermal processing of a sol-gel (surfactant-templated) synthesis.
- Assess the impact of macropores and their size to hierarchical macro-mesoporous architectures and the following activity.
- Investigate physicochemical properties of co-catalysts, and understand how these impact upon support activity by post-functionalisation of mesoporous and macro-mesoporous TiO_2 surfaces using copper and platinum.
- Test the different mesoporous and macro-mesoporous photocatalysts to evaluate the most influential properties that affect their activity for three different reactions (Methyl Orange degradation, water splitting and CO_2 photoreduction), and compare their activity across the series and to existing commercial or related catalysts in literature.

Chapter 2

Experimental

2 Experimental

2.1 Synthesis

2.1.1 Chemicals

Titanium (IV) n-butoxide (ACROS Organics, 99.0%), Pluronic F-127 (Sigma – Aldrich), Nitric acid (Fisher, 70%), Ethanol (Fisher, analytical reagent grade), Styrene (Sigma Aldrich, >99%), Potassium Persulphate (Sigma Aldrich, >99%) Copper (II) nitrate trihydrate (ACROS Organics, 99%), Chloroplatinic acid hexahydrate (ACROS Organics, 99.9%. Trace metal basis), Methyl Orange (Sigma – Aldrich, Reag. Ph. Eur.), sodium sulphite (Sigma – Aldrich, 98%), commercial anatase (ACROS Organics, 98.0%), rutile (Sigma – Aldrich, 99.99%) and P25 (Sigma – Aldrich, 99.5%).

2.1.2 Synthesis of mesoporous titania

Mesoporous TiO_2 was synthesised through surfactant templating synthesis (**Figure 2.1)** where non – ionic triblock copolymer Pluronic F-127 (12,600 g mol^{-1}, 7.7 g) was dissolved in ethanol (120 ml) followed by HNO_3 (6.3 ml) and titanium (IV) n-butoxide (16 ml) under rapid stirring. The solution was left stirring at room temperature for 6h and then transferred to the oven for solvent evaporation at 50 ^{o}C for 18 h. The resulting gel was calcined in a muffle furnace at temperatures between 300 – 900 ^{o}C (1 ^{o}C min^{-1}) for 4 h and finally ground to a fine powder.

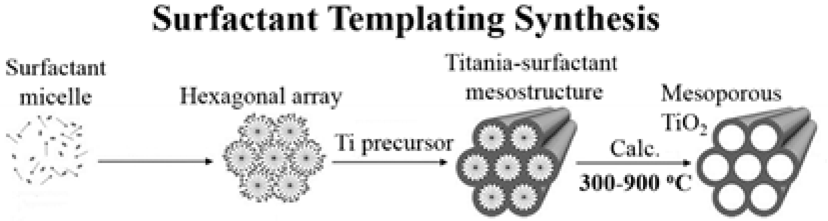

Figure 2.1 Schematic representation of the surfactant templating synthesis.

2.1.3 Synthesis of polystyrene beads

Polystyrene beads were synthesised by an emulsifier-free emulsion polymerization using a modified literature protocol[168]. The large scale reaction was performed on Radleys Reactor Ready 2000 ml (**Figure 2.2**). Depending on the desired polystyrene bead size water solvent volume was varied. Deionised water (**Table 2.1**) was outgassed with N_2 under stirring at room temperature overnight. Styrene (105 ml) was separately washed with an equal volume (100 ml) of 0.1 M NaOH solution (×5) and deionised water (×5). Potassium persulphate initiator solution was independently prepared by dissolving 0.33 g in 50 ml of deionised water at 80 °C under N_2 and stirring. The reactor was heated to 80 ^{o}C, then styrene was first slowly dropwise injected into the reactor and after 1 h initiator potassium persulphate solution was added. The reaction mixture was left stirring (300 rpm) at 80 °C for 24 h. The product polystyrene beads were recovered by centrifugation for 2 h at 8000 rpm to get ordered similar size PS beads and left to dry at RT for 3-4 days. To obtain reasonable SEM data, the size of the resulting polystyrene beads was determined using the polymer emulsion collected at the end of the synthesis. Polystyrene beads that were isolated and dried from the synthesis medium did not redisperse well in any solvents.

Figure 2.2 Radleys Reactor Ready 2000 ml used for polystyrene beads synthesis.

Table 2.1 Polystyrene bead size and corresponding reaction conditions.

PS bead size (SEM) / nm	Water solvent volume / ml
140	1000
200	850
310	400

In order to achieve large diameter beads, small scale polystyrene bead synthesis adapted from Im et al. method[169] where deionised water (5 ml) and ethanol (40 ml) was outgassed with N_2 under stirring at 80 °C for 1 h. Styrene (5 ml) was separately washed with an equal volume (10 ml) of 0.1 M NaOH solution (×5) and deionised water (×5). Potassium persulphate initiator solution was independently prepared by dissolving required amount (**Table 2.2**) in 5 ml of ethanol under N_2 and stirring at room temperature. Firstly, polyvinylpyrrolidone (PVP, 0.4 g) was dissolved in the reaction solution, then styrene was injected dropwise and lastly, initiator potassium persulphate solution was added. The reaction mixture was left stirring (300 rpm) at 80 °C for 24 h. The product polystyrene beads were recovered by centrifugation for 2 h at 8000 rpm in order to get ordered similar size PS beads and left to dry at RT for 3-4 days.

Table 2.2 Potassium persulphate mass and corresponding PS bead size.

PS bead size (SEM) / nm	Potassium persulphate/ g
240	0.178
290	0.330

2.1.4 Synthesis of macro-mesoporous titania

Macro-mesoporous TiO_2 was prepared by soft-hard templating combining a sol-gel method discussed above (**2.1.2 Synthesis of mesoporous titania**) with hard polystyrene template (**2.1.3 Synthesis of polystyrene beads**). During synthesis block copolymer Pluronic F-127 (7.68 g; 12 600 g mol^{-1}) was dissolved in ethanol (120 ml) with the addition of nitric acid (6.3 ml). Ti (IV) n-butoxide (16 ml) was added slowly dropwise to the reaction mixture and left stirring for 6h at room temperature. Five minutes before the end of stirring, polystyrene beads (4 g) were introduced as a hard template to form macropore framework. The resulting sol solution was left aging in Petri dishes in the oven for solvent evaporation at 50 ^{o}C for 18 h then calcined at 400 ^{o}C (1 ^{o}C min^{-1}) for 8h under air.

2.1.5 Cu deposition

A family of copper loaded titania materials were prepared by deposition of 0.02 – 12.33 wt% Cu on mesoporous TiO_2 500 °C and 0.1 wt% on mesoporous TiO_2 400 – 800 ^{o}C and macro-mesoporous TiO_2 supports by incipient wetness impregnation method using Cu (II) nitrate trihydrate precursor in deionised water. The aqueous solution was stirred in the dark at 50 ^{o}C for 17 h till the dry powder was obtained. The resulting solid was re-calcined at 400 ^{o}C (ramp rate 10 ^{o}C min^{-1}) under flowing O_2 gas (10 ml min^{-1}) for 2 h and ground to a fine powder.

2.1.6 Pt deposition

Platinum functionalised materials were prepared by subsequent wet impregnation of chloroplatinic acid hexahydrate solution of chosen concentration on the mesoporous TiO_2 series 300 – 900 ^{o}C (**2.1.2 Synthesis of mesoporous titania**) and macro-mesoporous TiO_2 supports (**2.1.4 Synthesis of macro-mesoporous titania)** series to achieve 1.8 wt% Pt loading. The aqueous slurry was stirred in the dark at 50 °C for 18 h until a dry powder was obtained, and the resulting solid subsequently reduced at 100 °C (ramp rate of 10 °C.min^{-1}) under flowing hydrogen (10 ml.min^{-1}) for 1 h, and finally ground to a fine powder.

2.2 Characterisation techniques

2.2.1 Nitrogen porosimetry

Nitrogen porosimetry is a quantitative method involving nitrogen physisorption to accessible surfaces under pressure to measure textural and physical characteristics of porous materials, for example, pore diameter, volume, shape, specific surface area, bulk and absolute densities. Nitrogen sorption isotherms were recorded on Nova 4000e and Nova 4200e porosimeters and data were analysed using the Quantachrome NovaWin v11.03 software. Samples were degassed at 120 ^{o}C under vacuum for 16 h prior the analysis.

Adsorption/desorption isotherms are recorded based on the volume of nitrogen adsorbed/desorbed at different relative pressures (P/P_o) and provide information about the structure and properties of the material. Adsorption, at constant temperature and pressure, reduces the entropy of a system, therefore the enthalpy of adsorption must be exothermic (negative)[170] for gas surface collisions to take place (Gibbs free energy).[171] There are two types of collisions between gas molecules and the surface of the sample: either elastic (i.e. no interaction), or inelastic where energy loss from the adsorbate to the adsorbent make this an exothermic process. If resulting energy loss prevents desorption and no more energy is transferred through the formation of chemical bonds, it is assigned as physisorption.[35] N_2 physisorption can occur only at temperatures below the adsorbate boiling point[171], due to the weak/low enthalpy of adsorption. The enthalpy of condensation (vaporisation) from adsorbate-adsorbate interactions is very similar to the enthalpy of adsorption, which allows multilayer formation.[172]

N_2 adsorption and multilayer formation occurs at liquid nitrogen temperature (-196 ^{o}C) and rises from induced temporary dipoles due to fluctuation in electron density, known as London forces.[171] Nitrogen porosimetry involves gradually dosing N_2 and recording the adsorbed amount at a known pressure and constant temperature (dynamic equilibrium where the rate of adsorption is equal to the rate of desorption).[172] An isotherm is constructed by plotting the amount of adsorbate against the partial pressure of the system. The shape of the isotherm reveals information about layers of N_2 molecules on the surface. Based on IUPAC nomenclatures there are 6 different types of isotherms (**Figure 2.3**). [173, 174]

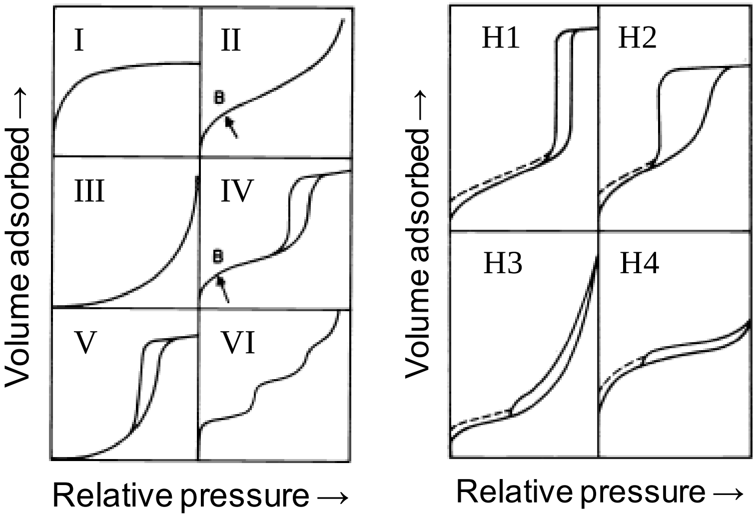

Figure 2.3 Six types of different isotherms and 4 types of hysteresis loop based on IUPAC nomenclature where x-axis corresponds to P/P_o and y-axis to volume adsorbed (g cm^{-3}). Adapted from reference 175.

Type I depicts a microporous material – short distance between adsorbate-adsorbent leads to strong interaction, type II is characteristic of a non-porous or macroporous material, type III is the consequence of stronger adsorbate-adsorbate interactions compared to adsorbate-adsorbent, type IV and V exhibit a hysteresis loop, which is the result of capillary condensation in the mesoporous materials and type VI shows a gradual formation of adsorbate layer on a highly uniform surface.[175] Hysteresis loops, observed in type IV and V, appear because of differences in the adsorption and desorption processes and provide an insight into mesopore environment. Adsorption arises via a capillary condensation mechanism, from the pore walls inwards, whereas desorption starts at the liquid surface, at the pore opening. Evaporation occurs at a lower pressure compared to condensation where the interactions are stronger due to the close proximity of adsorbate and pore wall, and that produces the hysteresis.[172] The hysteresis shape depends on the pore shapes and there are four types (**Figure 2.3)**: H1 from uniform pore sizes, whereas H2 - non-uniform ink-bottle shape pores, H3 and H4 are the results of slit type pores.[175]

In order to quantify specific surface area, pore size and volume, sorption isotherms are not sufficient thus theoretical calculations need to be applied. The most common mathematical model to calculate specific surface area is BET (Brunauer-Emmett-Teller)[176] (**Equation 2.1**) which is an extension of Langmuir theory to accommodate multilayer formation via additional parameter c. The theory assumes that adsorbent molecules are distributed on the surface in infinite layers without any interaction with each other and each layer obeys Langmuir theory. It calculates the volume of adsorbent (V_m) corresponding to a mono layer of gas adsorbed on the solid surface at the linear region P/P_o= 0.05-0.35.

$$\frac{1}{V[(P_o/P)-1]} = \frac{c-1}{V_m c}\left(\frac{P}{P_o}\right) + \frac{1}{V_m c}\ ; \quad V_m = \frac{1}{(gradient + intercept)}; \quad c = \frac{(gradient)}{(intercept)} + 1$$

Equation 2.1 BET equation, where P and P_o are the equilibrium and saturation pressure, V is adsorbed volume and V_m is adsorbed monolayer volume, c is the BET constant.

The obtained monolayer volume V_m is used to calculate the total surface area (**Equation 2.2**) assuming closed packed N_2 molecules with 0.162 nm^2 occupied area (s). [171, 172, 174]

$$Surface\ Area = \frac{(V_m N_A s)}{V}$$

Equation 2.2 Total surface area equation, where N_A is Avogadro's number, s - adsorption cross-section (0.162 nm^2) and V is adsorbed volume.

For mesopore size and volume, the BJH (Barrett-Joyner-Halenda) method is employed which uses a modified Kelvin equation (**Equation 2.3**).[172] It evaluates partial pressure at which adsorbate will spontaneously condense (and evaporate) in a cylindrical pore at multilayer sample coverage. The average pore size is equal to the sum of Kelvin radius (radius of the meniscus in the pore) calculated from desorption data for relative pressures >0.35 and statistical thickness (t) of the adsorbed film (estimated using t-plot). The total pore volume is determined from the maximum amount of gas adsorbed at P/P_o =1 and conversion of the gas volume into the liquid volume. Multilayer formation is modelled mathematically to calculate a layer thickness (t), as a function of increasing relative pressure (P/P_o) in the linear range of 0.2-0.5, which is known as a t-plot. The slope of the t-plot is equal to the area of those pores (mesopores and macropores) that can form multilayer while micropores cannot. For a known monolayer volume following adsorbate layers can be evaluated.[172]

$$ln\frac{P}{P_o} = \frac{-2\gamma V_m}{r_k RT} cos\theta$$

Equation 2.3 Modified Kelvin equation, P/P_o – relative pressure of vapour in equilibrium with condensed gas meniscus, r_k is the Kelvin radius, γ – liquid surface tension, θ – adsorbate surface contact angle (0 for N_2, cos(0)=1), R – universal gas constant and T is temperature.

2.2.2 X-ray Diffraction (XRD)

X-ray diffraction is a technique where the crystalline atoms cause a beam of X-rays to diffract into many specific directions and by measuring the angles and intensities of these diffracted beams crystalline phase content, order, crystallite size, d-spacing, pore wall thickness and lattice parameters can be determined. There are two types of XRD techniques: wide angle determining crystallinity and crystallite size and low angle which provides pore packing information. Powder X-ray diffraction eliminates the need for a single crystal, instead, a small sample of the material grounded to a powder are used, allowing nanocomposites, hierarchical structures and metal nanoparticles to be studied.

XRD patterns were recorded on a Bruker D8 Advance diffractometer (40 kV, 40 mA) fitted with a LynxEye high-speed strip detector which uses Cu Kα (1.54 Å, 8.04 keV) source with a nickel filter, calibrated against a SiO_2 standard. Wide angle patterns were recorded over a range of 2θ = 10-80° (step size 0.02°, scan speed 0.020 ° s^{-1}) and low angle patterns over a range of 2θ = 0.45-8° (step size 0.01°, scan speed 0.014 ° s^{-1}).

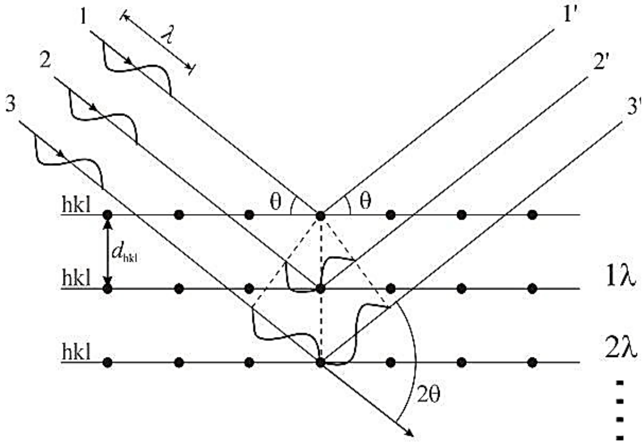

Figure 2.4 Schematic representation of X-ray interaction with crystal lattice.

X-ray photons generated in a Cu anode via demotion of higher energy electron to lower energy vacancy are fired at the powder sample. Monochromatic X-ray striking a polycrystalline sample give rise to a cone of diffraction from the endless array of orientations/planes. The atoms in crystalline materials are arranged in a regular order, resulting in planes of atoms that scatter the X-ray by different amounts depending on the plane spacing d. Only scattering of electrons that are in phase will form constructive interference (amplification of the wave) from crystal planes (wide angle) or ordered pore walls (low angle) leading to diffraction pattern characteristic of the specific material (**Figure 2.4**). The angle at which the peaks occur in the spectra is related to the d-spacing of the plane of the crystal lattice. Based on Bragg's Law (**Equation 2.4**) constructive interference for set diffraction angles (θ) is detected exclusively if the distance between scatters (d) is equal to an integer (n) multiplied by the X-ray wavelength (λ). Crystal structure of the material and lattice dimensions can be determined.

$$\lambda n = 2d\sin\theta$$

Equation 2.4 Bragg's Law.

From the wide angle XRD data, average crystallite sizes were estimated from line broadening based on full width half maximum (FWHM) of diffraction peaks using Scherrer equation (**Equation 2.5**).[177] Minimum detectable crystallite size is ~ 2 nm[178]. In general, smaller particle size leads to broader peaks[179]. For peaks to be sharp, slightly away of the 2θ, destructive interference needs to occur. Only small amount of the diffracted waves are out-of-phase thus many planes are needed to completely remove waves. When the crystallites are in nanoscale the number of planes and thus the destructive interference is insufficient and results in broader peaks. Peak fitting was performed using Diffrac.Eva software.

$$PS_{ave} = \frac{k\lambda}{\sqrt{(FWHM)^2 - S^2)Cos\theta}}$$

Equation 2.5 Scherrer equation for particle size, where PS_{ave} = particle size (Å), FWHM= full width half maximum of the peak, S = 0.15 (systematic broadening caused by diffractometer); k = 0.9 (constant).

In addition, percentages of anatase and rutile crystalline phase can be determined from XRD diffractograms using Spurr – Myer's equation (**Equation 2.6**) where I_R and I_A are the intensities of the rutile TiO_2 (110) and anatase TiO_2 (101) peaks.[180]

$$\%\ Anatase = \frac{1}{1+1.265\frac{I_R}{I_A}}x100\ \% \text{ and } \%\ Rutile = \frac{1}{1+0.8\frac{I_A}{I_R}}x100\%$$

Equation 2.6 Spurr – Myer's equation for quantifying anatase rutile mixtures with XRD, where I_A and I_R are relative/integral intensities of the most intense anatase and rutile peaks respectively.

The peak height and position is directly related to the unit cell arrangement of the crystal structure or ordered pores. There are seven crystal systems that are used to classify the structure of crystalline materials which are incorporated into the basic lattice types (cubic, face-centred cubic, base-centred cubic and body-centred cubic) to form one of 14 unique 'Bravais Lattices'.[181] The lattice spacing *a* of the catalysts for the tetragonal systems is determined from the relationship between Bragg's law and Miller indices (**Equation 2.7**) which are used to notate planes in Bravais lattice. Wide angle X-ray measurements pick up diffraction of different Brag angles which correspond to individual planes, allowing full crystal structure to be detected.[182, 183] From the low angle XRD data lattice (d) and pore spacing (a) were calculated for the hexagonal mesopore architectures d (100) where $\sqrt{(h^2 + k^2 + l^2)} = 1$ simplifies the equation.

$$d = \frac{\lambda\sqrt{(h^2+k^2+l^2)}}{2Sin\theta} \text{ and } a = \frac{2d}{\sqrt{3}}$$

Equation 2.7 Relationship between Bragg's law and Miller indices for lattice (d) and pore (a) spacing calculations where λ - wavelength of Cu Kα radiation (0.154nm); h, k, l - Miller indices; θ - diffraction angle.

2.2.3 Electron microscopy

HRSTEM (High-resolution scanning transmission electron microscopy) and SEM (Scanning electron microscopy) analyses were employed to observe the surface structure of the synthesised catalysts e.g. porosity, particle and composite dimensions through localised direct imaging of samples. STEM images were recorded on a JEOL 2100F FEG STEM operating at 200 keV and equipped with a spherical aberration probe corrector (CEOS GmbH) at the University of Birmingham by Dr C. Parlett and Dr M. Isaacs. Samples were prepared for microscopy by dispersion in methanol and drop-casting onto a copper grid coated with a holey carbon support film (Agar Scientific). Images were analysed using ImageJ v1.46r software. SEM images were recorded on a Carl Zeiss EVO MA15 W SEM operating at 10 kV at the University of Leeds. Samples were placed on aluminium stubs using adhesive carbon tape and coated with gold to reduce charging.

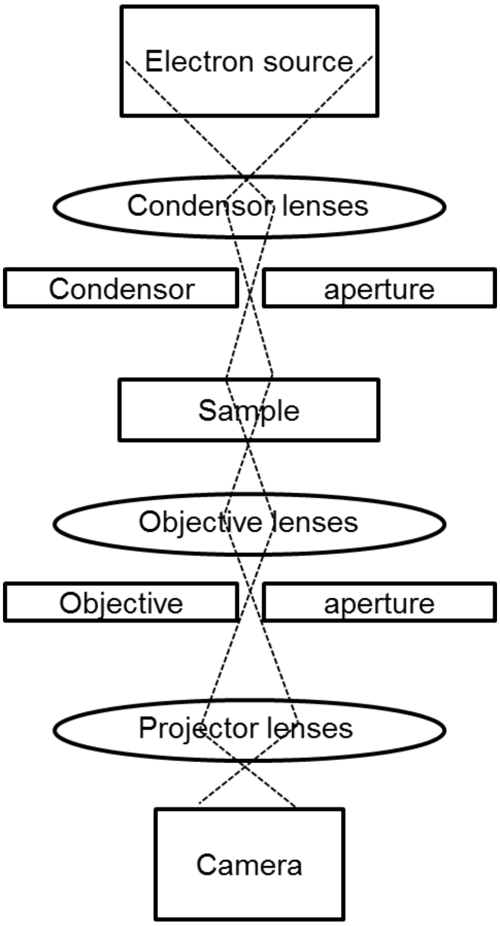

Figure 2.5 A schematic representation of HRSTEM imaging. Adapted from ref 185.

The wavelength of electrons (~12.3 pm at 10 kV decreasing to 2.5 pm at 200 kV) is considerably shorter than both visible light (380 – 750 nm) in an optical microscope and X-ray radiation, enhancing microscope resolution to an atomic level under high-resolution STEM conditions.[184] STEM is a microscopy technique in which a beam of electrons raster over sample and is transmitted through an ultra-thin specimen by multiple electromagnetic lenses and it interacts or not with the specimen while passing through which produces Z contrast - a black and white image (**Figure 2.5**). [184, 185] A 2D image is produced where the contrast depends on many of features, including thickness, atomic mass and density of the sample. Depending on the weight of the atomic nuclei the electrons are scattered differently allowing to separate phase of composite materials; the higher the atomic mass of the element the stronger it diffracts and appears brighter.[186]

SEM images are developed by detection of secondary electrons that form from the shift of a k orbital (1s) electron.[184] The low energy (50 eV) secondary electrons induce surface sensitivity as their escape from the bulk is obstructed. The electron beam raster over the sample and the beam's position is combined with the detected signal to produce a 3D image where contrast is generated from the morphology of the sample. Surface, with the same angle as the beam, is brightest with increasing darkening as surfaces tilt towards being parallel to the beam.

2.2.4 Inductively coupled plasma optical emission spectroscopy (ICP-OES)

ICP-OES was employed for quantitative elemental analysis of samples through utilisation of microwave digestion system to detect the amounts various elements e.g. Cu and Pt present in a sample even in sub ppb limits. ICP- OES was performed using Thermo iCAP 7000 ICP-OES and a calibrated to an element standard (Sigma Aldrich, 1000 ppm) made up to give concentrations of 1, 10, 25, 50 and 100 ppm. Samples were digested in nitric, sulphuric and hydrofluoric acids in a microwave digester prior analysis.

ICP-OES is a type of emission spectroscopy that uses the inductively coupled plasma to produce excited atoms and ions that emit electromagnetic radiation at wavelengths characteristic of a particular element. The ions are produced using an argon plasma source, which is heated to around 8000 ^{o}C to form an ion. The aqueous solution containing sample is passed through a nebuliser, allowing the sample to enter the plasma torch as an aerosol. The sample immediately collides with the electrons and charged ions in the plasma and is broken down into ions. The molecules break down to corresponding atoms which then lose electrons and recombine regularly in the plasma, giving off radiation at the characteristic wavelengths of the elements involved.

2.2.5 X-ray photoelectron spectroscopy (XPS)

XPS is a surface-sensitive quantitative spectroscopic technique that measures the elemental composition (parts per thousand), empirical formula, chemical environment, coating thickness and oxidation state of the elements within a material. XPS data were collected using a Kratos AXIS HSi instrument, equipped with a charge neutraliser and using a monochromated Al Kα (1486.6 eV) X-ray source. High-resolution spectra were recorded using pass energy of 40 eV. Data obtained was analysed and fitted using CasaXPS Version 2.3.15. All spectra were charged corrected to the 1s carbon region at 284.6 eV with elemental sensitivity factors applied to quantify sample composition. Errors were estimated by varying a Shirley background across reasonable limits.

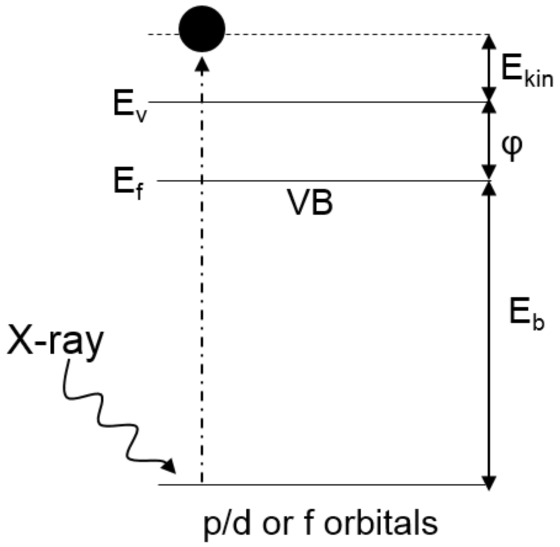

Figure 2.6 Illustration of photoelectron ejection where E_{kin} – photoelectron kinetic energy, E_b – electron binding energy, φ – spectrometer work function, E_f – Fermi level, E_v – vacuum level.

XPS spectrum is obtained by irradiating a material with X-rays beam while simultaneously measuring the kinetic energy and number of escaping electrons. Mg Kα (1253.6 eV) and Al Kα (1486.6 eV) are classified as soft X-rays due to their low energy compared to XAS (**2.2.6 X-ray adsorption spectroscopy**) and do not require synchrotron radiation.[187] This technique is based on the principles of the photoelectric effect, mainly that altering the energy of the incoming radiation affects the kinetic energy of the released photoelectrons; materials absorb X-ray photons and eject core-level photoelectrons with different kinetic energies (**Figure 2.6**).[170, 179] Kinetic energies depend on the element and its environment, such as orbital and the coordination/oxidation state. XPS probes only the surface of the material because of only a short distance that an electron can escape (1-3 nm) and thus is performed in UHV conditions (typically <10^{-9} bar). The short escape distance (mean free path) is due to interactions between ejected electron and electrons of other atoms.[188] Generally, spectra are plotted as a function of the binding energy which is calculated using kinetic energy relationship in **Equation 2.8.** Spectrometer work function represents the energy required (ionisation potential) to eject an electron at the Fermi level into the vacuum.[179]

$$E_{kin} = h\nu - E_b - \varphi$$

Equation 2.8 Relationship between the kinetic energy of ejected electrons and the binding energy of the photoelectrons, where E_{kin} – photoelectron kinetic energy, hν – photon energy of X-ray, E_b – electron binding energy, φ – spectrometer work function.

The calculated binding energies can be matched to a database of standards from the National Institute of Standards and Technology (NIST) photoelectron spectroscopy database to determine the chemical identity and gain information regarding the chemical environment.[189] Oxidation state and sample composition influence shift of binding energy of an element.[188] For example, the binding energy of Pt(II) is 1.4 eV higher than Pt(0) due to the greater attractive force of the nucleus felt by 76 electrons over 78. In most cases, outermost filled electron shell is probed because it experiences the greatest effect of the changes and would give the strongest signal.

When electrons are ejected, orbitals with angular momentum (> 0, i.e. s, p, d and f orbitals) are influenced by spin coupling between orbital angular momentum (l) and electron spin (m_s) magnetic fields, with the sum of the two giving total angular momentum (j). This interaction is either favourable or not, as is either anti-clockwise (+½) or clockwise (-½) and thus two values for j exist.[179] Peak doublets with ratios equal to $2j+1$ observed in XPS spectra are a result of this spin coupling. For d orbitals the intensity ratio is 3:2, as l= 2 and thus j= 5/2 and 3/2. Favourable coupling increases binding energy and occurs when forces oppose, j= 3/2. Energy donation from an escaping photoelectron to another bound electron causes asymmetric peak broadening towards higher binding energies. This reduces the measured kinetic energy value of the escaping photoelectron and thus artificially inflates its reported binding energy. Photoelectrons formed further from the surface loose more energy which leads to the stepped background of XPS spectra.

Ti(0) possess Ti $2p_{3/2}$=453.9 eV, while Ti(II) $2p_{3/2}$=455.5 eV and Ti(III) $2p_{3/2}$=457.3 eV binding energies for the Ti atoms in TiO_2 species. Ti 2p peak has significantly split spin-orbit components. The binding energies for Ti(IV) (TiO_2) 2p core levels correspond to Ti $2p_{3/2}$ =458 eV and Ti $2p_{1/2}$ =464 eV. Ti metal gives asymmetric peak shapes while TiO_2 – symmetric. Pt 4f XP spectra of Pt(0), Pt(II) (PtO) and Pt(IV) (PtO_2) display spin–orbit split doublets of 4f7/2 = 71 eV, 4f7/2 =72.4 eV and 4f7/2 = 74.9 eV respectively with Pt metal peaks being asymmetric shape like for titanium while Pt(II) and Pt(IV) peaks - symmetric.

2.2.6 X-ray adsorption spectroscopy (XAS)

XAS (X-ray adsorption spectroscopy) measurements is an effective technique to evaluate oxidation state and local environments of the atoms, even at ultra-low quantities. Experiments were conducted at XAFS beamline at Elletra Synchrotron Trieste (Italy) using a Si(111) and Si(311) double crystal fixed exit monochromator with silicon drift detector to record fluorescence. Fluorescence and transmission spectra of Cu (8987.96 eV) K-edge were acquired of the powder catalyst samples after dilution with BN. XANES and EXAFS spectra were normalised, background subtracted, and fitted to Cu_2O, CuO, Cu_2NO_3 and Cu foil standards, using the Athena and Artemis components of the IFEFFIT software suite (1.2.11d) respectively. EXAFS fittings using the Artemis software were performed by Dr C. M. A. Parlett.

XAS, similarly, to XPS, involves the generation of photoelectrons, however, instead of direct evaluation, the technique assesses their influence on the resulting X-ray photon adsorption. This eliminates the need for ultra-high vacuum systems and permits characterisation of materials under atmospheric conditions and more importantly the option of in-situ/operando measurements.[190] Adsorption of X-ray photons, ejects an electron as a photoelectron if its energy is greater than the binding energy of the electron.[188] Generally, electrons from a shell close to the nucleus are targeted, which results in transformations with increasing energy demand. When photoelectron is discharged, the atom is excited by virtue of the unfilled electron orbital and affects subsequent X-ray photon adsorption. Fluorescence, ‘electron-hole’ shifting or adsorption of scattered photoelectrons, including backscattering of the original, can partially stabilise this excitation state. X-ray absorption is modulated by the constructive and destructive interference of photoelectron waves scattered by neighbouring atoms that are photoexcited.[179] Obtained spectra provides bulk information regarding both electronic and local geometric environment, even where sample lacks periodicity.[187]

Generally, photon energies are set from ~300 eV below to ~1000 eV above the adsorption edge, this being the minimum energy required for X-ray photon adsorption (photoelectron generation). XANES region (which is first 100 eV after the adsorption edge) by using photoelectron and valence electron interactions provides oxidation state information.[179, 188] A result of the relatively low photoelectron kinetic energy which arises due to the close proximity between incident X-rays and electron binding energy, EXAFS region spans for ~1000 eV or as far as oscillations are observed. These photoelectrons possess higher kinetic energy, on the grounds of the increasing incident X-ray energy, which allow them to transmit further. Single and multiple scattering of the photoelectrons by the surrounding atoms provides information about local geometry.

XAS for Cu(I) and Cu(II) species show three/two distinct features: a weak pre-edge feature around 8977 eV, a strong rising-edge feature around 8986 eV, and an intense white line around 8996; these are attributed to dipole-forbidden $1s \rightarrow 3d$ (not observed for Cu(I) species), $1s \rightarrow 4p_z$ (or 4px,ypz for Cu(I) species) and $1s \rightarrow 4p$ (continuum) transitions respectively.

2.2.7 Temperature programmed oxidation (TPO)

Thermogravimetric analysis (TGA) is a thermal analysis method which monitors the evolution of physical and chemical properties of the materials a function of temperature, via associated mass losses and heat flow (endothermic or exothermic processes). Mass variation changes of the solid that are measured as a function of increasing temperature over constant heating rate or as a function of time with constant temperature with the application including oxidation, reduction, desorption reactions under suitable gas atmosphere. TPO is a type of TGA where the mass change of the solid is measured as a function of increasing temperature under oxidative conditions (oxygen gas flow). TPO analysis was conducted using Mettler Toledo TGA – DSC 2 thermal analyser equipped with an autosampler. Data was collected from 45-800 ^{o}C (10 ^{o}C min^{-1}) under flowing N2/O2 (40:20 v/v 60 ml min^{-1}). The instrument usually consists of a high-precision balance connected to a sensor with a thermocouple to accurately measure the temperature within the furnace chamber. The sample is placed on the sensor together with reference pan.

2.2.8 UV-vis spectroscopy

UV-vis spectroscopy enables to measure optical properties of the materials in solution and solid state. It is a vital tool for quantitatively detecting dissolved quantities of highly conjugated organic dye molecules. For liquid UV-vis optical absorption measurements, Thermo Scientific Evolution 220 UV-vis spectrophotometer equipped with Xe lamp and Vision software was used. The absorption spectra of methyl orange degradation reaction mixture were recorded in the 200-700 nm range using 0.4 ml quartz micro-cuvettes. For the time profiles and the initial rate calculation, the 464 nm Methyl Orange peak is followed.

Molecules possessing π or non-bonding electrons as well as semiconductors can absorb energy from UV-vis light to excite electrons from lower energy level (HOMO for molecules; valence band for semiconductors) to higher energy level (LUMO, conductance band respectively). If light absorption occurs in visible region compounds are coloured. The energy absorbed in an electronic transition between ground (lower) to excited (higher) states and the relationship with the frequency or wavelength of radiation producing the transition is expressed in Planck-Einstein relation (**Equation 2.9**).

$$\Delta E = h\nu = h\frac{c}{\lambda}$$

Equation 2.9 Planck-Einstein relation where h is Planck's constant, ν-frequency, c-speed of light, λ-wavelength.

Methyl orange molecule is a chromophore and appears orange in water solution. The delocalised electrons of conjugated bonds of the molecule are excited by UV-vis light and produce two bands: $\pi \rightarrow \pi^*$ (464 nm) and $n \rightarrow \pi^*$ (277 nm) (**Figure 2.7**). UV-vis spectroscopy of molecules, the energy absorbed is determined by the difference between HOMO and LUMO where the larger difference leads to the lower wavelength of absorption and vice versa. The position of the absorption band is equal to the energy of a wavelength of radiation required to excite the electron. The intensity of the absorption depends on the probability of interaction between light and electronic system and energy required for excitation. Beer-Lambert's law (**Equation 2.10**) is applied to calculate absorbance.[191]

$$A = \varepsilon c l$$

Equation 2.10 Beer-Lambert's law where A- measured absorbance, ε-molar absorptivity, l-path length of the cuvette, c-concentration.

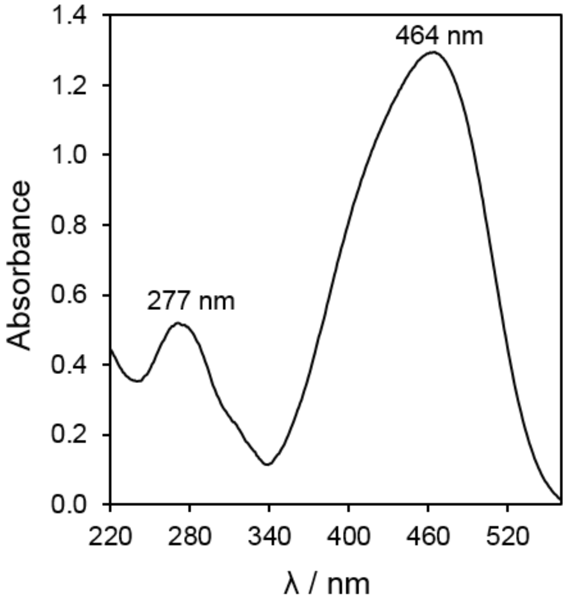

Figure 2.7 Methyl Orange molecule in water UV-vis absorbance spectrum.

2.2.9 Band gap calculations

Solid DRUVS (Diffuse reflectance UV-vis spectroscopy) spectra of semiconductors measure electron excitation from valence to conductance band – the band gap of the catalyst. It was recorded on a Thermo Scientific Evolution 220 spectrophotometer equipped with an ISA – 220 accessory.

The band gap of the semiconductor plays a very important role in the photocatalytic activity. It indicates the difference between the top of the valence band (VB), filled with electrons, and the bottom of the empty conductance band. Usually, metals do not have any band gap or it is lower than 0.05 eV, while for insulators the band gap is usually greater than 3.5 eV leaving semiconductors in between.

Electrons present in a valence band undergo electron transition when enough energy is shone on the semiconductor. There are two types of valence to conductance band transitions – direct and indirect (**Figure 2.8**).[192] In direct transition (marked a) an electron is promoted from the highest level of the valence band to the lowest level of the conductance band and an additional phonon is not required. While indirect transitions (marked c) require an additional phonon to conserve momentum. Line b illustrates forbidden in this case direct transition which needs more energy because it disobeys selection rules. The graph clearly shows the defined edge between CB and VB which corresponds to the band gap and can be observed using UV-vis absorption techniques (**Figure 2.8**).

Figure 2.8 Illustration of electronic transitions that can occur in semiconductors where a – direct transition, b – forbidden direct transition, c – indirect. Reprinted from ref 192.

A band gap is called direct, if electrons of the valence band maximum and holes of conductance band minimum possess the same momentum and kinetic energy and electrons directly absorb a photon. In an indirect band gap, the maximum energy of the valence band occurs at different values to the momentum of the conduction band minimum, thus an additional energy input of a phonon is required to promote an electron. As seen in **Figure 2.9**[193] anatase exhibits an indirect band gap that is smaller than its direct band gap. Therefore the most energetically efficient and most likely transition will be an indirect allowed transition (**Figure 2.9 a**). For rutile, on the other hand, its indirect band gap is very similar to its direct therefore direct allowed transition (**Figure 2.9 b**) is more likely because indirect transitions require one additional photon to conserve the momentum. Forbidden transitions can take place but the probability is extremely low.

Figure 2.9 Calculated energy-band structures for rutile and anatase. Reprinted from ref 193.

The band gaps were determined from a Tauc plot using a Kubelka-Munk function from absorption of diffuse reflectance spectra. The expression proposed by Tauc, Davis and Mott. $(h\vartheta\alpha)^{1/n} = A(h\vartheta - E_g)$, where h-Planck's constant, ϑ - vibrational frequency, α - absorption coefficient, E_g –band gap, A – proportional constant, where $h\vartheta = 1239.852/\lambda$ (wavelength). The value of n depends on the nature of transition occurring: either direct or indirect allowed band gap transitions. Controversial assumptions are found regarding the value of n and consequently the value of the exponential. Some authors use a power of 0.5 (n=2) for the indirect transition and power=2 (n=0.5) for direct and vice versa.[194, 195] The acquired absorbance spectrum is converted to the Kubelka-Munk function where the absorption coefficient (α) is proportional to absorbance (a) and thus interchanged. A graphic representation was used to calculate band gap (Eg) of materials: the Tauc plot applying Kubelka-Munk function - vertical axis of $(ah\vartheta)^{1/n}$ against $(h\vartheta)$ horizontal is plotted where a is absorbance and n corresponds to either direct or indirect allowed band gap transitions. The major band gap transition due to anatase is considered to be indirect allowed (n=2).[193] A Straight line tangent to the point of inflection, which is found by taking the first derivative of the curve, is drawn. The value at which tangent line intersects horizontal photon energy axis corresponds to the band gap of the material.

2.2.10 Time – resolved photoluminescence (TRPL)

Time-resolved photoluminescence spectra of the as-prepared samples in an aqueous suspension (1 mg. ml^{-1}) were recorded on an F-4500FL rapid scanning fluorescence spectrometer at an excitation wavelength of 380 nm at York University by Ben Coulson.

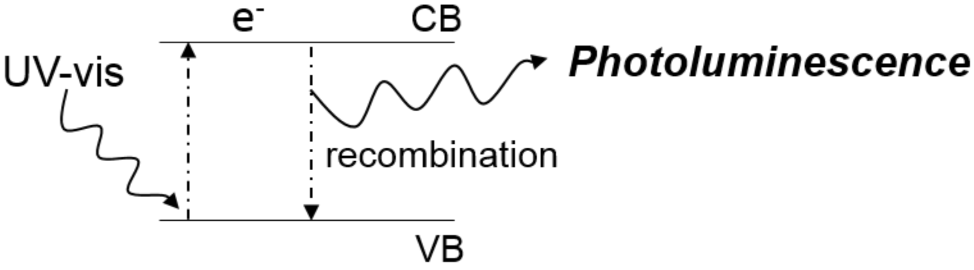

Figure 2.10 Energy diagram illustrating photoluminescence origin.

Semiconductor materials absorb high energy photons and excite electrons to conductance band. When electrons recombine they return to valence band and energy in the form of photons is emitted (**Figure 2.10**).[196] A plot of emission against time for any given excitation wavelength is known as emission spectrum (**Figure 2.11**). The peak in the spectrum corresponds to the instrument response (pulse) and only the tail of the peak (exponential) is fitted.

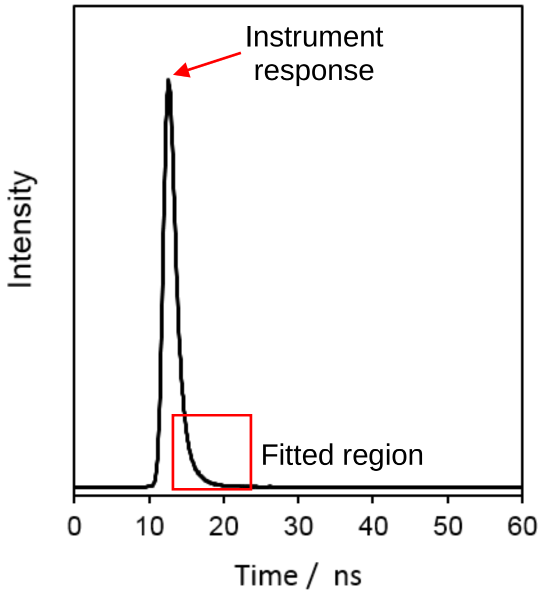

Figure 2.11 A representative photoluminescence spectrum of TiO_2 catalyst.

The charge carrier lifetimes (t) are calculated by fitting TRPL spectra using **Equation 2.11** where number of $B_1e^{\left(\frac{-t}{t_1}\right)}$ fragments depends on how well the function fits the spectra. The decay curves were modelled in the F4500 software using a ‘tail fit’ model. The fitting software generates τ and *B* values and χ^2 which indicates the best fit. The average carrier lifetime (t_{avg}) combines multiple lifetime constants in **Equation 2.12.**

$$R(t) = B_1e^{\left(\frac{-t}{t_1}\right)} + B_2e^{\left(\frac{-t}{t_2}\right)} \ldots$$

Equation 2.11 Time-resolved photoluminescence fitting function where t is the lifetime constant of the charge carriers, B – the contribution of each lifetime constant to the overall signal, R – number of counts (arbitrary) at a time.

$$t_{avg} = \frac{B_1t_1^2 + B_2t_2^2}{B_1t_1+B_2t_2}$$

Equation 2.12 The average carrier lifetime equation.

2.3 Photocatalytic reactions

2.3.1 Methyl Orange decomposition

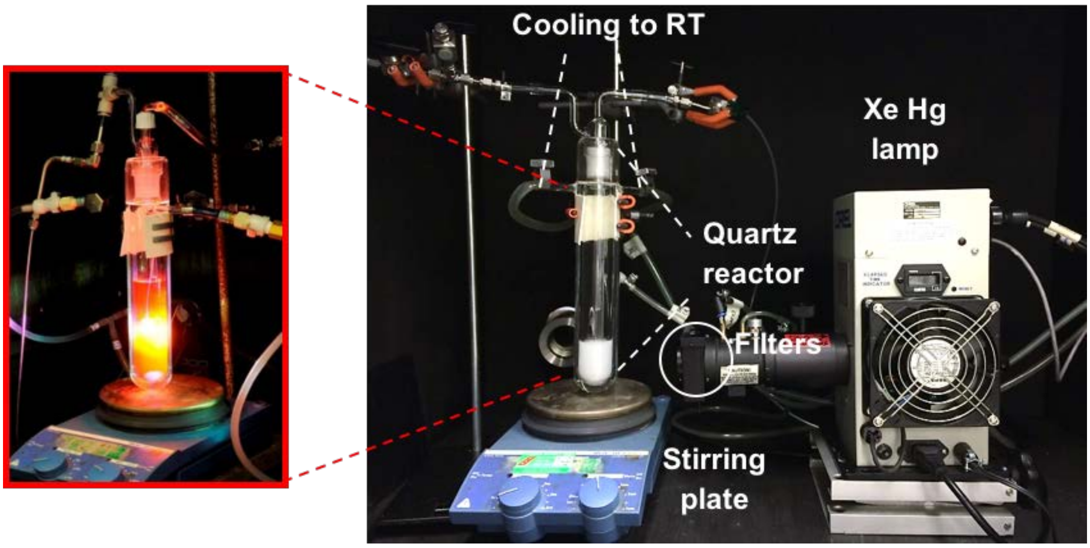

Figure 2.12 Methyl Orange degradation reaction set up.

Photocatalytic Methyl Orange (MO) degradation tests of all photocatalysts were performed in a sealed 150 ml quartz photoreactor (27 mm i.d.) with a cooling system (recirculating cooling jacket connected to a Huber Minichiller) set to room temperature (20 °C) (**Figure 2.12**). 50 mg of catalyst was added to 50 ml of 20 ppm MO solution and stirred (625 rpm) in the dark for 1 h to establish the adsorption-desorption equilibrium. The reaction mixture was subsequently irradiated (26 $mW.cm^{-2}$ reactor internal flux measured using G & R labs 200 light meter, inside and outside of the reactor) with UV-vis light spectra under stirring by a 200 W Newport Oriel Instruments 66002 Hg Xe arc lamp employing water filter to remove infrared wavelengths (**Figure 2.13**).Reactions were periodically sampled and centrifuged to separate the catalyst, and UV-Vis absorption spectra recorded on Thermo Scientific Evolution 220 spectrophotometer. Initial rates were calculated employing MO multi-point calibration curve (7 concentrations from 1-50 ppm, R^2=0.998) of the most intense 464 nm peak (**2.2.8 UV-vis spectroscopy**) and normalised to the mass of catalyst. Values reported are the mean of 3 repeats.

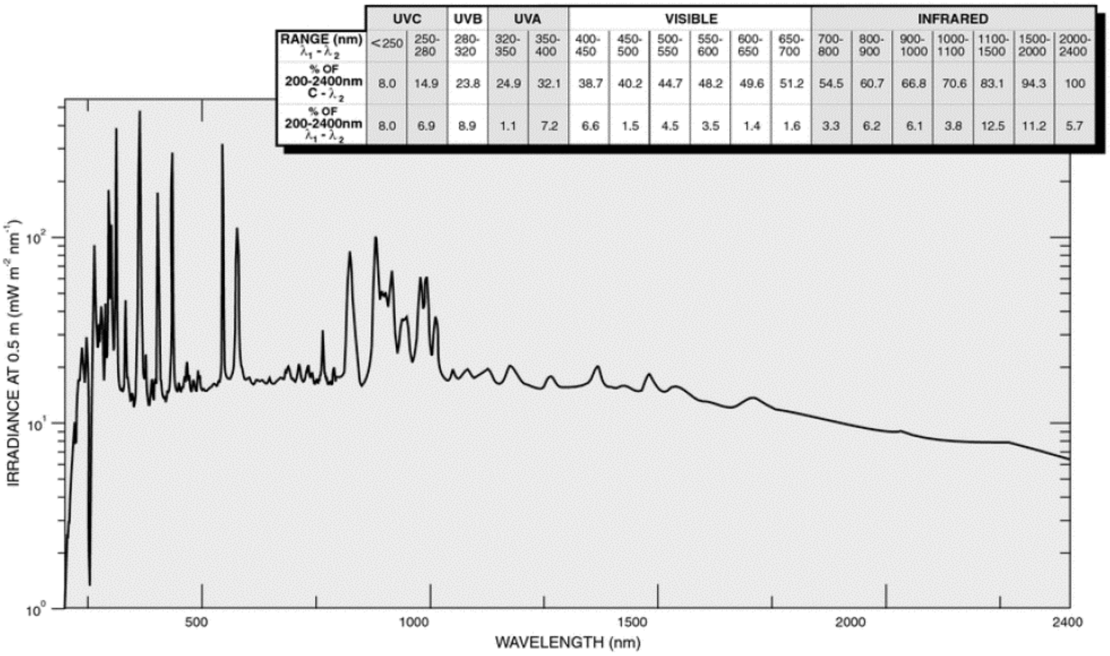

	UVC		UVB	UVA		VISIBLE						INFRARED						
RANGE (nm) $\lambda_1 - \lambda_2$	<250	250-280	280-320	320-350	350-400	400-450	450-500	500-550	550-600	600-650	650-700	700-800	800-900	900-1000	1000-1100	1100-1500	1500-2000	2000-2400
% OF 200-2400nm $C - \lambda_2$	8.0	14.9	23.8	24.9	32.1	38.7	40.2	44.7	48.2	49.6	51.2	54.5	60.7	66.8	70.6	83.1	94.3	100
% OF 200-2400nm $\lambda_1 - \lambda_2$	8.0	6.9	8.9	1.1	7.2	6.6	1.5	4.5	3.5	1.4	1.6	3.3	6.2	6.1	3.8	12.5	11.2	5.7

Figure 2.13 Light intensity map for 200 W Newport Oriel Instruments 66002 Hg Xe arc lamp.

2.3.2 Water splitting and carbon dioxide reduction

Water splitting and photocatalytic CO_2 reduction were performed in a sealed 320 ml stainless steel photoreactor (**Figure 2.14**) with a quartz window and a cooling system (recirculating cooling jacket connected to a Huber Minichiller) set to room temperature (20 ^{o}C) using a 200 W Hg-Xe arc lamp (150 mW.cm^{-2}) with beam turning mirror whose spectral output is shown in **Figure 2.13**. For water splitting reaction, 50 mg of sample was dispersed in 50 ml of 0.5 M Na_2SO_3 aqueous solution (sulphite as a hole scavenger) and ultrasonicated for 10 min to obtain a uniform dispersion. Subsequently, the reaction mixture was purged with He (15 ml/min) for 1 h to remove air from the system. For CO_2 photoreduction, 20 mg of the catalyst was dispersed by ultrasonication in 50 ml of deionised water. Prior the illumination, the reaction mixture was purged with CO_2 (15 ml/min) for 1 h to degas air from the solution and saturate it with CO_2.

Aliquots of the reaction gas mixture were periodically withdrawn in both reactions to measure gas products with a 1 ml air-tight gas syringe for analysis on a Shimadzu Tracera GC-2010 Plus gas chromatography fitted with a Carboxen1010 (30 m × 0.53 mm × 0.1 μm) column with a He carrier gas and Barrier Ionization Detector. Liquid products were also analysed periodically on an Agilent 1260 HPLC fitted with a Hi-Plex column, however, no carbon-containing liquid products were detected.

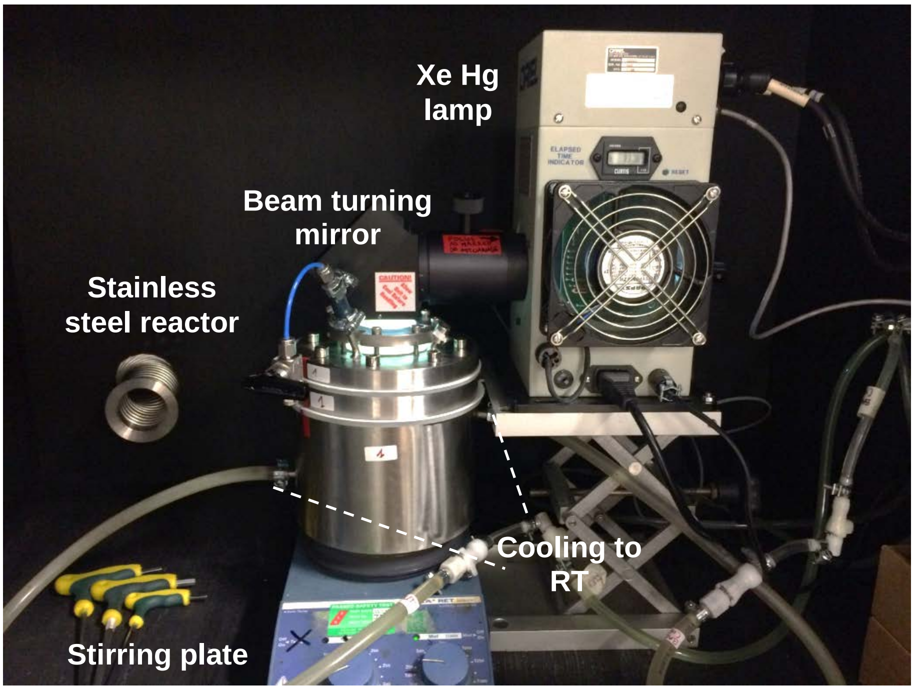

Figure 2.14 Water splitting and CO_2 *reaction set up.*

Gas chromatography is a technique, used to identify, separate or analyse gas or volatile compounds. Separation occurs due to different affinities of components to stationary phase, present in the column, and mobile phase (carrier gas). Molecules, which interact strongly with the stationary phase, leave the column later and vice versa. GC is fitted with BID, barrier discharge ionisation detector, which creates ionisation from a helium-based, dielectric barrier discharge plasma. Compounds that elute from the GC column are ionised by this plasma energy, produce an electric current and then is detected by the collection electrode and processed as peaks. Data are often recorded as chromatograms and then using peak integration (the area under the peak) which is proportional to the concentration of constituents, is calculated. In order to get concentration from peak area, results should be calibrated. Calibration is based on response factors obtained by varying known product concentration.

Chapter 3

Mesoporous TiO_2 photocatalysts

3 Mesoporous titania photocatalysts

Commercial P25 titania, composed of anatase and rutile crystallites which display synergistic photocatalysis due to heterojunction formation is one of the most common starting points for academic and industrial research.[28, 29] However, P25 suffers from a low surface area (50 $m^2.g^{-1}$), wide band gap (restricting it to UV light absorption) and rapid recombination of photo-excited charge carriers.[197, 198] Consequently, significant research efforts have focused on developing high area, nanocrystalline thermally stable titanias with enhanced photophysical properties by forming small nanoparticles – like mesoporous single crystals (MSC)[198] or incorporation of porosity. [199, 200]

Numerous soft/hard template methods (**Figure 3.1**) with diverse precursors are employed in order to overcome common challenges: disordered or/and thermally unstable mesostructure, poor crystallinity or domination of anatase phase.[201] [202] This involves sol-gel,[203] hydrothermal,[204] solvothermal,[205] microwave[206] and sonochemical[207] synthesis methods. Templates act as structure-directing agents to form mesopore frameworks. A soft-templating method was adapted to synthesise the mesoporous TiO_2 series discussed in this chapter (**2.1.2 Synthesis of mesoporous titania**) with an aid of a surfactant template. Surfactant-templating methods can include cationic (e.g. alkyl trimethylammonium), anionic (Perfluorooctanesulfonate), non-ionic diblock (Brij 56) and non-ionic triblock (F127, P123) etc. surfactants. As a result, mesoporous TiO_2 can adopt various structures such as 2D hexagonal,[208] 3D cubic,[209] hollow-sphere,[210] worm-hole like,[211] sphere-like[212] etc.

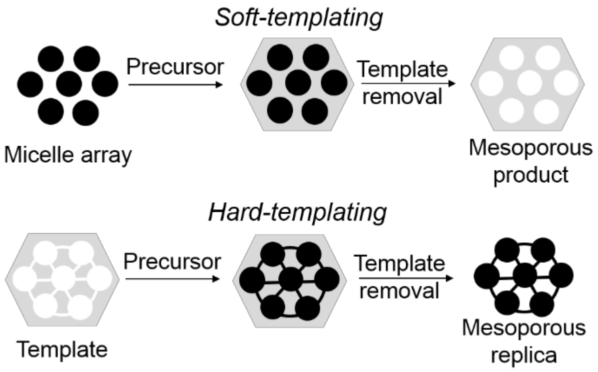

Figure 3.1 Soft and hard templating methods of synthesizing mesoporous oxides.

Antonelli et al[213] synthesised the first high internal surface area (200 $m^2.g^{-1}$), mesoporous TiO_2 with uniform (3.2 nm) pores via a modified sol-gel synthesis using titanium alkoxides and phosphate surfactants. High area (150-240 $m^2.g^{-1}$) and highly crystalline mesoporous titania microspheres with average pore diameters ~4.5 nm were more recently synthesised via evaporation induced self-assembly and acetic acid mediated sol-gel chemistries.[214] However, mesoporous TiO_2 catalysts with such mesopores are only amenable to substrates with small hydrodynamic diameters and may suffer mass transport limitations for bulky molecules (such as azo dyes). Yang et al [215] reported a straightforward route to thermally stable ordered larger-pore (6.5 nm) semicrystalline anatase mesoporous TiO_2 (205 $m^2.g^{-1}$). Nevertheless, the synthesis involves $TiCl_4$ precursor, which is highly volatile and in the contact with humid air, it forms TiO_2 and HCl,[216] resulting in the hazardous environment, especially if synthesised on the large scale.

Via a lengthy, multi-step route, involving ethylenediamine protective groups, well-ordered large pore (10 nm) pure anatase mesoporous TiO_2 (158 $m^2.g^{-1}$) has been prepared, the thermal stability and photoactivity of this material for 2, 4-dichlorophenol degradation were investigated by Zhou et al[217] The highly crystalline anatase mesoporous TiO_2 exhibited better photocatalytic activity than P25, nonetheless, charge carrier separation was limited in this single phase material. Likewise, Atitar and co-workers[218] looked into the impact of calcination temperature on the photocatalytic activity of disordered broad size distribution mixed-phase mesoporous TiO_2 (165 $m^2.g^{-1}$) in imazapyr and phenol oxidation reactions. It is surprising to note that calcination of disordered mesoporous titanias failed to induce any systematic variation in the anatase:rutile phase composition or photoactivity for the decomposition reactions. The effect of thermal processing (up to 600 °C) on the structure and crystallite size of the wormhole-like mesoporous TiO_2 (149 $m^2.g^{-}$) was investigated and photocatalytic activity in Rhodamine B degradation was tested by Kesong et al.[211] The results displayed an increase in crystallite size, a decrease in surface area and only the anatase crystalline form. The most active was the sample calcined at 400 °C, explained by the theory of the optimum crystallite size[219] (10 nm) and surface area (136 $m^2.g^{-1}$).

A great effort was devoted to achieving optimal mesoporous TiO_2 materials, [199, 201, 202, 213, 214, 217, 218] nevertheless, tuning the structural and physicochemical properties of semiconductor photocatalysts, and their resulting reactivity, in a predictable fashion remains challenging. It is well established that titania photoactivity is predominantly influenced by structural and electronic properties,[19, 20] which may be tuned via crystal structure engineering (**1.3 Titania photocatalysts**).[21] The commonly studied metastable anatase and stable rutile phases both exhibit wide band gaps (3.2 eV and 3.0 eV respectively)[36], with anatase-rich mixtures with rutile proposed optimal for the photocatalysis due to charge separation across their interface.[25, 26, 220] Density functional calculations have also highlighted the importance of crystal facets for anatase, with surface energies and photoactivity of decreasing from (001) 0.90 J m^{-2} > (100) 0.53 J m^{-2} > (101) 0.44 J m^{-2}.[48, 49] Surface defects such as oxygen vacancies (V_o) and Ti^{3+} sites also enhance TiO_2 photoactivity,[43] alongside particle size effects which dictate an optimum for 25-40 nm particles due to competition between light harvesting, scattering, bulk/surface recombination and geometric surface area.[41] The understanding of these properties could aid breakthrough in the production of more efficient photocatalysts.

Pure titania has a rapid electron-hole recombination rate and a wide band gap aiding absorption of ultraviolet light.[193] A popular approach to enhance TiO_2 activity is a promotion with transition metals or their oxides to maximise the lifetime of photogenerated charge carriers, activate reactants and improve absorption of light.[102, 221] Various copper oxidation states and environments can be put forward as the promoter candidates, with specific modes of action; charge carrier trapping or injection of excited electrons to conductance band of TiO_2 (**1.4 Promotion of titania photocatalysts**). Sajjad et al. investigated copper loading effect on mesoporous TiO_2 prepared using ionic liquid assistance, where both Cu(I) and Cu(II) components were formed.[222] The research showed 2 wt% Cu(I) acted as the active species by favouring formation of oxygen vacancies. Correspondingly, Tseng and his colleagues showed that the most active Cu species on non-porous titania for CO_2 photoreduction is 2 wt % Cu(I) as well.[223] Liu and co-workers studied copper doped titanias as photocatalytic CO_2 reduction materials, which revealed the critical dependence of activity on promoter dispersion, with optimal efficiency occurring in systems exhibiting maximum dispersions, obtained for loadings ≤ 0.03 wt%.[88] This is the only structural activity correlation that can be identified whilst any attributes due to changing phase, species size or morphology, with changing dopant levels, remains unclear at the most active ultra-dilute Cu levels. The ill-defined nature of the copper present is the key interest: the oxidation state and the local environment of the copper promoter, as either atomically isolated species,[85] a component of TiO_2 framework[87] or oxide nanocrystallites.[86] Addition of Cu can increase both the electron-hole separation efficiency and the adsorption of visible light, leading to the enhanced photocatalytic activity under the full solar spectrum.

The noble-metal, such as Pt, promotion is another way of improving the TiO_2 photocatalyst performance.[95, 96, 202] The different work functions and Fermi levels of platinum in comparison to the band-gap structure of the titania leads to the formation of the Schottky barrier that aids a separation of the electron-hole charge carriers and significantly increases the photoactivity (**1.4.1 Surface trapping**).[95] Ismail et al.[91] fabricated a platinum promoted mesoporous TiO_2 via Pt photodeposition on the mesoporous TiO_2 support synthesised via a one-step sol-gel process involving F127 surfactant template. The photocatalyst exhibited 2-fold higher photocatalytic activity in the di-chloroacetic acid degradation compared to the P25, which is accounted for the Pt promotion, lower light scattering effect of the ordered pores and improved diffusion. In addition, it was demonstrated that the post-modification of the mesoporous TiO_2 gives better photoactivity than nanocomposites, where Pt is incorporated during the titania synthesis. TiO_2 nanotube arrays promoted by Pt nanoparticles via solvothermal methodology were investigated by Feng and co-workers.[224] The synthesis yielded a uniform distribution of Pt nanoparticles with average diameter of 3.4 nm and a broad size distribution spanning from 1.8 – 4.9 nm. In the CO_2 photoreduction reaction, the Pt promoted nanotube arrays showed superior methane and ethane production rates. The excellent photoactivity was attributed to the high particle dispersion coupled with efficient electron diffusion properties across the nanotube arrays.

Various authors investigated the influence of the deposition techniques[225] and loading[226] on the promoter species and activity but understanding the impact of the mesoporous TiO_2 structure is the key. The ability to grow small or even monoatomic metal particles would offer improved photocatalytic performance while greatly reducing the costs by using only small amounts of promoter species. In this chapter, the impact of calcination temperature on surfactant-templated mesoporous TiO_2 and the mesopore framework influence on the Cu and Pt promoters is explored. The relationship between mesoporosity and the properties of the mesoporous TiO_2 could give an insight on how to further improve the photoactivity. Photocatalysts were made via simple inexpensive safe easily scaled-up surfactant templating synthesis and deposited with Cu or Pt via the classical wet-impregnation process. The photocatalytic activity was tested in methyl orange degradation, water splitting and CO_2 reduction reactions.

3.1 Characterisation of mesoporous titania series

Seven different mesoporous TiO_2 materials (meso-TiO_2) were prepared using a newly developed surfactant templating method at different calcination temperatures from 300 to 900 °C (**2.1.2 Synthesis of mesoporous titania**). The characteristics of freshly designed materials were investigated *via* a range of techniques. The key interest is the variation of structural and physicochemical properties with thermal processing conditions.

3.1.1 Nitrogen porosimetry

N_2 porosimetry allows evaluation of the structural properties of the titania framework. N_2 adsorption/desorption curves (**Figure 3.2**) of meso-TiO_2-300 - 700 display Type IV isotherms typical for mesoporous materials with H2 type hysteresis loop as a consequence of differing capillary condensation and evaporation within mesopores during adsorption and desorption respectively. Hysteresis indicates either restricted pore entrance (ink bottle shape) or irregular channel structure of mesopore framework. The decrease in the hysteresis loop size and shift towards higher relative pressure with increasing calcination temperature evidence loss of mesopore framework. Consequently, meso-TiO_2-800 and meso-TiO_2-900 exhibit Type II isotherm with no observed capillary condensation indicating absence of mesoporosity.[174]

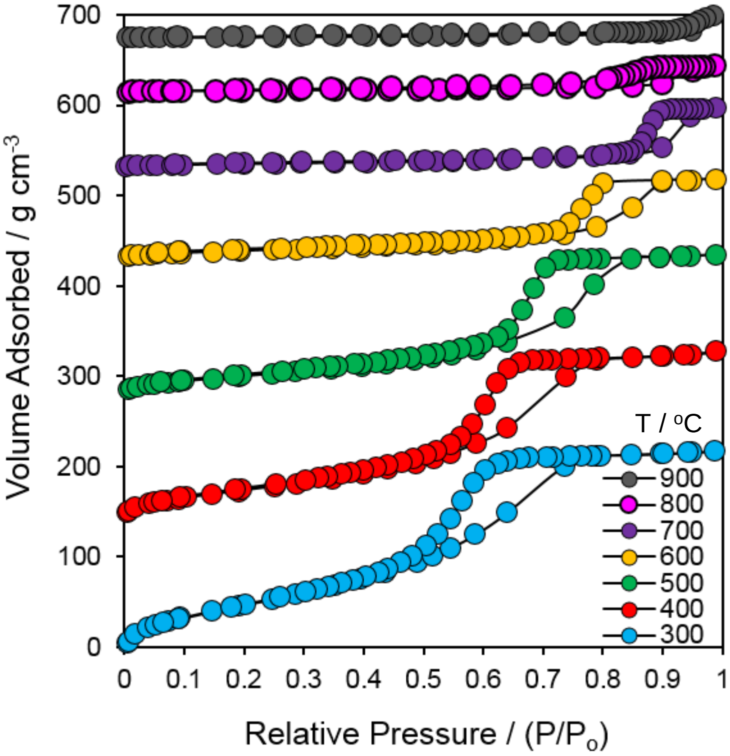

Figure 3.2 Stacked isotherm plot of meso-TiO_2 series with different calcination temperatures from 300 to 900 °C.

Table 3.1 Summary of N_2 porosimetry results of meso-TiO_2 series of meso-TiO_2 series with different calcination temperatures from 300 to 900 °C.

Sample	BET / m^2 g^{-1}	Mesopore size / nm	Mesopore volume / g cm^{-3}
300	313 (±31)	4.6 (±0.5)	0.41 (±0.04)
400	194 (±19)	5.4 (±0.5)	0.34 (±0.03)
500	126 (±13)	6.5 (±0.7)	0.28 (±0.03)
600	51 (±5)	9.7 (±1.0)	0.15 (±0.02)
700	19 (±2)	16.0 (±1.6)	0.11 (±0.01)
800	8 (±1)	-	-
900	4 (±0.4)	-	-

Specific surface area (**Table 3.1**) is estimated by using BET (Brunauer – Emmett - Teller) method with the highest value of 313 m^2 g^{-1} for the meso-TiO_2-300 sample and drastically decreased with increasing calcination temperature with a minimum of 4 m^2 g^{-1} for the meso-TiO_2-900 sample. The same trend is observed for mesopore volume (**Table 3.1**) with highest being 0.41 g cm^{-3} for the meso-TiO_2-300. The decline of surface area and mesopore volume is caused by a significant increase in mesopore size from 4.6 nm to 16 nm (**Table 3.1**) which is linked to the rapid growth of anatase and rutile nanocrystallites (**3.1.2 X-ray diffraction**), which form the walls of the mesopores. Sintering of TiO_2 nanocrystallites collapses the mesopore structure by obstructing the pores and forming irregular packing containing voids. Samples meso-TiO_2-300 – 500 have a narrow BJH pore size distribution (**Figure 3.3**) implying that the materials have regular mesopore channels. With the increase of calcination temperature to 600 °C, the mesopore size distribution becomes broader. T-plot calculations reveal the absence of micropores.

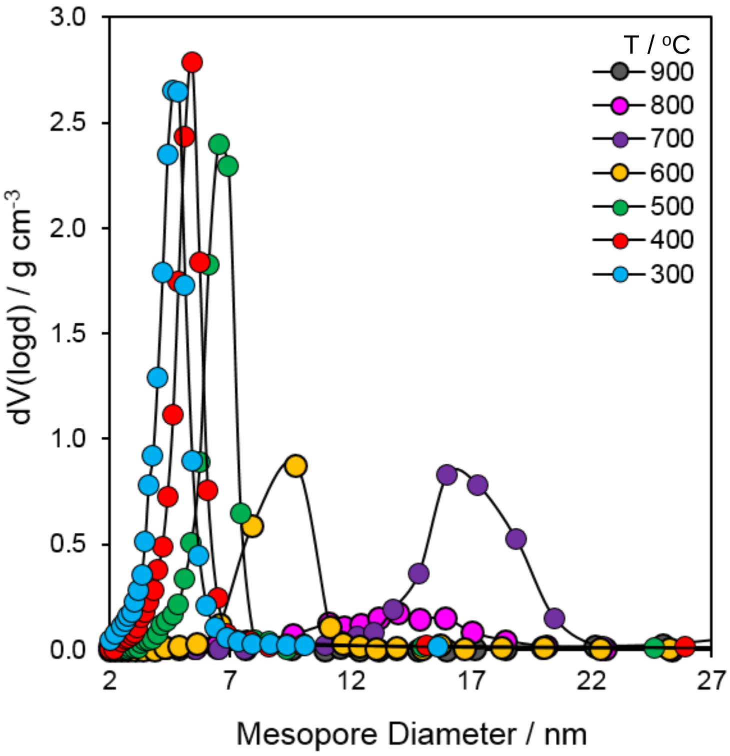

Figure 3.3 Mesopore size distribution of meso-TiO$_2$ series with different calcination temperatures from 300 to 900 °C.

3.1.2 X-ray diffraction

Ex-situ wide angle XRD diffractograms (**Figure 3.4**) for meso-TiO_2-300 – 900 display seven well-resolved diffraction peaks indexed (101), (004), (200), (105,211), (204), (116,220), (215) corresponding to anatase crystalline phase.[227] Furthermore, samples meso-TiO_2-500 – 900 exhibit additional peaks analogous to rutile crystalline phase. As calcination temperature increases, anatase crystalline phase is being transformed to rutile[228] whose content rises greatly from 3% to 75% (**Table 3.2**) with sample meso-TiO_2-800 being an unusual exception (in more detail investigated in the paragraph **3.1.3 Raman spectroscopy**).

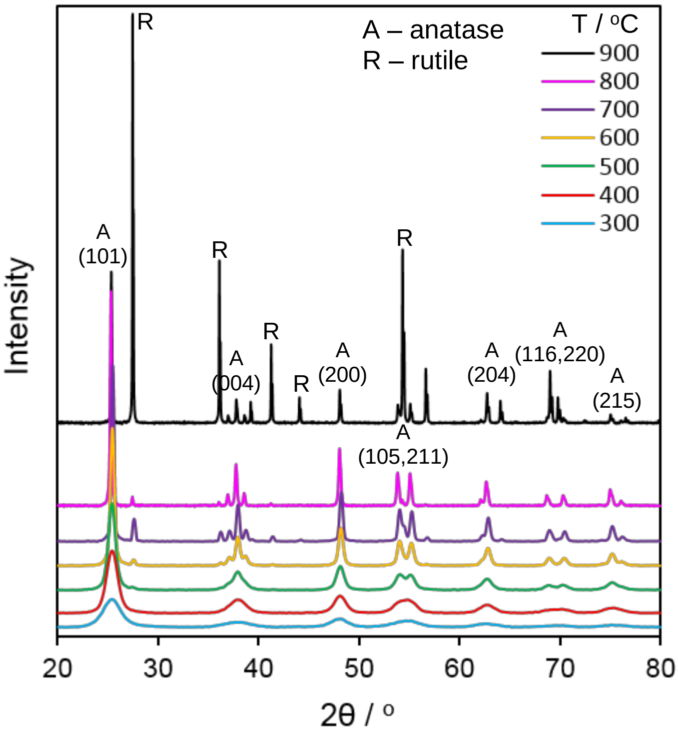

Figure 3.4 Wide angle XRD patterns of meso-TiO_2 series with different calcination temperatures from 300 to 900 °C.

Anatase and rutile nanocrystallites sizes are estimated using Scherrer formula[177] from the average of FWHM of (101), (200), (215) anatase and (110) rutile reflections and summarised in **Table 3.2**. As meso-TiO_2 calcination temperature increases both anatase and rutile nanocrystallites grow much larger indicating sintering of TiO_2 phases. Unit cell parameters (**Table 3.2**) of tetragonal ($a=b\neq c$, $\alpha=\beta=\gamma=90^o$) anatase crystalline phase, calculated using $d_{(200)}$ lattice spacing remains unchanged across the series and are in a good agreement with the literature (a=b=3.78 Å) [227]. Rutile phase unit cell parameters for all rutile containing samples are a=b=4.58Å, analogous to the literature. [228]

Table 3.2 Summary of XRD results of meso-TiO$_2$ series.

Sample	Crystalline phase	Nanocrystallite size / nm	Anatase unit cell a (=b) / Å	d_{10} spacing / nm	Pore spacing a / nm	Pore wall thickness / nm
300	Anatase	5 (±0.1)	3.78 (±0.04)	9.3 (±0.1)	10.7 (±1.1)	6.1 (±0.6)
400	Anatase	7 (±0.1)	3.78 (±0.04)	10.6 (±0.1)	12.3 (±1.2)	6.9 (±0.7)
500	97% Anatase 3% Rutile	11 (±0.1) 29 (±0.3)	3.78 (±0.04)	-	-	-
600	96%Anatase 4% Rutile	20 (±0.2) 35 (±0.4)	3.77 (±0.04)	-	-	-
700	85% Anatase 15% Rutile	31 (±0.3) 46 (±0.5)	3.77 (±0.04)	-	-	-
800	96% Anatase 4% Rutile	40 (±0.4) 62 (±0.6)	3.78 (±0.04)	-	-	-
900	25% Anatase 75% Rutile	64 (±0.6) 109 (±1.1)	3.78 (±0.04)	-	-	-

An in-situ wide angle XRD (**Figure 3.5**) experiment was performed using as prepared meso-TiO$_2$. The sample was heated to 900 ^{o}C at the same 1 ^{o}C / min ramp rate as for standard calcination, with 1 h hold after every 100 ^{o}C, when the XRD diffractograms were recorded. Evolution of seven well-resolved diffraction peaks indexed (101), (004), (200), (105,211), (204), (116,220), (215) equivalent to anatase crystalline phase are observed. Development of anatase crystalline phase including the size of nanocrystallites (**Table 3.3**) in 100 – 400 ^{o}C in – situ XRD patterns is analogues to samples calcined at 300 and 400 ^{o}C. On the contrary, in - situ formation of secondary rutile crystalline phase (marked R) is seen solely at 900 ^{o}C and it is only 5% of the sample while calcined meso-TiO$_2$ samples displayed 3% rutile phase formation already at 500 ^{o}C and at 900 ^{o}C it is as high as 75%. Moreover, in-situ XRD recorded nanocrystallites are significantly smaller (especially for rutile) compared to ex – situ calcined meso-TiO$_2$ materials (**Table 3.3**). This is a result of only 1 h hold time at each particular temperature during the in – situ experiment contrary to the catalyst calcination operated at the chosen temperature for 4h. Not only minimum 500 ^{o}C temperature but also sufficient hold time is required to form rutile crystalline phase. On the other hand, longer hold times lead to the formation of larger nanocrystallites and as discussed in porosimetry data, increase in the crystallite size cause decrease in specific surface area and mesopore volume.

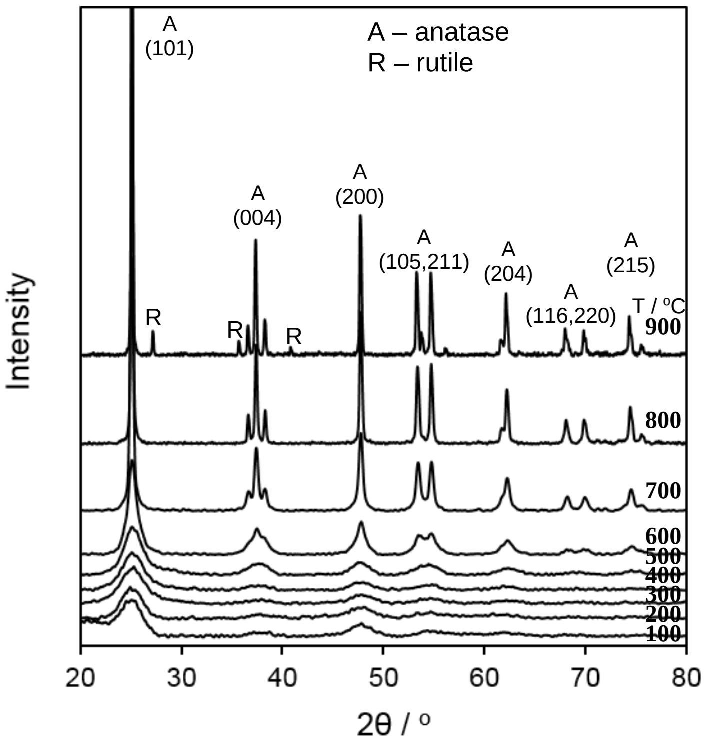

Figure 3.5 In - situ wide angle XRD experiment results of meso- TiO_2.

Table 3.3 Comparison of nanocrystallite sizes of calcined and in – situ formed meso-TiO_2.

Sample	Calcined materials: nanocrystallite size / (anatase, rutile) nm	In-situ nanocrystallite size / nm
100	-	5 (±0.1)
200	-	6 (±0.1)
300	5 (±0.1)	6 (±0.1)
400	7 (±0.1)	7 (±0.1)
500	11 (±0.1), 29 (±0.3)	7 (±0.1)
600	20 (±0.2), 35 (±0.4)	12 (±0.1)
700	31 (±0.3), 46 (±0.5)	22 (±0.2)
800	40 (±0.4), 62 (±0.6)	34 (±0.3)
900	64 (±0.6), 109 (±1.1)	43 (±0.4), 55 (±0.6)

Only samples 300 and 400 from the meso-TiO_2 series display a single peak in the low angle X-ray diffraction patterns (**Figure 3.6**) indicating short ranges of regular spacing between the mesopores with overall mesostructure being worm-hole as for the rest of meso-TiO_2-500 – 900 materials. Values of mesopore layer spacing d_{10}, pore spacing *a* and pore wall thickness are calculated from (10) reflection of two-dimensional hexagonal mesostructure (**Table 3.2**).[182, 183] Pore wall thickness is obtained by subtracting pore size given from N_2 porosimetry data from pore spacing. For both meso-TiO_2-300 and 400 samples, it is equal to anatase nanocrystallite size which forms pore walls. Carbons, remains of the Pluronic F127 template, could, in theory, hold the shape of mesostructured but LA XRD pattern of uncalcined meso-TiO_2 does not have a peak in LA XRD proving that short ranges of ordered mesopores are formed via calcination and is not a result of the presence of carbons, especially in meso-TiO_2-300 sample (**3.1.6 Temperature programmed oxidation**).

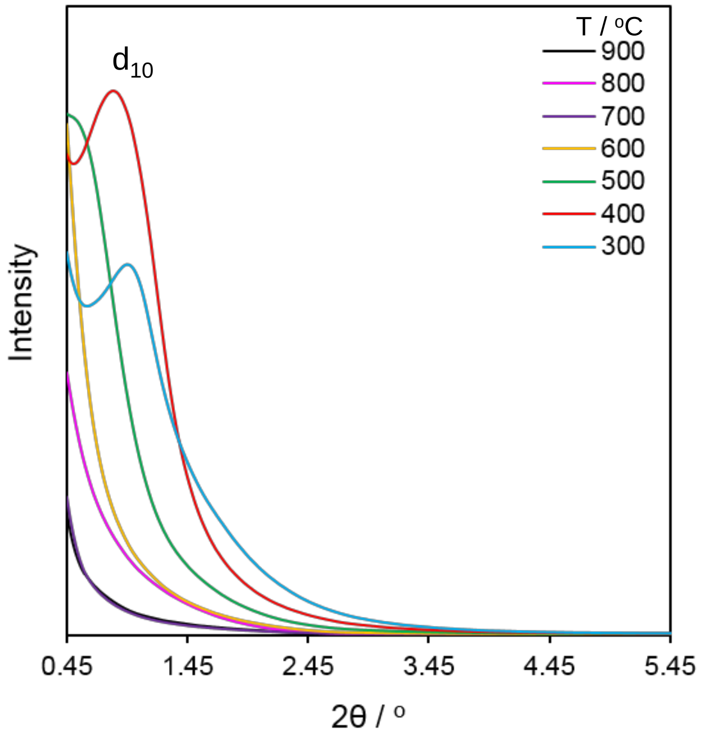

Figure 3.6 Low angle diffractograms of meso-TiO_2 series with different calcination temperatures from 300 to 900 °C.

3.1.3 Raman spectroscopy

In the WA XRD measurements, the sample meso-TiO_2-800 did not fit the trend of increasing rutile crystalline phase content with increasing calcination temperature. For the meso-TiO_2-800 material it is expected to have higher than 15% rutile content, however, it is just 4% which raises a question if all rutile is detected by XRD or if there any crystallites smaller than 2 nm or the amounts are beyond XRD threshold. **Figure 3.7** shows the Raman spectrum for meso-TiO_2-800 catalyst with 5 peaks observed, where those at 150 (E_g), 400 (B_{1g}), 520 (A_{1g} + B_{1g}) and 640 (E_g) cm^{-1} corresponds to anatase phase while 200 (E_g) cm $^{-1}$ corresponds to rutile.[229] The ratio 19:1 of the peak intensity of strongest anatase and rutile peaks indicate 95% of anatase and 5% of rutile which is in a good agreement with XRD results. It is unknown why at 800 °C calcination the rutile formation is inhibited and forms only 4% instead of expected between 15 – 75%. The sample has been synthesised on three different occasions but demonstrated the same 4% rutile content.

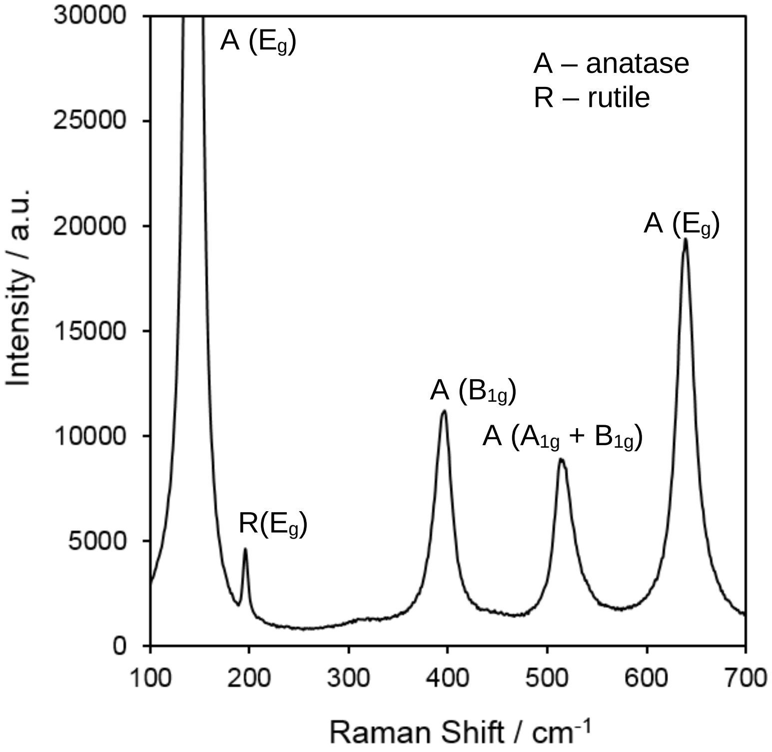

Figure 3.7 Raman spectrum of meso-TiO_2-800 sample.

3.1.4 High-resolution scanning transmission electron microscopy

Meso-TiO_2-400 exhibits the strongest LA XRD diffraction peak indicating the presence of an ordered mesopore framework. HRSTEM images (**A – C**) of meso-TiO_2-400 sample presented in **Figure 3.8** supports this conclusion – image **A** demonstrates continuous channels with short ranges of order resembling a hexagonal array arrangement. Image **B** gives a closer look at the areas of ordered channels with uniform mesopore size of ~6 nm, which is in a good agreement with porosimetry data, and its worm-like surrounding mesostructure. Image **C** displays anatase nanocrystallites of ~7 nm which is in a great agreement with WA XRD data. In addition, lattice fringes d_{101} ~3.5 Å are seen in the picture that corresponds to the most predominant (101) anatase facet d=3.5 Å (WA XRD data).

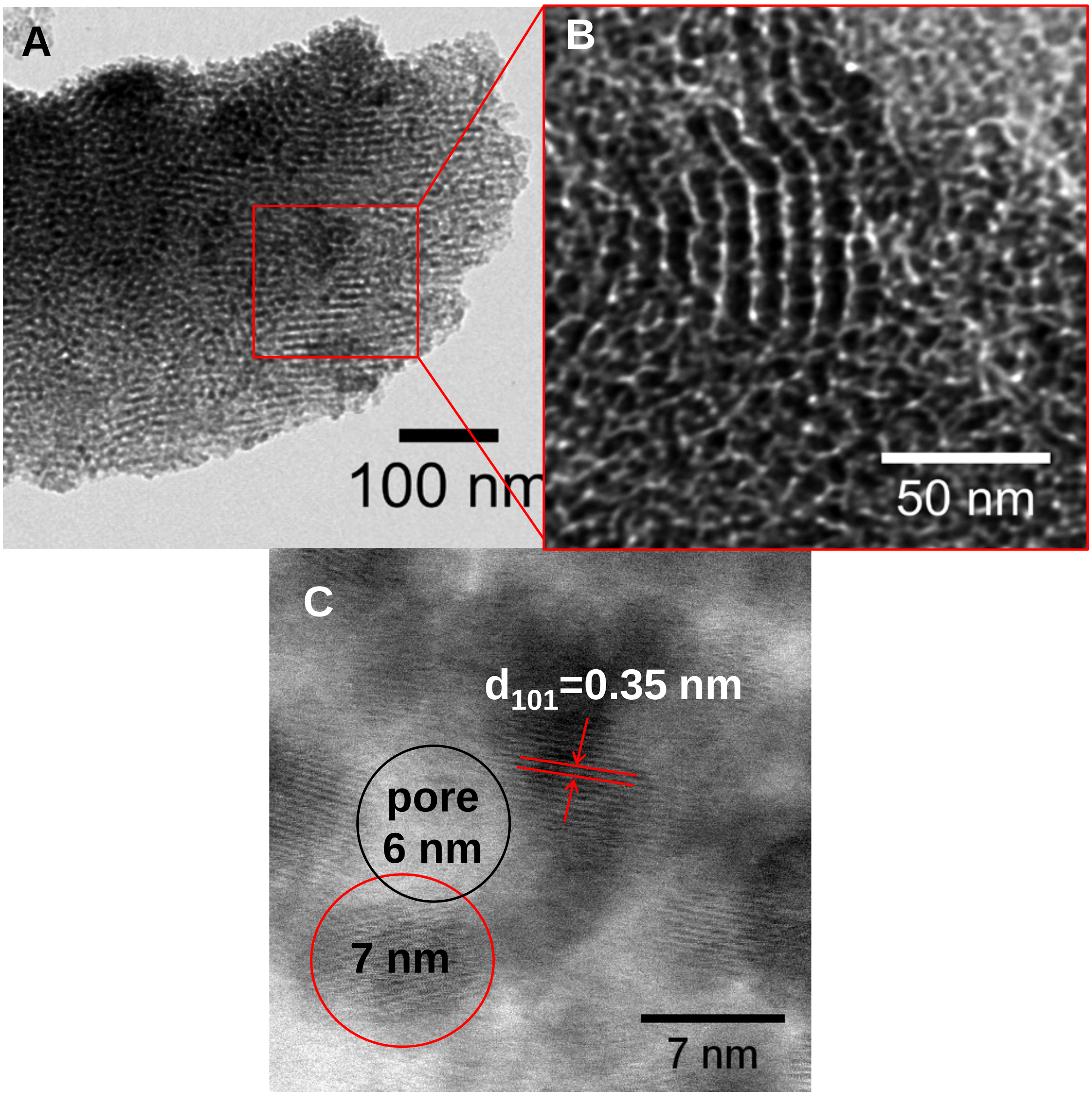

Figure 3.8 HRSTEM images of meso-TiO_2-400.

3.1.5 X-ray photoelectron spectroscopy

The XPS spectra of meso-TiO_2 series Ti 2p region is shown in **Figure 3.9.** The binding energies for 2p Ti core levels found at 458 and 464 eV correspond to Ti $2p_{3/2}$ and Ti $2p_{1/2}$ levels respectively.[189] The Ti $2p_{3/2}$ and Ti $2p_{1/2}$ peaks are symmetrical which indicates uniform chemical environment in all samples. Increase in calcination temperature leads to a shift of both Ti peaks to lower binding energy. The shift of binding energy from 458.58 eV in meso-TiO_2-300 to 458.10 eV in meso-TiO_2-900 catalysts suggests an increase in the electron charge density of the Ti^{+4} ion. This dependence of XPS bands to calcination temperature is an influence of a significant increase in nanocrystallite size.[230] All samples displayed 2:1 oxygen to titanium surface atomic ratio, as expected for TiO_2 structure.

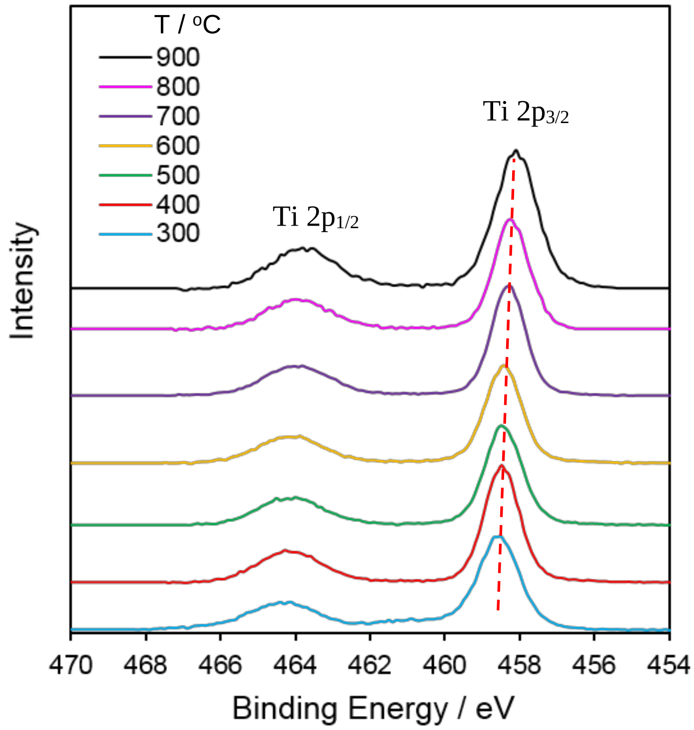

Figure 3.9 XPS spectra of Ti 2p region of meso-TiO_2 series with different calcination temperatures from 300 to 900 °C.

3.1.6 Temperature programmed oxidation

Results of TPO data summarised in **Table 3.4** show mass loss decreases for samples prepared with increasing calcination temperature from 20% for meso-TiO_2-300 sample to 1% for meso-TiO_2-600 sample. No mass loss is observed for materials meso-TiO_2-700 – 900. The graphs of mass loss (**Figure 3.10**) and derivative of the mass loss (**Figure 3.11**) reveal two type of species desorbing from the surface. The decrease in mass at temperatures up to 150 °C is assigned to physisorbed atmospheric and crystalline water which decreases from 5% for meso-TiO_2-300 sample to 1% for meso-TiO_2-600 sample. Based on complementary heat flow data (**Figure 3.12**) the mass losses from 150 to 450 °C correspond to an exothermic reaction, most feasibly the combustion of carbon species like partially combusted F127 organics (coke) present in the samples. Even though samples have been calcined over this range of combustion, it has been performed in a muffle furnace, under steady air conditions, most likely leading to some residual carbons being trapped within the structure. Meso-TiO_2-300 has significantly more carbon content than meso-TiO_2-400 – 500 samples which contain only 3% and 1% respectively. Moreover, for the latter samples, a small amount of carbon is lost by combustion up to 300 °C indicative of F127 surfactant and residual carbons. The carbon loss for meso-TiO_2-300 material is seen up to ~500 °C due to the same F127 or residual carbons trapped within the mesopores framework. During the calcination, the crystalline phase is formed more rapidly than carbon species are removed (due to air being steady in the muffle furnace), thus remains in the structure.

Table 3.4 Summary of TPO results of meso-TiO_2 series with different calcination temperatures from 300 to 900 °C.

Calc. temp. / °C	Water loss (up to 150 °C) / %	Carbon loss (150 – 500 °C) / %	Total mass loss / %
300	5.4 (±0.16)	14.6 (±0.44)	20.0 (±0.60)
400	3.3 (±0.10)	2.7 (±0.08)	6.0 (±0.18)
500	1.9 (±0.06)	1.3 (±0.04)	3.2 (±0.10)
600	0.7 (±0.02)	0.5 (±0.01)	1.2 (±0.04)
700	-	0.3 (±0.01)	0.3 (±0.01)
800	-	0.1 (±0.004)	0.1 (±0.004)
900	-	0.3 (±0.01)	0.3 (±0.09)

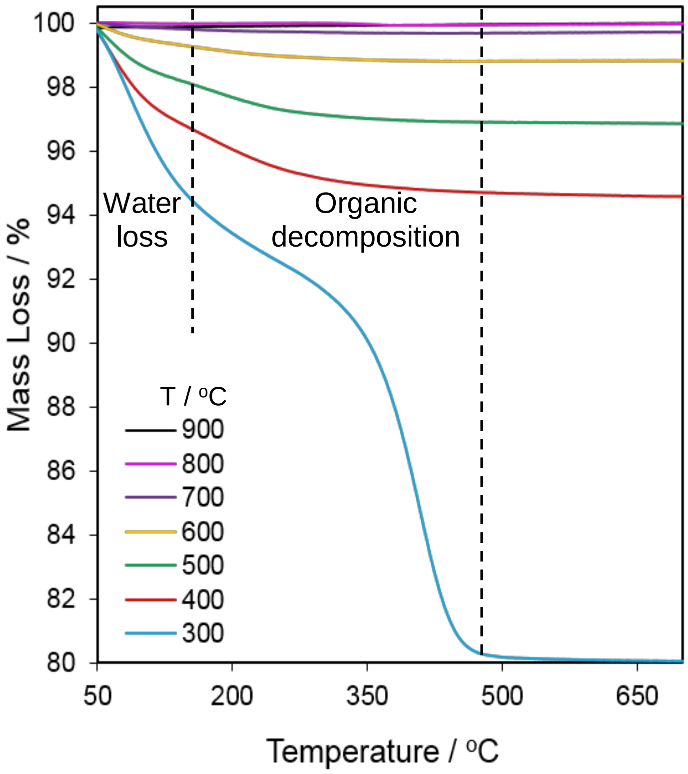

Figure 3.10 Mass loss % of meso-TiO_2 series with different calcination temperatures from 300 to 900 °C.

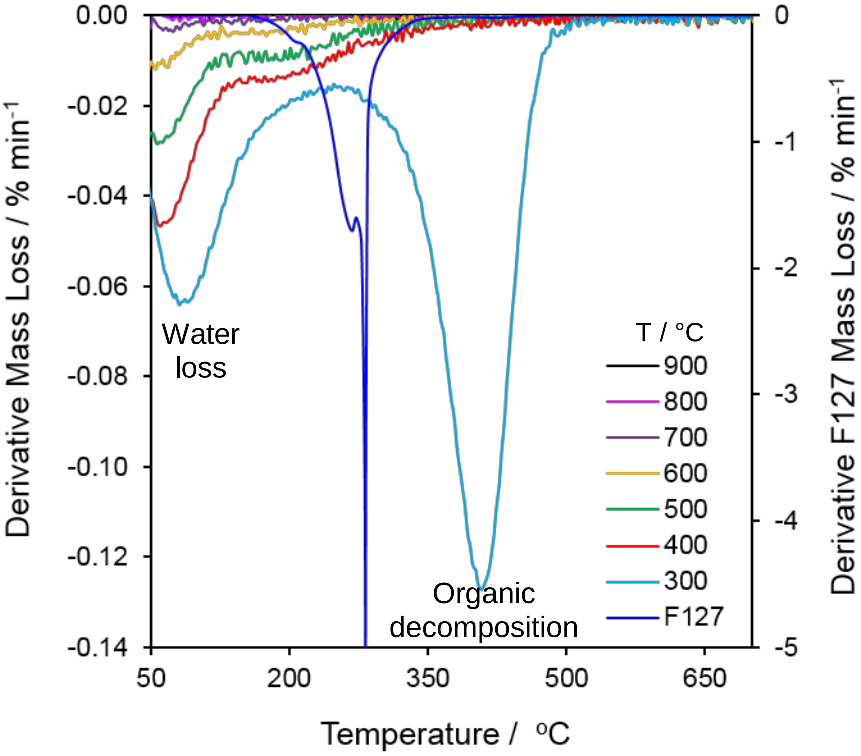

Figure 3.11 Derivative of mass loss of meso-TiO_2 series with different calcination temperatures from 300 to 900 °C.

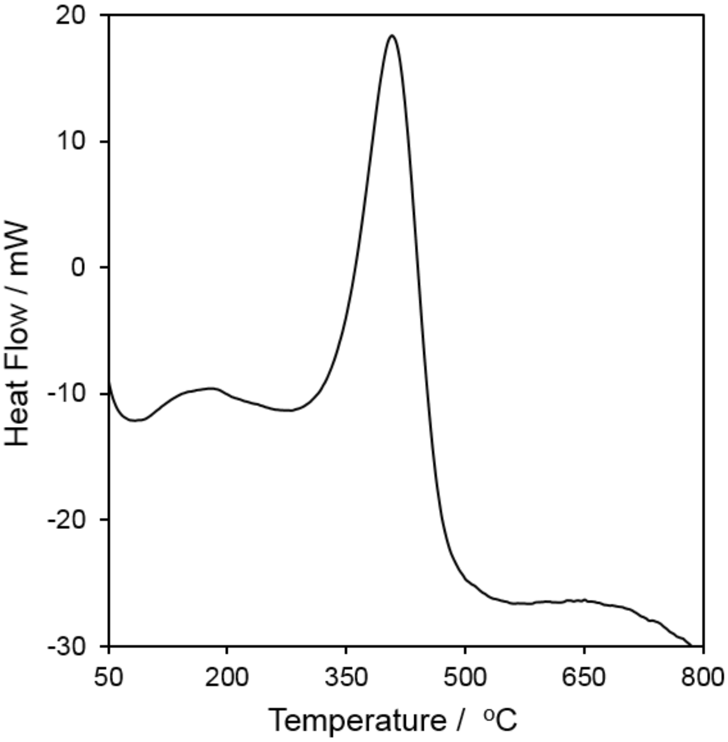

Figure 3.12 Temperature programmed oxidation heat flow data of meso-TiO_2-300 sample.

3.1.7 Diffuse reflectance UV-vis spectrophotometry

Recorded solid diffuse reflectance UV-vis optical absorption spectra (**Figure 3.13**) and Tauc plot (**Figure 3.14**) of meso-TiO_2-300 – 900 reveals a trend between calcination temperature and optical properties of the materials. Sample 300 possesses a dark brown colour due to high (15 wt%) carbon content which masks the band gap of the material by absorbing all light in UV – vis range. Spectra (**Figure 3.13**) of materials meso-TiO_2-400 – 900 have a sharp edge in the absorption so-called the band gap of the material. The sharp edge of the band gap is observed in the DRUVS because, the light with lower energy than the difference between the valence and conductance bands, is not sufficient to excite an electron from the valence to conductance band leading and this light is not absorbed.[35] Band gap absorption edges shifts from ~350 – 415 nm towards the visible region (~380 – 435 nm) with increasing calcination temperature.

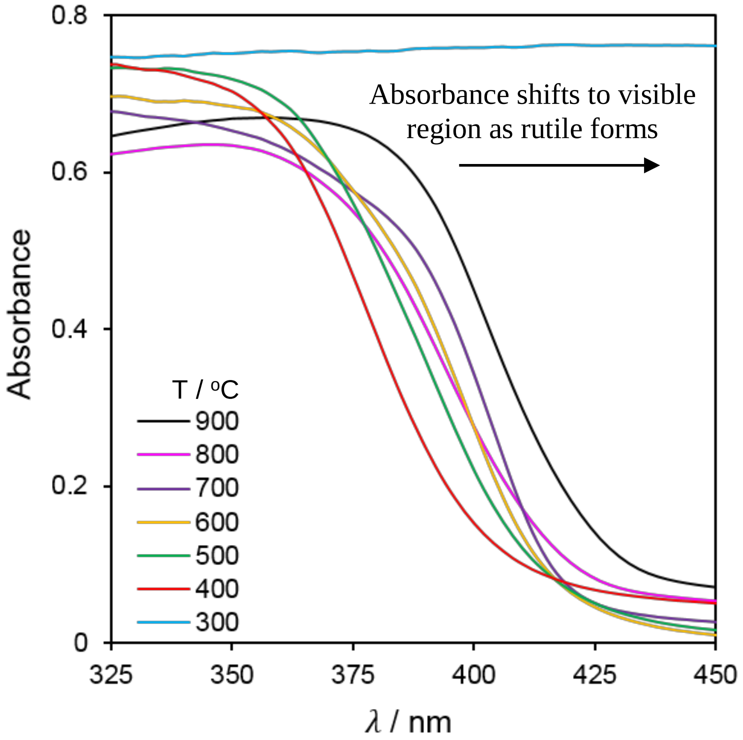

Figure 3.13 UV – vis absorption spectra of meso-TiO_2 series with different calcination temperatures from 300 to 900 °C.

The values of the band gaps of the materials are evaluated using Tauc plots (**Figure 3.14)**. Band gap energies of meso-TiO_2 semiconductors decrease from 3.07 to 2.90 eV with increasing calcination temperature. The shift of absorption edge to the more visible region and a decrease in the band gap with increasing temperature is a result of the increase in rutile phase content from 0% in meso-TiO_2-400 sample to 75% in meso-TiO_2-900 sample. The values of the band gaps of meso-TiO_2-600 and meso-TiO_2-800 are in an agreement with the results of the rutile % obtained by Raman and WA XRD. An additional effect that can influence a band gap is a nanocrystallite (particle) size – an optical band gap decreases with increasing size of the nanocrystallite (and vice versa). This phenomenon is called quantum size effect.[39] It is usually more pronounced in quantum dots or thin films where the sizes are very small (below 2-3 nm) rather than the bulk materials.[231] In this case sample meso-TiO_2-600 and meso-TiO_2-800 has exact the same 2.97 eV band gap but possess significantly different nanocrystallite size (20 and 40 nm respectively) evidencing no quantum size effect.

Sample	Band Gap / eV
300	-
400	3.07 (±0.02)
500	3.02 (±0.02)
600	2.97 (±0.02)
700	2.94 (±0.02)
800	2.97 (±0.02)
900	2.90 (±0.02)

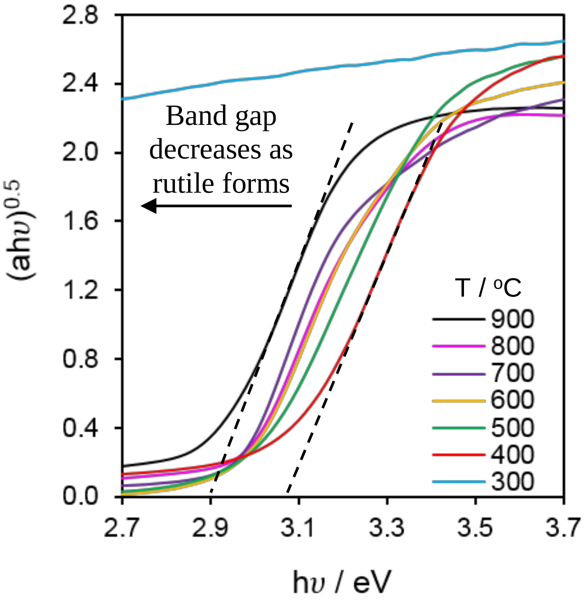

Figure 3.14 Tauc plot and corresponding band gap values of meso-TiO_2 series with different calcination temperatures from 300 to 900 °C.

Figure 3.15 (a) illustrates how an increase in rutile (R) vs anatase (A) content in the commercial samples shifts absorption from the UV to the visible region. The most commonly used commercial catalyst P25, which contains 85% anatase and 15% rutile, displays an absorption edge corresponding to a combination of both phases. The Tauc plot (**Figure 3.15 (b)**) of commercial materials display a decrease in band gap from 3.12 eV for pure anatase sample (63 nm crystallite size) to 2.90 eV for 96% Rutile material (86 nm). The P25 catalyst, which contains 85% anatase (21 nm) and 15% rutile (39 nm), exhibits a band gap of 2.95 eV. The commercial catalysts demonstrate the same trend observed in meso-TiO$_2$ semiconductors (**Figure 3.14**) where the band gaps decrease with increasing amounts of rutile and calculated band gaps are in the same range.

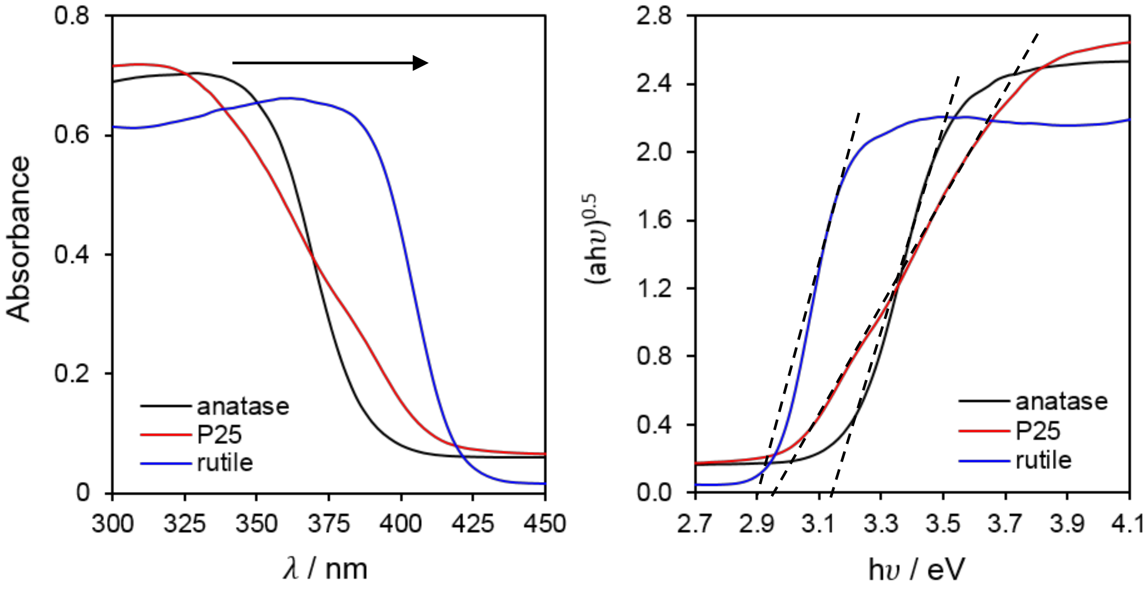

Figure 3.15 (a) UV – vis absorption spectra of commercial TiO$_2$ catalysts (b) Tauc plot and corresponding band gap of commercial catalysts.

3.1.8 Time – resolved photoluminescence

Time-resolved photoluminescence (PL) spectroscopy was performed to determine photogenerated charge carrier dynamics of meso-TiO_2-400, 500, 700 and 800 photocatalysts (**Figure 3.16**). Results were obtained using 380 nm excitation and 470 nm emission wavelengths from the decay curves fitted to a double-exponential function. The average carrier lifetime is calculated (**Table 3.5**) employing $t_{avg} = \frac{B_1\,t_1^2+B_2\,t_2^2}{B_1\,t_1+B_2\,t_2}$ formula (**2.2.10 Time – resolved photoluminescence**). Constants B_1 and B_2 represent non-radiative and radiative relaxation processes, t_1 and t_2 correspond to decay lifetimes associated with the recombination of photogenerated holes and electrons.[232] The average radiative lifetime (t_{avg}) is fitted to arise from two separate components, designated t_1 and t_2. The value of t_{avg} increases with calcination temperature with the highest t_{avg} =11.18 ns for meso-TiO_2-700 as a result of the increase in t_2 (attributed to radiative relaxation processes originating from the indirect formation of self-trapped excitons) and therefore the overall increase in the average radiative lifetime is likely due to improved charge separation across a type-II, staggered anatase/rutile heterojunction interface.[233, 234] All the samples display prolonged charge carrier lifetime compared to that of commercial P25 sample. Increase in the charge carrier lifetime demonstrates inhibited recombination and a higher probability for the redox reactions to take place. The activity should increase with prolonged lifetime of the electrons and holes.

Table 3.5 TRPL data of meso-TiO_2-400, 500, 700, 800 and P25.

Calcination temperature / °C	t_1 / ns	t_2 / ns	B_1	B_2	t_{avg} / ns	χ^2
400	2.2 (±0.1)	(8.5 ±0.4)	(595 ±10)	(121 ±10)	5.0	1.10
500	1.4 (±0.01)	(22.6 ±1.9)	(2435 ±15)	(35 ±2)	5.4	1.10
700	2.2 (±0.1)	(17.0 ±1.1)	(381 ±7)	(76 ±4)	11.2	1.10
800	2.2 (±0.1)	(13.3 ±0.9)	(389 ±6)	(49 ±4)	7.0	1.11
P25	1.0 (±0.02)	(2.6 ±0.1)	(3190 ±57)	(610 ±66)	1.5	1.17

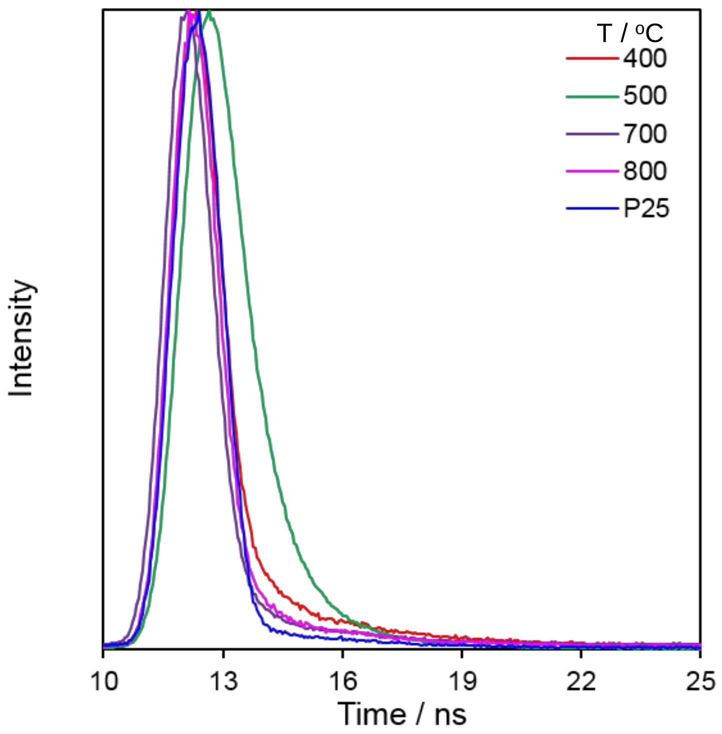

Figure 3.16 Time-resolved photoluminescence spectra of meso-TiO$_2$ series with different calcination temperatures from 300 to 900 °C.

3.1.9 Summary of the key characteristics of mesoporous titania series

Table 3.6 Summarises the main physicochemical and electronic properties of the 7 meso-TiO$_2$ samples synthesised using different calcination temperatures from 300 to 900 ^{o}C.

Calcination Temp / ^{o}C	**BET / m^{2}.g^{-1} (a)**	**Mesopore size / nm (b)**	**Mesopore volume / g.cm^{-3} (b)**	**TiO$_2$ Phase (XRD)**	**Nanocrystallite size / nm(c)**	**Band Gap / eV (d)**	**Total mass loss (H$_2$O) / % (e)**
300	313 (±31)	4.6 (±0.5)	0.41 (±0.04)	Anatase	5 (±0.1)	-	20 (±0.6) (5)
400	194 (±19)	5.4 (±0.5)	0.34 (±0.03)	Anatase	7 (±0.1)	3.07 (±0.02)	6 (±0.2) (3)
500	126 (±13)	6.5 (±0.7)	0.28 (±0.03)	97% Anatase 3% Rutile	11 (±0.1) 29 (±0.3)	3.02 (±0.02)	3 (±0.1) (2)
600	51 (±5)	9.7 (±1.0)	0.15 (±0.02)	96%Anatase 4% Rutile	20 (±0.2) 35 (±0.4)	2.97 (±0.02)	1 (±0.04) (1)
700	19 (±2)	16.0 (±1.6)	0.11 (±0.01)	85% Anatase 15% Rutile	31 (±0.3) 46 (±0.5)	2.94 (±0.02)	0
800	8 (±1)	-	-	96% Anatase 4% Rutile	40 (±0.4) 62 (±0.6)	2.97 (±0.02)	0
900	4 (±0.4)	-	-	25% Anatase 75% Rutile	64 (±0.6) 109 (±1.1)	2.90 (±0.02)	0

[a]N$_2$ BET; [b]from BJH desorption isotherm; [c]mean particle diameter from XRD via Scherrer analysis; [d]DRUVS; [e]TPO;

3.2 Photocatalytic performance of mesoporous titania series

The photocatalytic activity of the mesoporous TiO_2 series characterised above was studied using the photocatalytic decomposition of methyl orange and H_2 production via water splitting reaction under UV-vis light.

3.2.1 Methyl Orange decomposition

The initial approach of testing the photocatalytic activity of meso-TiO_2 was by investigation of photodegradation of 20 ppm Methyl Orange (MO) aqueous solution (**Figure 3.17 (a)**). Prior to illumination, the catalysts were stirred in the dark for one hour to achieve MO adsorption equilibrium. After one hour up 15 % of MO adsorbed on the meso-TiO_2-300 and only 3% on the remaining samples. The values are based on the difference between the absorption of the stock solution and t_o (absorption after 1 hour stirring in the dark before the light source is turned on). To ensure that no further adsorption takes place a test in the dark was performed for the most active meso-TiO_2-700 sample which displayed no further adsorption (**Figure 3.17 (a)**). The illumination of the dye under the UV-vis light in the absence of the photocatalyst for 5h showed no photolysis (**Figure 3.17 (a)**).

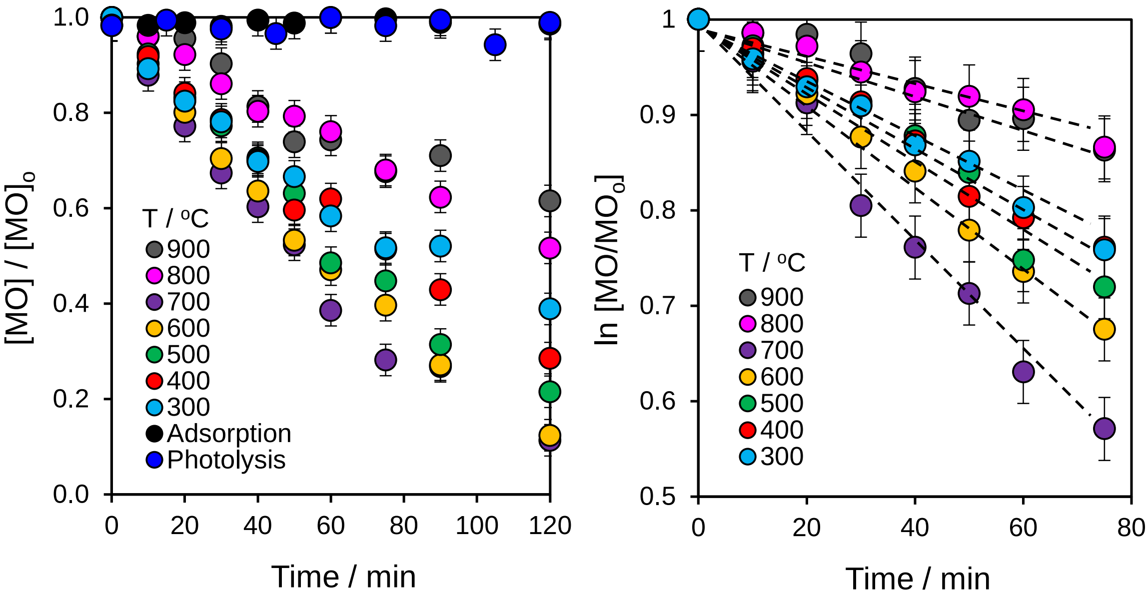

Figure 3.17 (a) Time profiles of the percentage of Methyl Orange degradation including adsorption and photolysis tests (b) ln [MO] vs time profiles of meso-TiO_2 series with different calcination temperatures from 300 to 900 °C under UV-vis.

Ln [MO/MO$_o$] versus time profiles (**Figure 3.17 b**) indicate first order rate kinetics with the rate constants summarised in **Table 3.7**. The first order kinetics are commonly observed in the Methyl Orange degradation reactions over the titania catalysts.[235, 236] Moreover the R^2 index over the linear 75 min region is closer to 1 for the ln [MO/MO$_o$] vs t graphs. All synthesised materials show promising photocatalytic activity under UV-vis irradiation. To more accurately evaluate MO photodegradation mass normalised initial rates are calculated and presented in **Figure 3.18**. Initial rates increase with increasing calcination temperature with the most active catalyst that was calcined at 700 °C. Above this calcination temperature, the initial rates significantly drop (**Figure 3.18 a**). The dramatic decline of the activity at meso-TiO_2 800 and 900 samples mark the formation of large nanocrystallites (60 – 140 nm) leading to the absolute destruction of the mesopore framework and domination of a rutile crystalline phase. As a result, the majority of the loss in activity wass observed at 800 and 900 °C calcination temperatures. The prepared mesoporous TiO_2 samples are thermally stable up to 700 °C, therefore further investigation of the photocatalytic activity will focus on meso-TiO_2-300 – 700 samples. Meso-TiO_2-300 sample which is black in colour and has 15% of carbon species present, which is known to work as catalyst poison.[237]

Table 3.7 First order rate constant k of meso-TiO_2 series with different calcination temperatures from 300 to 900 °C. Determined using ln [MO] vs time data under UV-vis.

Calcination temp. / °C	k / min^{-1}
300	0.0086 (±0.0001)
400	0.0089 (±0.0001)
500	0.0105 (±0.0001)
600	0.0126 (±0.0001)
700	0.0169 (±0.0002)
800	0.0055 (±0.0001)
900	0.0056 (±0.0001)

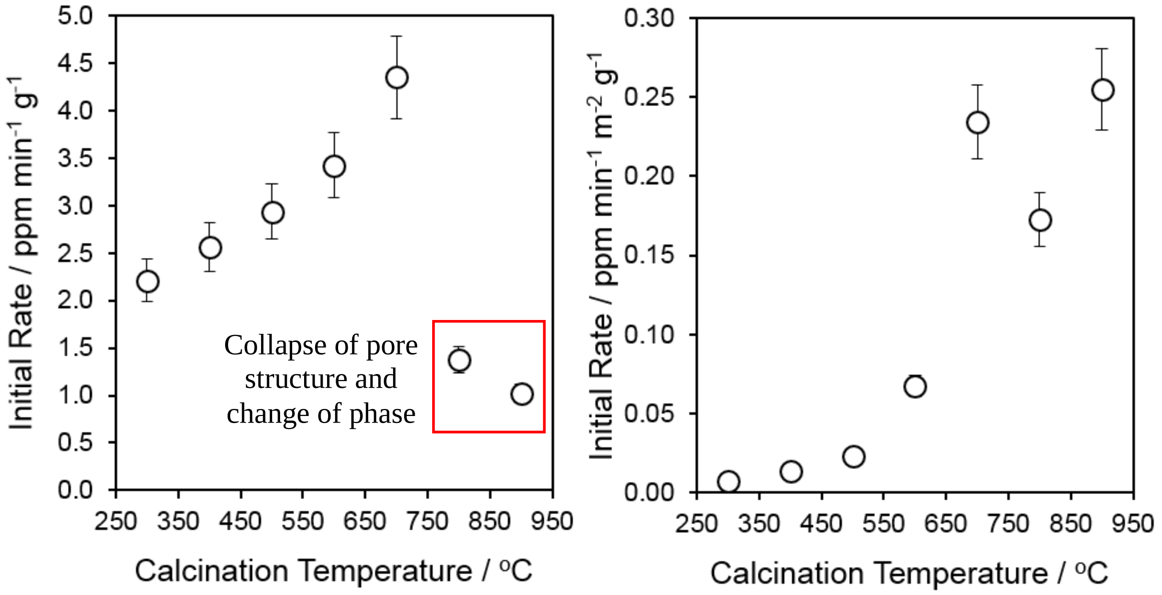

Figure 3.18 (a) Initial rates vs calcination temperature of meso-TiO_2 series with different calcination temperatures from 300 to 900 °C (b) Initial rates of (a) normalised to surface area of the catalysts from the N_2 porosimetry results under UV-vis irradiation.

Since calcination simultaneously alters the structural and optical properties of mesoporous titanias, it is difficult to unequivocally identify the origin of the rate enhancement. Increase in calcination temperature leads to a larger average mesopore diameter and as a result a decrease in surface area. Initial rates in **Figure 3.18 a** were normalised to surface area and displays the same trend, not a straight line, indicating that surface area does not have an effect on the photocatalytic activity of meso-TiO_2 series (**Figure 3.18 b**). Furthermore, the phase transformation from anatase to rutile takes place and it directly influences the band gap of the materials. Increase in calcination temperature leads to higher crystallinity together with the drastic growth of crystallite size. Low calcination temperature semicrystalline materials suffer from fast electron-hole recombination owing to a large number of defects.[238]

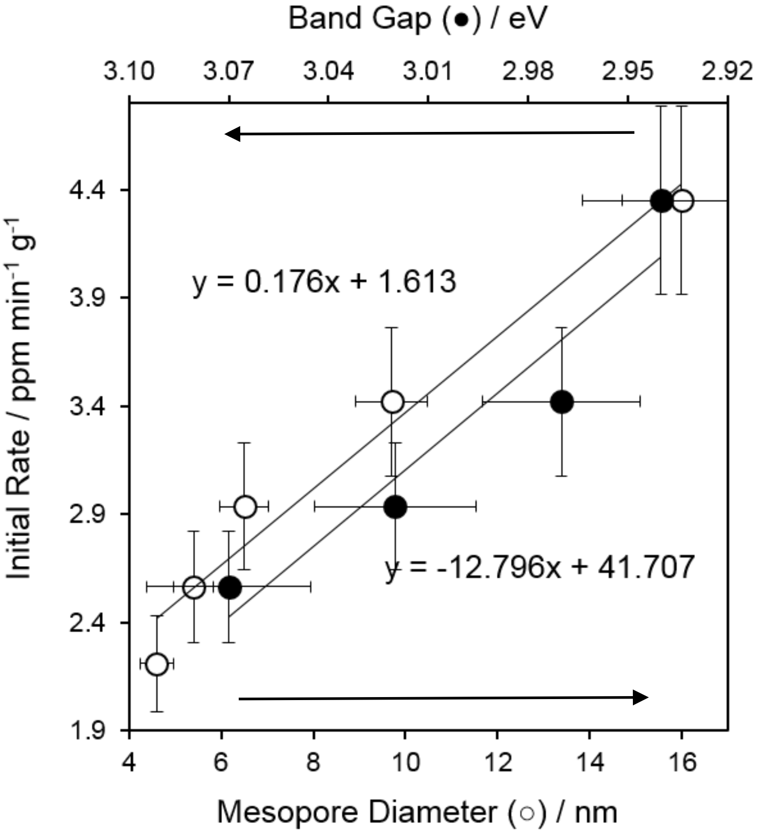

Figure 3.19 Initial rates vs band gap and mesopore diameter of meso-TiO_2 series with different calcination temperatures from 300 to 700 °C under UV-vis.

In this case, initial rate is affected by two key parameters: structural - mesopore diameter and electronic – rutile content/band gap, as illustrated in **Figure 3.19**. The photocatalytic activity linearly increases with increasing mesopore diameter and decreasing band gap energy which is controlled by the anatase:rutile content. The former may be readily understood in terms of improved mass transport of the bulky dye into the mesopore network through Knudsen diffusion, for which the diffusion coefficient is proportional to pore diameter.[239, 240] Based on the value of the coefficient *a* from the function of y=*a*x+y displayed on the graph, photocatalysts performance is more sensitive to the band gap change, where the coefficient *a* is 100 fold higher (*a*=-12.796), than it is to mesopore size increase (*a*=0.176). Diffusion limitation is a minor factor because the major increase of mesopore diameter from 5 nm to 16 nm only doubles the initial rate. The hydrated Methyl Orange molecule is approx. 2.6 nm, and fits in the smallest 5 nm mesopores. However, the absolute destruction of the mesopore structure and the growth of very large crystallites drastically reduces the photocatalytic activity as it is seen in the meso-TiO_2-800 and 900 samples, even though they have a suitable band gap. The enhancement of photocatalytic performance with decreasing band gap is solely due to increasing amounts of rutile formed in addition to the dominant anatase phase. Mixed phase junction improves charge separation and as a result, reduce recombination by transfer of excited electrons from anatase to rutile at the interface. The interface creates defect sites with unique adsorption and charge trapping properties.[233, 241] The time-resolved photoluminescence data (**Table 3.5**) shows the average radiative lifetime (t_{avg}), fitted to arise from two separate components, designated t_1 and t_2. t_{avg} increases with calcination temperature with the highest t_{avg} =11.18 ns for meso-TiO_2-700 as a result of the increase in t_2 (attributed to radiative relaxation processes originating from the indirect formation of self-trapped excitons) and therefore the overall increase in the average radiative lifetime is likely due to improved charge separation, prolonged charge carrier lifetime and reduced recombination across a type-II, staggered anatase/rutile heterojunction interface.[233, 234]

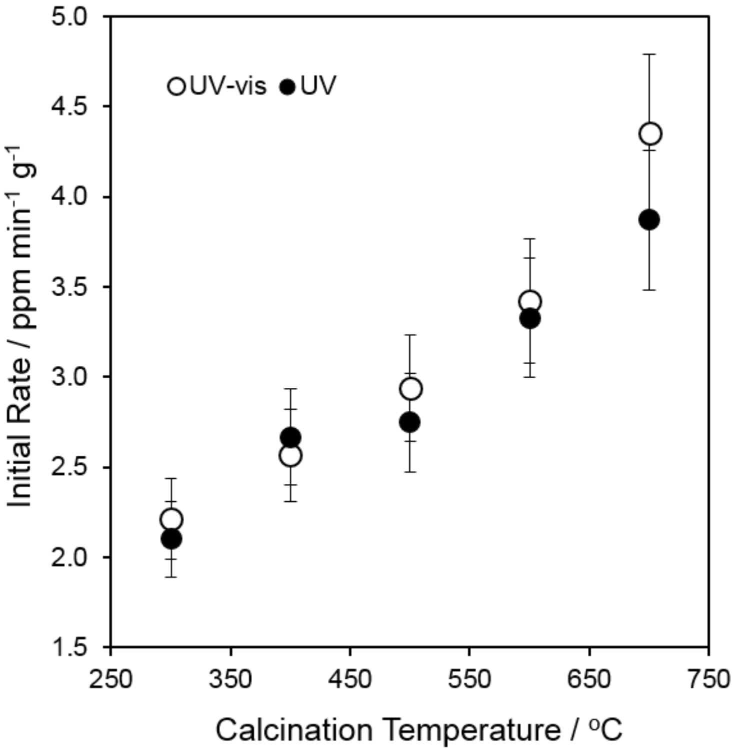

Figure 3.20 Initial rates vs calcination temperature of meso-TiO_2 series with different calcination temperatures from 300 to 700 °C under UV-vis and UV light irradiations.

The activity of meso-TiO_2 series was also tested in solely UV light (<400 nm). It displays no difference in the photodegradation of MO by samples meso-TiO_2-300 and 400 under UV or UV-vis light irradiation (**Figure 3.20**). It is suggesting that there is no significant Methyl Orange dye sensitisation because the majority of light absorption by MO is under visible light (**Figure 2.7**).[135]

The meso-TiO_2-500 and 700 samples cannot be included in this comparison because these samples contain the rutile phase, which can absorb in the visible light region (>400 nm).

The initial rate of commercial P25 tested under the exact same conditions as meso-TiO_2 series displayed 9 ppm.min^{-}.g^{-1}, which is twice more active than the most active meso-TiO_2-700 sample. However, based on observations, since P25 was manufactured commercially, it was a much finer powder and dispersed significantly better in the aqueous solution compared to meso-TiO_2 series, ground by mortar and pestle.

3.2.2 Water splitting

The photocatalytic activity of meso-TiO_2 series in H_2 production via water splitting is presented in **Figure 3.21.** Calcination of meso-TiO_2 exerted a similar effect on photocatalytic hydrogen production from water splitting under UV-Vis irradiation to that observed for MO degradation (**3.2.1 Methyl Orange decomposition**); hydrogen production rate increases almost linearly with increasing meso-TiO_2 calcination temperature with the meso-TiO_2-700 sample being most active. At calcination temperatures higher than 700 °C, rate decreases due to loss of pore structure and sintering of crystallites. The decline of activity is not as sharp as for MO tests indicating that mesopore structure has less influence on performance.

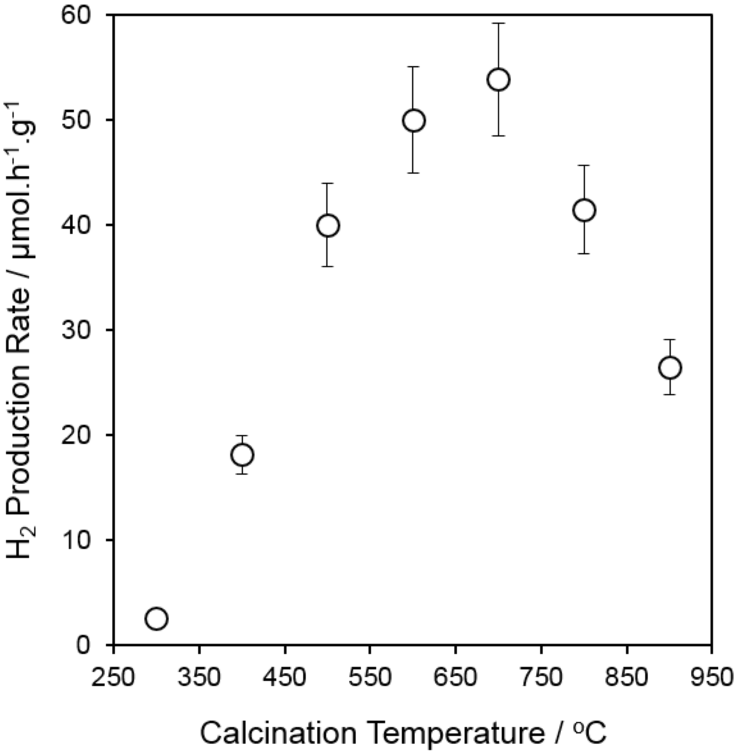

Figure 3.21 H_2 production rates of meso-TiO_2 series with different calcination temperatures from 300 to 900 °C under UV-vis.

Figure 3.22 demonstrates an exponential increase in activity with increasing mesopore diameter with no considerable difference above 7 nm. In this instance mesopore expansion cannot be responsible for the (dramatic) 25-fold rate-enhancement observed, since chemical mass transport of water will never be rate-limiting in aqueous solution. In addition, products in this reaction are notably smaller than the MO molecule, thus intra-structural diffusion is not a limiting factor. The significant increase in H_2 productivity with calcination temperature mirrors the concomitant decrease in band gap and must arise from the phase transition from anatase→rutile. As discussed above for MO degradation, this phase transition is expected to result in a type-II staggered semiconductor heterojunction, thereby increasing charge carrier lifetimes and hence activity for any photocatalytic process. Furthermore, it is important to recall that the energetic position of the conduction band minimum (CBM) should be more negative than the reduction potential of water (−0.41 V vs SHE at pH 7) to produce H_2 ($2H^+ + 2e^- \rightarrow H_2$).[242] In water splitting reaction, electronic effects are the key factors affecting photocatalytic activity while structural components have very little influence. The H_2 production rate of commercial P25 tested under the exact same conditions as meso-TiO_2 series displayed 50 µmol.h^{-1}.g^{-1} rate which correlates well with the most active meso-TiO_2-600 and meso-TiO_2-700 photocatalysts.

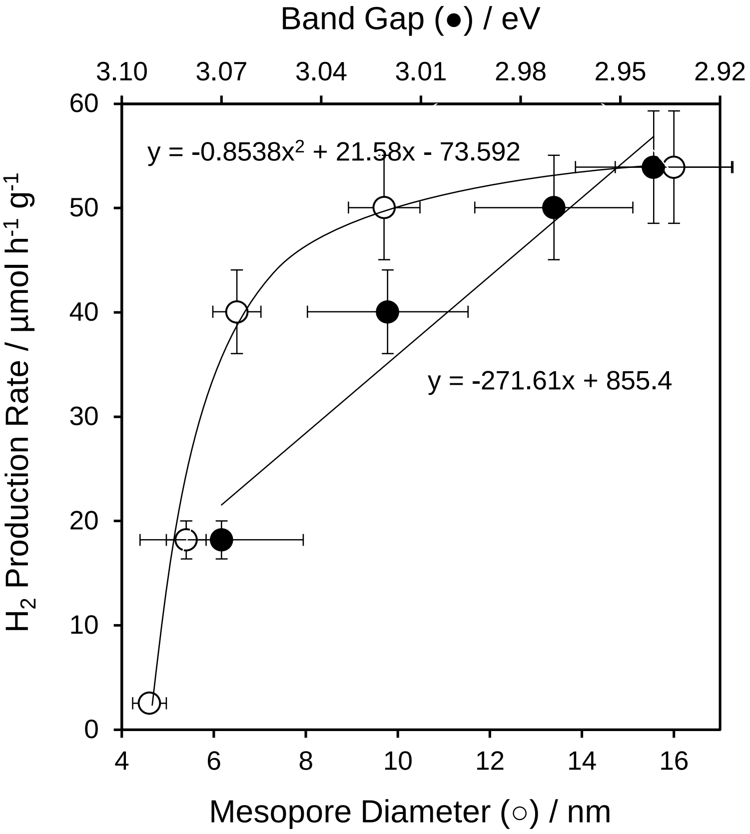

Figure 3.22 H_2 production rate vs band gap and mesopore diameter of meso-TiO_2 series with different calcination temperatures from 300 to 700 °C under UV-vis irradiation.

3.3 Characterisation of 0.02 – 12.33 wt% Cu promoted mesoporous titania 500 ºC

Previously evaluated meso-TiO_2-500 catalyst support (**3.1 Characterisation of mesoporous titania series**) was synthesised on the large scale and promoted with Cu at six different loadings from 0.02 to 12.33 wt% by classic wet impregnation method using $Cu(NO_3)_2.3H_2O$ as a precursor. Due to the large scale synthesis, there might be some very small differences in the characteristics of meso-TiO_2-500 with the previous (**3.1 Characterisation of mesoporous titania series**) chapter. In general, this support offers the optimal trade-off between textural properties such as high surface area and rutile content/band gap (**Table 3.6**), the latter desirable for heterojunction formation and enhanced photoactivity. Meso-TiO_2 materials proved to be fairly active catalysts under UV light, but inactive in visible light irradiation. The primary goal of promotion with Cu is to enhance the catalyst performance in the UV-vis range. Cu oxides are well known for their ability to absorb light in the visible region due to their small 1 – 2.2 eV band gaps.[243] The characteristics of newly produced catalysts is examined to confirm the retention of mesoporous TiO_2 support properties and to identify Cu species.

3.3.1 Nitrogen porosimetry

N_2 porosimetry was performed to establish the retention of the structural properties of meso-TiO_2-500 support which was impregnated with 0.02 – 12.33 wt% Cu loadings. N_2 adsorption/desorption curves (**Figure 3.23**) of the support and Cu-impregnated samples are identical and display Type IV isotherms typical for mesoporous materials with H2 type hysteresis loop because of differing capillary condensation and evaporation within mesopores during adsorption and desorption respectively. Hysteresis indicates either restricted pore entrance (ink bottle shape) or irregular in channel structure of mesopore framework.[174]

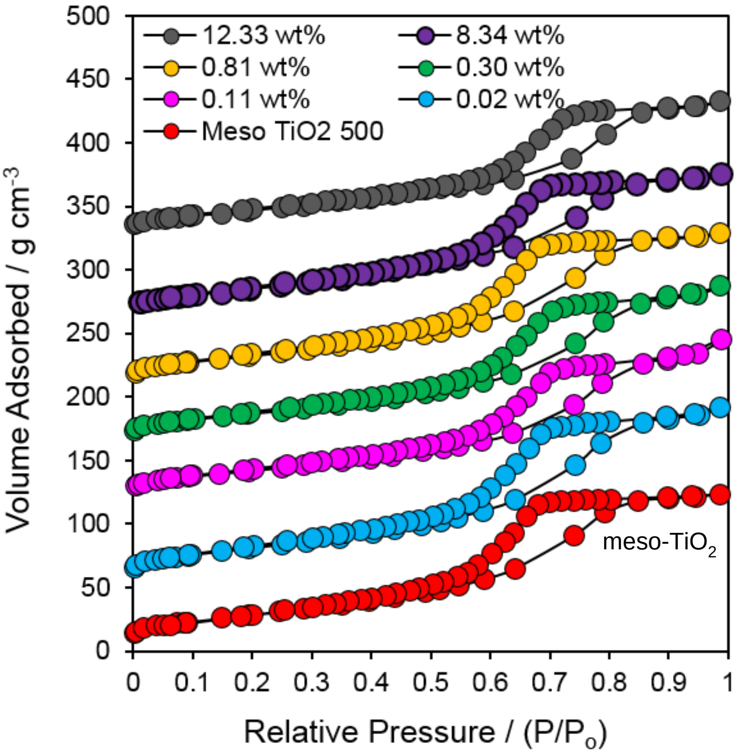

Figure 3.23 Stacked isotherm plot of 0.02 – 12.33 wt% Cu on meso-TiO_2-500 support.

Specific surface area (**Table 3.8**) for Cu promoted samples is estimated using BET (Brunauer – Emmett - Teller) method with an average value of 98 m^2 g^{-1} and matches that of the meso-TiO_2-500 support. The average mesopore volume of 0.21 g cm^{-3} (**Table 3.8**) and 6.2 nm mesopore size (**Figure 3.24**) are also in a good agreement with values for the support.

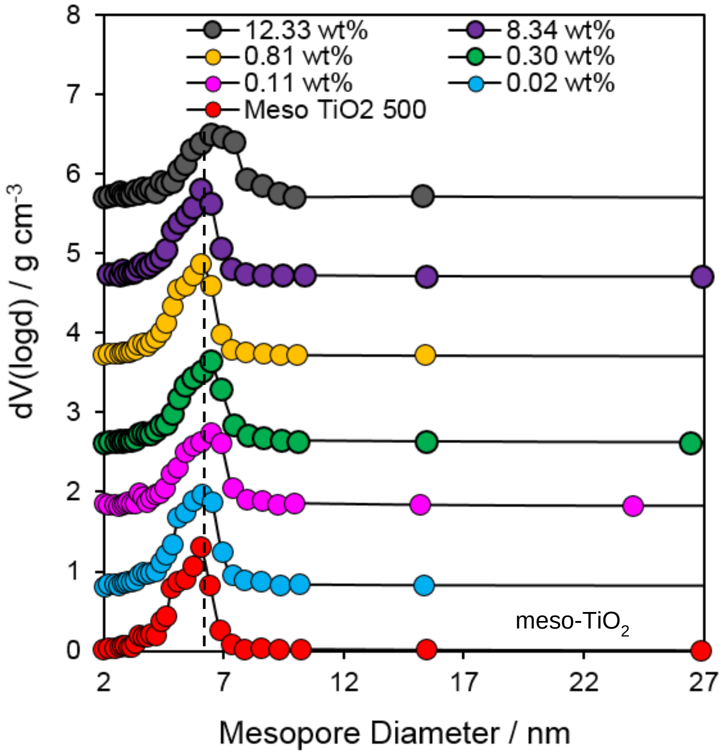

Figure 3.24 Mesopore size distribution of 0.02 – 12.33 wt% Cu on meso-TiO$_2$-500 support.

Table 3.8 Summary of N$_2$ porosimetry results of 0.02 – 12.33 wt% Cu on meso-TiO$_2$-500 support.

Cu / wt%	BET / m^2 g^{-1}	Mesopore size / nm	Mesopore volume / g cm^{-3}
Meso TiO$_2$ 500 (support)	107 (±11)	6.0 (±0.6)	0.21 (±0.02)
0.02	115 (±12)	6.1 (±0.6)	0.24 (±0.02)
0.11	91 (±9)	6.5 (±0.7)	0.21 (±0.02)
0.30	99 (±10)	6.4 (±0.6)	0.21 (±0.02)
0.81	101 (±10)	6.1 (±0.6)	0.21 (±0.02)
8.34	98 (±10)	6.1 (±0.6)	0.20 (±0.02)
12.33	84 (±8)	6.4 (±0.6)	0.18 (±0.02)

3.3.2 X-ray diffraction

Ex-situ wide angle XRD diffractograms (**Figure 3.25**) for 0.02 – 12.33 wt% Cu/meso- TiO_2 and the support display identical X-ray patterns with seven well-resolved diffraction peaks indexed (101), (004), (200), (105,211), (204), (116,220), (215) corresponding to a solely anatase crystalline phase. Additionally, only the 12.33 wt% sample exhibited CuO species peaks (marked *) revealing that CuO nanocrystallites in the remaining samples are smaller than 2 nm or the amounts are beyond the XRD detection limits.

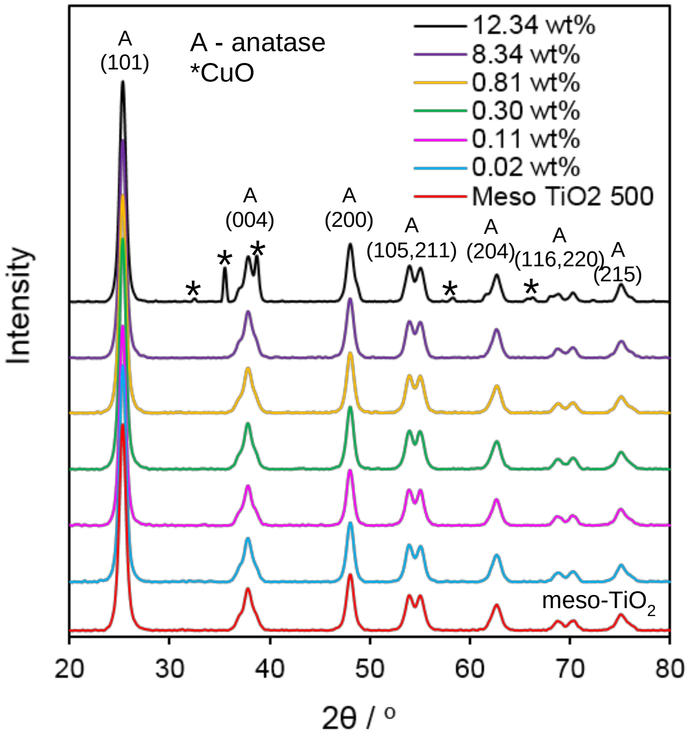

Figure 3.25 Wide angle XRD patterns of 0.02 – 12.33 wt% Cu on meso-TiO_2-500 support.

Anatase crystallites sizes were estimated using the Scherrer formula from the average of FWHM of (101), (200), (215) and all possess an equal diameter of 11 nm (**Table 3.9**) across all Cu loadings. This diameter matches the 11 nm anatase crystallite diameter of the support meso-TiO_2-500. The CuO crystallites of the 12.34 wt% loading sample are estimated to be 34 nm using $2\theta=35.5\ ^{\circ}$ (111). Unit cell parameters (**Table 3.9**) of tetragonal ($a=b\neq c$, $\alpha=\beta=\gamma=90^{\circ}$) anatase crystalline phase is calculated using $d_{(200)}$ lattice spacing and are the same for all materials and are in a good agreement with the literature (a=b=3.78 Å).[227] None of the samples display any peaks in their low angle X-ray diffraction patterns.

Table 3.9 Summary of XRD results of 0.02 – 12.33 wt% Cu on meso-TiO_2-500 support.

Cu / wt%	Crystalline phase	Nanocrystallite size / nm	Anatase unit cell a (=b) / Å
Meso TiO_2 500 (support)	Anatase	11 (±0.1)	3.78 (±0.04)
0.02	Anatase	11 (±0.1)	3.78 (±0.04)
0.11	Anatase	11 (±0.1)	3.78 (±0.04)
0.30	Anatase	11 (±0.1)	3.78 (±0.04)
0.81	Anatase	11 (±0.1)	3.78 (±0.04)
8.34	Anatase	11 (±0.1)	3.78 (±0.04)
12.33	Anatase	11 (±0.1)	3.78 (±0.04)

3.3.3 Inductively coupled plasma optical emission spectrometry

ICP – OES confirmed the successful preparation of a range of Cu loadings (**Table 3.10**). The aim is a wide range of loadings spanning from ultra-low 0.03 to higher 10 wt% values. The range of 0.02 – 12.33 wt% is determined for the resulting catalysts which are in a good agreement with the theoretical desired values.

Table 3.10 ICP – OES data of 0.02 – 12.33 wt% Cu on meso-TiO_2-500 support.

Theoretical Cu loading / wt%	Experimental ICP - OES Cu loading / wt%
0.03	0.02 (±0.001)
0.10	0.11 (±0.003)
0.30	0.30 (±0.009)
0.50	0.81 (±0.024)
5.00	8.34 (±0.250)
10.00	12.33 (±0.370)

3.3.4 X-ray absorption spectroscopy

Copper co-catalysts can promote titania by various means, including trapping of the charge carriers at the semiconductor surface and/or electron injection into the titania conduction by metallic nanoparticles, [244-246] heterojunction formation between discrete copper oxide and titania nanoparticles, [247, 248] or framework substitution of copper cations accompanied by band energy modification and/or charge transport.[249, 250] It is critical to identify copper chemical environment within Cu/meso-TiO_2 series to interpret their mode of activity. The oxidation state and the local environment of copper atom, as either atomically isolated species or smaller than 2 nm nanocrystallites are of interest. WA XRD of loadings 0.02 – 8.34 wt% displayed no peaks corresponding to Cu species indicating crystallites being smaller than ~2 nm or the amounts being beyond XRD threshold. Employment of XPS for surface species identification is also complicated due to comparable binding energies of copper metal and copper(I) oxide, with the only subtle difference in the spectra from weak satellite peaks as well as ultra-low copper concentrations that are beyond signal to noise ratio.[189] The ultra-low Cu loadings within some samples prohibits quantification and discrimination of Cu species and size using laboratory X-ray sources. Hence the local chemical environment and oxidation state of Cu species were probed by Cu K-edge X-ray absorption spectroscopy (XAS -synchrotron beam source).

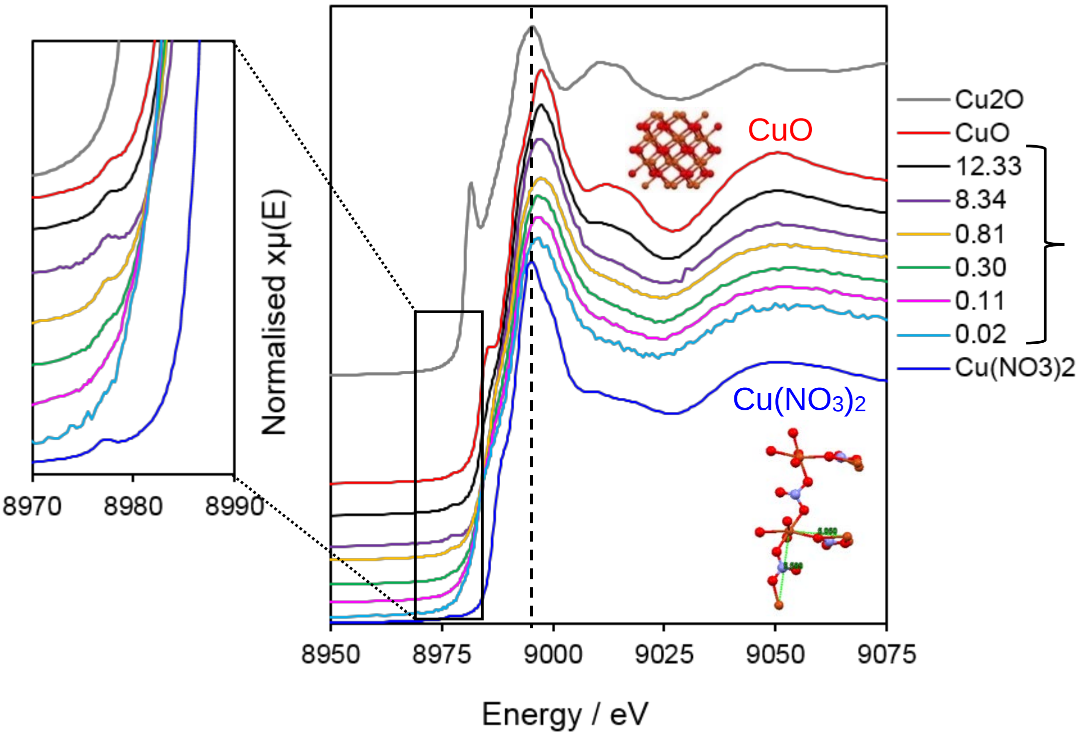

Figure 3.26 XAS spectrum of 0.02 – 12.33 wt% Cu on meso-TiO_2-500 support and reference Cu_2O, CuO and $Cu(NO_3)_2$.

Background subtracted, normalised XANES spectra of the 0.02-12.33 wt% Cu/meso-TiO_2 series and Cu_2O, CuO and $Cu(NO_3)_2$ references are shown in **Figure 3.26**. The copper local environment evolves from that reminiscent of the Cu(II) nitrate trihydrate complex to that of bulk CuO with increasing Cu loading, with spectra exhibiting three distinct features: a weak pre-edge feature around 8977 eV, a strong rising-edge feature around 8986 eV, and an intense white line around 8996; these are attributed to dipole-forbidden 1s→3d (not observed for Cu(I) species), 1s→$4p_z$ (or 4px,ypz for Cu(I) species) and 1s→4p (continuum) transitions respectively. Least squares spectral fitting to Cu, Cu_2O, CuO and $Cu(NO_3)_2$ references identified only Cu(II) in all Cu/meso-TiO_2 samples (**Figure 3.27**), with loadings ≥0.81 wt% a good fit to CuO, and those <0.3 wt% an excellent fit to a mononuclear copper species. However, **Figure 3.26** reveals that the pre-edge feature characteristic of Cu(II) only emerges for Cu loadings ≥0.3 wt%, and hence copper atoms in the ultra-dilute Cu/meso-TiO_2 materials appear electronically similar to Cu(I) but structurally similar to those in mononuclear complexes. Fitting of the corresponding EXAFS spectra of the 0.1 wt% Cu/meso-TiO_2 sample revealed only Cu-O scatterers around 1.94 Å, with no Cu-Cu interatomic distances (**Table 3.11**, K^3 **Figure 3.28 (a)** and R^3 **Figure 3.28 (b)**), consistent with isolated Cu(I) species either within the titania framework or decorating the semiconductor surface. The Cu-O nearest neighbour coordination number of 2.5 (versus 4 for both CuO and $Cu(NO_3)_2$) for 0.1 wt% Cu/meso-TiO_2 is consistent with either anion vacancy formation upon framework substitution of Ti(IV) with Cu(I), or atomically-dispersed, undercoordinated Cu(I) atoms at the titania surface. Since copper was introduced by post-modification of mesoporous titania, employing a comparatively low-temperature processing step, the latter scenario is more feasible. The constant band gap, and anatase lattice parameter and crystal size, following the addition of ultra-low Cu concentrations to the parent meso-TiO_2, supports the hypothesis that single copper atoms are dispersed over titania.

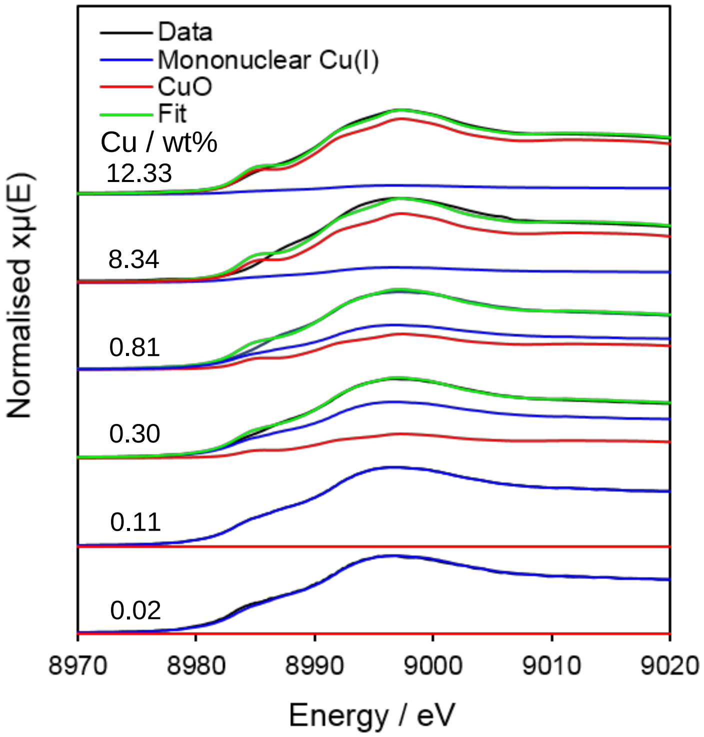

Cu / wt%	Mononuclear Cu (I) / %	CuO / %
0.02	100 (±0.1)	0
0.11	100 (±0.1)	0
0.30	71.7 (±0.1)	28.3 (±0.1)
0.81	57.4 (±0.1)	42.6 (±0.1)
8.34	20.2 (±0.1)	79.8 (±0.1)
12.33	11.2 (±0.1)	88.8 (±0.1)

Figure 3.27 Fitting and summary of % of mononuclear Cu (I) species and CuO from fitted XANES region of 0.02 – 12.33 wt% Cu on meso-TiO_2-500 support.

Table 3.11 EXAFS fitting data of 0.11 and 12.33 wt% Cu on meso-TiO_2-500 support.

Sample	1st Shell Scatter	2nd Shell scatter	3rd Shell scatter	4th Shell scatter	5th Shell scatter
Cu	Cu	Cu	Cu	-	-
CuO	O	O	Cu	Cu	Cu
$Cu(NO_3)_2$	O	O	N	-	-
12.33 wt.% Cu	O	O	Cu	Cu	Cu
0.11 wt.% Cu	O	O	N	-	-

Sample	1st shell CN	2nd shell CN	3rd shell CN	4th shell CN	5th shell CN
Cu	12	6	24	-	-
CuO	4	2	4	4	2
$Cu(NO_3)_2$	4	2	2	-	-
12.33 wt.% Cu	3.6	1.8	2.0	2.0	1.0
0.11 wt.% Cu	2.5	0	0	-	-

Sample	1st shell R	2nd shell R	3rd shell R	4th shell R	5th shell R
Cu	2.55 (2.57)	3.6 (3.62)	4.42 (4.43)	-	-
CuO	1.96 (1.96)	2.78 (2.78)	2.90 (2.90)	3.08 (3.08)	3.17 (3.17)
$Cu(NO_3)_2$	1.97 (1.98)	2.54 (2.55)	2.72 (2.73)	-	-
12.33 wt.% Cu	1.95 (1.96)	2.78 (2.78)	2.90 (2.90)	3.08 (3.08)	3.17 (3.17)
0.11 wt.% Cu	1.94 (1.98)	0	0	-	-

Sample	1st shell σ	2nd shell σ	3rd shell σ	4th shell σ	5th shell σ	r-factor
Cu	0.0098 (±0.0010)	0.0157 (±0.0016)	0.0162 (±0.0016)	-	-	2.60%
CuO	0.0043 (±0.0004)	0.0146 (±0.0015)	0.0060 (±0.0006)	0.0068 (±0.0007)	0.0198 (±0.0020)	2.46%
$Cu(NO_3)_2$	0.0036 (±0.0004)	0.0287 (±0.0029)	0.0073 (±0.0007)	-	-	1.00%
12.33 wt.% Cu	0.0054 (±0.0005)	0.0241 (±0.0024)	0.0063 (±0.0006)	0.0075 (±0.0008)	0.0556 (±0.0057)	1.65%
0.11 wt.% Cu	0.0033 (±0.0003)	0	0	-	-	1.30%

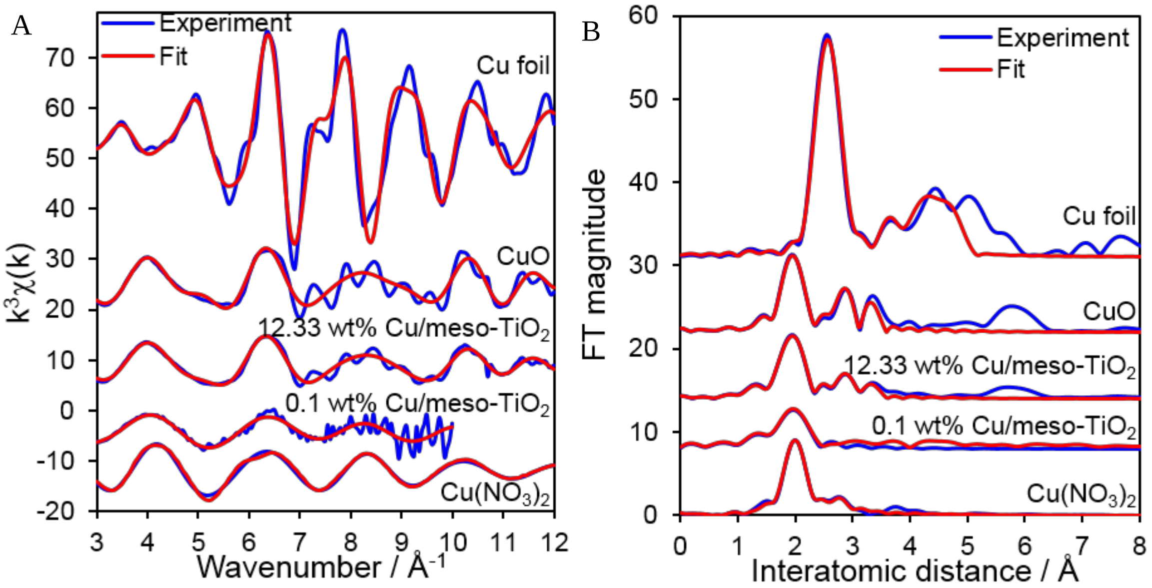

Figure 3.28 (a) k^3factor from EXAFS spectra of 0.11 and 12.33 wt% Cu/meso-TiO_2-500 catalysts (b) R^3factor from EXAFS spectra of 0.11 and 12.33 wt% Cu/meso-TiO_2-500 catalysts.

3.3.5 Diffuse reflectance UV-vis spectrophotometry

Recorded solid diffuse reflectance UV-vis optical absorption spectra (**Figure 3.29**) and Tauc plots (**Figure 3.30**) for 0.02 – 12.33 wt% Cu/meso-TiO_2 500 demonstrate a systematic evolution in optical properties of the parent meso-TiO_2 with increasing loading of Cu functionalisation. The absorption spectra of the catalysts all displayed a sharp edge in absorption which progressively shifted from ~350 – 450 nm → more visible ~430 – 550 nm region with increasing Cu loading. This was accompanied by increased absorption between 400-600 nm possibly due to interface states arising from charge transfer between TiO_2 and Cu(I)/Cu(II) species, and the emergence of a new absorption band spanning 580-900 nm associated with d-d transitions in CuO[251] for loadings ≥0.3 wt%. The band gaps of materials are calculated using Tauc plots (**Figure 3.30**). The band gap energies of the photocatalysts decrease from 3.00 eV for the parent titania to 1.10 eV for 12.33 wt% Cu sample. The shift of the absorption edge to a more visible region and a decrease in the band gap with increasing Cu loading is a result of the formation of bulk CuO[252] (in accordance with XRD), which usually possess a visible band gap from 1 to 2.2 eV.[243] In DRUVS measurements recorded absorbance/reflectance is inevitably dominated by the lowest available energy absorption, in this case, Cu.

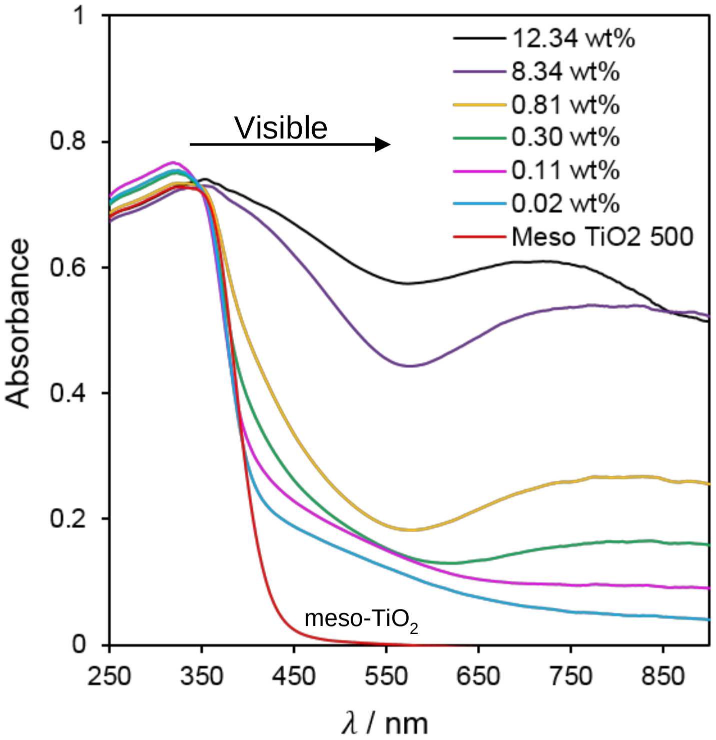

Figure 3.29 UV – vis absorption spectra of 0.02 – 12.33 wt% Cu on meso-TiO_2-500 support.

Sample	Band Gap / eV
Meso-TiO$_2$-500 (support)	3.00 (±0.02)
0.02	3.00 (±0.02)
0.11	3.00 (±0.02)
0.30	2.87 (±0.02)
0.81	2.59 (±0.02)
8.34	1.40 (±0.01)
12.33	1.10 (±0.01)

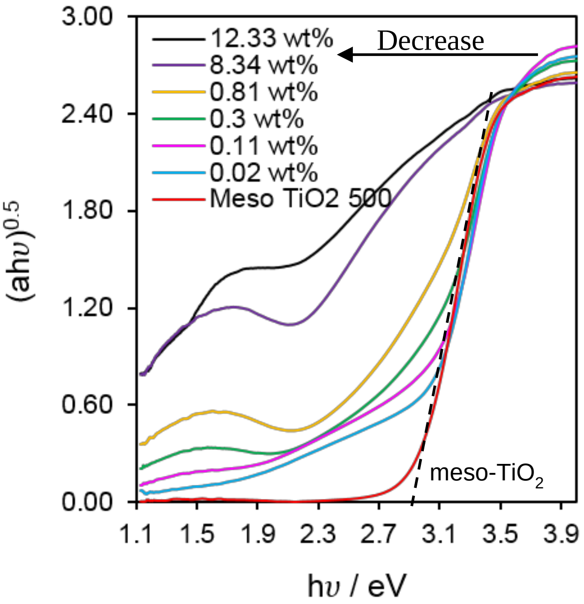

Figure 3.30 Tauc plot of 0.02 – 12.33 wt% Cu on meso-TiO$_2$-500 support and corresponding band gap values.

3.3.6 Summary of the key characteristics of 0.02 – 12.33 wt% Cu promoted mesoporous titania 500 °C

Table 3.12 Summarises the main physicochemical and electronic properties of 0.02 – 12.33 wt% Cu on the meso-TiO$_2$-500 support.

Cu / wt%(a)	**Mononuclear Cu (I) / %**	**CuO / %**	**BET / m^2.g^{-1}(b)**	**Mesopore size / nm(c)**	**Mesopore volume / g.cm^{-3}(c)**	**TiO$_2$ Phase (XRD)**	**Nanocrystallite size / nm(d)**	**Band Gap / eV(e)**
Meso-TiO$_2$ (support)	-	-	107 (±11)	6.0 (±0.6)	0.21 (±0.02)	Anatase	11 (±0.1)	3.00 (±0.02)
0.02	100 (±0.1)	0	115 (±12)	6.1 (±0.6)	0.24 (±0.02)	Anatase	11 (±0.1)	3.00 (±0.02)
0.11	100 (±0.1)	0	91 (±9)	6.5 (±0.7)	0.21 (±0.02)	Anatase	11 (±0.1)	3.00 (±0.02)
0.30	71.7 (±0.1)	28.3 (±0.1)	99 (±10)	6.4 (±0.6)	0.21 (±0.02)	Anatase	11 (±0.1)	2.87 (±0.02)
0.81	57.4 (±0.1)	42.6 (±0.1)	101 (±10)	6.1 (±0.6)	0.21 (±0.02)	Anatase	11 (±0.1)	2.59 (±0.02)
8.34	20.2 (±0.1)	79.8 (±0.1)	98 (±10)	6.1 (±0.6)	0.20 (±0.02)	Anatase	11 (±0.1)	1.40 (±0.01)
12.33	11.2 (±0.1)	88.8 (±0.1)	84 (±8)	6.4 (±0.6)	0.18 (±0.02)	Anatase	11 (±0.1)	1.10 (±0.01)

[a]*ICP – OES;* [b]*N$_2$ BET;* [c]*from BJH desorption isotherm;* [d]*Mean particle diameter from XRD via Scherrer analysis;* [e]*DRUVS;*

3.4 Characterisation of 0.1 wt% Cu promoted mesoporous titania 400 - 800 °C

The meso-TiO_2 series prepared using calcination temperatures ranging from 400 – 800 °C, as discussed in **3.1 Characterisation of mesoporous titania series**, was promoted with 0.1 wt% Cu by the wet impregnation method using $Cu(NO_3)_2.3H_2O$ as a precursor. In this case, the supports characterised in **3.1 Characterisation of mesoporous titania series** are directly used for the Cu addition. The 0.1wt% was chosen as the most active loading from the results covered in **3.5 Photocatalytic performance of Cu promoted mesoporous titania series**. The characteristics of the newly produced catalysts were examined to confirm the retention of meso-TiO_2 qualities and investigate the influence of the support on the Cu species and its resulting activity.

3.4.1 Nitrogen porosimetry

N_2 porosimetry allows the evaluation of the structural properties of meso-TiO_2-400 - 800 support series after deposition with Cu. N_2 adsorption/desorption curves (**Figure 3.31**) of the promoted catalysts display the exact same trend seen in nitrogen porosimetry of the bare meso-TiO_2 series: samples 0.1 wt% Cu/meso-TiO_2-400 - 500 demonstrate type IV isotherms typical for mesoporous materials with an H2 type hysteresis loop revealing either restricted pore entrance (ink bottle shape) or variation in channel structure of mesopore framework; the 0.1 wt% meso-TiO_2-800 sample exhibits a Type II isotherm with no significant hysteresis loop indicating absence of mesoporosity. [174]

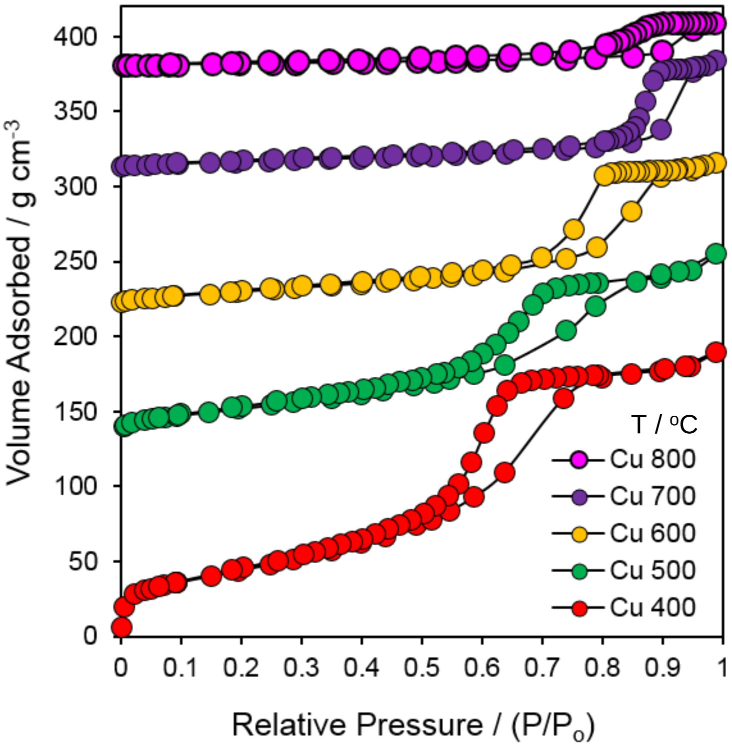

Figure 3.31 Stacked isotherm plot of 0.1 wt% Cu on meso-TiO_2-400 - 800 supports.

The specific surface area (BET, Brunauer-Emmett-Teller method), mesopore volume and mesopore size (BJH, Barrett-Joyner-Halenda) of 0.1 wt% Cu mesoporous series are summarised in **Table 3.13**. In addition, the data collected for bare meso-TiO_2-400 – 800 supports are presented for comparison. The Cu promoted materials displayed the same tendency for the reduced surface area and mesopore volume and a significant increase in mesopore size (**Figure 3.32**) with increasing calcination temperature. In comparison with the bare support, the surface areas of Cu/meso-TiO_2-400 and 500 samples are slightly lower but there is no major change in either mesopore size or in mesopore volume. It is evident that the supports retain their mesoporous structure after the Cu wet impregnation process.

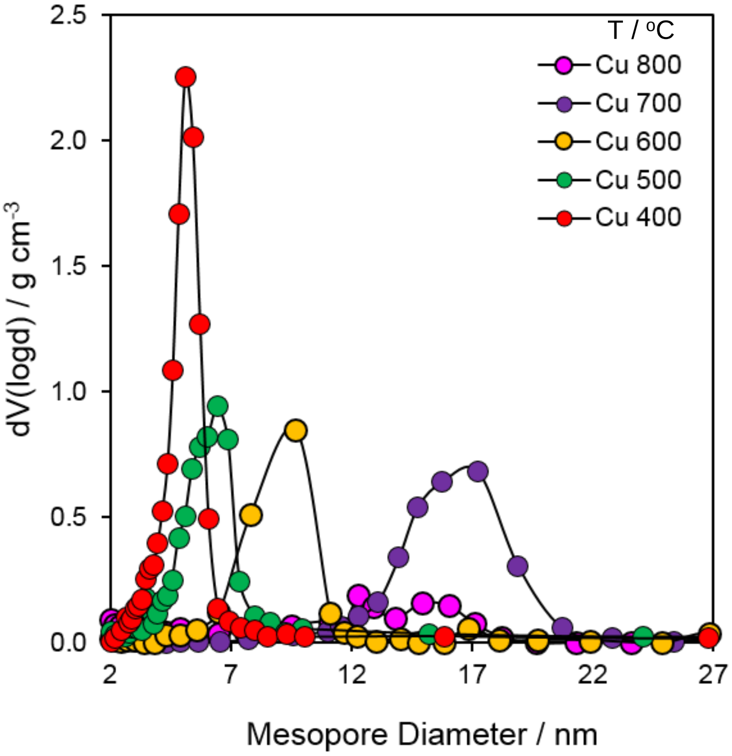

Figure 3.32 Mesopore size distribution of 0.1 wt% Cu on meso-TiO_2 400 - 800 supports.

Table 3.13 Summary of N_2 porosimetry results of 0.1 wt% Cu on meso-TiO_2-400 - 800 supports. On the right the corresponding values of the support before Cu promotion.

	0.1 wt% Cu promoted meso-TiO_2			meso-TiO_2 supports		
Sample	BET / m^2 g^{-1}	Mesopore size / nm	Mesopore volume / g cm^{-3}	BET / m^2 g^{-1}	Mesopore size / nm	Mesopore volume / g cm^{-3}
400	167 (±17)	5.1 (±0.5)	0.32 (±0.03)	194 (±19)	5.4 (±0.5)	0.34 (±0.03)
500	91 (±9)	6.5 (±0.7)	0.21 (±0.02)	126 (±13)	6.5 (±0.7)	0.28 (±0.03)
600	54 (±5)	9.7 (±1.0)	0.16 (±0.02)	51 (±5)	9.7 (±1.0)	0.15 (±0.02)
700	24 (±2)	15.8 (±1.6)	0.12 (±0.01)	19 (±2)	16.0 (±1.6)	0.11 (±0.01)
800	11 (±1)	-	-	8 (±1)	-	-

3.4.2 X-ray diffraction

Ex-situ wide angle XRD diffractograms (**Figure 3.33**) of the 0.1 wt% Cu/meso-TiO_2 series display X-ray patterns with seven well-resolved diffraction peaks indexed (101), (004), (200), (105,211), (204), (116,220), (215) corresponding to anatase.[227] Moreover, samples meso-TiO_2-600 – 800 exhibit rutile crystalline phase. The Cu-impregnated mesoporous TiO_2 XRD results are the same as for the parent support.

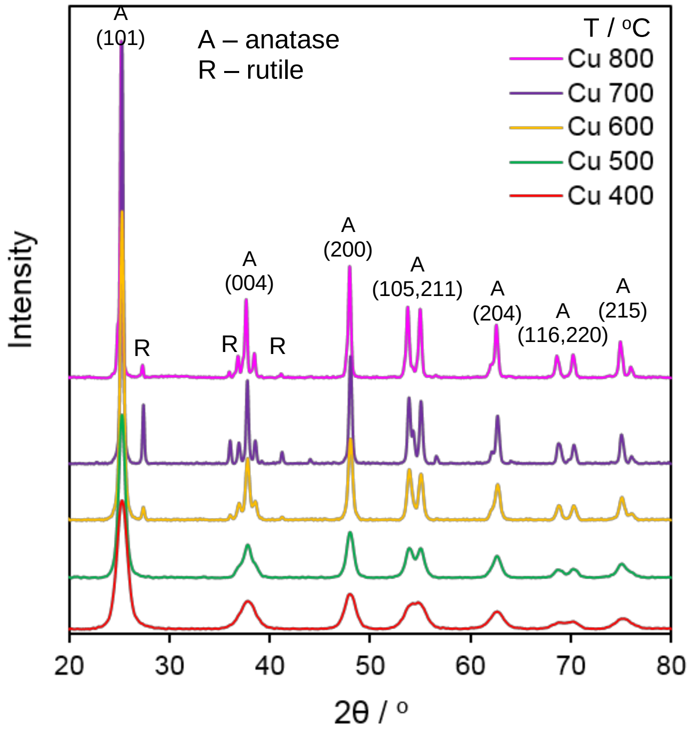

Figure 3.33 Wide angle XRD patterns of 0.1 wt% Cu on meso-TiO_2 400 - 800 supports.

Anatase and rutile nanocrystallite sizes for 0.1 wt% Cu/meso-TiO_2 were estimated using the Scherrer formula (**Table 3.14**) and were found to be in a close agreement with those of the bare support. The trend of crystallite sintering with increasing calcination temperature is observed for both series: before and after Cu deposition. There is no major change in the unit cell parameter either.

Table 3.14 Summary of XRD results of 0.1 wt% Cu on meso-TiO$_2$-400 to 800 supports.

	0.1 wt% Cu promoted meso-TiO$_2$			meso-TiO$_2$ supports		
Sample	Crystalline phase	Crystallite size / nm	Anatase unit cell a (=b) / Å	Crystalline phase	Crystallite size / nm	Anatase unit cell a (=b) / Å
400	Anatase	7 (±0.1)	3.78 (±0.04)	Anatase	7 (±0.1)	3.78 (±0.04)
500	Anatase	11 (±0.1)	3.78 (±0.04)	Anatase	11 (±0.1) 29 (±0.3)	3.78 (±0.04)
600	96% Anatase 4% Rutile	20 (±0.2) 39 (±0.4)	3.78 (±0.04)	96% Anatase 4% Rutile	20 (±0.2) 35 (±0.4)	3.77 (±0.04)
700	85% Anatase 15% Rutile	31 (±0.3) 48 (±0.5)	3.78 (±0.04)	85% Anatase 15% Rutile	31 (±0.3) 46 (±0.5)	3.77 (±0.04)
800	96% Anatase 4% Rutile	35 (±0.4) 53 (±0.5)	3.78 (±0.04)	96% Anatase 4% Rutile	40 (±0.4) 62 (±0.6)	3.78 (±0.04)

LA XRD data (**Figure 3.34)** display a shoulder that resembles a similar peak seen in LA XRD data (**3.1.2 X-ray diffraction**) for the bare meso-TiO$_2$-400 support, however, it appears to be smaller. N$_2$ porosimetry data of Cu-promoted meso-TiO$_2$ series shows retention of the mesopore framework and also no change in crystallinity is observed in WA XRD. The decrease in the peak intensity is more likely an experimental artefact due to the amounts of the sample being very small.

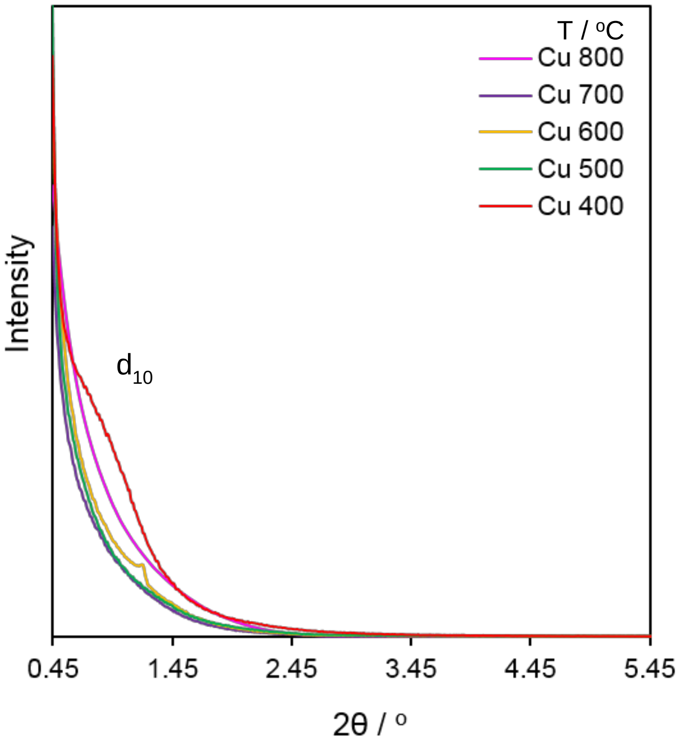

Figure 3.34 Low angle XRD patterns of 0.1 wt% Cu on meso-TiO$_2$-400 to 800 supports.

3.4.3 Inductively coupled plasma optical emission spectrometry

ICP – OES was employed to determine the precise Cu loading present on the meso-TiO_2-400 – 800 supports. The aim of the synthesis is to replicate the 0.11wt% Cu/meso-TiO_2-500 loading, which is the most active Cu loading out of all 0.02 – 12.33 wt% loadings on the single support. The resulting 0.13 wt% loadings on meso-400, 600 – 800 are very close to the intended value of 0.11 wt%. Since the difference is relatively small, all the samples are labelled as 0.1 wt% Cu loading (**Table 3.15**).

Table 3.15 ICP – OES determined Cu loadings on meso-TiO_2-400 to 800 supports.

Theoretical Cu loading / wt%	Experimental ICP - OES Cu loading / wt%
Cu 400	0.13 (±0.004)
Cu 500	0.11 (±0.003)
Cu 600	0.13 (±0.004)
Cu 700	0.13 (±0.004)
Cu 800	0.13 (±0.004)

3.4.4 X-ray absorption spectroscopy

The previous discussion of different Cu loadings on the same mesoporous TiO_2 support (**3.3.4 X-ray absorption spectroscopy)** examined in detail the importance of determining copper oxidation state and chemical environment as either atomically isolated species or smaller than 2 nm nanocrystallites. Cu species has a direct impact on the photocatalyst activity (**3.5 Photocatalytic performance of Cu promoted mesoporous titania series**). However, XRD of 0.1 wt% Cu/meso-TiO_2 series displayed no peaks corresponding to Cu species indicating crystallites smaller than ~2 nm or the amounts being beyond the detection limits. The ultra-low 0.1 wt% Cu loading is invisible in laboratory X-ray sources thus Cu species was probed by Cu K-edge X-ray absorption spectroscopy (XAS -synchrotron beam source). Only 0.1 wt% Cu/meso-TiO_2-500 and 800 out of all Cu/meso-TiO_2-400 – 800 series were analysed by XAS due to time constraint.

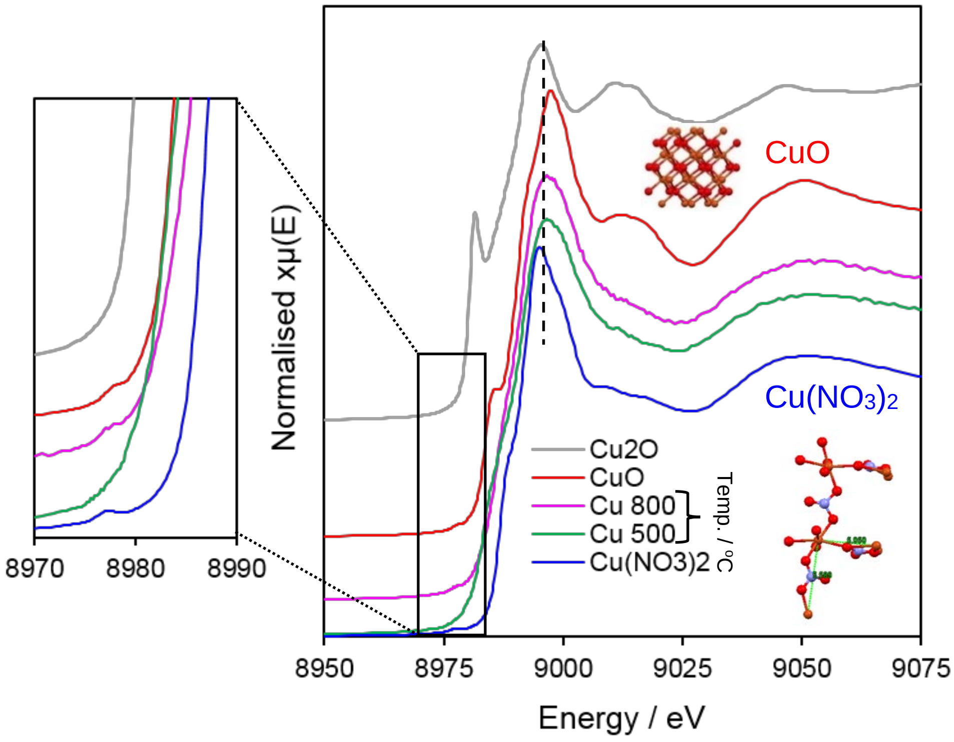

Figure 3.35 XAS spectrum of 0.1 wt% Cu on meso-TiO_2 400 - 800 supports and reference CuO and $Cu(NO_3)_2$.

Background subtracted, normalised XANES spectra of the 0.1 wt% Cu/meso-TiO_2-500 and 800 and Cu_2O, CuO and $Cu(NO_3)_2$ references are shown in **Figure 3.35**. From the previous discussion (**3.3.4 X-ray absorption spectroscopy and 3.4.4 X-ray absorption spectroscopy)** it is apparent that Cu loading and TiO_2 support changes copper oxidation state and its local environment. The copper local environment evolves from that reminiscent of the Cu(II) nitrate trihydrate complex to that of bulk CuO with change in meso-TiO_2 support, with spectra exhibiting three distinct features: a weak pre-edge feature around 8977 eV, a strong rising-edge feature around 8986 eV, and an intense white line around 8996; these are attributed to dipole-forbidden $1s \rightarrow 3d$ (not observed for Cu(I) species),

$1s \rightarrow 4p_z$ (or 4px,ypz for Cu(I) species) and $1s \rightarrow 4p$ (continuum) transitions respectively. Least squares spectral fitting to Cu, Cu_2O, CuO and $Cu(NO_3)_2$ references identified only Cu(II) in both 0.1 wt% Cu/meso-TiO_2 samples (**Figure 3.36**), where 0.1 wt% Cu/meso-TiO_2-500 sample is perfect fit to a mononuclear copper species while 0.1 wt% Cu/meso-TiO_2-800 material contains mixture of 42% mononuclear and 58% of bulk CuO. Nevertheless, **Figure 3.35** demonstrates that the pre-edge feature characteristic of Cu(II) only arise for 0.1 wt% Cu/meso-TiO_2-800. Despite both catalysts possessing the same 0.1 wt% loading, copper atoms in 0.1 wt% Cu/meso-TiO_2-500 electronically resemble Cu(I) oxidation and structurally are similar to mononuclear complexes. While 0.1 wt% Cu/meso-TiO_2-800 is a mixture of this mononuclear Cu (I) species and majority bulk CuO which induces the pre-edge feature.

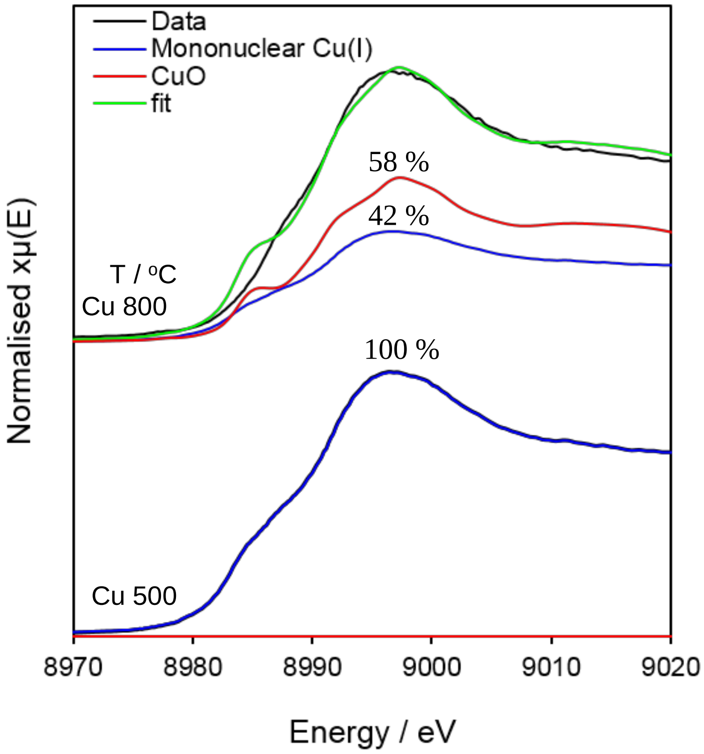

Figure 3.36 Fitting of XANES region of 0.1 wt% Cu on meso-TiO_2-400 to 800 supports.

The variation in Cu species based on the meso-TiO_2 support can be explained by the dramatically different surface area where meso-TiO_2-500 support has a surface area of 126 $m^2\ g^{-1}$ while meso-TiO_2-800 only 8 $m^2\ g^{-1}$. Larger surface area of meso-TiO_2-500 support allows the formation of isolated mononuclear Cu(I) while the lower surface of meso-TiO_2-800 forces Cu aggregate leading to CuO formation.

3.4.5 Diffuse reflectance UV-vis spectrophotometry

The results of solid diffuse reflectance UV-vis optical absorption spectra **Figure 3.37 a** and **Tauc plot b** for 0.1 wt% Cu/meso-TiO_2 demonstrate Cu promotion caused no significant changes in light absorption or band gap (**Table 3.16**). The absorbance shifts to the more visible region and band gaps decrease with increasing calcination temperature as they do in the bare support materials. **Table 3.16** shows a direct comparison of band gaps calculated before and after Cu promotion that are in a good agreement and fits well within a 0.008% error margin.

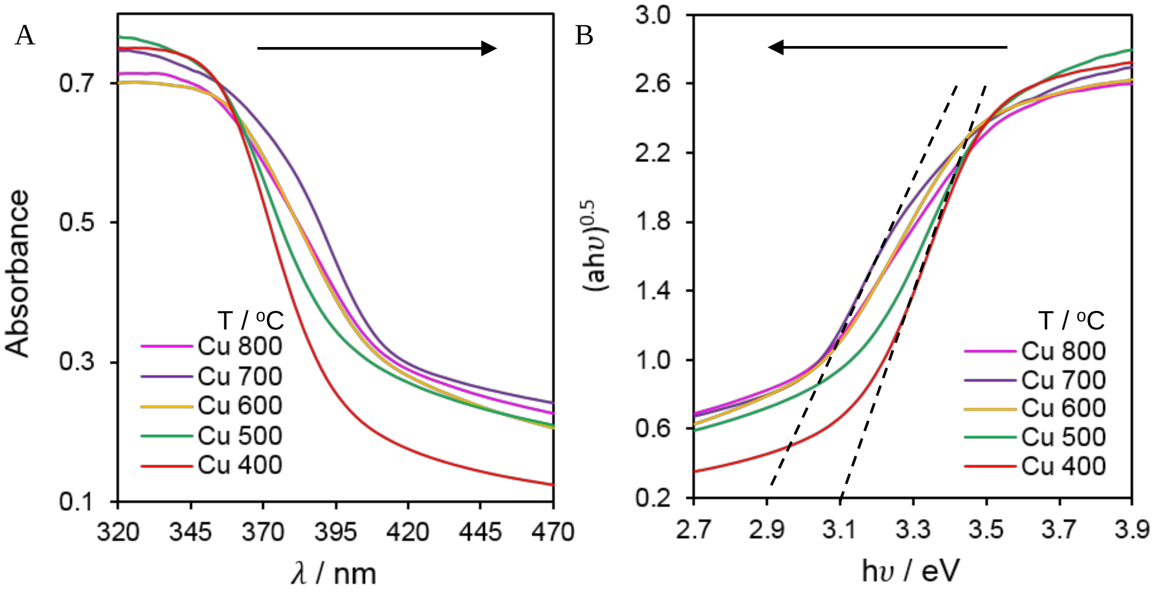

Figure 3.37 (a) UV – vis absorption spectra and (b) Tauc plot of 0.1 wt% Cu on meso-TiO_2-400 to 800 supports.

Table 3.16 Band gap values of 0.1 wt% Cu promoted mesoporous TiO_2 series.

	0.1 wt% Cu promoted meso-TiO_2	meso-TiO_2 supports
Sample	Band Gap / eV	Band Gap / eV
400	3.10 (±0.02)	3.07 (±0.02)
500	3.00 (±0.02)	3.02 (±0.02)
600	2.90 (±0.02)	2.97 (±0.02)
700	2.85 (±0.02)	2.94 (±0.02)
800	2.90 (±0.02)	2.97 (±0.02)

3.4.6 Summary of the key characteristics of 0.1 wt% Cu promoted mesoporous titania 400 - 800 ºC

Table 3.17 Summarises the main physicochemical and electronic properties of the 0.1 wt% Cu promoted meso-TiO$_2$ series with different calcination temperatures from 400 to 800 °C.

Samples	Cu loading / wt%(a)	Mononuclear Cu (I) / %	CuO / %	BET / m^2.g^{-1}(b)	Mesopore size / nm(c)	Mesopore volume / g.cm^{-3}(c)	TiO$_2$ Phase (XRD)	Nanocrystallite size / nm(d)	Band Gap / eV(e)
Cu 400	0.13 (±0.004)	-	-	167 (±17)	5.1 (±0.5)	0.32 (±0.03)	Anatase	7 (±0.1)	3.10 (±0.02)
Cu 500	0.11 (±0.003)	100 (±0.1)	0	91 (±9)	6.5 (±0.7)	0.21 (±0.02)	Anatase	11 (±0.1)	3.00 (±0.02)
Cu 600	0.13 (±0.004)	-	-	54 (±5)	9.7 (±1.0)	0.16 (±0.02)	96% Anatase 4% Rutile	20 (±0.2) 39 (±0.4)	2.90 (±0.02)
Cu 700	0.13 (±0.004)	-	-	24 (±2)	15.8 (±1.6)	0.12 (±0.01)	85% Anatase 15% Rutile	31 (±0.3) 48 (±0.5)	2.85 (±0.02)
Cu 800	0.13 (±0.004)	42.0 (±0.1)	58.0 (±0.1)	11 (±1)	-	-	96% Anatase 4% Rutile	35 (±0.4) 53 (±0.5)	2.90 (±0.02)

[a]ICP – OES; [b]N$_2$ BET; [c]from BJH desorption isotherm; [d] Mean particle diameter from XRD via Scherrer analysis; [e]DRUVS;

3.5 Photocatalytic performance of Cu promoted mesoporous titania series

The photocatalytic activity of 0.02 – 12.33 wt% Cu/meso-TiO_2-500 and 0.1wt% Cu/meso-TiO_2-400 – 800 series characterised above was studied using the photocatalytic decomposition of Methyl Orange and H_2 production via water splitting under the UV-vis light. The initial aim of Cu deposition was to enhance the photocatalyst light absorption in both UV and visible light regions. The dependence of activity on Cu loading and resulting promoter type (mononuclear Cu (I) vs CuO) is identified. Moreover, the impact of copper on the photocatalytic performance meso-TiO_2 supports is examined.

3.5.1 Methyl Orange decomposition

The prime approach of testing the photocatalytic activity of Cu promoted mesoporous titania is the photodegradation of a 20 ppm aqueous solution of Methyl Orange. The **Figure 3.38** shows the reaction profiles of 0.02 – 12.33 wt% Cu on meso-TiO_2-500 support versus time. Prior to illumination, catalysts were stirred in the dark for one hour to achieve adsorption equilibrium. Materials display only ~3% MO adsorption. The illumination of the dye in the absence of the photocatalyst for 2h showed no photolysis (**Figure 3.17**).

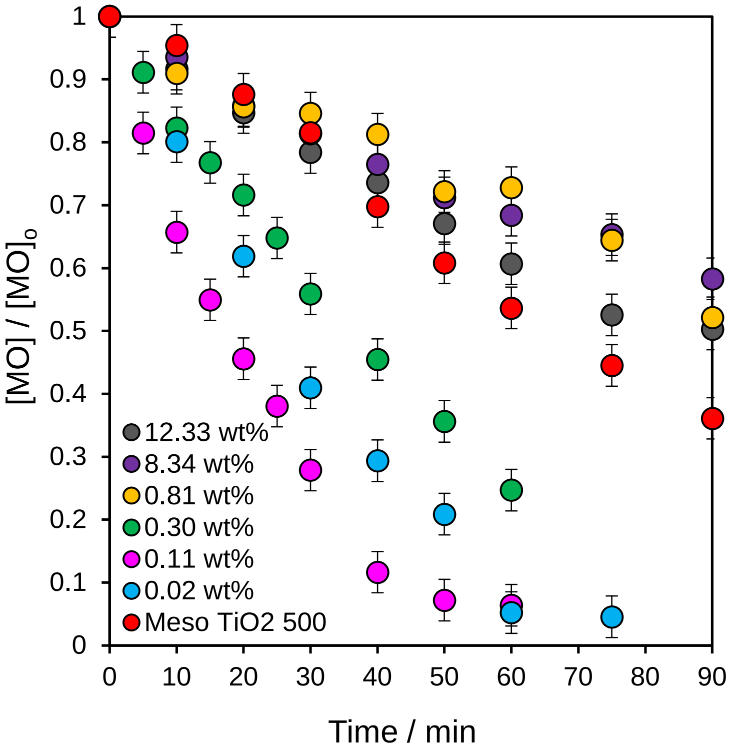

Figure 3.38 Time profiles of the percentage of Methyl Orange degradation of 0.02 – 12.33 wt% Cu on meso-TiO_2-500 support under UV-vis irradiation.

The photocatalytic performance of 0.02 – 12.33 wt% Cu/meso-TiO_2-500 series for photodegradation of Methyl Orange pollutant under UV - Vis irradiation is presented in **Figure 3.39 (a)**. Mass normalised initial reaction rates are inversely proportional to copper loading. The activity of 0.81 – 12.33 wt% loadings are very close to meso-TiO_2-500 support and is significantly enhanced at ultra-low loadings of 0.02 - 0.3 wt% with 0.11 wt% being the most active. To explain this trend, the % of both Cu species obtained from XAS data (**Figure 3.27**) are plotted together with the initial rates. A fivefold increase in activity at ultra-low Cu loadings directly correlates with the concentration of mononuclear Cu (I) species. While domination of bulk CuO species at high 0.81 – 12.33 wt% Cu loadings has very little effect on meso-TiO_2-500 activity. Both 0.02 wt% and 0.11 wt% Cu samples contain 100% mononuclear Cu(I), however, the activity slightly drops for 0.02 wt% sample due to the very low loading. To conclude, the formation of mononuclear Cu(I) species accounts for the significant improvement of meso-TiO_2-500 activity at 0.02 – 0.30 wt% loadings. The critical dependence of activity on promoter species, with optimal efficiency occurring at ultra-low loadings, is identified.

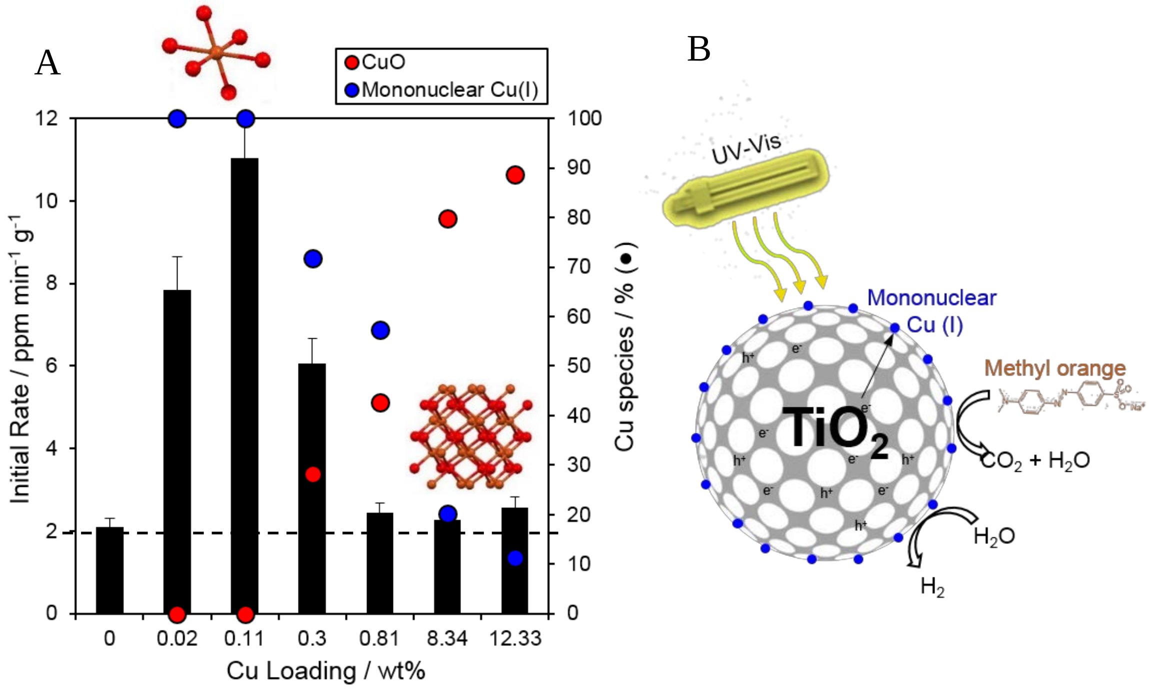

Figure 3.39 (a) Initial rate vs Cu loading wt% and corresponding % of Mononuclear Cu(I) and CuO under UV-vis light (b) Schematic representation of mononuclear Cu(I) mode of activity.

Table 3.18 Time-resolved photoluminescence results of bare meso-TiO_2-500 and 0.02 wt% promoted support and CuO standard. Titania based materials were excited with 380 nm wavelength while CuO - 470 nm.

Sample	t_1 / ns	B_1	χ^2
500	1.4 (±0.01)	2435 (±15)	1.4 (±0.01)
0.02 wt% 500	5.6 (±0.02)	2328 (±7)	5.6 (±0.02)
CuO	3.5 (±0.02)	1019 (±6)	3.5 (±0.02)

Most importantly, Cu promoted materials were additionally tested in the solely visible light irradiation (>400 nm, 8 mW cm^{-2}) but the only active catalyst was 12.33 wt% Cu/meso-TiO$_2$-500 with an initial rate of 0.244 ppm.min^{-1}.g^{-1}. This confirms that Cu(I) species did not significantly modify the band gap of the titania support and the lack of activity under visible light irradiation of 0.02 – 0.3 wt% Cu catalysts supports the results of band gap energy absorptions in the UV region (**3.3.5 Diffuse reflectance UV-vis spectrophotometry**). The observed poor initial rate of 12.33 wt% sample arose solely from the visible absorbing CuO phase. Samples 0.81 – 12.33 wt% Cu all display a shift of the band gap to visible light absorption by CuO species and should be active under the visible light however the activity is negligible from CuO despite its impact on optical properties. CuO displays poor performance as a promoter, probably due to its smaller valence band maximum relative to the meso-TiO$_2$-500 anatase parent (~2.66 versus 2.95 eV)[253] which offers a lower thermodynamic driving force for catalytic oxidation. In addition, the large size of CuO nanoparticles (34 nm for 12.33 wt% Cu) and corresponding insufficient interfacial contact leads to inefficient heterojunction formation with titania. Moreover, the operating conditions of the much lower visible irradiation energy of 8 mW cm^{-2} vs 26 mW cm^{-2} of UV-vis cause decrease in the activity. The results discussed above demonstrate that the goal of enabling TiO$_2$ to absorb visible light through the addition of Cu was achieved. However, the activity is very low compared to when irradiating with UV light.

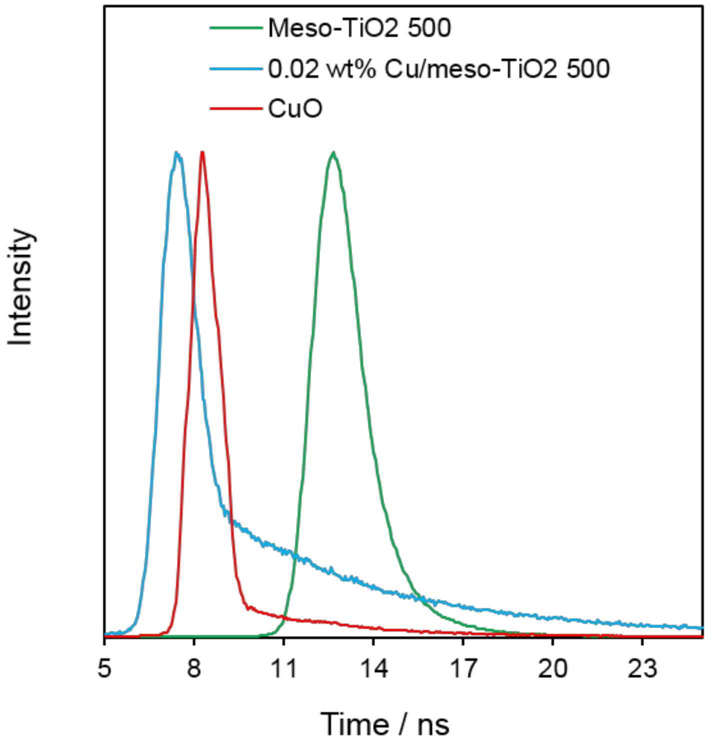

Figure 3.40 Time-resolved photoluminescence spectra of the meso-TiO$_2$-500 support, 0.02 wt% Cu/meso-TiO$_2$-500 and CuO reference samples.

An enhanced photoactivity at ultra-low loadings is observed: mononuclear Cu(I) promotes Ti performance under UV light. The isolated nature of the mononuclear Cu (I) and promotion of activity only in UV light suggest that mononuclear Cu (I) works as a charge carrier trap (not as a light absorbing species) at the catalyst surface (**Figure 3.39 (b)**). Since copper was introduced by post-modification of mesoporous titania, employing a comparatively low-temperature processing step, the surface deposition is more feasible. The constant band gap, and anatase lattice parameter and crystal size, following the addition of ultra-low Cu concentrations to the parent meso-TiO_2, supports the hypothesis that single copper atoms are dispersed over titania. Time-resolved photoluminescence data of the 0.02 wt% Cu/meso-TiO_2 (**Table 3.18, Figure 3.40**) in this case has only one type of excitation, t_1 at 380 nm. The 0.02 wt% Cu/meso-TiO_2, promoted by mononuclear Cu(I) species, highlight a significant increase in the average charge carrier relaxation time t_1 relative to the bare meso-TiO_2-500 support. The novel synthesised material exhibited charge carrier lifetimes twice as long as that for the CuO standard but it is important to note that the excitation wavelength for CuO is in the visible light region (480 nm). The proposed mode of action is that the titania support generates electron and hole charge carriers and when they reach the surface of the catalyst, they get trapped. The latter phenomenon is ascribed to the creation of oxygen vacancies upon introducing Cu(I) species into the titania framework; these oxygen vacancies likely capture photoexcited electrons to form F-centres,[254] thereby suppressing charge carrier recombination, prolonging lifetime promoting either direct hole oxidation or indirect hydroxyl oxidation mechanisms (**1.5.1 Methyl Orange decomposition Equation 1.2 A or B-D**).[83] The initial intent of Cu deposition was to improve photocatalysts absorption of visible light, which still needs further optimisation, but a new aspect of atomically-dispersed Cu as a great promoter species has been demonstrated.

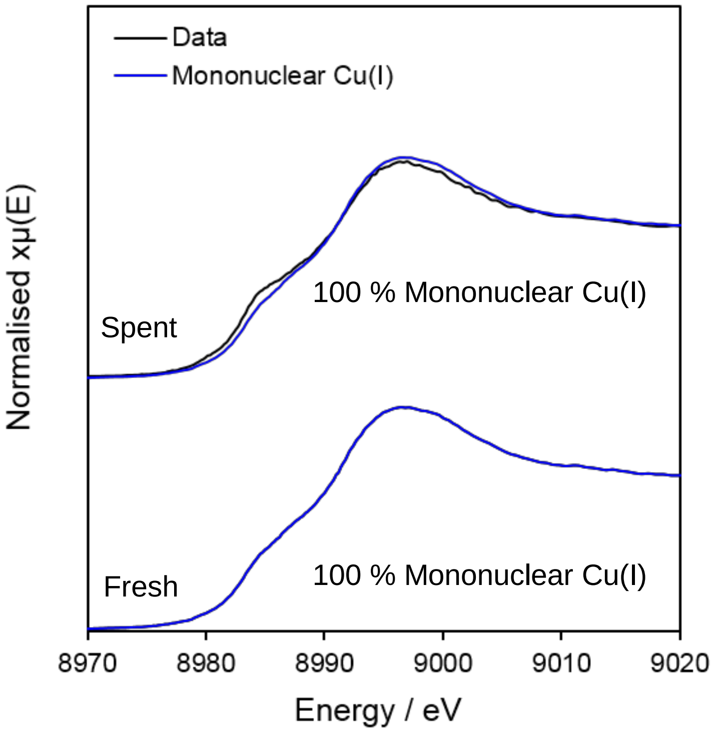

Figure 3.41 Fitting of XANES region of 0.11 wt% Cu/meso-TiO_2-500 fresh and spent catalyst.

Comparison of fitted XANES spectra (**Figure 3.41**) fresh and spent 0.11 wt% meso-TiO_2-500 catalyst, which was the most active catalysts in the previous studies (**Figure 3.39**), shows that mononuclear Cu(I) species remains unchanged. After the reaction, the catalyst is recovered by centrifuging the reaction mixture and separating the solid from the liquid. The separated catalyst is washed 3 times with deionised water and dried at room temperature. The 0.02 wt% Cu/meso-TiO_2 catalyst also exhibited excellent stability, with negligible loss in photodegradation activity over three consecutive recycles (**Figure 3.42**), consistent with preservation of Cu(I) isolated sites observed for ultra-low loading from the XANES analysis.

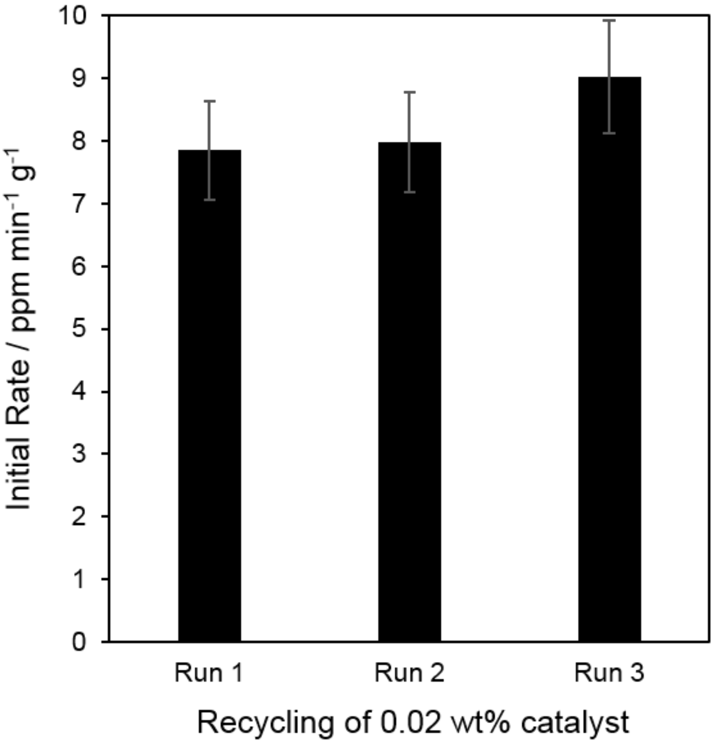

Figure 3.42 Results of three cycles of recovery tests of 0.02 wt% Cu meso-TiO_2-500 under UV-vis irradiation.

The effect of the calcination temperature of the meso-TiO_2-400 – 800 on the photocatalytic activity of 0.1 wt% Cu loading and resulting mononuclear Cu(I) species were investigated (**Figure 3.43**). For the more accurate comparison mass normalised initial rates are calculated and presented in **Figure 3.44** together with those achieved with the unpromoted mesoporous TiO_2 series. Initial rates for 0.1 wt% Cu mesoporous TiO_2 are 3 to 4 times faster than pure supports and display a volcano curve with the 0.1 wt% Cu/meso-TiO_2-500 being the most active and 0.1 wt% Cu/meso-TiO_2-800 being the least active. The volcano trend for the promoted materials is different from the unpromoted mesoporous TiO_2 series which demonstrates an increase in activity with calcination temperature. The % of Cu species obtained from XAS data (**3.4.4 X-ray absorption spectroscopy**) is displayed together with initial rate to interpret the superior activity. All meso-TiO_2-400 – 800 retained 0.1 wt% loading but, depending on the support, either mononuclear Cu(I) promoter species or inactive CuO is formed. The optimum meso-TiO_2-500 support promotes 100% mononuclear Cu(I) species formation producing the best photocatalytic activity. On the other hand, the least active meso-TiO_2-800 favours 58% CuO and only 42% of the mononuclear Cu(I). The formation of the active mononuclear Cu(I) component depends not only on the loading of Cu but also on the nature of the mesopore TiO_2 support used. Meso-TiO_2 supports have different surface areas, mesopore framework and crystallinity. The development of isolated mononuclear Cu(I) is promoted by supports combining sufficient surface area and mesopore diameter, which allows good diffusion of $Cu(NO_3)_2.3H_2O$ precursor and dispersion to form isolated mononuclear Cu(I) species.

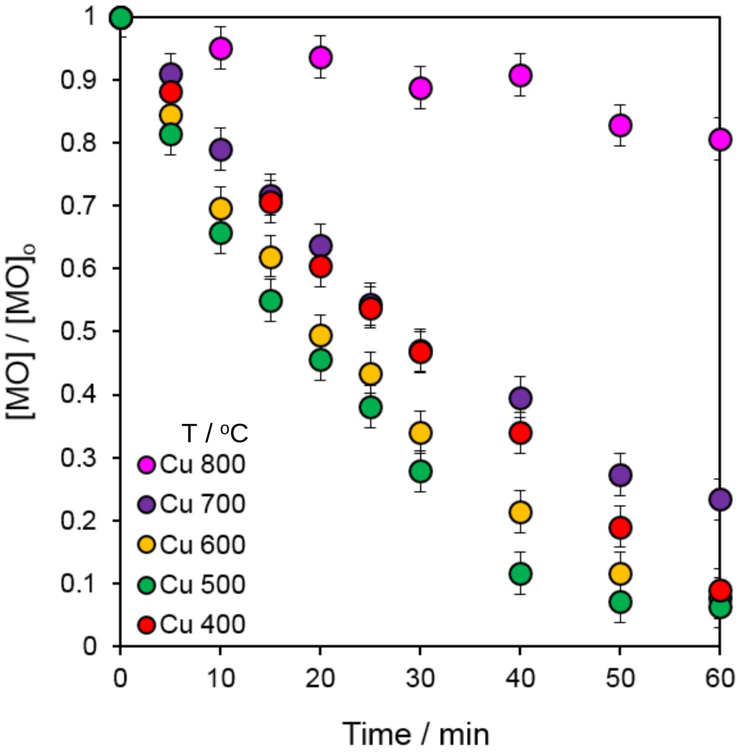

Figure 3.43 Time profiles of the percentage of methyl orange degradation of 0.1 wt% Cu on meso-TiO_2 400 - 800 supports under UV-vis light.

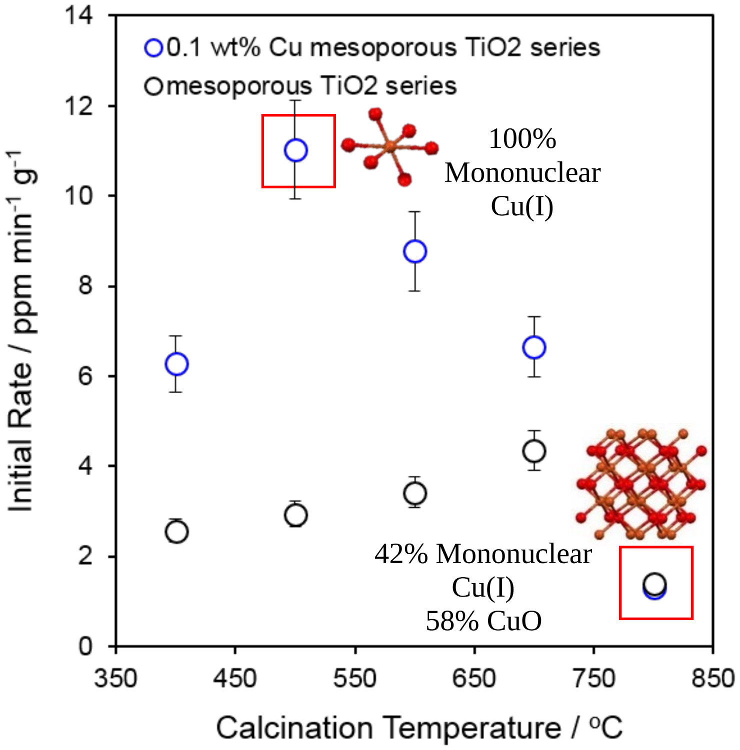

Figure 3.44 Initial rate of 0.1 wt% Cu on different meso-TiO_2 supports calcined at 400 – 800 °C and corresponding % of mononuclear Cu (I) and CuO under UV-vis irradiation. The graph includes unpromoted meso-TiO_2 series activity.

3.5.2 Water splitting

Figure 3.45 illustrates H_2 production rates achieved by the 0.02 – 12.33 wt% Cu promoted meso-TiO_2-500 series for water splitting under UV - Vis irradiation. To explain this trend, the % of both Cu species obtained from XAS data (**Figure 3.26**) are plotted together with the mass normalised initial rates. In the Methyl Orange degradation reaction (**3.5.1 Methyl Orange decomposition**) the activity is significantly enhanced by the formation of 100% mononuclear Cu(I) species at ultra low 0.02 - 0.3 wt% loadings. In contrast to MO degradation, photocatalytic H_2 production over Cu/meso-TiO_2-500 exhibited a volcano dependence on copper loading, reaching a maximum for 0.81 wt% Cu, a material comprising ~60 % mononuclear Cu(I) species and 40 % CuO. The lack of promotion at low Cu loadings, wherein only Cu(I) species exist, is understandable in terms of the preceding hypothesis that Cu(I) doping introduces F-centres into the meso-TiO_2 framework (which trap photoexcited electrons required for H_2 production). Similarly, the baseline activity of the 12.33 wt% Cu/meso-TiO_2-500 which is dominated by crystalline CuO is also explicable, since the CBM of CuO lies ~0.96 eV below that necessary to reduce protons,[253] and therefore cannot contribute directly to H_2 production as a semiconductor photocatalyst. The origin of the synergy between Cu(I) and CuO responsible for the 3-4-fold rate-enhancement observed for the 0.81 wt% Cu/meso-TiO_2-500 remains unclear, but highlights the impact of subtle variations in the composition of doped titania on corresponding photophysical/catalytic properties.

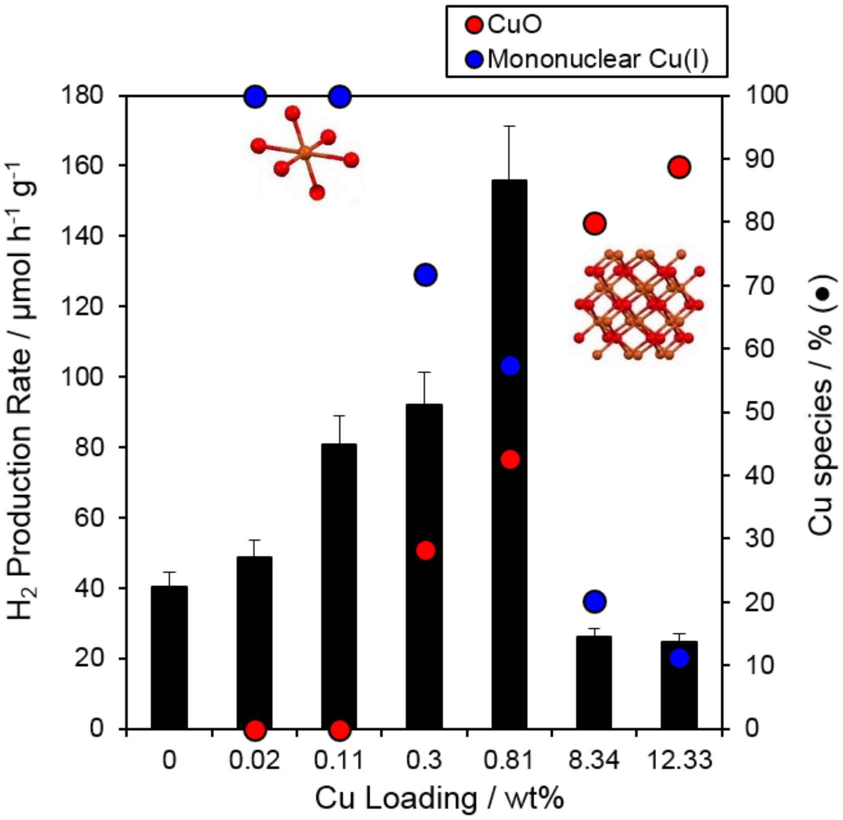

Figure 3.45 H_2 production rate vs Cu loading wt% and corresponding % of Mononuclear Cu(I) and CuO of 0.02 – 12.33 wt% Cu on meso-TiO_2-500 support under UV-vis light.

Figure 3.46 shows the H_2 production rate for singular 0.1 wt% loading deposited on different mesoporous TiO_2 supports calcined at 400 – 800 °C. The volcano trend with the most active 0.1 wt% Cu meso TiO_2-500 coincides with the trend in the MO degradation tests (**Figure 3.44**). In the case of the data shown in **Figure 3.46**, the wt% of Cu remains the same and the only change in Cu species is observed. Catalysts that possess higher amounts of mononuclear Cu(I) are more active than those containing CuO. In the water splitting reaction, as in the Methyl Orange degradation, a volcano curve (**Figure 3.46**) with the most active 0.1 wt% Cu meso-TiO_2-500 being that with the highest mononuclear Cu(I) content. All meso-TiO_2-400 – 800 retained 0.1 wt% loading but, depending on the support, either mononuclear Cu(I) promoter species or inactive CuO is formed. The optimum meso-TiO_2-500 support promotes 100% mononuclear Cu(I) species formation producing the best photocatalytic activity. On the other hand, the least active meso-TiO_2-800 favours 58% CuO and only 42% of the mononuclear Cu(I).

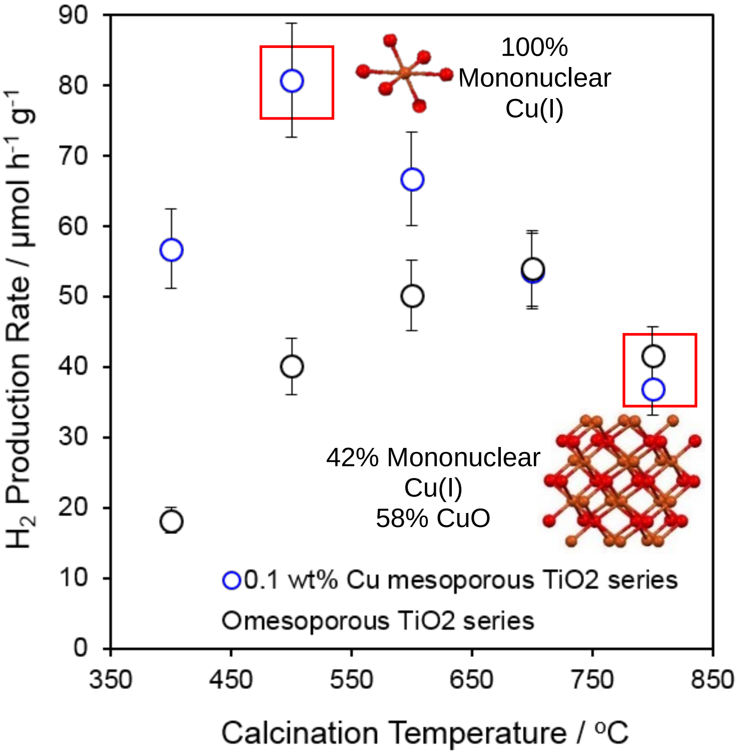

Figure 3.46 H_2 production rate of 0.1 wt% Cu on different meso-TiO_2 supports calcined at 400 – 800 °C and corresponding % of mononuclear Cu (I) and CuO under UV-vis irradiation. The graph includes unpromoted mesoporous TiO_2 series activity.

3.6 Characterisation of Pt promoted mesoporous titania series

The meso-TiO_2-300 – 900 series, discussed in **3.1 Characterisation of mesoporous titania series,** was promoted with Pt via a straightforward wet impregnation method using chloroplatinic acid ($H_2PtCl_6.6H_2O$). A single 1 wt% Pt loading was chosen for all the materials as one of the most commonly used active platinum loadings.[94, 255] The retention of structural properties of the mesoporous TiO_2 support and the impact of Pt on the improvement of the photocatalytic activity was investigated via a range of techniques. Furthermore, the nature of the active Pt promoter species and the effect of the different supports have been identified.

3.6.1 Nitrogen porosimetry

N_2 porosimetry was employed to evaluate if the structural properties of the mesoporous framework are affected by Pt deposition. N_2 adsorption/desorption curves (**Figure 3.47**) of Pt/meso-TiO_2-300 to 700 display Type IV isotherms with H2 type hysteresis loops indicating mesoporosity. Samples Pt/meso-TiO_2-800 - 900 exhibit a Type II isotherm with no capillary condensation suggesting a loss of porosity. The trend of decreasing mesoporosity with increasing calcination temperature exhibited by meso-TiO_2 supports is preserved.

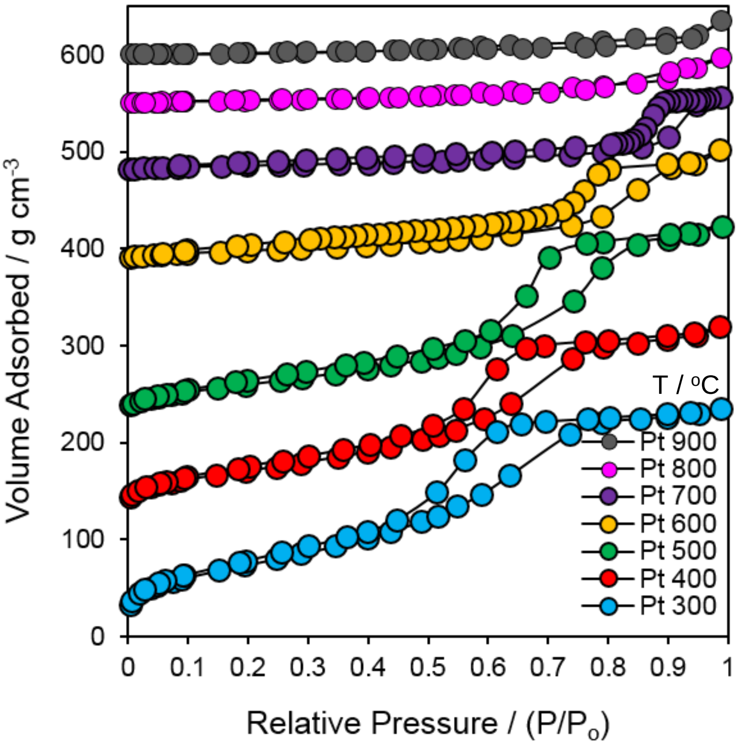

Figure 3.47 Stacked isotherm plot of Pt promoted meso-TiO_2-300 – 900 supports.

The specific surface areas (BET) of Pt-promoted meso-TiO_2 series (**Table 3.19**) underwent no significant change, with only a small increase in BET observed with regards to parent meso-TiO_2. The only notable reduction in surface area of Pt/meso-TiO_2-300 sample. The mesopore volume (**Table 3.19**) and mesopore diameter (**Figure 3.48, Table 3.19**) remain unchanged.

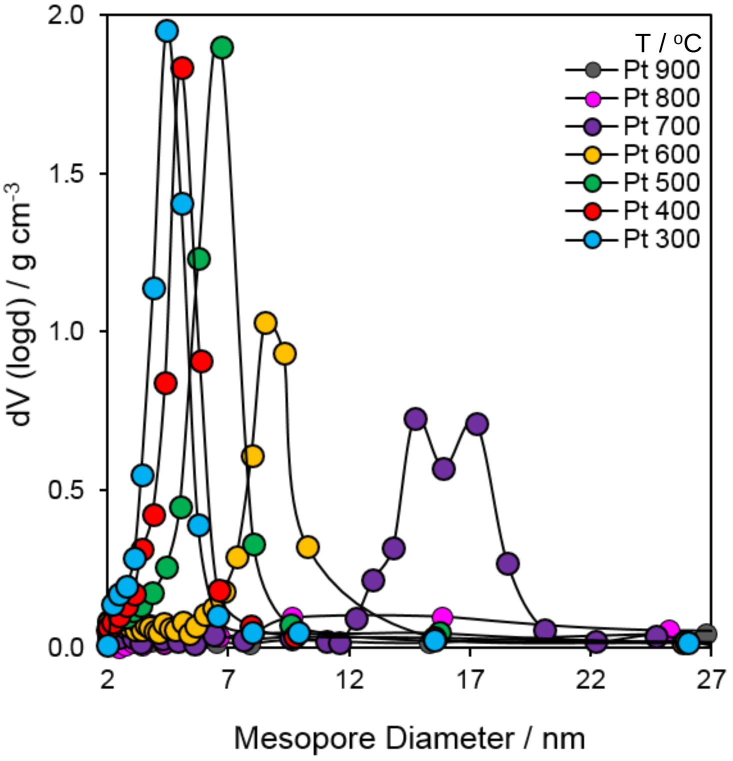

Figure 3.48 Mesopore size distribution of Pt promoted meso-TiO_2-300 - 900 supports.

Table 3.19 Summary of N_2 porosimetry results of Pt promoted meso-TiO_2-300 - 900 supports and comparison to bare meso-TiO_2 supports.

	Pt promoted meso-TiO_2			meso-TiO_2 support		
Sample	BET / $m^2 g^{-1}$	Mesopore size / nm	Mesopore volume / $g\ cm^{-3}$	BET / $m^2 g^{-1}$	Mesopore size / nm	Mesopore volume / $g\ cm^{-3}$
300	273 (±27)	4.5 (±0.5)	0.39 (±0.04)	313 (±31)	4.6 (±0.5)	0.41 (±0.04)
400	188 (±19)	5.0 (±0.5)	0.33 (±0.03)	194 (±19)	5.4 (±0.5)	0.34 (±0.03)
500	150 (±15)	6.7 (±0.7)	0.34 (±0.03)	126 (±13)	6.5 (±0.7)	0.28 (±0.03)
600	82 (±8)	8.5 (±0.9)	0.20 (±0.02)	51 (±5)	9.7 (±1.0)	0.15 (±0.02)
700	23 (±2)	16.0 (± 1.6)	0.13 (±0.01)	19 (±2)	16.0 (±1.6)	0.11 (±0.01)
800	16 (±2)	-	-	8 (±1)	-	-
900	13 (±1)	-	-	4 (±0.4)	-	-

3.6.2 X-ray diffraction

Ex-situ wide angle XRD diffractograms (**Figure 3.49**) of the Pt/meso-TiO_2 series display seven well-resolved diffraction peaks (indexed (101), (004), (200), (105,211), (204), (116,220), (215)) corresponding to a crystalline anatase phase.[227] In addition, samples Pt/meso-TiO_2-500 – 900 exhibit peaks assigned to rutile crystalline phase. Anatase and rutile nanocrystallites sizes and unit cell parameters are analogous to the meso TiO_2 supports and are summarised in **Table 3.20**. Promotion with Pt does not affect the crystallinity of the meso-TiO_2 supports. No Pt peaks are detected in WA XRD patterns nanocrystallites in the remaining samples is smaller than 2 nm or the amounts are beyond the XRD detection limits.

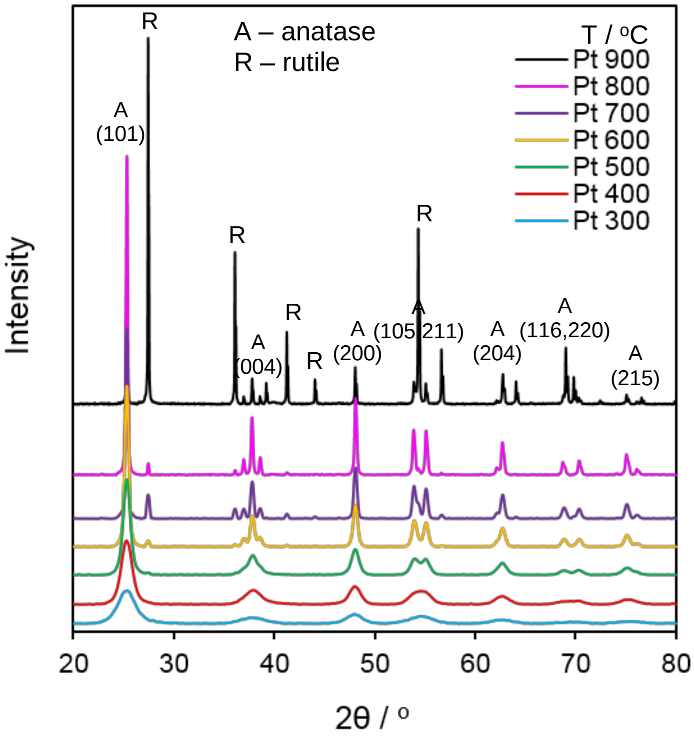

Figure 3.49 Wide angle XRD patterns of Pt promoted meso-TiO_2-300 - 900 supports.

LA XRD data of Pt/meso-TiO_2-300 and 400 exhibit a shoulder in the low angle X-ray diffraction patterns (**Figure 3.50**), that resembles a similar peak seen in LA XRD data (**3.1.2 X-ray diffraction**) for the bare meso-TiO_2-300 and 400 supports. This indicates short range regular spacing between the mesopores with the overall mesostructure being worm-hole like as were the rest of the meso-TiO_2-500 – 900 materials (**3.1.2 X-ray diffraction**). However, low angle peaks of the Pt/meso-TiO_2-300 - 400 supports appear to be significantly less intense. N_2 porosimetry data of Pt-promoted meso-TiO_2 series shows retention of the mesopore framework and also no change in crystallinity is observed in WA XRD. The decrease in the peak intensity is more likely an experimental artefact due to the amounts of the sample being very small.

Table 3.20 Summary of XRD results of Pt promoted meso-TiO_2-300 - 900 supports.

	Pt promoted meso-TiO_2			meso-TiO_2 supports		
Sample	Crystalline phase	Crystallite size / nm	Anatase unit cell a (=b) / Å	Crystalline phase	Crystallite size / nm	Anatase unit cell a (=b) / Å
300	Anatase	5 (±0.1)	3.79 (±0.04)	Anatase	5 (±0.1)	3.78 (±0.04)
400	Anatase	7 (±0.1)	3.79 (±0.04)	Anatase	7 (±0.1)	3.78 (±0.04)
500	97% Anatase	11 (±0.1)	3.78 (±0.04)	97% Anatase	11 (±0.1)	3.78 (±0.04)
	3% Rutile	31 (±0.3)		3% Rutile	29 (±0.3)	
600	95% Anatase	20 (±0.2)	3.78 (±0.04)	96% Anatase	20 (±0.2)	3.77 (±0.04)
	5% Rutile	33 (±0.3)		4% Rutile	35 (±0.4)	
700	84% Anatase	31 (±0.3)	3.78 (±0.04)	85% Anatase	31 (±0.3)	3.77 (±0.04)
	16% Rutile	45 (±0.5)		15 % Rutile	46 (±0.5)	
800	95% Anatase	41 (±0.4)	3.78 (±0.04)	96% Anatase	40 (±0.4)	3.78 (±0.04)
	5% Rutile	62 (±0.6)		4% Rutile	62 (±0.6)	
900	27% Anatase	73 (±0.7)	3.78 (±0.04)	25% Anatase	64 (±0.6)	3.78 (±0.04)
	73% Rutile	91 (±0.9)		75% Rutile	109 (±1.1)	

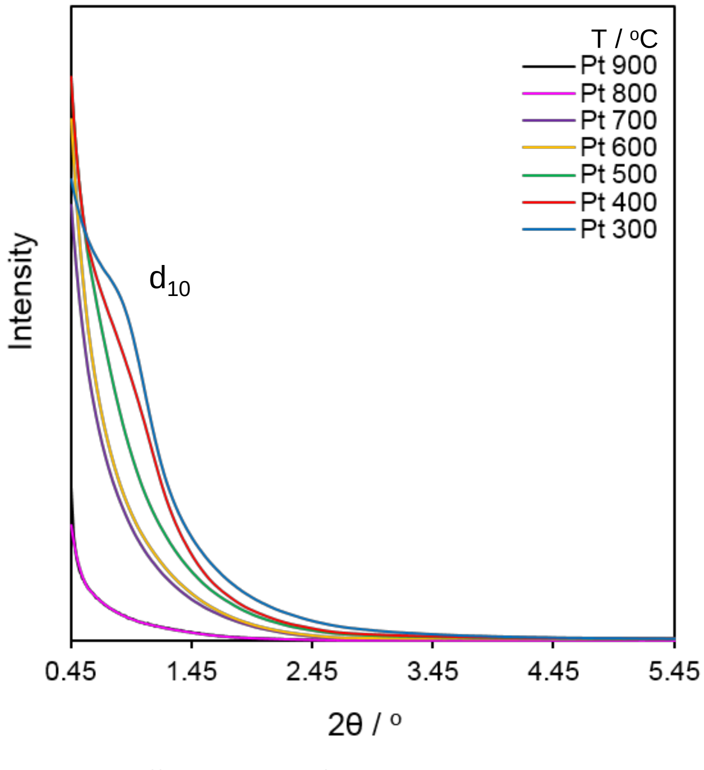

Figure 3.50 Low angle diffractograms of Pt promoted meso-TiO_2-300 - 900 supports.

3.6.3 High-resolution scanning transmission electron microscopy

HRSTEM images of Pt meso-TiO_2 were used to establish the Pt nanocrystallite sizes of the Pt promoted meso-TiO_2 series which are undetectable in WA XRD measurements. In **Figure 3.51** image **A** displays a representative example of Pt distribution on the mesoporous TiO_2 support of Pt/meso-TiO_2-500 sample. Image B and C shows ~1.65 nm Pt particles both in the pores and on the catalyst surface. Image C also features lattice fringes d_{101} ~3.5 Å which correspond to the most predominant (101) anatase facet d=3.5 Å (**3.6.2 X-ray diffraction**). The same information is provided in **Figure 3.52** and **Figure 3.53** for samples Pt/meso-TiO_2-700 and Pt/meso-TiO_2-900 respectively. The average Pt particle size of Pt/meso-TiO_2-700 is 2.95 nm and 4.8 nm for meso-TiO_2-900. Mesoporous TiO_2 supports calcined at higher temperatures dictate larger Pt crystallite formation most likely due to significantly lower surface areas. In the Pt/meso-TiO_2-900 sample, particles are higher than 2 nm threshold of the XRD instrument, however, at low 1 wt% loading, excellent dispersion of Pt on TiO_2 [256] and intense peaks of the very large anatase and rutile crystallites (73, 91 nm respectively) cause the absence of Pt peaks in the wide angle XRD diffractograms (**3.6.2 X-ray diffraction**).

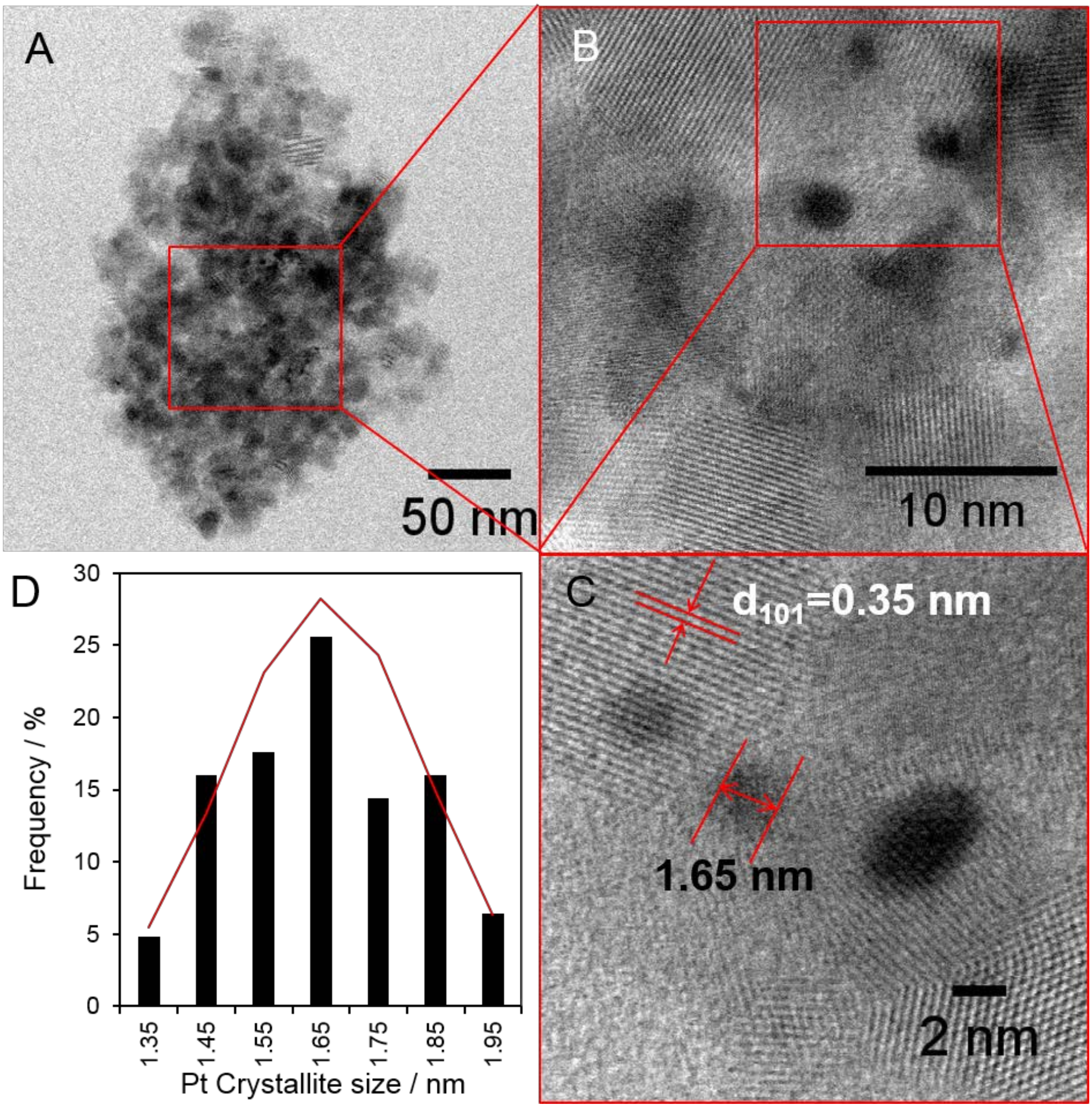

Figure 3.51 HRSTEM images and Pt particle size distribution of Pt/meso-TiO_2-500.

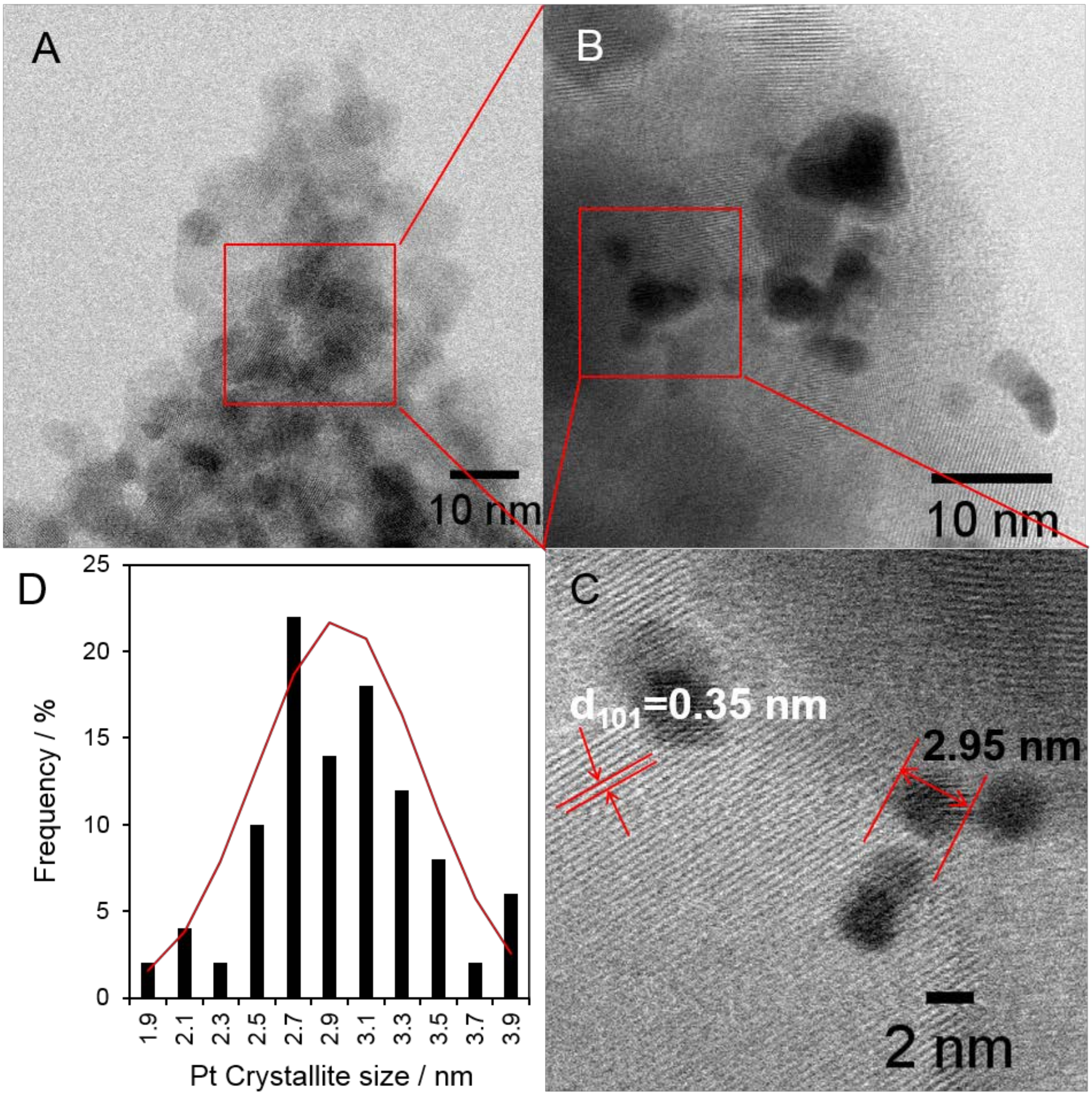

Figure 3.52 HRSTEM images and Pt particle size distribution of Pt/meso-TiO$_2$-700.

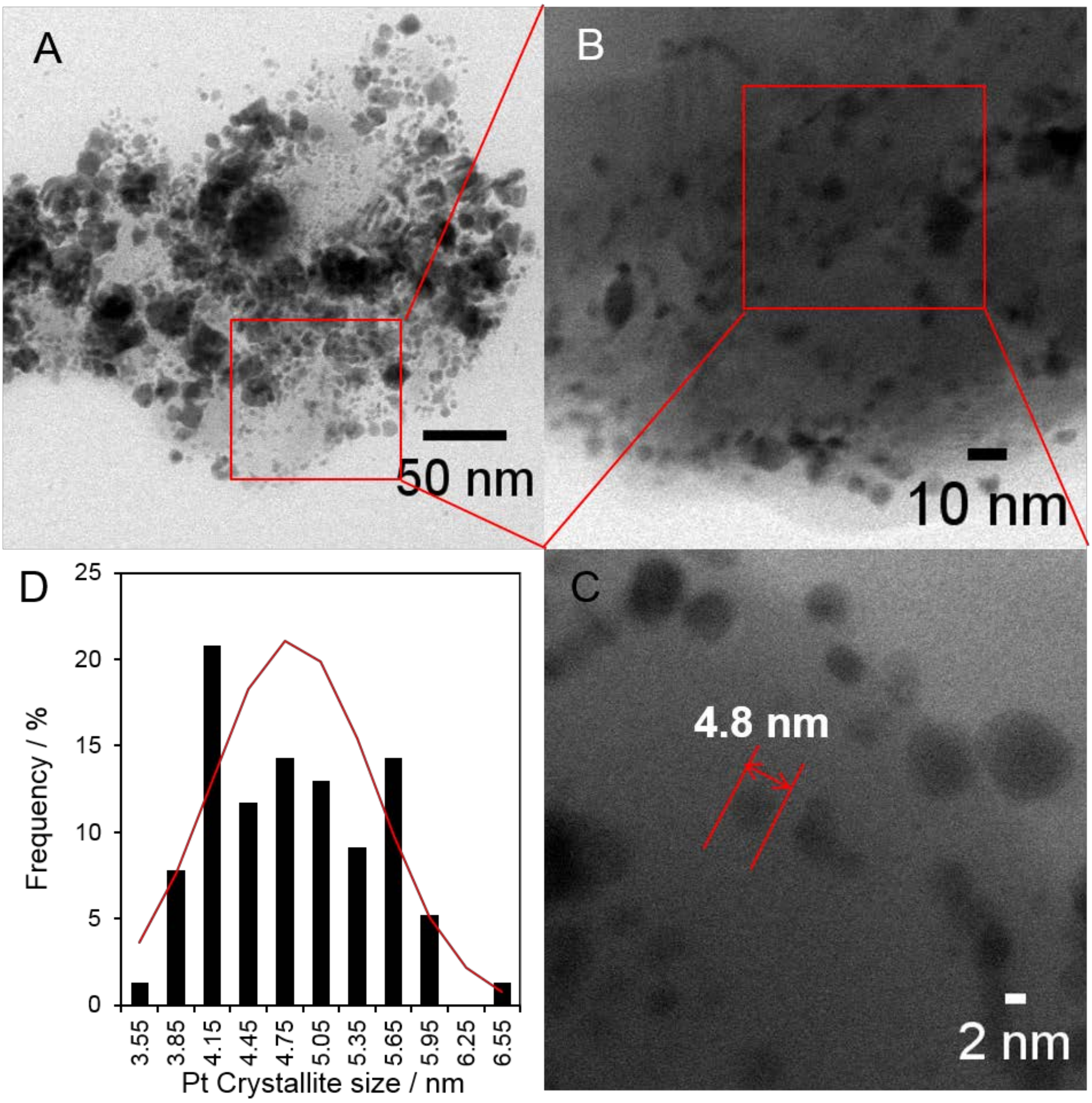

Figure 3.53 HRSTEM images and Pt particle size distribution of Pt/meso-TiO$_2$-900.

3.6.4 Inductively coupled plasma optical emission spectrometry

ICP – OES was employed to ratify the deposition of Pt (which is not visible on WA XRD data **Figure 3.49**) on mesoporous TiO_2 300 – 900 °C supports (**Table 3.21**). A value of 1.8 wt.% loading was measured for all the catalysts. It is higher than the theoretical value of 1 wt%, which was intended, due to an error in purity of the chloroplatinic acid hexahydrate reagent.

Table 3.21 Pt loadings on meso-TiO_2-300 – 900 supports.

Sample	Pt loading / wt%
Pt 300	1.84 (±0.06)
Pt 400	1.83 (±0.05)
Pt 500	1.85 (±0.06)
Pt 600	1.84 (±0.06)
Pt 700	1.80 (±0.05)
Pt 800	1.82 (±0.05)
Pt 900	1.80 (±0.05)

3.6.5 X-ray photoelectron spectroscopy

The Ti 2p regions of the XPS spectra of the Pt/meso-TiO_2 series are shown in **Figure 3.54.** The binding energies for Ti 2p core levels found at 458 and 464 eV correspond to Ti $2p_{3/2}$ and Ti $2p_{1/2}$ levels respectively.[189] The Ti $2p_{3/2}$ and Ti $2p_{1/2}$ peaks are symmetric, which indicates a uniform chemical environment in all samples. The Ti region results mirror those of the support materials (**3.1.2 X-ray diffraction**). All samples displayed 2:1 oxygen to titanium surface atomic ratio, as expected for TiO_2 structure.

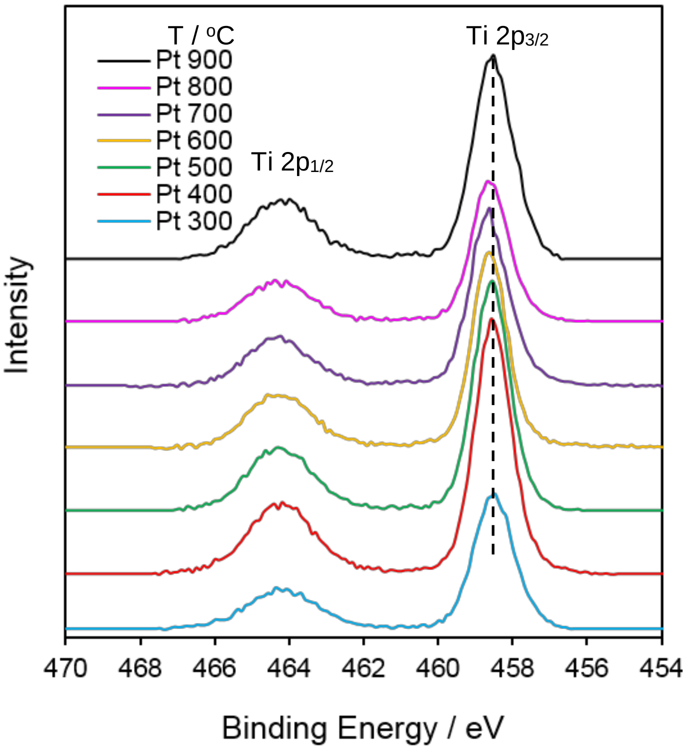

Figure 3.54 XPS spectra of Ti 2p region of Pt promoted meso-TiO_2-300 - 900 supports.

The Pt region of the Pt/meso-TiO_2 series (**Figure 3.55**) reveals three different Pt species. The binding energies of Pt 4f found at 71.0, 72.4 and 74.9 eV corresponds to Pt metal, Pt(II) and Pt(IV).[189] The surface atomic % (At%) and weight % (wt%) of each Pt species and Pt:Ti surface ratio are summarised in **Table 3.22**. The amounts of Pt species and Pt:Ti varies greatly depending on the mesoporous TiO_2 support. Increasing calcination of meso-TiO_2 series leads to higher Pt:Ti surface ratio. Since Pt loading on these materials remains constant the increase in Pt:Ti surface ratio is attributed to decrease in surface area of the TiO_2 supports (**3.6.1 Nitrogen porosimetry**) and sintering of titania crystallites (**3.6.2 X-ray diffraction**). Formation of Pt(II) is a stepping stone for Pt(IV) – photocatalysts that have higher % of Pt(II) contains more Pt(IV) as well. The development of oxidised species is promoted by smaller 1.65 nm particles while 4.8 nm particles lead to 56% Pt metal formation. The formation of Pt(0) species increases with increasing crystallite size (**Figure 3.56**).

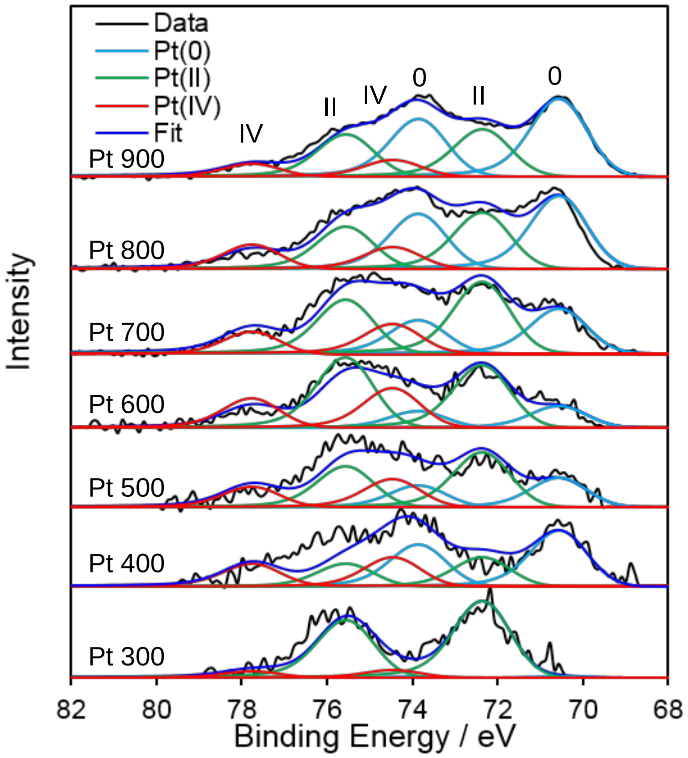

Figure 3.55 XPS spectra of Pt/meso-TiO_2 series Pt 4f region.

Table 3.22 Summary of % Pt species of Pt/meso-TiO_2-300 - 900 series.

Sample	Pt surface / At%	Pt surface / Wt%	Pt(0) / %	Pt(II)/ %	Pt(IV)/ %	Pt:Ti
Pt 300	0.20 (±0.01)	1.85 (±0.09)	2 (±0.1)	89 (±4)	9 (±0.5)	0.010
Pt 400	0.20 (±0.01)	1.61 (±0.08)	49 (±2)	26 (±1)	25 (±1)	0.008
Pt 500	0.20 (±0.01)	1.66 (±0.08)	26 (±1)	50 (±3)	24 (±1)	0.008
Pt 600	0.36 (±0.02)	2.91 (±0.16)	20 (±1)	56 (±3)	24 (±1)	0.014
Pt 700	0.64 (±0.03)	5.35 (±0.27)	31 (±2)	49 (±2)	20 (±1)	0.029
Pt 800	1.18 (±0.06)	9.44 (±0.48)	48 (±2)	38 (±2)	14 (±1)	0.052
Pt 900	1.24 (±0.06)	10.41 (±0.52)	56 (±3)	34 (±2)	10 (±0.5)	0.066

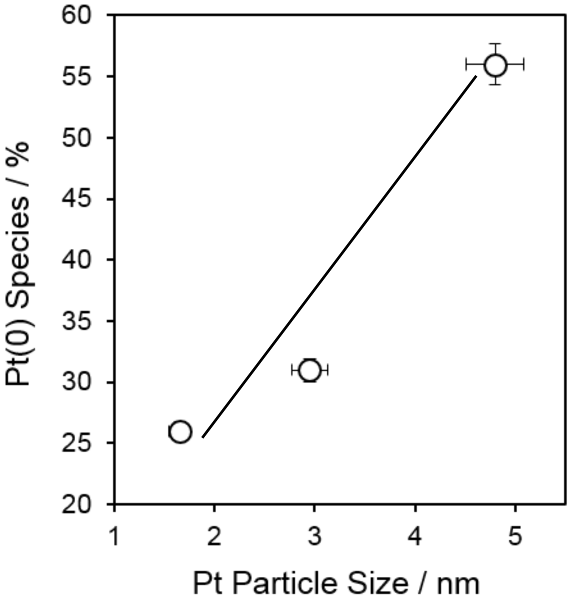

Figure 3.56 The Pt metal dependence on Pt particle size of Pt promoted meso-TiO_2 series.

3.6.6 Temperature programmed oxidation

TPO analysis of the Pt/meso-TiO_2-300 – 800 series displayed the same trend of the mass loss decrease with increasing calcination temperature like that of the titania support (**Figure 3.57**). The derivative of the mass loss (**Figure 3.58**) reveals three types of species desorbing from the surface, while only two are seen on bare supports (**Figure 3.11**). A decrease in mass at temperatures up to 150 °C is assigned to physisorbed atmospheric and crystalline water while the mass loss from 150 to 450 °C is assigned to combustion of carbons. The % of water and carbon losses for Pt/meso-TiO_2 (**Table 3.23**) come from meso-TiO_2-300 – 900 supports and are exactly the same (**3.1.6 Temperature programmed oxidation**). The mass decrease at >450 °C corresponds to a loss of PtO_x species and it reflects PtO_x amounts present on the different meso-TiO_2-300 – 900 supports (**3.6.5 X-ray photoelectron spectroscopy**).

Table 3.23 Summary of TPO results of Pt promoted meso-TiO_2-300 to 900 supports.

Sample	Water (<150 °C) / %	Carbon (150 – 450 °C) / %	PtO_x (>450 °C) / %	Total mass loss / %
Pt 300	5.8 (±0.17)	14.1 (±0.42)	0.9 (±0.91)	20.8 (±0.62)
Pt 400	3.8 (±0.12)	2.3 (±0.07)	1.3 (±0.04)	7.4 (±0.22)
Pt 500	2.3 (±0.07)	1.7 (±0.05)	0.7 (±0.02)	4.7 (±0.14)
Pt 600	0.9 (±0.03)	1.0 (±0.03)	0.6 (±0.02)	2.5 (±0.07)
Pt 700	-	0.3 (±0.01)	0.5 (±0.01)	0.8 (±0.03)
Pt 800	-	0.2 (±0.01)	0.4 (±0.01)	0.6 (±0.02)
Pt 900	-	0.3 (±0.01)	0.3 (±0.01)	0.6 (±0.02)

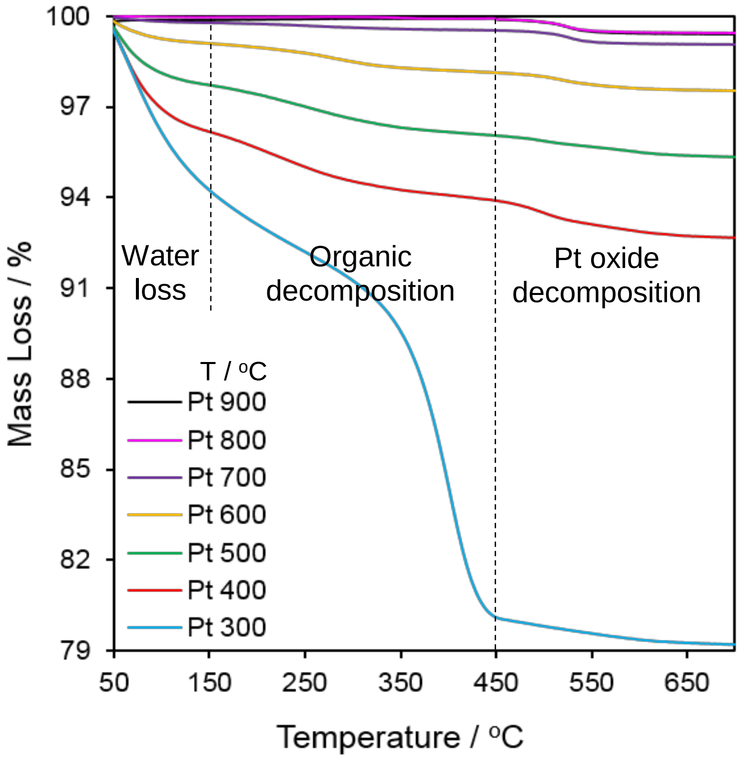

Figure 3.57 Mass loss % of Pt promoted meso-TiO$_2$300 to 900 supports.

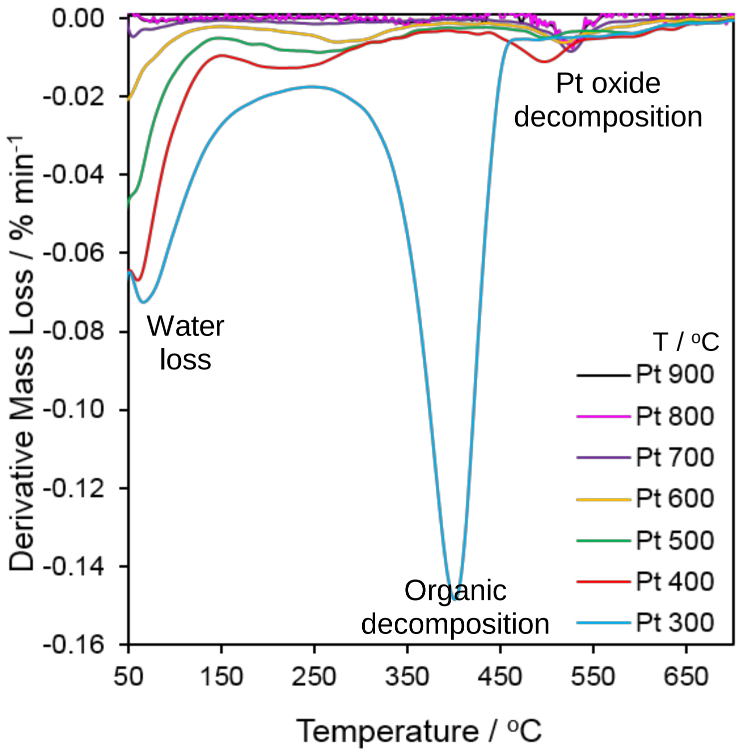

Figure 3.58 Derivative of mass loss of Pt promoted meso-TiO$_2$-300 to 900 supports.

3.6.7 Diffuse reflectance UV-vis spectrophotometry

Solid diffuse reflectance UV-vis optical absorption spectra and Tauc plots (**Figure 3.59**) were measured for Pt promoted meso-TiO$_2$-300 – 900 in order to assess the effect of Pt on the optical properties of the titania supports. Sample Pt/meso-TiO$_2$-300, like the pure support, absorbs all light in the UV – vis range owing to residual carbons present. Spectra (**Figure 3.59 (a)**) of Pt/meso-TiO$_2$-400 – 900 materials have a sharp band gap absorption edge. However, at wavelengths >400 nm, light is being absorbed even below the energy of the band gap absorption. Pure TiO$_2$ supports do not display this phenomenon, therefore it could be assigned to absorption by Pt species. The same trend of band gap absorption shifting to a visible region with increasing calcination temperature is seen as for the parent TiO$_2$.

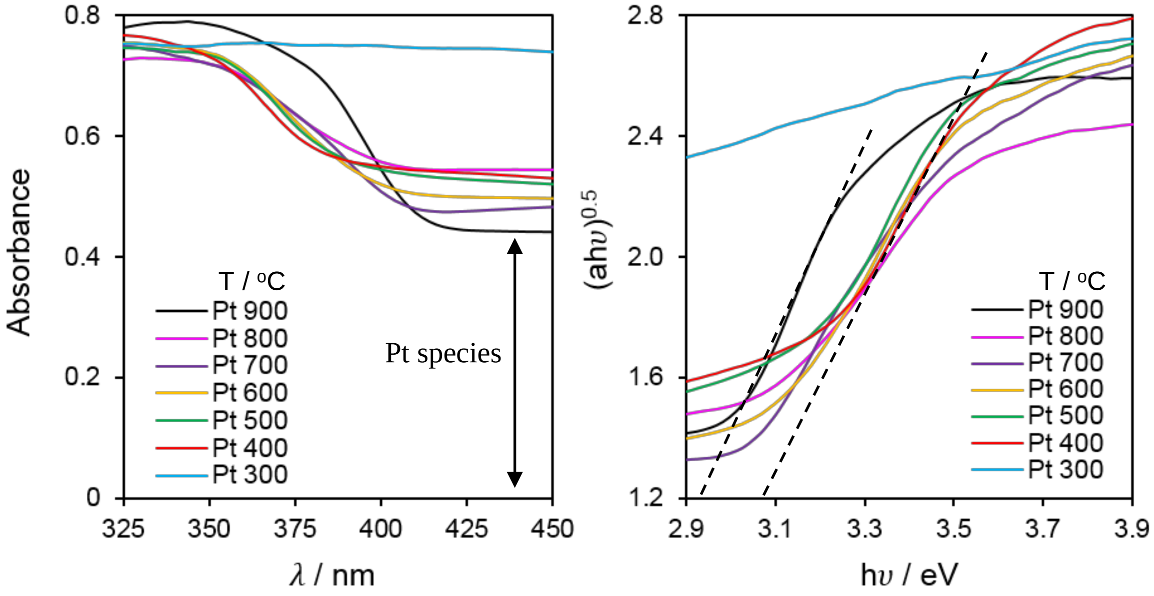

Figure 3.59 (a) UV – vis absorption spectra (b) Tauc plot of Pt promoted meso-TiO$_2$-300 to 900 supports.

Tauc plot (**Figure 3.59 (b)**) and the values of the band gaps (**Table 3.24**) exhibit an identical trend as the meso-TiO_2 supports: band gap energy decreases and shifts to a visible region with increasing amounts of rutile. Nonetheless, Pt promoted meso-TiO_2 exhibit slightly larger band gaps than the parent supports. Based on the theory, the Kubelka-Munk function is only accurate when materials are single oxides or doped composites, where modification is within the whole structure. When KM is used for the surface modified photocatalysts, the results are less accurate, because of the band bending which in this case occurs due to the Schottky barrier. As a result, the shift of the conductance and/or valence edges is observed and this influences the band gap evaluation via KM.[257-259] This is the most probable cause of the shift of the band gap values for Pt promoted series.

Table 3.24 Band gap values of Pt promoted meso-TiO_2-300 - 900 and corresponding values of the bare supports.

	Pt promoted meso-TiO_2	meso-TiO_2 support
Sample	Band Gap / eV	Band Gap / eV
300	-	-
400	3.09 (±0.02)	3.07 (±0.02)
500	3.04 (±0.02)	3.02 (±0.02)
600	2.98 (±0.02)	2.97 (±0.02)
700	2.95 (±0.02)	2.94 (±0.02)
800	2.97 (±0.02)	2.97 (±0.02)
900	2.92 (±0.02)	2.90 (±0.02)

3.6.8 Summary of the key characteristics of Pt promoted mesoporous titania series

Table 3.25 Summarises the main physicochemical and electronic properties of the Pt promoted meso-TiO_2 series with different calcination temperatures from 300 to 900 °C.

Sample	Pt loading / wt%(a)	SSA / $m^2.g^{-1}$ (b)	Mesopore size / nm (c)	Mesopore volume / $g.cm^{-3}$ (c)	TiO_2 Phase (XRD)	Nanocrystallite size / nm(d)	Band Gap / eV (e)	Total mass loss (H_2O) / % (f)
Pt 300	1.84 (±0.06)	273 (±27)	4.5 (±0.5)	0.39 (±0.04)	Anatase	5 (±0.1)	-	20.8 (±0.6) (5.8)
Pt 400	1.83 (±0.05)	188 (±19)	5.0 (±0.5)	0.33 (±0.03)	Anatase	7 (±0.1)	3.09 (±0.02)	7.4 (±0.2) (3.8)
Pt 500	1.85 (±0.06)	150 (±15)	6.7 (±0.7)	0.34 (±0.03)	97% Anatase 3% Rutile	11 (±0.1) 31 (±0.3)	3.04 (±0.02)	4.7 (±0.1) (2.3)
Pt 600	1.84 (±0.06)	82 (±8)	8.5 (±0.9)	0.20 (±0.02)	95% Anatase 5% Rutile	20 (±0.2) 33 (±0.3)	2.98 (±0.02)	2.5 (±0.1) (0.9)
Pt 700	1.80 (±0.05)	23 (±2)	16.0 (± 1.6)	0.13 (±0.01)	84% Anatase 16% Rutile	31 (±0.3) 45 (±0.5)	2.95 (±0.02)	0.8 (±0.03)
Pt 800	1.82 (±0.05)	16 (±2)	-	-	95% Anatase 5% Rutile	41 (±0.4) 62 (±0.6)	2.97 (±0.02)	0.6 (±0.02)
Pt 900	1.80 (±0.05)	13 (±1)	-	-	27% Anatase 73% Rutile	73 (±0.7) 91 (±0.9)	2.92 (±0.02)	0.6 (±0.02)

[a]ICP – OES; [b]N_2 BET; [c]from BJH desorption isotherm; [d]Mean particle diameter from XRD via Scherrer analysis; [e]DRUVS; [f]TPO;

3.7 Photocatalytic performance of Pt promoted mesoporous titania 300 – 900 °C

The photocatalytic activity of the Pt/meso-TiO_2 series characterised above was studied using the photocatalytic decomposition of Methyl Orange, H_2 production via water splitting reaction and CO_2 photocatalytic reduction under UV-vis light. The effect of Pt deposition on performance and mode of action is established and compared to pure and Cu promoted titania series.

3.7.1 Methyl Orange decomposition

The time profiles of Pt promoted meso-TiO_2 MO degradation under UV-vis light are presented in **Figure 3.60.** Prior to the illumination catalysts were stirred in the dark for one hour to achieve MO adsorption equilibrium. Pt promoted meso-TiO_2 catalysts display 30% MO dye adsorption. To check if no further adsorption takes place, an adsorption test in the dark was performed for the most active Pt meso-TiO_2-500 sample, which displayed no further adsorption**.** Photolysis was not observed for MO dye at 20 ppm concentration (**Figure 3.17**). Pt/meso-TIO_2-500 gave the fastest rate of MO decomposition while Pt/meso-TiO_2-300 the slowest.

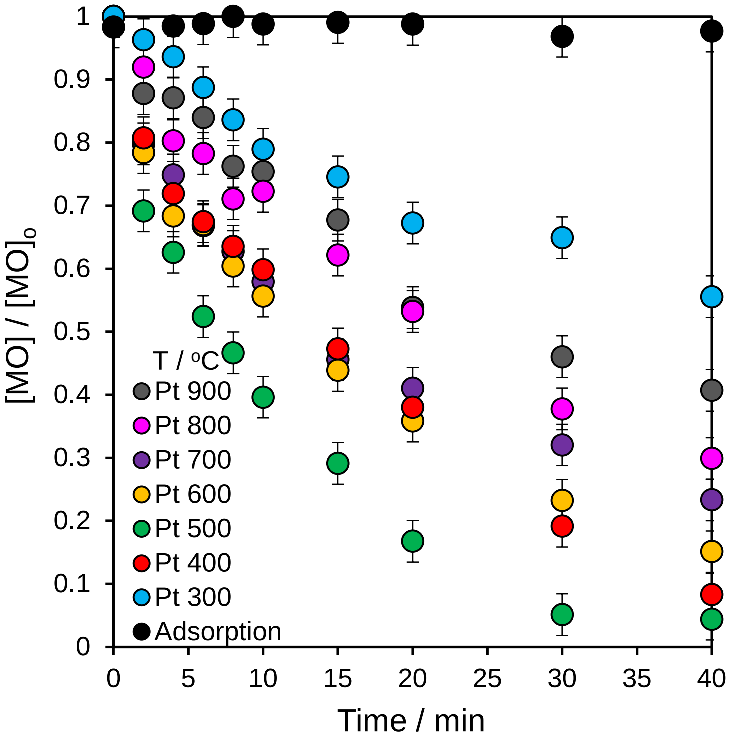

Figure 3.60 Time profiles of the percentage of methyl orange degradation of Pt promoted meso-TiO_2 300 to 900 supports including adsorption and photolysis tests under UV-vis light.

For a more accurate comparison, mass normalised initial rates (**Figure 3.61**) were calculated for the 1.8 wt% (0.092 mmol g^{-1}_{cat}) Pt/meso-TiO_2 series and compared to the 0.1 wt% (0.016 mmol g^{-1}_{cat}) Cu/meso-TiO_2 group of catalysts, where, in both cases, meso-TiO_2-400 – 800 supports are used. The Pt/meso-TiO_2 series was twice as active as the Cu promoted photocatalysts and five times more active than the support alone. The activity of the Pt photocatalysts follows a volcano trend with the most active being the Pt/meso-TiO_2-500. The trend is identical to the one observed for 0.11 wt% Cu/meso-TiO_2 photocatalysts, where either active mononuclear Cu(I) or inactive CuO species are formed depending on the support. All Pt meso-TiO_2 materials have the same wt% Pt loading thus the variable factor is the effect of the support on the Pt. XPS data (**3.6.5 X-ray photoelectron spectroscopy**) indicate that depending on the meso-TiO_2 support, Pt:Ti surface ratio changes. Higher support calcination temperatures lead to the higher Pt:Ti ratio due to a dramatic decrease in TiO_2 surface area and sintering of crystallites.

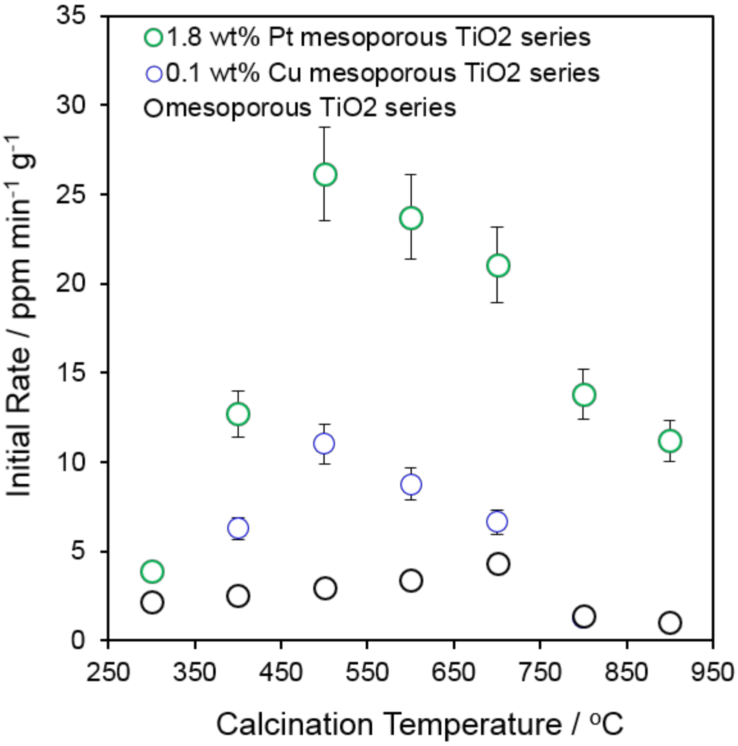

Figure 3.61 Initial rates of Pt/meso- TiO_2-300 – 900 together with 0.11 wt% promoted series and unpromoted meso-TiO_2 supports under UV-vis irradiation.

The dependence of the initial rate on the Pt:Ti ratio is demonstrated in **Figure 3.62**. The Pt/meso-TiO_2-300 sample is excluded from the Pt:Ti trend because of inactivity due to the poisoning by carbons (15%) (**3.1.6 Temperature programmed oxidation**). Activity decreases with increasing Pt:Ti surface ratio. In this case increase in Pt:Ti surface ratio indicates poorer Pt dispersion (Pt particle sintering **3.6.3 High-resolution scanning transmission electron microscopy**) owing to significantly decreasing the surface area of the meso-TiO_2 support (**3.6.1 Nitrogen porosimetry**) and drastically increasing TiO_2 crystallites size (**3.6.2 X-ray diffraction**). Variation in Pt species is also observed for different meso-TiO_2 supports but during the reaction, Pt(II) and Pt(IV) are reduced to Pt (0) (**Figure 3.64**). In theory, metallic platinum nanoparticles act as trap sites for the electron charge carriers by forming a Schottky barrier (**3.1.7 Diffuse reflectance UV-vis spectrophotometry**) and reducing recombination leading to an increased lifetime of the charge carriers (**Figure 3.63**).[95, 260, 261] Schottky barrier arises when metal is in contact with n-type semiconductor and electrons populate on metal species while holes remain on the semiconductor (TiO_2) if the Fermi level of the metal (in this case Pt) is lower than conductance band of the semiconductor (**1.4.1 Surface trapping**). Accumulated electrons on metal particles can then be used to carry out reduction reactions, while holes on the photocatalyst can be used to carry out the oxidation reactions. Pt metal is a very effective promoter for MO degradation, however, the price of Pt is too high to be used for depollution of water and cheaper options like Cu are available.

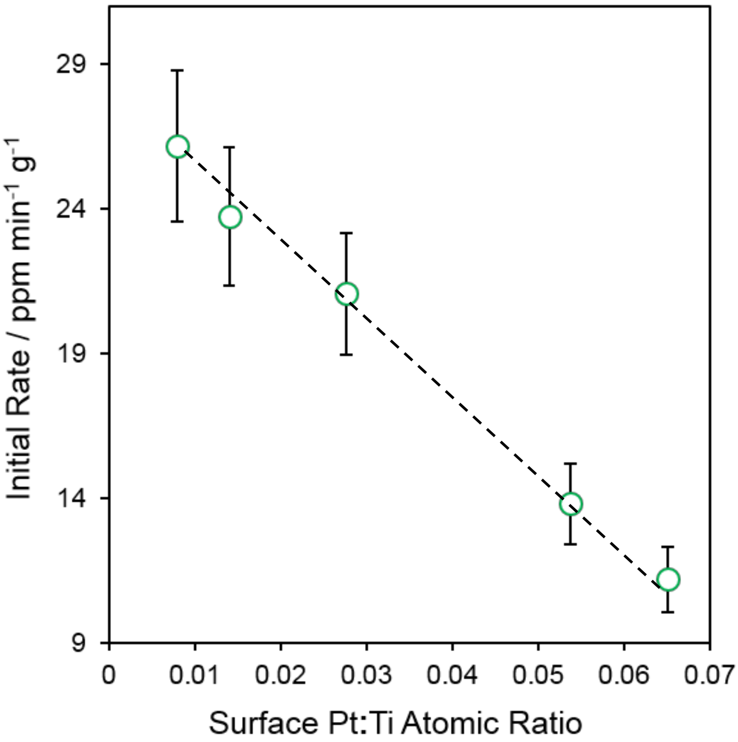

Figure 3.62 (a) Initial rates vs Pt species of Pt promoted meso-TiO_2-300 - 900 supports under UV-vis light.

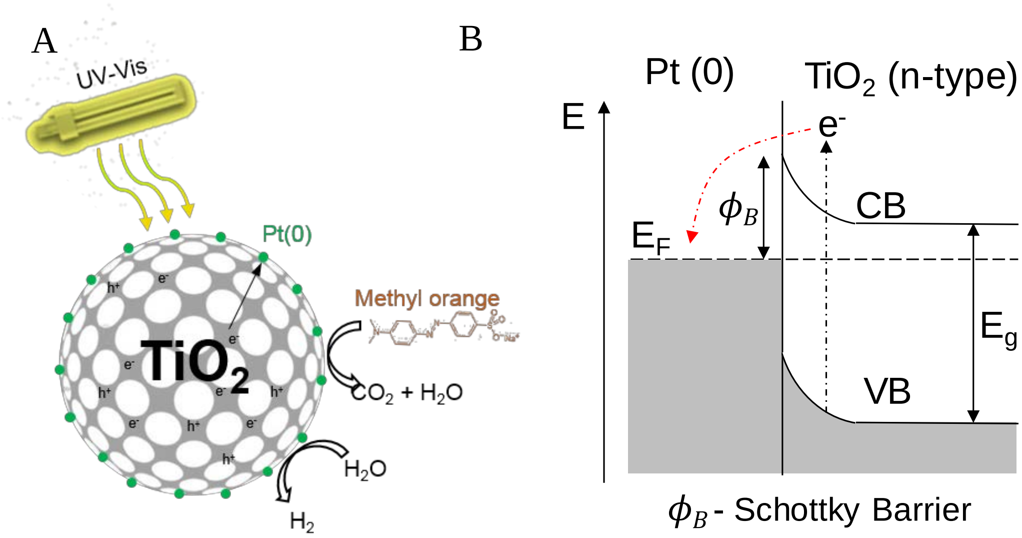

Figure 3.63 (a) Schematic representation of Pt mode of activity (b) Schottky barrier illustration.

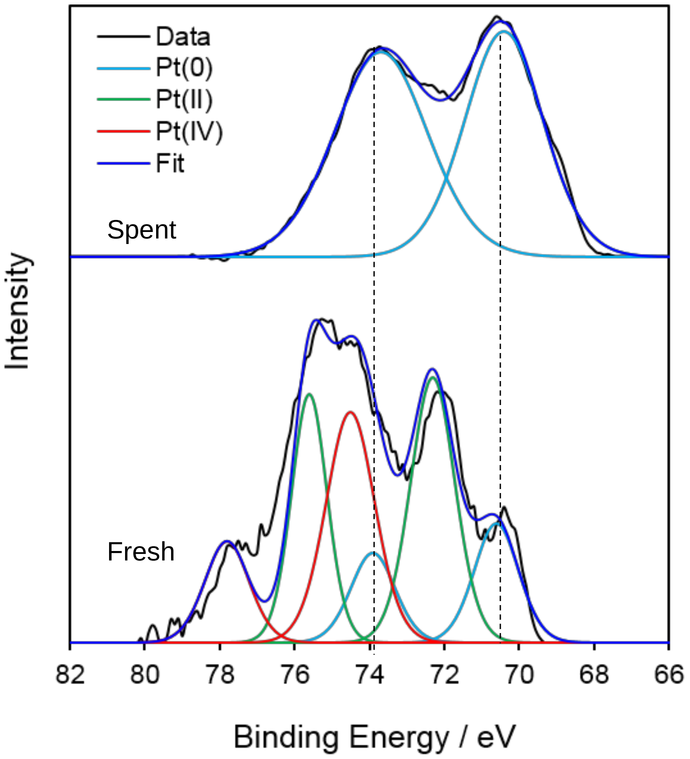

Figure 3.64 XPS data of Pt/meso-TiO_2-600 fresh and spent catalyst.

3.7.2 Water splitting

The H_2 production rate of Pt promoted meso-TiO_2-300 -900 photocatalysts follow a volcano trend (**Figure 3.65**) as observed in MO dye degradation tests (**Figure 3.61**). In this case, the Pt mesoporous TiO_2 series is eight times more active than Cu promoted photocatalysts and ten times more active than the titania support. The trend is identical to the one observed for 0.11 wt% Cu/meso-TiO_2 photocatalysts for both MO and WS reactions.

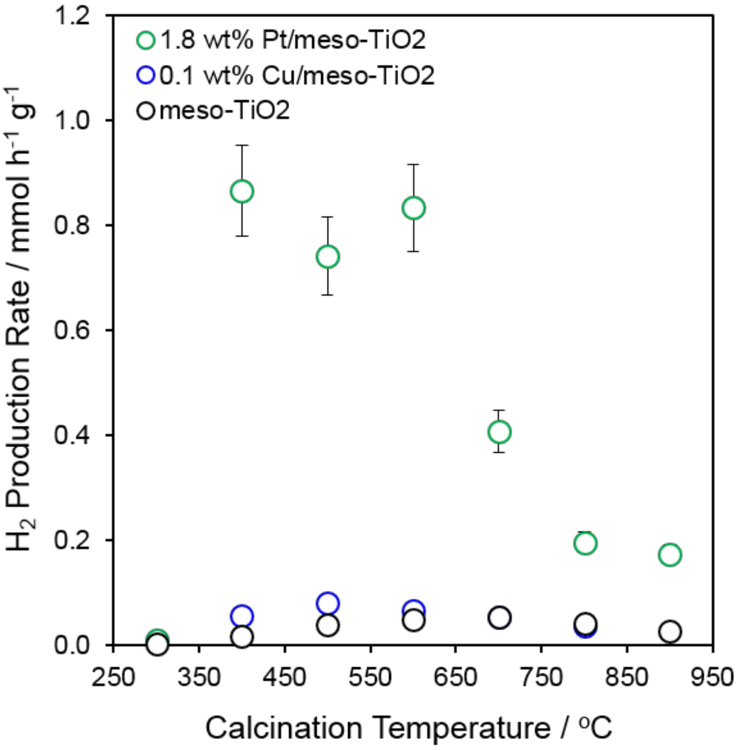

Figure 3.65 H_2 production rates of Pt promoted meso-TiO_2-300 - 900 supports together with 0.11 wt% Cu promoted meso-TiO_2 and unpromoted mesoporous TiO_2 supports under UV-vis irradiation.

The same dependence of activity on the Pt:Ti ratio as observed in Methyl Orange degradation is also seen in the water splitting reaction. The hydrogen production rate decreases with increasing Pt:Ti (**Figure 3.66**) because of increase in Pt:Ti surface ratio indicates poorer Pt dispersion owing to significant decrease in the surface area of the meso-TiO_2 support (**3.6.1 Nitrogen porosimetry**) and drastically increasing TiO_2 crystallites diameter (**3.6.2 X-ray diffraction**). The identified active Pt metal species, in theory, act as trap sites for the electron charge carriers, reducing recombination and pro-longing lifetime, which leads to the increased photoactivity (discussed in detail in **3.7.1 Methyl Orange decomposition and 1.4.1 Surface trapping**). Despite WS and MO degradation reactions being mechanistically very different, in both cases, the promoted photocatalysts display enhanced activity. The commercial 2 wt% Pt/P25 showed a low H_2 production rate of 0.2 mmol $h^{-1}.g^{-1}$ which is equal to the least active Pt/meso-TiO_2-800 and 900 photocatalyst and is five times less active than the most active 1.8 wt% Pt/meso-TiO_2-600 sample.

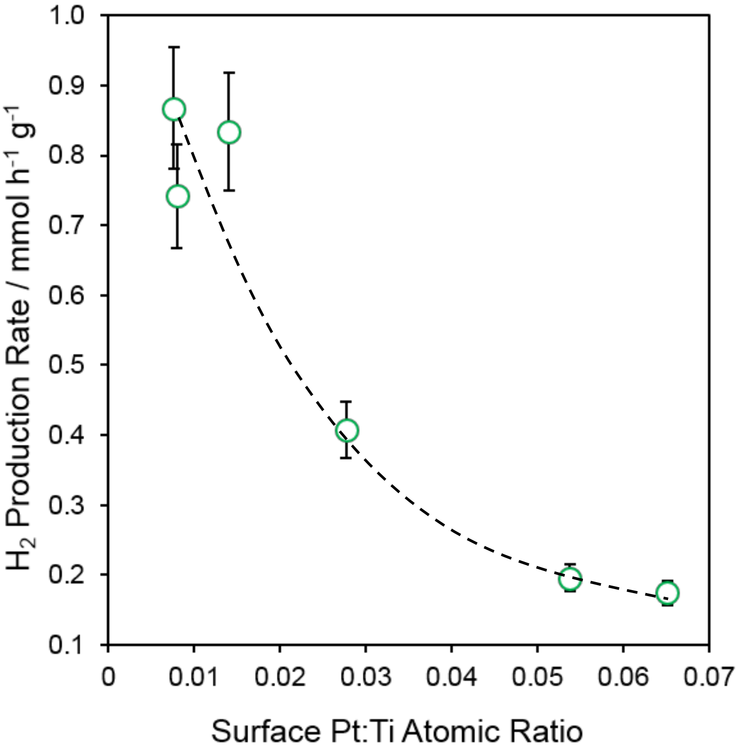

Figure 3.66 H_2 production rates vs surface Pt:Ti atomic ratio of Pt promoted meso-TiO_2-300 – 900 supports under UV-vis light.

3.7.3 Carbon dioxide reduction

The CO_2 photoreduction reaction yielded methane and hydrogen gas products only. The reaction was performed by saturating an aqueous catalyst suspension with CO_2 gas, and therefore, a H_2 production via side water splitting reaction is detected. The most important CH_4 product generation demonstrates a volcano trend with maximum generation rate of 1.5 μmol h^{-1} g^{-1} (**Figure 3.67**). The 1.8 wt% Pt promoted meso-TiO_2-300 – 900 series were the only catalysts to produce a significant amount of CO_2 reduction products to overcome GC detection limits. An identical volcano trend was seen in Methyl Orange degradation (**3.7.1 Methyl Orange decomposition**) and WS (**3.7.2 Water splitting**) reactions where activity improves with a decrease in Pt:Ti ratio. Increase in Pt:Ti surface ratio indicates poorer Pt dispersion owing to the significantly lower surface area of the meso-TiO_2 support (**3.6.1 Nitrogen porosimetry**) and drastically larger TiO_2 crystallites diameter (**3.6.2 X-ray diffraction**). As expected, methane production decrease with increase in surface Pt:Ti (**Figure 3.68**). Once again Pt metal is the promoter species which, in theory, trap the electrons and separates the charges, resulting in suppressed recombination and increased activity (discussed in detail in **3.7.1 Methyl Orange decomposition**).

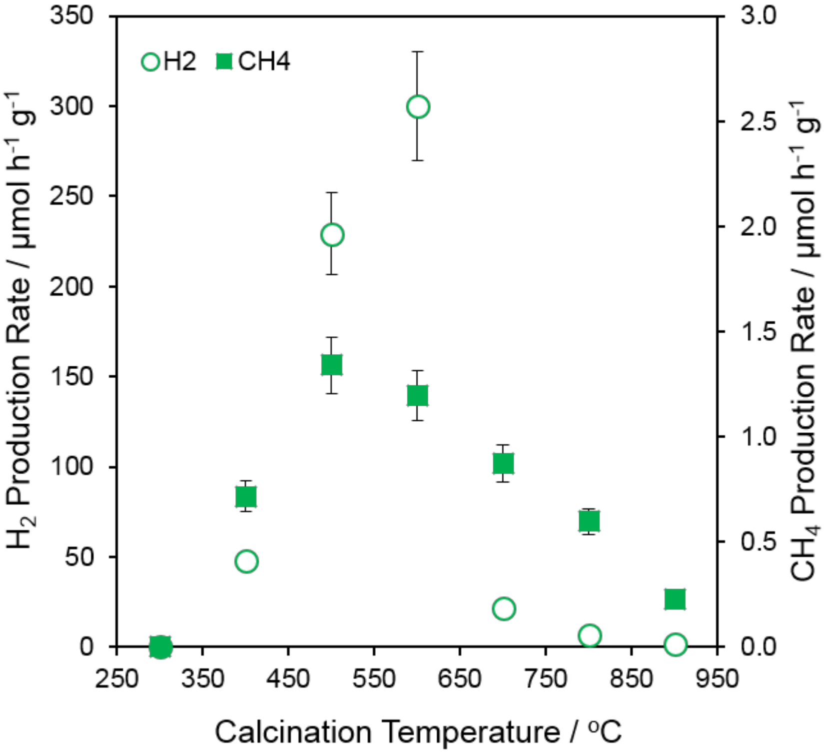

Figure 3.67 Methane production rate via CO_2 photoreduction by Pt promoted meso-TiO_2-300 - 900 supports under UV-vis irradiation.

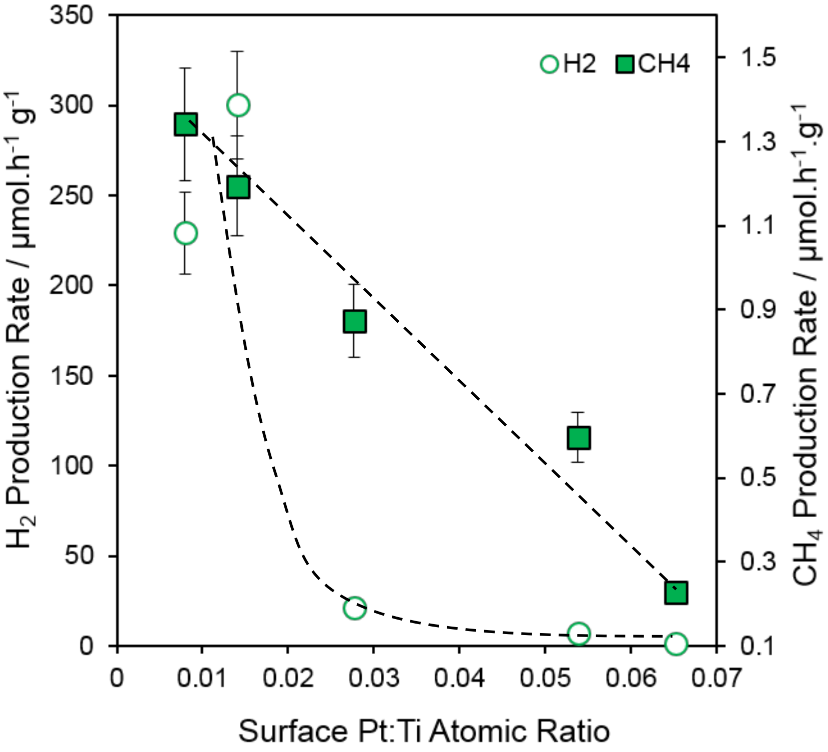

Figure 3.68 H_2 and CH_4 production rates vs surface Pt:Ti atomic ratio of Pt promoted meso-TiO_2-300 - 900 supports under UV-vis light.

3.8 Conclusions of the mesoporous titania photocatalysts

Control over the structural and photophysical properties of mesoporous titania enables the systematic transformation of the materials. A facile route is demonstrated to the high area (194 $m^2\ g^{-1}$), mesoporous TiO_2 with tunable pore diameter, anatase:rutile phase composition and corresponding electro-optical properties through thermal processing of a surfactant-templated sol-gel. The surface area and the mesopore structure is in a good agreement with the literature, where ordered 150 – 200 $m^2\ g^{-1}$ mesoporous TiO_2 are commonly synthesised.[211, 217, 218] Increasing calcination temperature from 300→700 °C induces progressive expansion of uniform mesopores from 5→16 nm respectively, and a concomitant decrease in surface area, accompanied by the transformation of smaller (11→31 nm) anatase to larger (30→46 nm) rutile nanocrystallites and slight band gap narrowing. Tunable textural and photophysical properties enable facile control over the photocatalytic activity for both Methyl Orange degradation (in the absence of dye sensitisation) and water splitting under UV-Vis irradiation. Initial rates of MO photodegradation exhibit a weak, direct correlation with mesopore diameter and a strong, direct correlation to rutile concentration expressed by the band gap, enabling over a two-fold rate enhancement through high-temperature calcination. The increase in the photoactivity is attributed to improved charge separation, prolonged charge carrier lifetime and reduced recombination across a type-II, staggered anatase/rutile heterojunction interface.[233, 234] Photocatalytic H_2 production is even more sensitive to the anatase→rutile phase transition, which confers a dramatic 25-fold increase in water splitting, likely due to a combination of heterojunction formation and the higher conduction band minimum of rutile titania. When the performance is compared to commercial P25 photocatalyst meso-TiO_2 series were twice less active in Methyl Orange most likely due to better P25 dispersion in the MO solution. On the other hand, in water splitting reaction P25 and meso-TiO_2-700 displayed the same H_2 production rate. All the samples displayed prolonged charge carrier lifetime compared to that of the commercial P25 sample with the most active meso-TiO_2-700 sample having 7 times longer lifetime than that of P25.

Post-functionalisation of mesoporous TiO_2 by wet-impregnation with ultra-low (0.1 wt%) concentrations of copper affords atomically-dispersed Cu(I) species, likely extra-framework decorating the surface of titania crystallites. Despite their high dilution, the incorporation of Cu(I) species results in a six-fold rate enhancement for Methyl Orange photodegradation relative to the unmodified (500 °C) mesoporous TiO_2, possibly due to the introduction of oxygen vacancies which may act as electron traps to increase charge carrier lifetimes. A symbiosis between Cu(I) and CuO over 0.81 wt% Cu/meso-TiO_2-500 increased photocatalytic H_2 production four-fold relative to the mesoporous anatase scaffold. This observation provides an important step towards understanding the synergy between copper promoter species and improved photocatalytic performance. The results correlate well with the previously performed studies which, first of all, indicated Cu(I) as the most common active Cu species. [222, 223] Secondly, Liu et al.[88] identified the importance of well-dispersed

Cu and the highest photocatalytic activity at ultra-low ≤ 0.03 wt% loadings. Moreover, different mesoporous TiO_2 supports dictate formation of different copper species. These findings give an insight into the rational synthetic approach to tunable Cu/mesoporous TiO_2 photocatalysts for environmental remediation and renewable energy. An in-depth comparison of the activity results with the literature is complicated because of the broad spectrum and complexity of the operating conditions used in literature, such as light intensity and distribution, change in stock solution concentrations, etc. However, in order to have a broader picture of how active Cu promoted meso-TiO_2 series are, the photoactivity of the photocatalysts were compared to the activity observed in the literature. Thu and co-workers synthesised 0.05 wt% copper-doped TiO_2 nanoparticles (surface area 65 $m^2.g^{-1}$) which degraded 50% Methyl Orange over 60 min (pH=9, 15 ppm, irradiated by 365 nm wavelength). The 0.1 wt% Cu/meso-TiO_2 and 0.02 wt% Cu/meso-TiO_2 described in this thesis are twice more active than the literature values, even in the higher 20 ppm MO concertation. Approximately 100 $\mu mol.h^{-1}$ H_2 hydrogen was produced (36 W cm^{-2} 365 nm) by using 0.8 wt% Cu/TiO_2 nanoparticles via sol-gel synthesis.[262] In this thesis, the most active 0.81 wt% Cu/meso-TiO_2 material showed 160 $\mu mol.h^{-1}$. It is important to note, that the light intensity is this reactor is only 150 $mW.cm^{-2}$ while the one in the publication is drastically larger - 36 W cm^{-2}.

Promotion with the 1.8 wt% Pt is another way of significantly enhancing the photocatalytic performance of meso-TiO_2-300 – 900 series. Pt wet-impregnated materials were twice as active as the Cu promoted photocatalysts and five times more active than the bare supports in the Methyl Orange degradation. Furthermore, the Pt/meso-TiO_2 series are eight times more active than Cu promoted photocatalysts and ten times more active than the titania supports in the WS reaction. The activity in all photocatalytic reactions (MO degradation, water splitting, CO_2 photoreduction) is strongly depended on mesoporous TiO_2 support. The dependence was expressed in Pt:Ti ratio; the activity increased with decreasing Pt:Ti ratio. In this case, small Pt:Ti ratio corresponds to better dispersed Pt because of the higher surface area of TiO_2 and small (~ 2 nm) Pt nanoparticles. Since the loading of the Pt was kept uniform for all the materials, the severe decrease in TiO_2 surface area across the series led to increase in Pt nanoparticles (~5 nm) and as a result - Pt:Ti ratio. Out of all materials synthesised so far, the only Pt/meso-TiO_2-300 – 900 produced methane via CO_2 photocatalytic reduction (1.3 $\mu mol.h^{-1}$ $.g^{-1}$). Selectivity solely to methane product is commonly observed for Pt/TiO_2 photocatalysts and the productivity is well within the range of 0.06 - 6 $\mu mol.h^{-1}$ $.g^{-1}$, detected in the literature.[263-265] Since the reaction takes place in aqueous media, the side water splitting reaction forms H_2 product. The significantly improved activity, in comparison to pure and Cu promoted series, arises from the metallic platinum nanoparticles, which, in theory, act as trap sites for electron charge carriers by forming a Schottky barrier. This leads to increased lifetimes of the carriers and reduced recombination. The Pt promoter species formed, relates well to the literature, where the Schottky barrier is often observed. [95, 96, 202] The most active Pt/meso-TiO_2 sample showed a five-fold increase in H_2 production rate in comparison with commercial 2 wt% P25.

The importance of tailoring both textural and photophysical properties of heterogeneous photocatalysts to optimise chemical mass transport, and the energetics and lifetime of charge carriers, emerge as principal design features. The key factors dominating the activities of Methyl Orange degradation and water splitting reactions are titania crystalline phase, percentage of Mononuclear Cu (I) species and dispersion of Pt(0) promoter. Furthermore, for the CO_2 reduction reaction, the presence of Pt(0) promoter species is essential and photocatalytic performance is dictated by Pt(0) distribution on the TiO_2 surface.

Chapter 4

Macro-mesoporous TiO_2 photocatalysts

4 Macro-mesoporous titania photocatalysts

Hierarchically ordered porous (HOP) materials can consist of micro and mesopores or meso and macropores or in rare occasions all three: micro-meso-macropores.[266] In the past few years, hierarchically ordered porous materials have received increasing interest as catalysts for adsorption, batteries, waste disposal and photocatalysis, with the merit of larger surface area, easier mass transport and enhanced optical properties.[267-269] The very first macro-mesoporous silica was synthesised in 1998 by Yang and co-workers[270] and since then the most well-established HOP materials are based on carbon and silica.[271]

Hierarchical TiO_2 has been previously fabricated via phase separation, spin-coating, nanocasting, hydrothermal and sol-gel methods.[272, 273] Most common sol-gel synthesis of hierarchical macro-mesoporous TiO_2 involves a combination of the hard template of polymer spheres like PSA or polystyrene to form macropores, and a surfactant templating synthesis involving non-ionic copolymers such as P123 and F127 for mesostructure fabrication.[274, 275] However, the relatively weak interaction between the macropore template and titania precursors, and the shrinkage of titania framework during the calcination process often result in disordered or broad size distribution macropores.[274] Moreover, it has proven difficult to synthesise macro-mesoporous TiO_2 materials with ordered mesopores as well, because fast hydrolysis and condensation steps of titania precursor lead to worm-hole like mesopore structures and stabilisation of a hexagonal mesopore array after the calcination has rarely been reported.[167] The overall ordered bimodal pore network is desired in order to achieve the best diffusional and optical properties.

Jin et al.[167] synthesised hierarchical ordered macro-mesoporous TiO_2 via surfactant templating synthesis involving P123 non-ionic triblock copolymer, P(St-MMA-SPMAP) (poly(styrene-methyl methacrylate-3-sulfopropyl methacrylate potassium salt) hard spheres and titanium chloride as titanium precursor. The resulting material shows disordered mesoporosity (mesopore diameter 5 nm) within well-ordered periodic inverse opal macropore walls (macropore diameter 170 nm) and 139 $m^2.g^{-1}$ surface area. The macro-mesoporous TiO_2 demonstrates higher surface area and better electrochemical performance than it's purely macroporous TiO_2 equivalent (99 m^2 g^{-1}). The improvement in the performance is attributed to the higher surface area and the presence of the mesoporosity which advances diffusion and provides a shorter path length for Li ions. Another publication presents successful one-pot fabrication of hierarchically ordered porous TiO_2 involving PSA colloidal spheres and P123 as macro and meso structure-directing agents respectively, and titanium chloride and titanium tetra*iso*propoxide as Ti precursors.[274] The synthesis yielded typical surface area (135 m^2 g^{-1}), ordered uniform face-centred cubic (fcc) macropore framework (macropore diameter 170 nm) and most importantly ordered hexagonal mesopore structure with narrow mesopore diameter (3.4 nm). The newly synthesised HOP TiO_2 displayed an increased light harvesting properties in the photocurrent measurements and 33% improved photoactivity in the Rhodamine B photodegradation reaction compared to the P25. As discussed in **3 Mesoporous titania photocatalysts** chapter the use of $TiCl_4$ precursor, which is highly volatile and in the contact with humid air, and it forms TiO_2 and HCl,[216] results in the extremely hazardous environment, especially if synthesised on the large scale. Wu and co-workers[276] synthesized macroporous TiO_2 with an inverse opal structure with four different macropore sizes (130, 250, 370 and 450 nm) and varied calcination temperature (550, 700 and 900 ^oC). The photodegradation of Rhodamine B results showed that the most active were the samples calcined at 700 ^oC and it was accounted to an optimal balance of uniformly sized nanocrystals, an excellent crystalline structure, specific surface area, a well-ordered macroporous structure and the band-gap energy. However, the activity dependence on macropore diameter is not well defined, the more active photocatalysts were the ones with macropore size identical to the wavelength of the irradiation (370 nm) as well as the very small diameter (130 nm) macroporous TiO_2. The comparison of characteristics and photoactivity between mesoporous and macro-mesoporous TiO_2 and the trends of macropore diameter to hierarchical macro-mesoporous TiO_2 remains unknown.

Macroporous TiO_2 display enhanced optical properties when the macropores form inverse opal structures in which by definition the pore arrangement is well ordered in three dimensions.[70-72] Commonly, the macropores are arranged in an fcc or hcp structures and each pore is connected to the twelve nearest neighbours. Highly ordered uniform diameter inverse opals exhibit a periodic modulation of the refractive index, and therefore behave as photonic crystals.[277] Photonic crystals exhibit a periodic dielectric constant, in the scale of the wavelength of the light, thus the light with certain energies is forbidden to propagate through the material in a particular crystallographic direction by the coherent Bragg diffraction.[278] This induces a stop-band reflection resulting in the range of energies reflected back. The stop-band reflection wavelength depends on the periodicity and dielectric constant of the photonic crystal. At the frequency edges of these stop bands, photons propagate with strongly reduced group velocity, therefore, they are called slow photons. Slow photons can be observed in periodic photonic structures at energies just above and below the photonic stop band. If the energy of the slow photons overlaps with the absorbance of the material (the conductance edge of the band gap), an enhancement of the absorption can be expected. [279, 280]

The enhanced optical properties of macroporous TiO_2 inverse opal structures with photonic crystal characteristics can significantly enhance macroporous TiO_2 photocatalytic performance. [281-283] Chen et al.[71, 72] demonstrated that the amplified photocatalytic activity occurs while using inverse TiO_2 opals and it is attributed to the slow-photon effect, utilizing slow photons with energies close to the electronic bandgap of the semiconductor. Furthermore, Zheng and et al.[284] designed an inverse-opal macroporous TiO_2 photonic crystals with photonic band gaps that are matched with the absorption peaks of the dyes (Methyl Orange, Rhodamine B, and Methylene Blue) and the photocatalytic activity of the corresponding samples are significantly improved because the slow photon effect on the edges of the photonic band gaps enhances the dye sensitization. The positions of the photonic stop bands are precisely tuned by controlling the polystyrene diameters. In addition, the materials show the higher activity and stability than TiO_2 nanoparticle film as a result of the slow photon effect, and the enhanced mass transfer. Ordered Pt promoted crystalline macro-mesoporous TiO_2 (12 nm mesopores and 300 nm macropores) were synthesised for a photocatalytic water splitting and showed 100 µmol.h^{-1}.g^{-1} production rate, which was more than double compared to macro-mesoporous tantalum, niobium, zirconia and aluminium oxides. However, the surface area of this hierarchical TiO_2 was very low (13 m^2 g^{-1}). The copper supported inverse opal titania were coated by sol-gel synthesis on the optical fibre reactor.[285] The inverse opal macroporous titania improved the quantum efficiency of the photoreduction of CO_2 to methanol in the presence of water vapour and UV light. Methanol production rates (36.4 nmol.g_{cat}^{-1}.h^{-1}) were comparable to those of a conventional fibre optic reactor using Cu supported unstructured titania but required much lower light intensity. To conclude, one-pot synthesis of highly ordered inverse opal materials with hierarchical macro-mesoporous TiO_2 structure with photonic crystal properties remains a challenging task.

To further improve the photocatalytic performance of hierarchical macro-mesoporous TiO_2, materials can be promoted by introducing transition metal species such as Cu and Pt to improve the light absorption and reduce electron and hole recombination. Wang et al.[286] fabricated a TiO_2 sponge, consisting of a macroporous framework with interconnected mesoporous channels, via co-gelation of lotus root starch with the TiO_2 precursor, followed by lyophilisation and subsequent calcination. This synthesis combined both the traditional hard-templating technique for well-defined macroporous architecture and soft-templating for intrapore connectivity. The photocatalytic CO_2 reduction to CH_4 over macro/mesoporous TiO_2 sponge was significantly enhanced from 5.13 ppm h^{-1} to 11.95 ppm h^{-1} by co-loading with Pt (0.9 wt%) and Cu (1.7 wt%) as a result of the improved separation of the hole and electron charge carriers. Different loadings of Pt nanoparticles (2 - 4wt%) were photodeposited on the surface of inverse opal TiO_2 and the photodegradation of acid orange was tested. [287] The photoactivity increased by 4-fold via dual synergistic optical and chemical slow photon in photonic crystal and the Pt nanocluster effects. While slow photons increased the effective path length of light, Pt nanoparticles extended the lifetimes of the charge carriers. Another group[288] further demonstrated that the recombination of photogenerated holes and electrons is effectively reduced by the Schottky barrier between Pt and TiO_2, as the platinised samples show higher photocurrents and the faster phenol degradation. The inverse opal Pt/TiO_2 materials with a photonic pseudo gap and photonic modes with slow group velocity that match to the irradiation wavelength, further improve the photocurrents and photocatalytic activity.

The aim is to synthesize uniform ordered hierarchical macro-meso-TiO_2 with uniform tunable macropore size and investigate the impact of the macropores to the photocatalytic activity. Also, the influence of the macro-mesopore framework to the Cu and Pt promoters is explored. Cu or Pt was deposited via the classical wet-impregnation process. The photocatalytic activity was tested in Methyl Orange degradation, water splitting and CO_2 reduction reactions.

4.1 Characterisation of macro-mesoporous titania series

Hierarchical macro-mesoporous TiO_2 photocatalysts (macro-meso-TiO_2) were prepared by adopting the mesoporous TiO_2 surfactant-templating synthesis, discussed in the previous chapter, and introducing polystyrene (PS) hard template. Five different polystyrene sizes were employed to achieve a range of macropore sizes. As a result, macro-meso-TiO_2 series with 140, 200, 240, 290 and 310 nm macropores were obtained by soft-hard templating. The characteristics of newly designed macro-meso-TiO_2 materials were investigated using a variety of techniques to assess the impact of incorporation of macropores to structural and electronic properties of the catalysts. The introduction of macroporosity can improve accessibility and diffusion of larger molecules. Furthermore, 3-D inverse opal ordered macroporous TiO_2 can demonstrate photonic crystal properties resulting in improved photoactivity. [284, 289]

4.1.1 High – resolution scanning transmission electron microscopy

HRSTEM images are used to establish polystyrene bead size which is further employed in macro-meso-TiO_2 photocatalysts synthesis. **Figure 4.1 (a)** is an example electron micrograph image of polystyrene beads of 370 nm diameter. During synthesis, PS beads are centrifuged to separate the solvent and as a result, beads form a close-packed ordered structure, however, STEM is run on samples while they are still in solution, thus the packing is not observed. **Figure 4.1 (b) – (f)** represent polystyrene bead size distributions which reveal average PS size of 370, 570, 660, 685 and 700 nm. **Figure 4.2** shows an HRSTEM image of hierarchical macro-meso-TiO_2 with 200 nm macropores. To synthesise this sample 370 nm PS beads were used and based on the SEM data, the macropore diameter is 140 nm (**4.1.2 Scanning electron microscopy**) and 140 nm is the label for this sample in the further text. HRSTEM images demonstrate hierarchical structure containing long-range uniform hexagonally ordered opal shape macropores imparted by polystyrene template and extended mesoscopic close-packed structure with 4 nm mesopores, resulting from the self-assembly of the F127 block copolymer. The mesopore network is perturbed by interpenetrating spherical macropores, which place geometric constraints on the hexagonal configuration of mesostructure.[290] Thus, short-range mesopore order, displayed by the meso-TiO_2-400 counterpart (**3.1.4 High-resolution scanning transmission electron microscopy**) prepared under comparable conditions, is not retained.

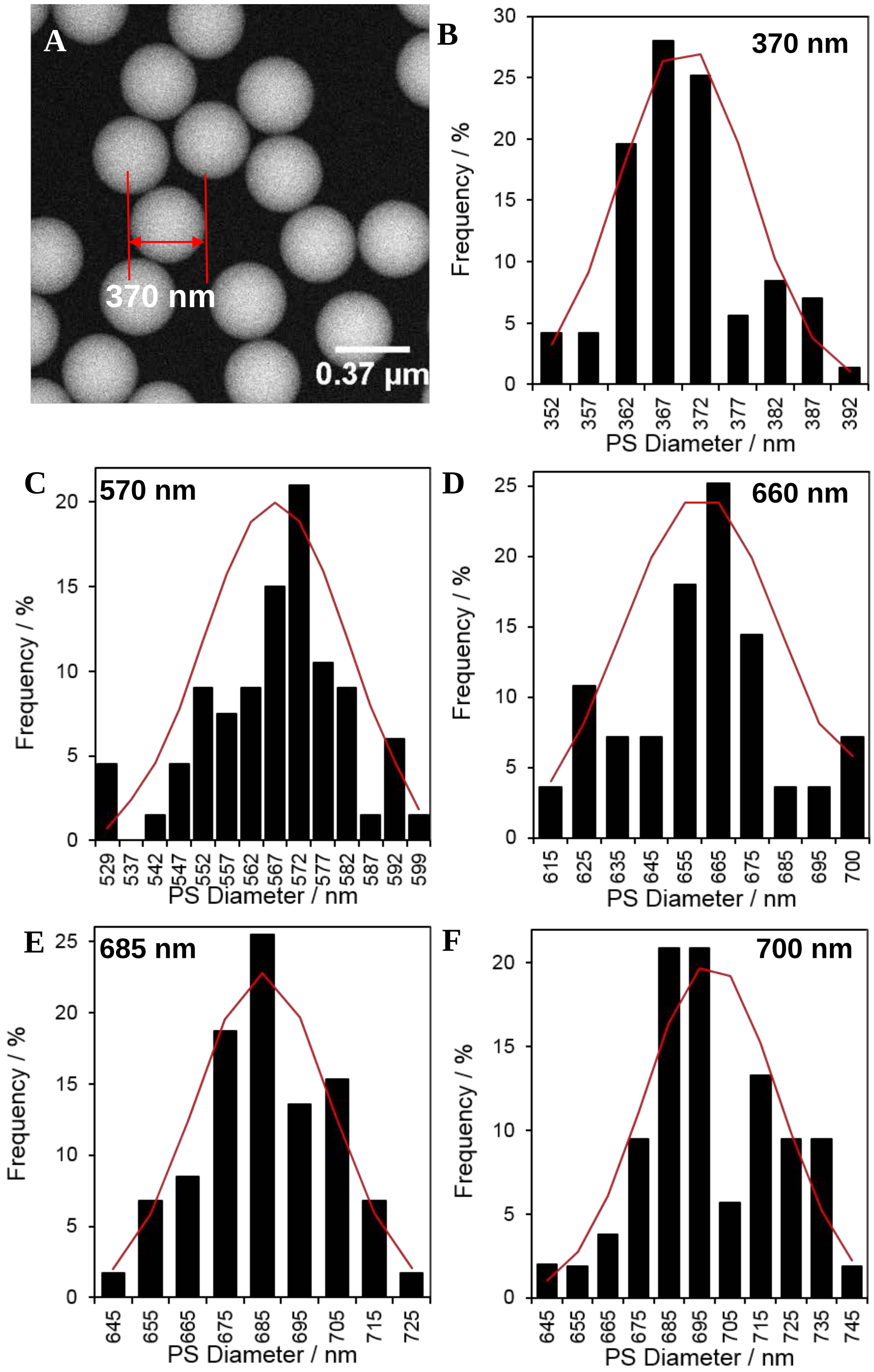

Figure 4.1 (a) HRSTEM image of 370 nm polystyrene beads (b) Bead size distribution of 370 nm (c) Bead size distribution of 570 nm (d) Bead size distribution of 660 nm (e) Bead size distribution of 685 nm (f) Bead size distribution of 700 nm.

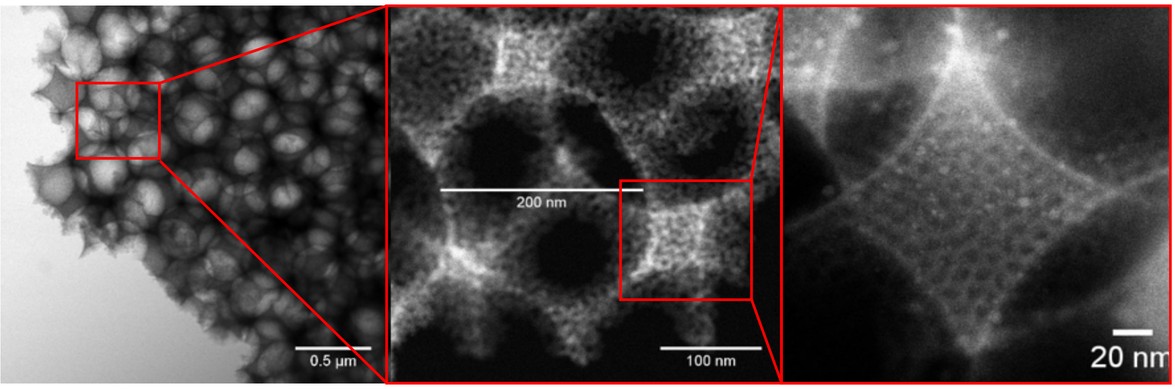

Figure 4.2 HRSTEM images of macro-meso-TiO_2 sample where 570 nm PS beads were used.

4.1.2 Scanning electron microscopy

Macro-meso-TiO_2 series morphology and macroporosity were imaged by scanning electron microscopy (SEM). **Figure 4.3 (a) – (j)** demonstrate representative images of the five supports with different macropore size. All images show the successful incorporation of an ordered uniform macropore network throughout titania crystallites (>70%), which based on the previous TEM and following N_2 porosimetry contain the meso-TiO_2 structure. The average 140, 200, 240, 290 and 310 nm macropore diameters (**Table 4.1**) are calculated using pore size distribution (**Figure 4.4**). When compared to the average polystyrene sphere size, macropore size is twice smaller indicating macropore contraction occurs during high temperature (400 °C) calcination. Images show large angular TiO_2 particles spanning a very wide range from one to hundred microns.

Table 4.1 Polystyrene bead and macropore sizes of macro-meso-TiO_2 series.

PS size TEM / nm	Macropore size SEM / nm
370 (±22)	140 (±8)
570 (±34)	200 (±12)
660 (±40)	240 (±14)
685 (±41)	290 (±17)
700 (±42)	310 (±19)

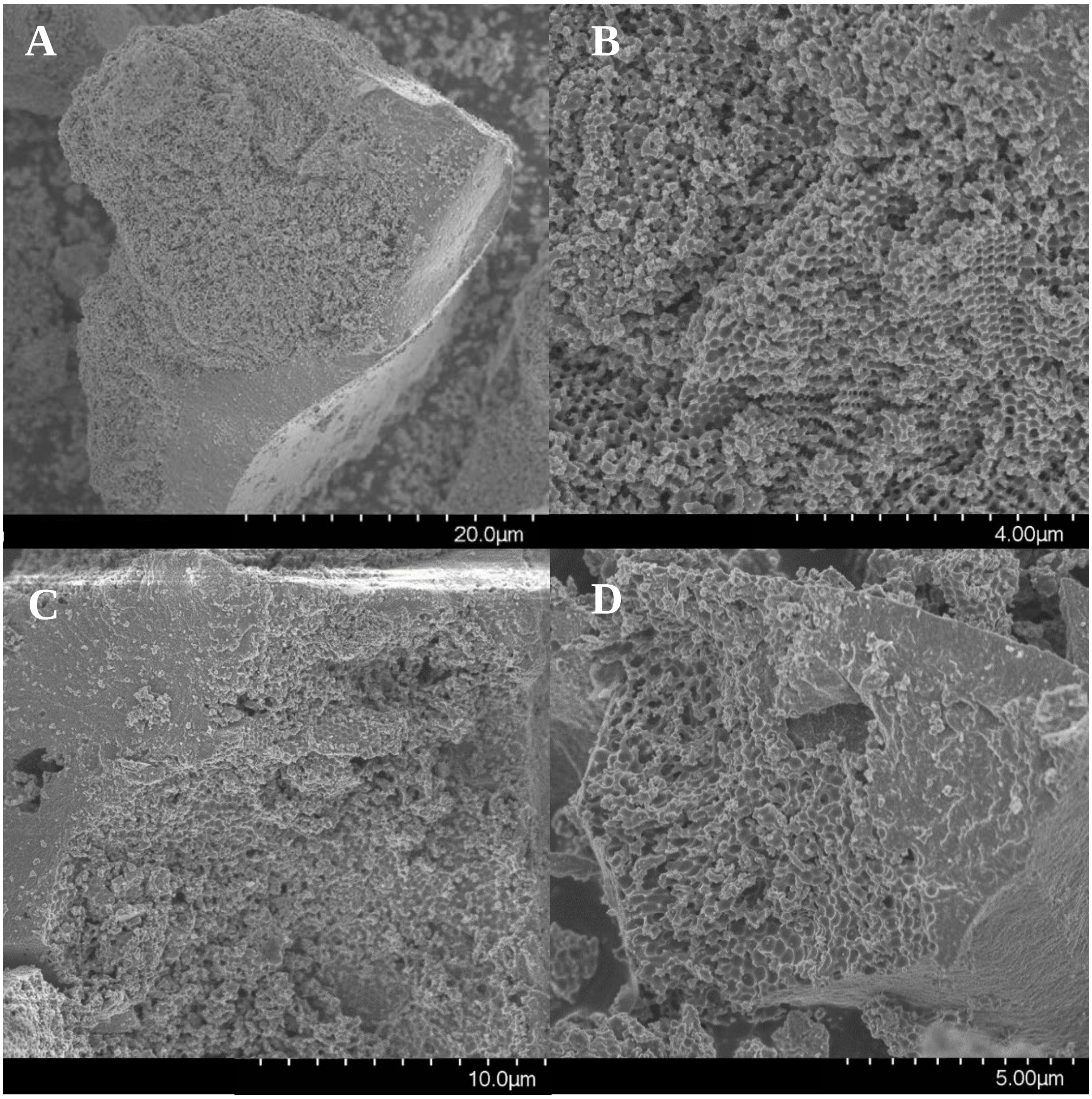
A
B
C
D
20.0µm
4.00µm
10.0µm
5.00µm

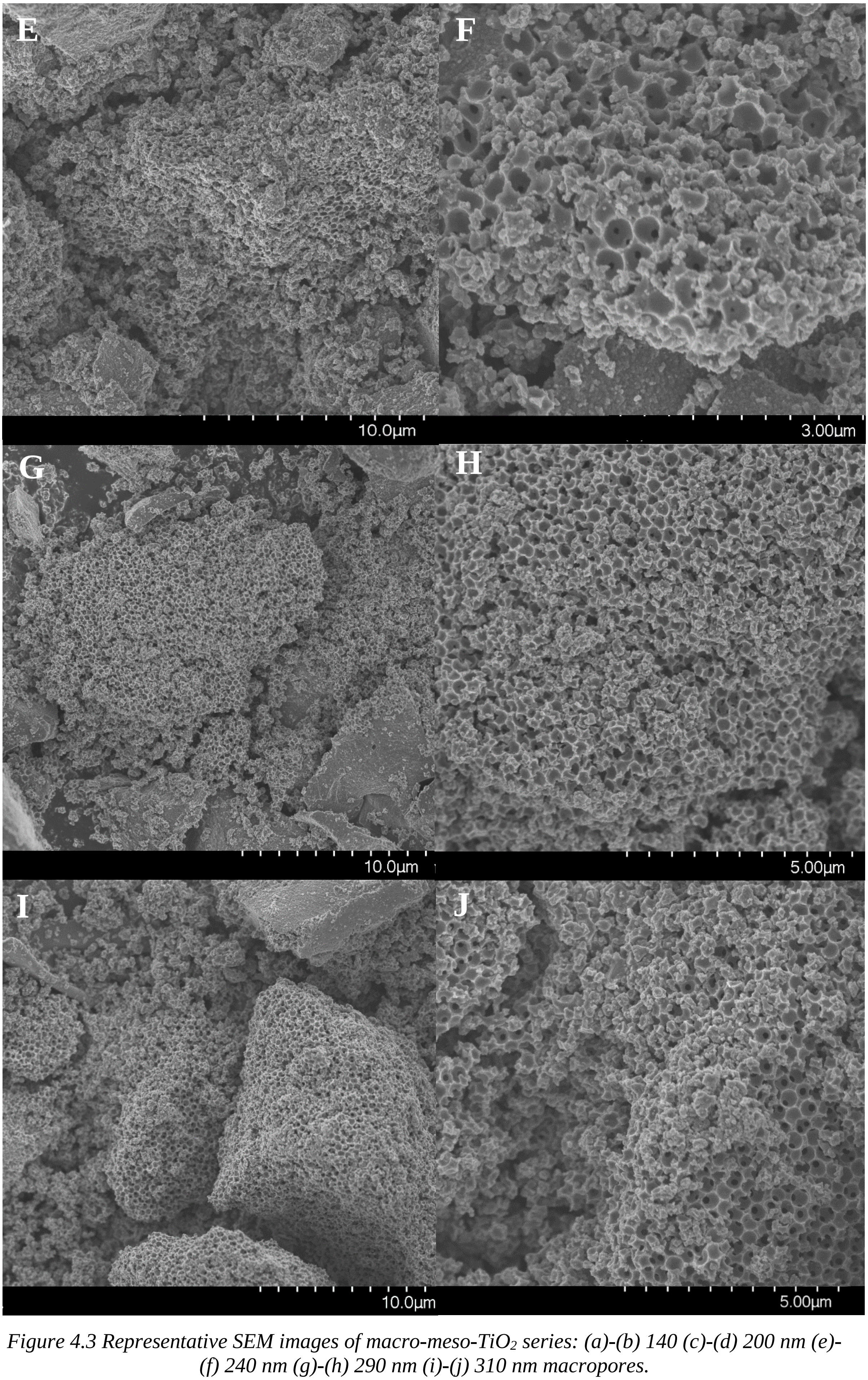

Figure 4.3 Representative SEM images of macro-meso-TiO$_2$ series: (a)-(b) 140 (c)-(d) 200 nm (e)-(f) 240 nm (g)-(h) 290 nm (i)-(j) 310 nm macropores.

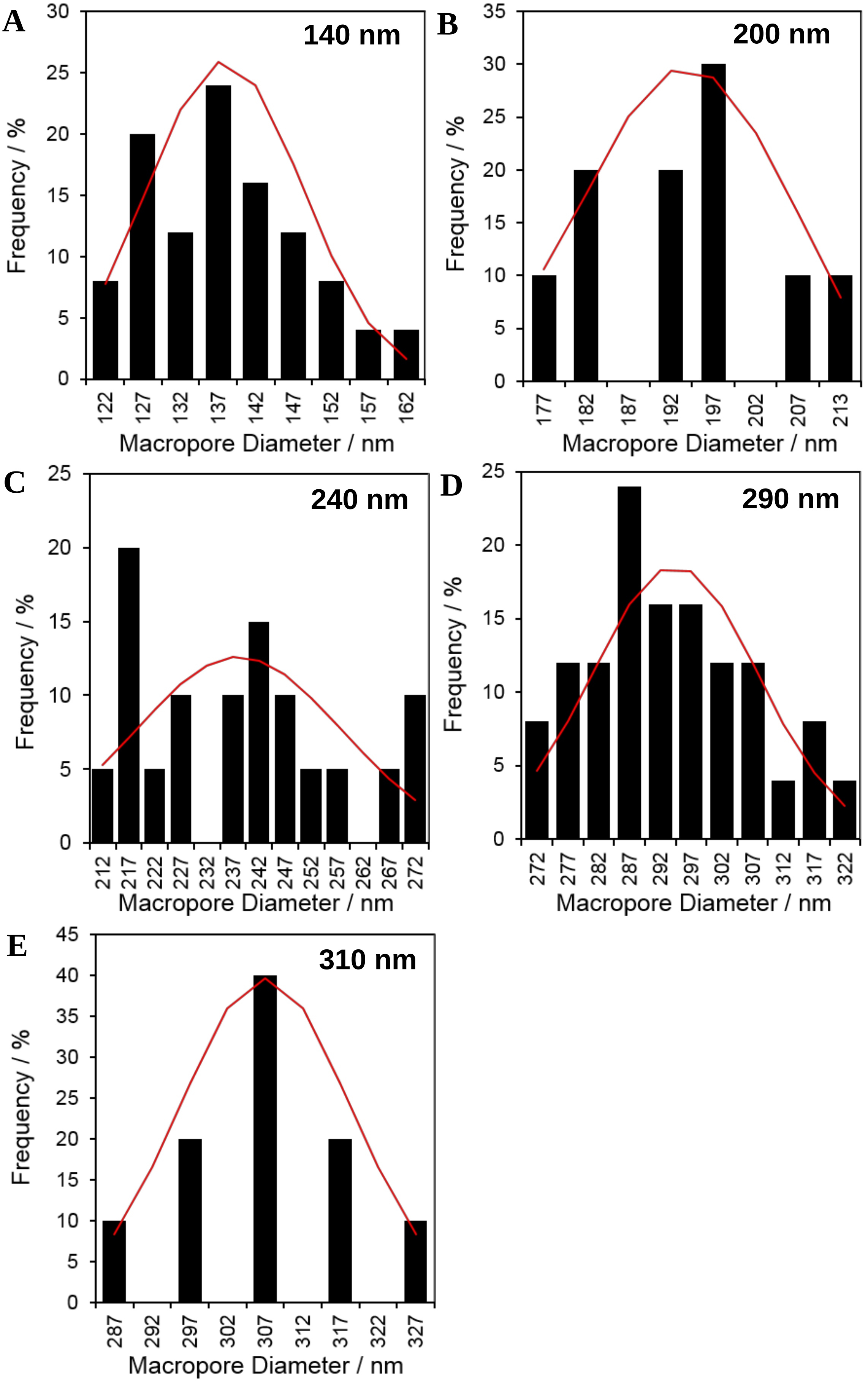

Figure 4.4 Macropores size distribution from SEM images (a) 140 nm (b) 200 nm (c) 240 nm (d) 290 nm (e) 310 nm of macro-meso-TiO_2 series.

4.1.3 Nitrogen porosimetry

N_2 porosimetry was used to assess mesopore framework properties within hierarchical macro-meso-TiO_2. N_2 adsorption/desorption isotherms (**Figure 4.5 (a)**) of mesopores within TiO_2 samples of different macropore sizes. The sizes ranging from 140 to 310 nm display Type IV isotherms with H2 type hysteresis loop as a consequence of differing capillary condensation and evaporation within mesopores during adsorption and desorption respectively. The hysteresis indicates either restricted pore entrance (ink bottle shape) or irregular channel structure of mesopore framework. [174]

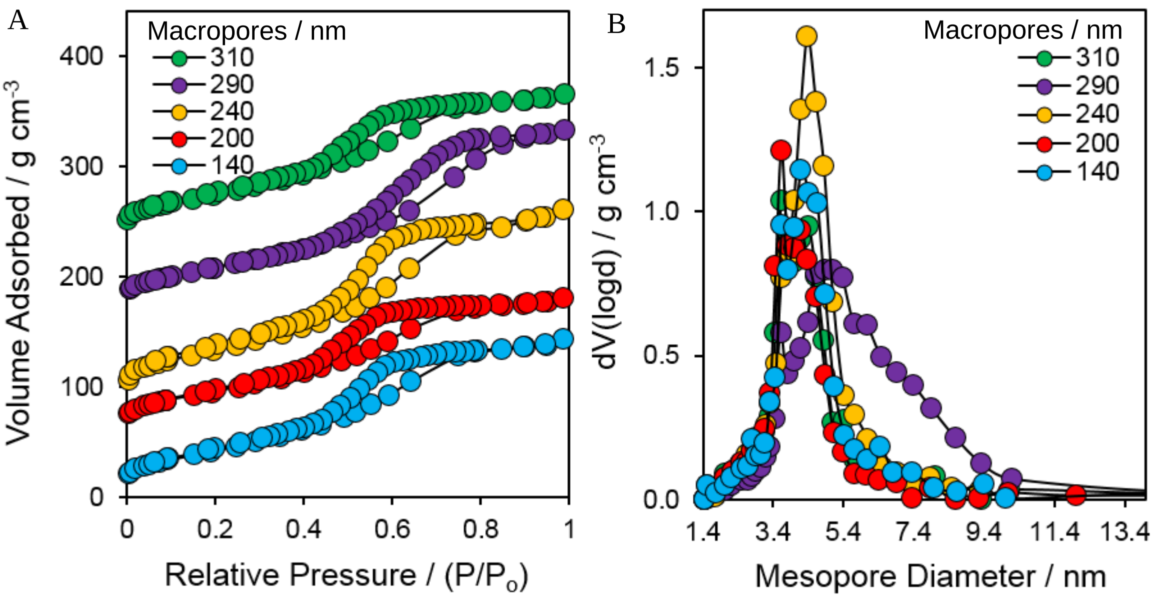

Figure 4.5 (a) Stacked isotherm plot (b) Mesopore size distribution of macro-meso-TiO_2 series with 140-310 nm macropores.

Table 4.2 Summary of N_2 porosimetry results of macro-meso-TiO_2 series with 140-310 nm macropores.

Macropore size / nm	BET / m^2 g^{-1}	Mesopore size / nm	Mesopore volume / g cm^{-3}
140	164 (±16)	4.2 (±0.4)	0.24 (±0.02)
200	155 (±16)	4.2 (±0.4)	0.21 (±0.02)
240	186 (±19)	4.4 (±0.4)	0.29 (±0.03)
290	162 (±16)	4.7 (±0.5)	0.27 (±0.03)
310	156 (±16)	4.4 (±0.4)	0.22 (±0.02)
Average	**165 (±17)**	**4.4 (±0.4)**	**0.25 (±0.03)**
Meso-TiO_2-400	**194 (±19)**	**5.4 (±0.5)**	**0.34 (±0.03)**

The average, 165 $m^2.g^{-1}$, specific surface area (**Table 4.2**) is estimated using BET model and it is only 20 $m^2.g^{-1}$ less than mesoporous equivalent – meso-TiO_2-400, a photocatalyst that has been synthesised using the identical method as macro-meso-TiO_2 series but without macropores. BJH pore size distribution (**Figure 4.5 (b)**) demonstrates a uniform 4 nm mesopore size for macro-meso TiO_2

series which is however 1 nm smaller than the meso-TiO$_2$ counterpart. The decrease in mesopore diameter is observed because during soft-hard templating procedure macropore framework limits how much mesopores can expand since mesopores are formed via surfactant-templating method while solid polystyrene spheres are used to form macropores. Macro-meso-TiO$_2$ series have an average 0.25 g cm^{-3} mesopore volume which is also lower than the meso-TiO$_2$-400 due to smaller mesopore diameter (**Table 4.2**). Incorporation of macropores to meso-TiO$_2$ only marginally affected mesopore framework by reduction of mesopore size.

4.1.4 X-ray diffraction

Wide angle XRD diffractograms (**Figure 4.6**) of macro-meso-TiO$_2$ 140 – 310 nm all displayed identical X-ray patterns with seven well-resolved diffraction peaks indexed (101), (004), (200), (105,211), (204), (116,220), (215) analogues to anatase crystalline phase. Anatase nanocrystallites sizes are estimated using Scherrer formula from the average of FWHM of (101), (200), (215) and are all 7 nm (**Table 4.3**). This value is in a good agreement with meso-TiO$_2$-400 counterpart. Unit cell parameters (**Table 4.3**) of the tetragonal ($a=b\neq c$, $\alpha=\beta=\gamma=90^{\circ}$) anatase crystalline phase is calculated using $d_{(200)}$ lattice spacing and are 3.79 Å for all the macropore sizes. Integration of macroporosity does not affect crystallinity of catalysts. Macro-meso-TiO$_2$ series do not exhibit a peak in the low angle X-ray diffraction contrary to the meso-TiO$_2$ equivalent. The mesopore network is perturbed by interpenetrating spherical macropores which place geometric constraints on the hexagonal configuration of mesostructure.[290] Thus, short-range mesopore order, observed in mesoporous TiO$_2$ equivalent (**3.1.2 X-ray diffraction**), is distorted.

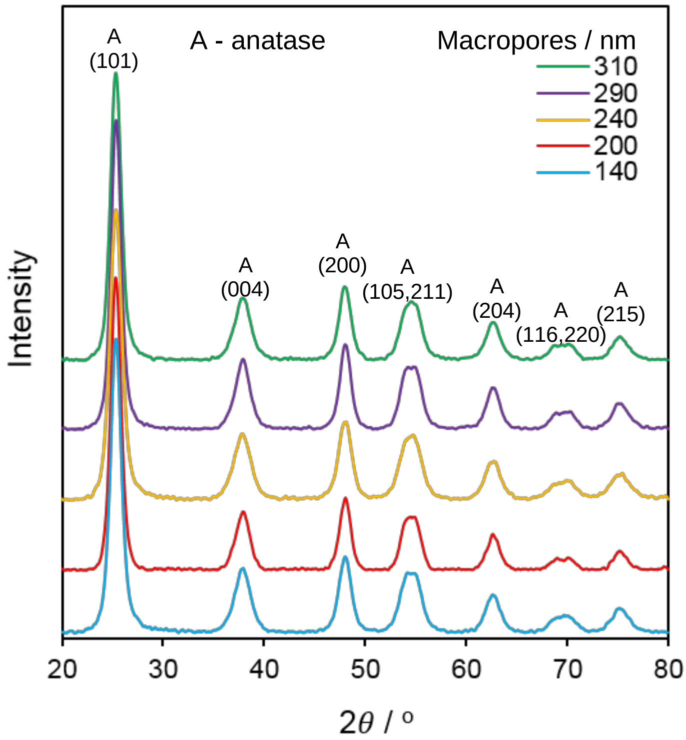

Figure 4.6 Wide angle XRD patterns of macro-meso-TiO$_2$ series with 140-310 nm macropores.

Table 4.3 Summary of XRD results of macro-meso-TiO_2 series with 140-310 nm macropores.

Macropore size / nm	Crystalline phase	Nanocrystallite size / nm	Anatase unit cell a (=b) / Å
140	Anatase	7 (±0.1)	3.79 (±0.04)
200	Anatase	7 (±0.1)	3.79 (±0.04)
240	Anatase	7 (±0.1)	3.79 (±0.04)
290	Anatase	7 (±0.1)	3.79 (±0.04)
310	Anatase	7 (±0.1)	3.79 (±0.04)
Average	**Anatase**	**7 (±0.1)**	**3.79 (±0.04)**
Meso-TiO_2-400	**Anatase**	**7 (±0.1)**	**3.78 (±0.04)**

4.1.5 Temperature programmed oxidation

TPO data of macro-meso-TiO_2 140 – 310 nm is summarised in **Table 4.4** and demonstrate average mass loss of 5.5%. The graph showing the derivative of the mass loss (**Figure 4.7**) displays two desorptions at different temperature ranges. The average 3.5% decrease in mass at temperatures up to 150 °C is assigned to physisorbed atmospheric and crystalline water while 1.9% mass loss from 150 to 400 °C correspond to carbon species. A small amount of carbon being lost up to 300 °C is indicative of the F127 surfactant. TPO results show evidence that removal of polystyrene template was successful. The macro-meso-TiO_2 series demonstrate slightly higher water but smaller carbon losses compared to meso-TiO_2-400 equivalent.

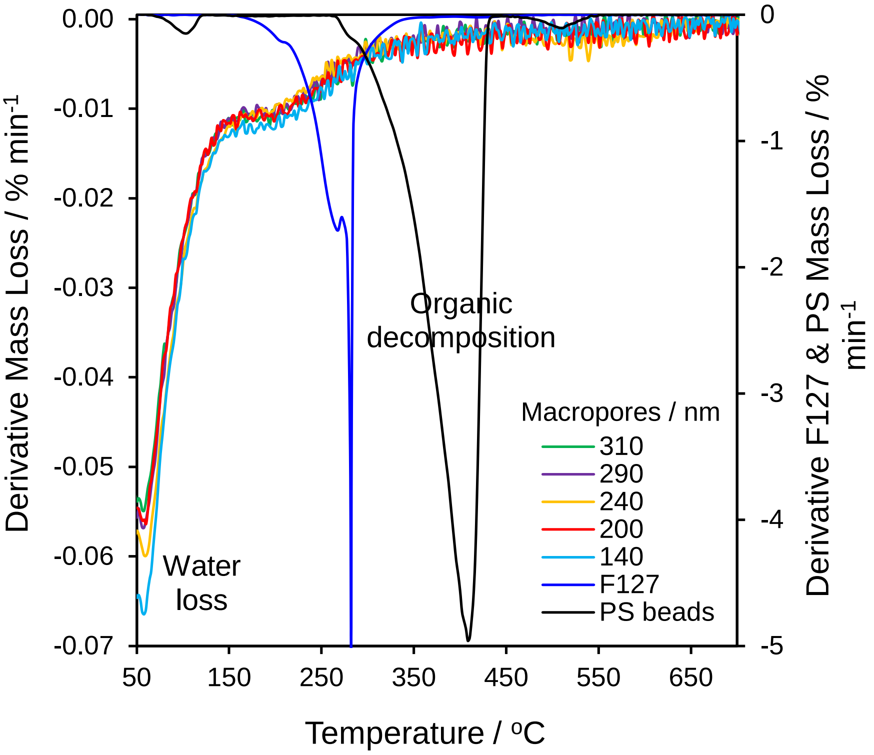

Figure 4.7 TPO derivative mass loss of macro-meso-TiO_2 series with 140-310 nm macropores.

Table 4.4 Summary of TPO results of macro-meso-TiO_2 series with 140-310 nm macropores.

Macropore size / nm	Water (up to 150 ºC) / %	Carbon (150 – 400 ºC) / %	Total mass loss / %
140	3.9 (±0.1)	2.1 (±0.1)	6.0 (±0.2)
200	3.4 (±0.1)	2.1 (±0.1)	5.5 (±0.2)
240	3.7 (±0.1)	2.0 (±0.1)	5.7 (±0.2)
290	3.4 (±0.1)	1.8 (±0.1)	5.2 (±0.2)
310	3.3 (±0.1)	1.9 (±0.1)	5.2 (±0.2)
Average	**3.5 (±0.1)**	**2.0 (±0.1)**	**5.5 (±0.2)**
Meso-TiO_2-400	**3.3 (±0.1)**	**2.7 (±0.1)**	**6.0 (±0.2)**

4.1.6 Diffuse reflectance UV-vis spectrophotometry

The results of solid diffuse reflectance UV-vis optical absorption spectra (**Figure 4.8 (a)**) and Tauc plot (**Figure 4.9**) of macro-meso-TiO_2 series demonstrate a 340 – 418 nm band gap absorption with the average band gap of 3.06 eV. They are in good agreement (within the error margin) with meso-TiO_2-400 counterpart displaying absorption at 340 – 418 nm and 3.07 eV band gap. In some cases, the inverse opal materials such as three-dimensional ordered macroporous TiO_2 exhibit photonic crystal properties, in particular, the presence of the stop bands – a spectral range of extensive reflectance.[291] In theory, titania compounds with ordered uniform 310 nm macropores (based on SEM) display a stopband (increased reflectance) at ~ 572 nm.[279] Unfortunately, the synthesised macro-meso-TiO_2 do not show any peaks of increased reflectivity (stop bands) (**Figure 4.8 (b)**), suggesting that photonic crystal type materials are not formed. No significant change of titania optical properties was observed with the introduction of macropores.

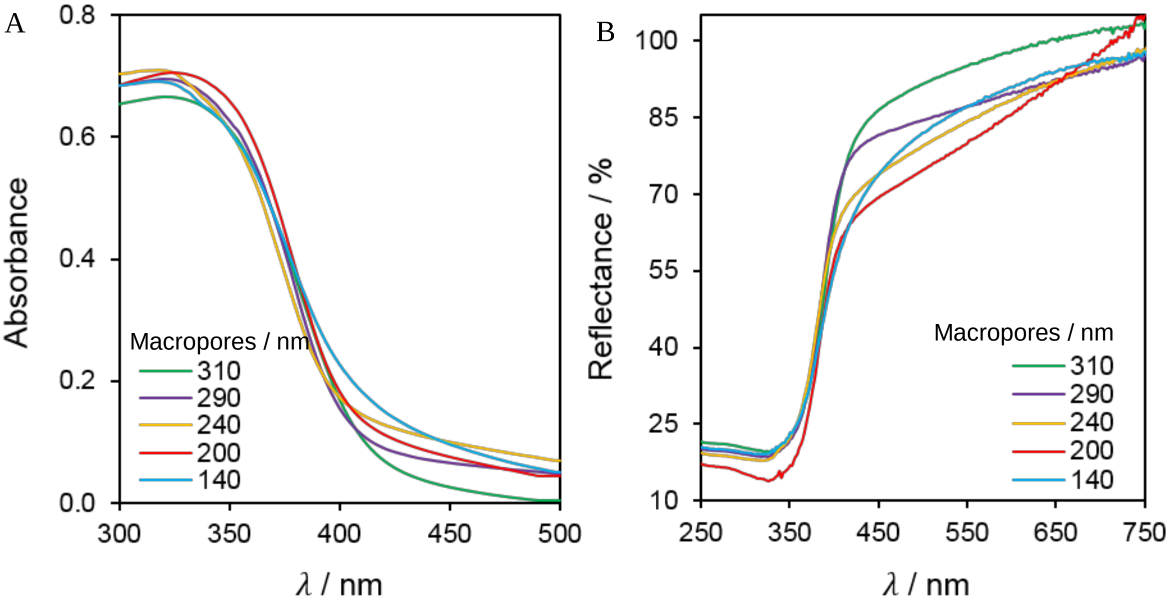

Figure 4.8 (a) UV – vis absorption spectra (b) % Reflectance of macro-meso-TiO_2 series with 140-310 nm macropores.

Macropore size / nm	Band gap / eV
140	3.02 (±0.02)
200	3.06 (±0.02)
240	3.10 (±0.02)
290	3.07 (±0.02)
310	3.03 (±0.02)
Average	**3.06 (±0.02)**
Meso-TiO$_2$-400	**3.07 (±0.02)**

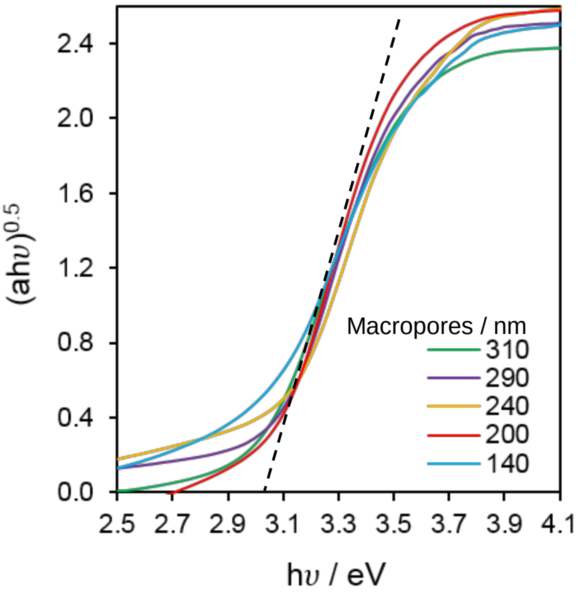

Figure 4.9 Tauc plot and band gap values of macro-meso-TiO$_2$ series with 140-310 nm macropores

.

4.1.7 Summary of the key characteristics of macro-mesoporous titania series

Table 4.5 Summarises the main physicochemical and electronic properties of macro-meso-TiO_2 series with 140-310 nm macropores and compares with mesoporous TiO_2 400 °C counterpart.

Macropore diameter / nm	**BET / $m^2.g^{-1}$ (a)**	**Mesopore size / nm (b)**	**Mesopore volume / $g.cm^{-3}$ (b)**	**TiO_2 Phase (XRD)**	**Nanocrystallite size / nm(c)**	**Band Gap / eV (d)**	**Total mass loss (H_2O) / % (e)**
140	164 (±16)	4.2 (±0.4)	0.24 (±0.02)	Anatase	7 (±0.1)	3.02 (±0.02)	6.0 (±0.2)
200	155 (±16)	4.2 (±0.4)	0.21 (±0.02)	Anatase	7 (±0.1)	3.06 (±0.02)	5.5 (±0.2)
240	186 (±19)	4.4 (±0.4)	0.29 (±0.03)	Anatase	7 (±0.1)	3.10 (±0.02)	5.7 (±0.2)
290	162 (±16)	4.7 (±0.5)	0.27 (±0.03)	Anatase	7 (±0.1)	3.07 (±0.02)	5.2 (±0.2)
310	156 (±16)	4.4 (±0.4)	0.22 (±0.02)	Anatase	7 (±0.1)	3.03 (±0.02)	5.2 (±0.2)
Average	**165 (±17)**	**4.4 (±0.4)**	**0.25 (±0.03)**	**Anatase**	**7 (±0.1)**	**3.06 (±0.02)**	**5.6 (±0.2)**
Meso-TiO_2-400	**194 (±19)**	**5.4 (±0.5)**	**0.34 (±0.03)**	**Anatase**	**7 (±0.1)**	**3.07 (±0.02)**	**6.0 (±0.2)**

[a] SEM; [b] N_2 BET; [c] from BJH desorption isotherm; [d] mean particle diameter from XRD via Scherrer analysis; [e] DRUVS; [f] TPO;

4.2 Photocatalytic performance of macro-mesoporous titania series

Photocatalytic activity of macro-meso-TiO_2 series characterised above was examined using the photocatalytic decomposition of Methyl Orange and H_2 production via water splitting reaction under UV-vis light irradiation. The key interest is the effect of macroporosity and macropore diameter on the activity of the catalysts. Produced photocatalysts were compared to the meso-TiO_2-400 counterpart which was synthesised via identical procedure without a hard template.

4.2.1 Methyl Orange decomposition

The initial testing of photocatalytic activity of macro-meso-TiO_2 with macropores from 140 to 310 nm was photodegradation of 20 ppm Methyl Orange (MO) aqueous solution. Prior to illumination catalysts were stirred in the dark for one hour to achieve MO adsorption equilibrium. Macro-meso-TiO_2 catalysts display 3% MO adsorption. The illumination of the dye in the absence of the photocatalyst for 5h showed no photolysis (**Figure 3.17 (a)**). The time profiles of MO degradation in **Figure 4.10** do not show an obvious trend for different macropore size.

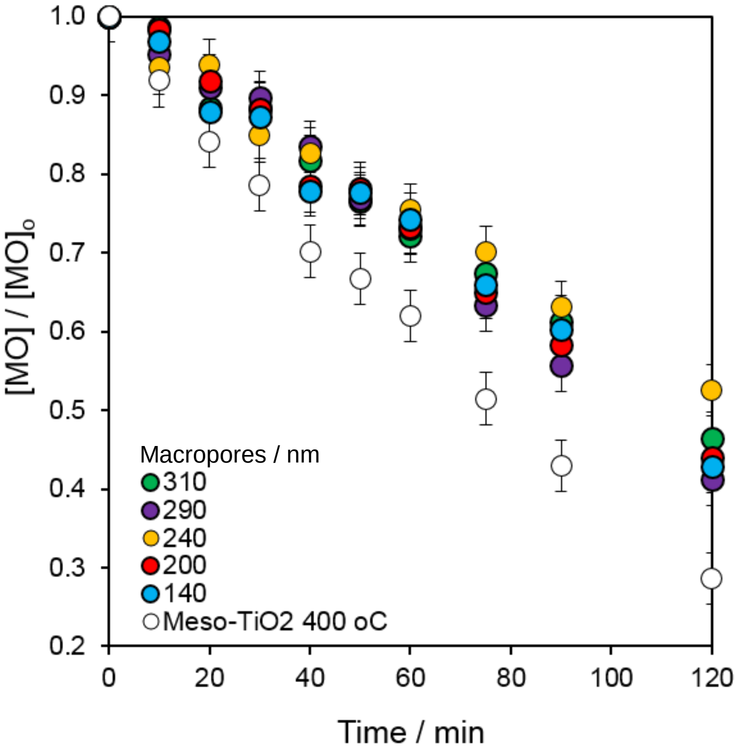

Figure 4.10 Time profiles of the percentage of Methyl Orange degradation by macro-meso-TiO_2 series with 140-310 nm macropores under UV-vis light.

For a more accurate comparison, mass normalised initial rates (**Figure 4.11**) were calculated and they showed uniform activity despite the change in the macropore size. The lack of dependence of activity to macropore diameter is maybe due to the relatively slow decomposition rate (in comparison to Cu or Pt promoted series) and diffusion within the macropores is not busy and limited. In addition, macro-meso-TiO_2 series was slightly less active than the meso-TiO_2-400 equivalent. It is important to note, that addition of the macroporosity to macro-meso-TiO_2 series did not significantly reduce or increase the overall surface area. Results of the initial rates are unexpected, because MO molecule is approx. 2.6 nm and in the previous chapter (**3.2.1 Methyl Orange decomposition**) it was identified that framework diffusion is a limiting factor. The introduction of macroporosity should assist accessibility to mesopores and resolve the diffusion constraint. The surprising outcome can be explained by a decrease in mesopore size from 5.4 nm in meso-TiO_2-400 counterpart to the average 4.4 nm in macro-meso-TiO_2 series (**4.1.3 Nitrogen porosimetry**). Despite macropores providing better access to reach mesopore framework, Methyl Orange molecules have restricted entrance to the actual mesopores, where the majority of the catalyst surface is. More detailed dependence of the activity on mesopore diameter was discussed in detail in **3.2 Photocatalytic performance of mesoporous titania series** paragraph. In pure macro-meso-TiO_2 series, the relationship between mesopore size and access to the mesopores is the key factor influencing the activity, not the overall framework diffusion.

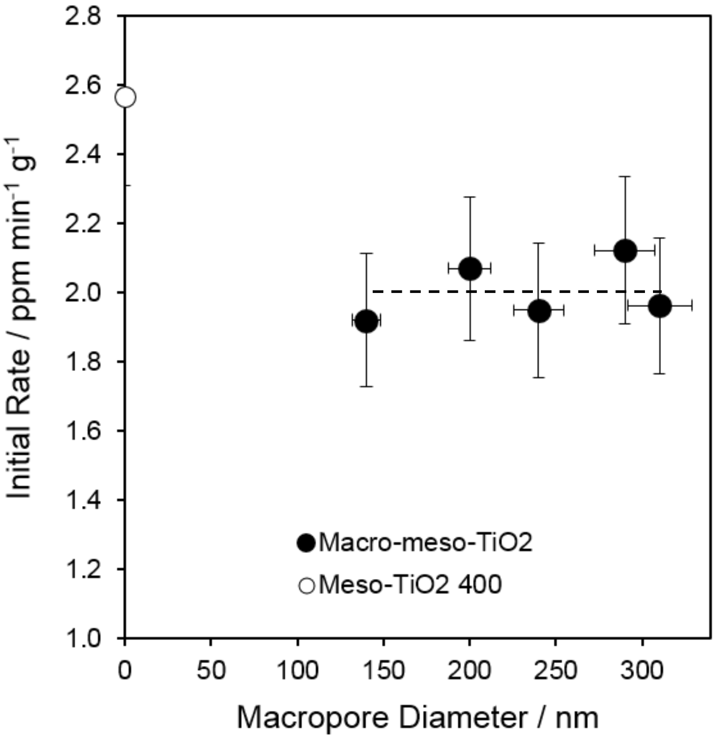

Figure 4.11 Initial rates of macro-meso-TiO_2 series with 140-310 nm macropores together with meso-TiO_2-400 equivalent under UV-vis irradiation.

The addition of macropores to the meso-TiO_2 structure can have a dual effect – influence on the framework diffusion, discussed above, and/or improved light absorption by the formation of the photonic crystal. Despite the absence of photonic crystal properties from DRUVS measurements (**4.1.6 Diffuse reflectance UV-vis spectrophotometry**), Methyl Orange degradation tests were also performed using monochromatic 365 nm light source, while previously full UV-vis spectrum was used. **Figure 4.12** and **Figure 4.13** demonstrate that despite the macropore size ranging from 140 to 310 nm (SEM), the activity was the same for all macropore diameters under monochromatic 365 nm light. Furthermore, it was twice smaller than the one under UV-vis irradiation. If the material forms a photonic crystal, depending on the macropore size, a certain irradiation wavelength would enhance the activity. The wavelength approximately should be twice the size of the macropore. Unfortunately, this phenomenon was not observed. However, the results are in a good agreement with diffuse reflectance UV-vis spectrophotometry (DRUVS) data.

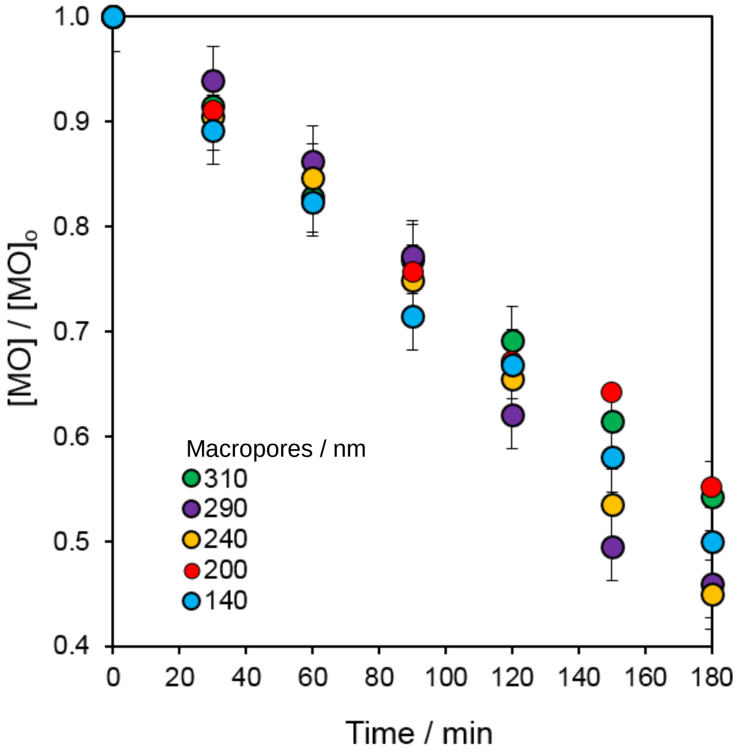

Figure 4.12 Time profiles of the percentage of Methyl Orange degradation by macro-meso-TiO$_2$ series with 140-310 nm macropores under monochromatic 365 nm light.

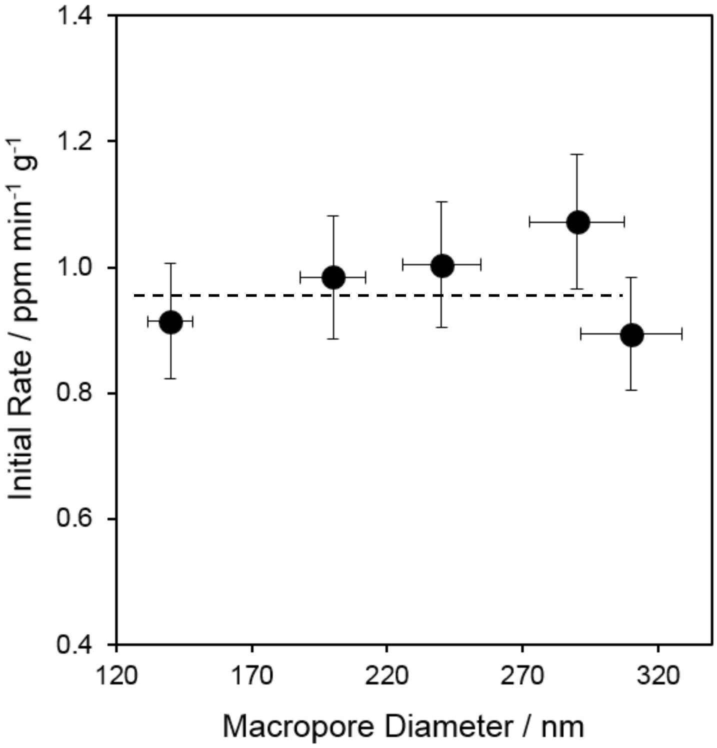

Figure 4.13 Initial rates of MO degradation under monochromatic 365 nm light by macro-meso-TiO$_2$ series with 140-310 nm macropores.

4.2.2 Water splitting

Photocatalytic activity in H_2 production via water splitting under UV-vis irradiation of macro-meso-TiO_2 series with macropores from 140 to 310 nm is presented in **Figure 4.14**. The rates of hydrogen production were the same regardless the variation in macropore size and were twice more active than the meso-TiO_2-400 counterpart. It is important to note, that addition of the macroporosity to macro-meso-TiO_2 series did not significantly reduce or increase the overall surface area. It is unsurprising that the rate is independent of macropore diameter because water diffusion cannot be a rate-limiting factor in a reactor full of water. Moreover, the previous investigation revealed the negligible impact of mesopore diameter on water splitting reaction (**3.2.2 Water splitting**). It is puzzling, how the incorporation of the macropores greatly improved the photoactivity. Based on DRUVS results (**4.1.6 Diffuse reflectance UV-vis spectrophotometry**) and MO photocatalytic tests under monochromatic 365 nm wavelength (**4.2.1 Methyl Orange decomposition**), it was established that addition of the macroporosity did not affect the optical properties of the catalysts. Even though, in theory, the reaction takes place on the all surface (external and mesopores), maybe in the water splitting case, more of the reactions occur on the external surface, which increases when the macropores are incorporated. The results showed that 140 nm macropores are sufficient.

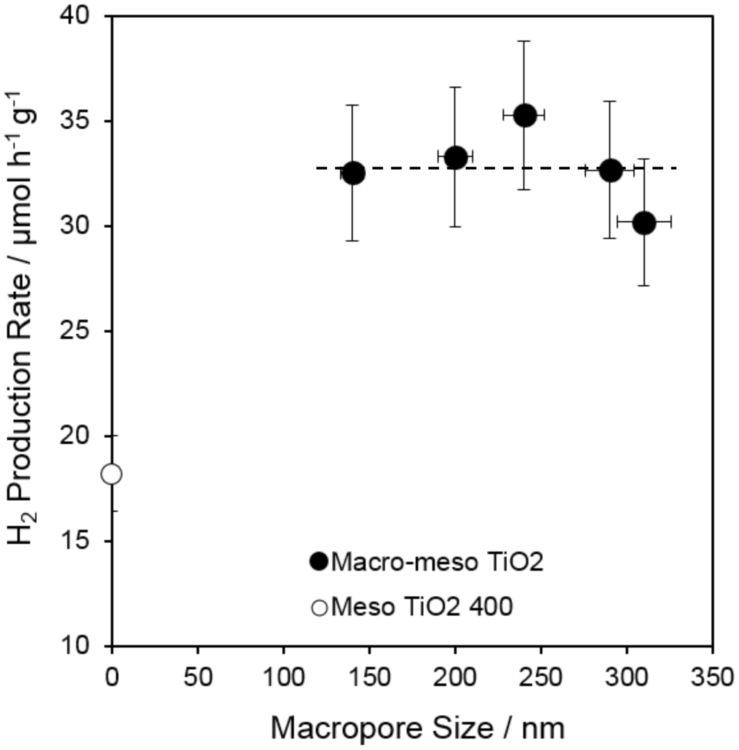

Figure 4.14 H_2 production rates of macro-meso-TiO_2 series with 140-310 nm macropores under UV-vis light.

4.3 Characterisation of 0.1 wt% Cu promoted macro-mesoporous titania series

Macro-meso-TiO_2 series with different macropore sizes from 140 to 310 nm discussed in **4.1 Characterisation of macro-mesoporous titania series** were deposited with 0.1 wt% Cu by classic wet impregnation method using $Cu(NO_3)_2.3H_2O$ as a precursor. The 0.1wt% has been chosen as the most active Cu loading from the photocatalytic activity evaluated in **3.5 Photocatalytic performance of Cu promoted mesoporous titania series.** The recently synthesised photocatalysts have been characterised to determine if the characteristics of macro-meso-TiO_2 support have been retained. In addition, the impact of the titania framework to metal deposition and the resulting activity was assessed. Characterisation and photoactivity were compared to 0.1 wt% Cu/meso-TiO_2-400 – an analogous mesoporous material, synthesised via identical method but without the macropores.

4.3.1 Nitrogen porosimetry

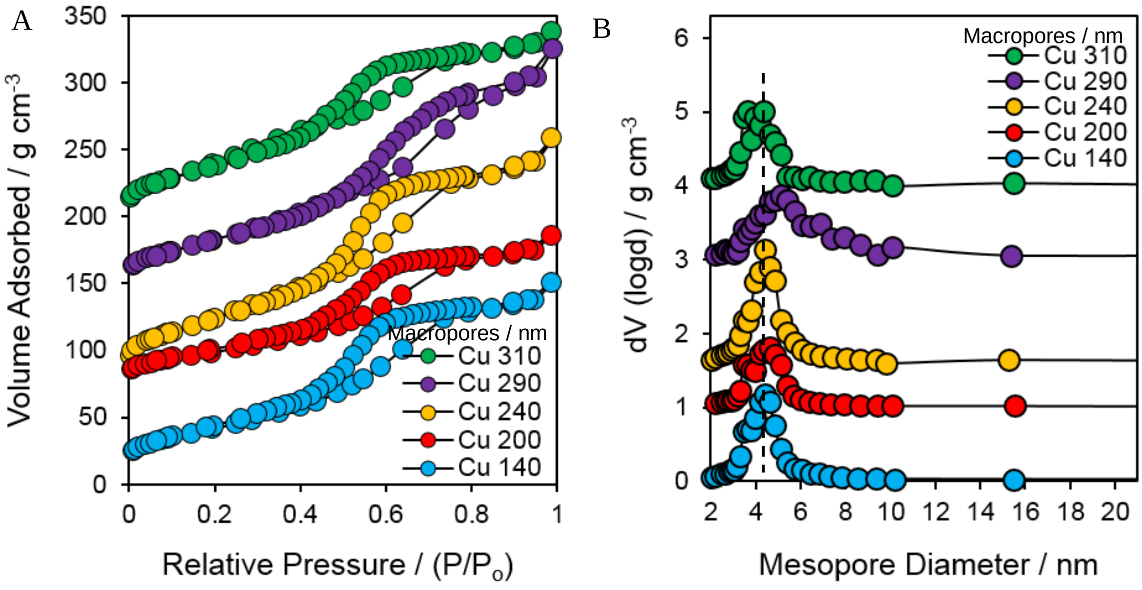

Figure 4.15 (a) Stacked isotherm plot (b) Mesopore size distribution of 0.1 wt% Cu/macro-meso-TiO_2 with 140-310 nm macropores.

N_2 porosimetry was employed to evaluate retention of mesopore framework of macro-meso-TiO_2 140 – 310 nm support after deposition with Cu. N_2 adsorption/desorption curves (**Figure 4.15 (a)**) of Cu promoted catalysts display identical isotherms to those of macro-meso-TiO_2 supports and 0.1 wt% Cu/meso-TiO_2: type IV isotherms with H2 type hysteresis loop indicating either restricted pore entrance (ink bottle shape) or irregular channel structure of mesopore framework.[174] Specific surface area (BET), mesopore volume and mesopore size (BJH, Barrett-Joyner-Halenda) of 0.1 wt% Cu/macro-meso-TiO_2 are summarised in **Table 4.6** and compared to unpromoted macro-meso-TiO_2 series and Cu/meso-TiO_2-400 equivalent. Cu promoted macro-meso-TiO_2 showed average 175 m^2.g^{-1} surface area, 4.4 nm mesopores and 0.26 g.cm^{-3} mesopore volume demonstrating that the supports retained their qualities after Cu impregnation process. In comparison with 0.1 wt%, Cu/meso-TiO_2 counterpart, pore diameter (**Figure 4.15 (b)**) and thus pore volume are slightly lower.

Table 4.6 Summary of N_2 porosimetry results of 0.1 wt% Cu/macro-meso-TiO_2 series. On the right-hand side, the corresponding values of the macro-meso-TiO_2 support before Cu promotion. At the bottom of the table values for Cu promoted and unpromoted meso-TiO_2 equivalents are presented.

	0.1 wt% Cu promoted macro-meso-TiO_2			macro-meso-TiO_2 support		
Macropore size / nm	BET / m^2 g^{-1}	Mesopore size / nm	Mesopore volume / g cm^{-3}	BET / m^2 g^{-1}	Mesopore size / nm	Mesopore volume / g cm^{-3}
Cu 140	155 (±16)	4.4 (±0.4)	0.25 (±0.03)	164 (±16)	4.2 (±0.4)	0.24 (±0.02)
Cu 200	154 (±15)	4.4 (±0.4)	0.20 (±0.02)	155 (±16)	4.2 (±0.4)	0.21 (±0.02)
Cu 240	189 (±19)	4.1 (±0.4)	0.25 (±0.03)	186 (±19)	4.4 (±0.4)	0.29 (±0.03)
Cu 290	210 (±21)	4.4 (±0.4)	0.31 (±0.03)	162 (±16)	4.7 (±0.5)	0.27 (±0.03)
Cu 310	168 (±17)	5.1 (±0.5)	0.31 (±0.03)	156 (±16)	4.4 (±0.4)	0.22 (±0.02)
Average	**175 (±18)**	**4.4 (±0.4)**	**0.26 (±0.03)**	**165 (±17)**	**4.4 (±0.4)**	**0.25 (±0.03)**
Cu meso TiO_2 400 °C and meso TiO_2 400 °C	**167 (±17)**	**5.1 (±0.5)**	**0.32 (±0.03)**	**194 (±19)**	**5.4 (±0.5)**	**0.34 (±0.03)**

4.3.2 X-ray diffraction

Wide angle XRD diffraction patterns (**Figure 4.16**) of 0.1 wt% Cu/macro-meso-TiO_2 with macropores ranging from 140 to 310 nm exhibit seven well-resolved diffraction peaks indexed (101), (004), (200), (105,211), (204), (116,220), (215) corresponding to solely anatase crystalline phase. The average sized 7 nm anatase nanocrystallites are estimated using Scherrer formula (**Table 4.7**). There is no major change in the unit cell parameters. The Cu impregnated macro-meso-TiO_2 series results are exactly the same as the parent support, therefore, impregnation with Cu does not affect crystallinity of the macro-meso-TiO_2. Moreover, 0.1 wt% Cu/macro-meso-TiO_2 data matches with the Cu promoted and unpromoted meso-TiO_2 counterparts. Despite the support, at 0.1 wt% Cu loadings Cu peaks are not present due to atomically dispersed Cu species (**4.3.4 X-ray absorption spectroscopy**).

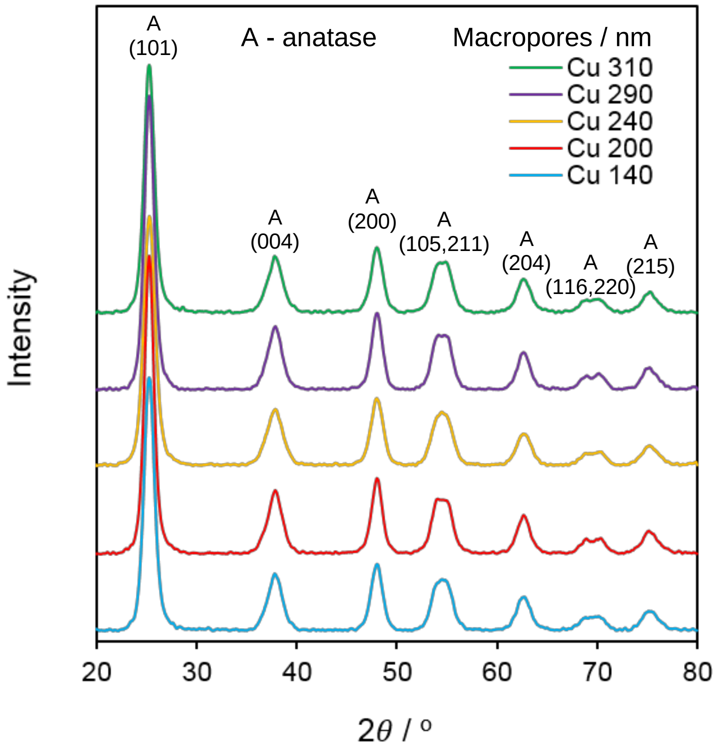

Figure 4.16 Wide angle XRD patterns of 0.1 wt% Cu/macro-meso-TiO_2 series.

Table 4.7 Summary of XRD results of 0.1 wt% Cu macro-meso-TiO_2 series with 140-310 nm macropores.

	0.1 wt% Cu promoted macro-meso TiO_2			macro-meso TiO_2 support		
Macropore size / nm	Crystalline phase	Crystallite size / nm	Anatase unit cell a (=b) / Å	Crystalline phase	Crystallite size / nm	Anatase unit cell a (=b) / Å
Cu 140	Anatase	7 (±0.1)	3.78 (±0.04)	Anatase	7 (±0.1)	3.79 (±0.04)
Cu 200	Anatase	7 (±0.1)	3.78 (±0.04)	Anatase	7 (±0.1)	3.79 (±0.04)
Cu 240	Anatase	7 (±0.1)	3.78 (±0.04)	Anatase	7 (±0.1)	3.79 (±0.04)
Cu 290	Anatase	7 (±0.1)	3.78 (±0.04)	Anatase	7 (±0.1)	3.79 (±0.04)
Cu 310	Anatase	7 (±0.1)	3.78 (±0.04)	Anatase	7 (±0.1)	3.79 (±0.04)
Average	**Anatase**	**7 (±0.1)**	**3.78 (±0.04)**	**Anatase**	**7 (±0.1)**	**3.79 (±0.04)**
Cu/meso-TiO_2-400 and meso-TiO_2-400	**Anatase**	**7 (±0.1)**	**3.78 (±0.04)**	**Anatase**	**7 (±0.1)**	**3.78 (±0.04)**

4.3.3 Inductively coupled plasma optical emission spectrometry

Cu promoted macro-meso TiO_2 loadings (**Table 4.8**) are equivalent to the 0.1 wt% Cu/meso-TiO_2-400 counterpart. Moreover, it closely matches the desired 0.11 wt% (**3.5 Photocatalytic performance of Cu promoted mesoporous titania series**) and can be rounded to 0.1 wt%.

Table 4.8 ICP – OES determined Cu loadings of 0.1 wt% Cu macro-meso-TiO_2 series with 140-310 nm macropores.

Macropore size / nm	Cu loading / wt%
Cu 140	0.15 (±0.005)
Cu 200	0.13 (±0.004)
Cu 240	0.13 (±0.004)
Cu 290	0.13 (±0.004)
Cu 310	0.15 (±0.005)
Average	**0.14 (±0.004)**
0.1 wt% Cu/meso-TiO_2-400	**0.13 (±0.004)**

4.3.4 X-ray absorption spectroscopy

3.3.4 X-ray absorption spectroscopy section discusses in detail the importance of identifying copper oxidation state and chemical environment which has a direct impact on activity within Cu promoted titania materials (**3.5 Photocatalytic performance of Cu promoted mesoporous titania series**). However, the ultra-low 0.1 wt% Cu loading was invisible in laboratory X-ray sources thus Cu species was probed by Cu K-edge X-ray absorption spectroscopy (XAS -synchrotron beam source).

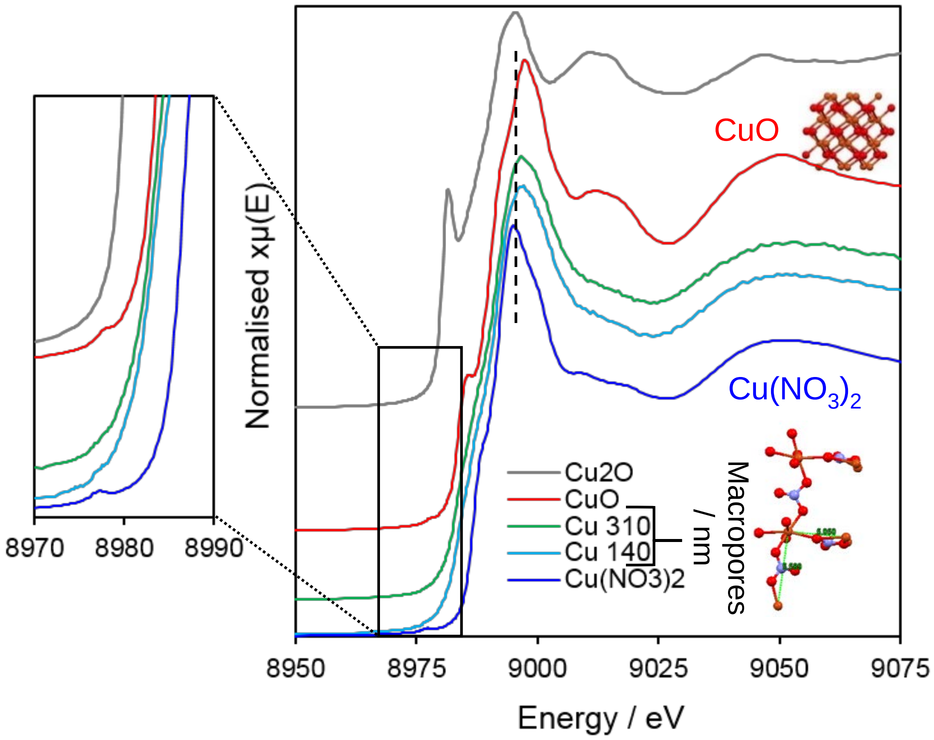

Figure 4.17 XAS spectrum of 0.1 wt% Cu macro-meso-TiO_2 series with 140-310 nm macropores and reference Cu_2O, CuO and $Cu(NO_3)_2$.

Background subtracted, normalised XANES spectra of the 0.1 wt% Cu/macro-meso-TiO_2 series and Cu_2O, CuO and $Cu(NO_3)_2$ references are shown in **Figure 4.17**. From the previous results (**3.3.4 X-ray absorption spectroscopy and 3.4.4 X-ray absorption spectroscopy)** it is evident that Cu loading and TiO_2 support changes copper oxidation state and its local environment. The spectra of 0.1 wt% Cu/macro-meso-TiO_2 with 140 and 310 nm macropore diameter display a strong rising-edge feature around 8986 eV and an intense white line around 8996; these are attributed to $1s \rightarrow 4p_z$ (or 4px,ypz for Cu(I) species) and 1s→4p (continuum) transitions respectively. In this case, the local environment of Cu species strongly resembles Cu(II) nitrate trihydrate complex rather than bulk CuO indicating isolated Cu species. Least squares spectral fitting to Cu, Cu_2O, CuO and $Cu(NO_3)_2$ references identified only Cu(II) oxidation state in all Cu/macro-meso-TiO_2 samples with uniform fit to a mononuclear copper and CuO mixture (**Figure 4.18**). Nonetheless, it uncovers that these samples do not display the pre-edge feature characteristic of Cu(II). Therefore, the majority of copper species (73% for 140 nm and 78% for 310 nm samples) is electronically alike Cu(I) but structurally resemble mononuclear complexes where single copper atoms are dispersed over titania. Ultra-low copper concentration was introduced by post-modification (wet-impregnation) of macro-meso-TiO_2, which involves a relatively low calcination temperature, moreover, samples demonstrate constant band gap, anatase lattice parameter and crystal size which supports the hypothesis. Despite the variation in macropore diameter Cu species deposited on macro-meso-TiO_2 support remained the same.

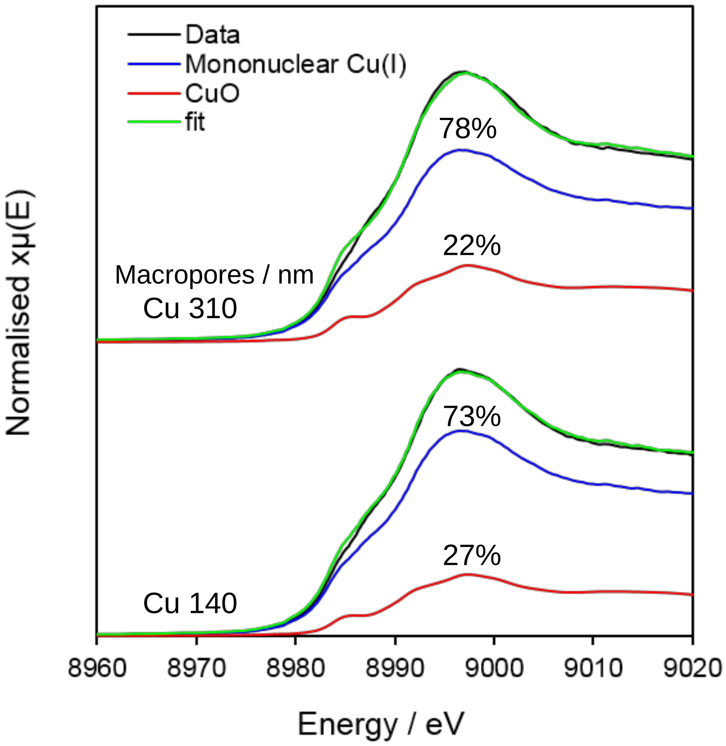

Figure 4.18 XANES region fitting and % of mononuclear Cu (I) species and CuO of mesoporous TiO_2 exhibiting 140 and 310 nm macropore size.

4.3.5 Diffuse reflectance UV-vis spectrophotometry

Recorded solid diffuse reflectance UV-vis optical absorption spectra (**Figure 4.19 (a)**) and Tauc plot (**Figure 4.19 (b)**) of 0.1 wt% Cu/macro-meso-TiO_2 show 340 – 418 nm region of the band gap absorption with the average band gap of 3.06 eV, which are identical to macro-meso-TiO_2 support materials (**Table 4.9**). Moreover, values are in a good agreement (within the error margin) with 0.1 wt% Cu/meso-TiO_2-400 counterpart featuring 3.1 eV band gap. DRUVS results confirm that deposition of 0.1 wt% Cu does not influence light absorption and the resulting band gaps of the Cu/macro-meso-TiO_2 catalysts.

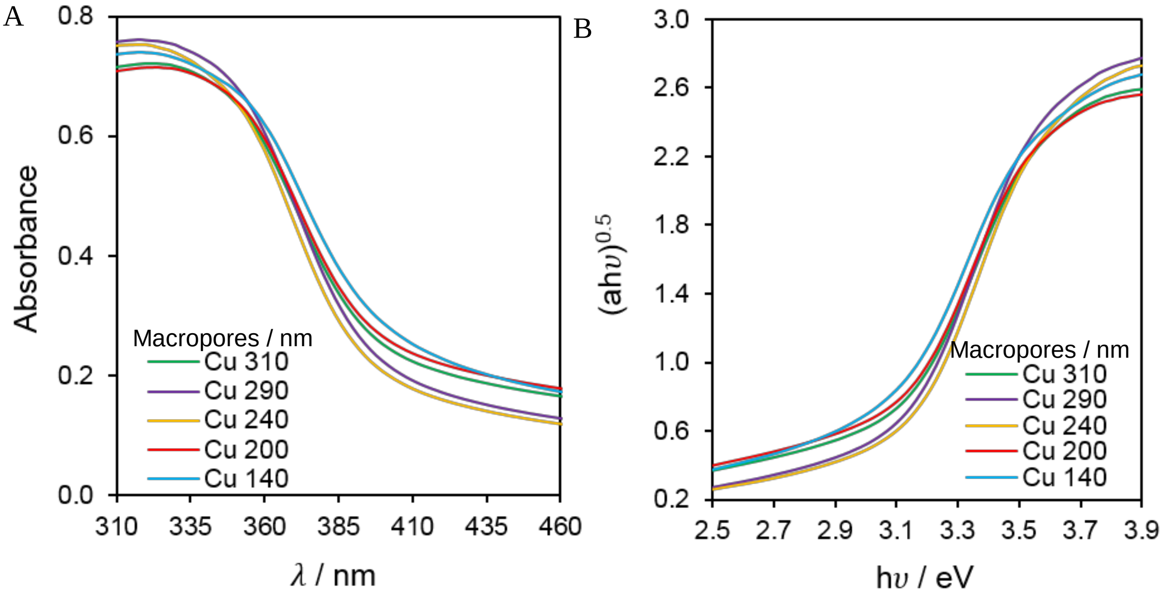

Figure 4.19 (a) UV – vis absorption spectra and (b) Tauc plot of 0.1 wt% Cu macro-meso-TiO_2 series with 140-310 nm macropores.

Table 4.9 Summary of the band gap values of 0.1 wt% Cu macro-meso-TiO_2 series with 140-310 nm macropores.

	0.1 wt% Cu promoted macro-meso TiO_2	macro-meso TiO_2 supports
Macropore size / nm	Band Gap / eV	Band Gap / eV
Cu 140	3.01 (±0.02)	3.02 (±0.02)
Cu 200	3.05 (±0.02)	3.06 (±0.02)
Cu 240	3.10 (±0.02)	3.10 (±0.02)
Cu 290	3.07 (±0.02)	3.07 (±0.02)
Cu 310	3.05 (±0.02)	3.03 (±0.02)
Average	**3.06 (±0.02)**	**3.06 (±0.02)**
0.1 wt% Cu/meso-TiO_2-400 and meso-TiO_2-400	**3.10 (±0.02)**	**3.07 (±0.02)**

4.3.6 Summary of the key characteristics of 0.1 wt% Cu promoted macro-mesoporous titania series

Table 4.10 Summarises the main physicochemical and electronic properties of the 0.1 wt% Cu/macro-meso-TiO$_2$ *series with 140-310 nm macropores and compares with 0.1 wt% Cu/meso-TiO*$_2$*-400 counterpart.*

Samples	**Cu loading / wt%**$^{(a)}$	**Mononuclear Cu (I) / %**	**CuO / %**	**BET / m**^{2}**.g**$^{-1(b)}$	**Mesopore size / nm**$^{(c)}$	**Mesopore volume / g.cm**$^{-3(c)}$	**TiO**$_2$ **Phase (XRD)**	**Nanocrystallite size / nm**$^{(d)}$	**Band Gap / eV**$^{(e)}$
Cu 140	0.15 (±0.005)	73.0 (±0.1)	27.0 (±0.1)	155 (±16)	4.4 (±0.4)	0.25 (±0.03)	Anatase	7 (±0.1)	3.01 (±0.02)
Cu 200	0.13 (±0.004)	-	-	154 (±15)	4.4 (±0.4)	0.20 (±0.02)	Anatase	7 (±0.1)	3.05 (±0.02)
Cu 240	0.13 (±0.004)	-	-	189 (±19)	4.1 (±0.4)	0.25 (±0.03)	Anatase	7 (±0.1)	3.10 (±0.02)
Cu 290	0.13 (±0.004)	-	-	210 (±21)	4.4 (±0.4)	0.31 (±0.03)	Anatase	7 (±0.1)	3.07 (±0.02)
Cu 310	0.15 (±0.005)	78.0 (±0.1)	22.0 (±0.1)	168 (±17)	5.1 (±0.5)	0.31 (±0.03)	Anatase	7 (±0.1)	3.05 (±0.02)
Average	**0.14 (±0.004)**	**75.5 (±0.1)**	**24.5 (±0.1)**	**175 (±18)**	**4.4 (±0.4)**	**0.26 (±0.03)**	**Anatase**	**7 (±0.1)**	**3.06 (±0.02)**
Cu/meso-TiO$_2$**-400**	**0.13 (±0.004)**	**-**	**-**	**167 (±17)**	**5.1 (±0.5)**	**0.32 (±0.03)**	**Anatase**	**7 (±0.1)**	**3.10 (±0.02)**

[a]*ICP – OES;* [b]*N*$_2$ *BET;* [c]*from BJH desorption isotherm;* [d]*Mean particle diameter from XRD via Scherrer analysis;* [e]*DRUVS;*

4.4 Photocatalytic performance of 0.1 wt% Cu promoted macro-mesoporous titania series

The catalytic activity of 0.1 wt% Cu promoted macro-meso-TiO_2 with macropores ranging from 140 to 310 nm were studied using the photocatalytic decomposition of Methyl Orange and H_2 production via water splitting under UV-vis light. The impact of copper on the photocatalytic performance of macro-meso-TiO_2 supports is investigated. Moreover, materials are compared to 0.1 wt% Cu/meso-TiO_2-400 counterpart which was synthesised via identical procedure without incorporation of macropores.

4.4.1 Methyl Orange decomposition

The initial way of testing the photocatalytic activity of Cu promoted mesoporous titania is photodegradation of 20 ppm Methyl Orange (MO) aqueous solution (**Figure 4.20**). Prior to the illumination catalysts were stirred in the dark for one hour to achieve adsorption equilibrium and it displays 3% MO adsorption. The illumination of the dye in the absence of the photocatalyst for 2h showed no photolysis.

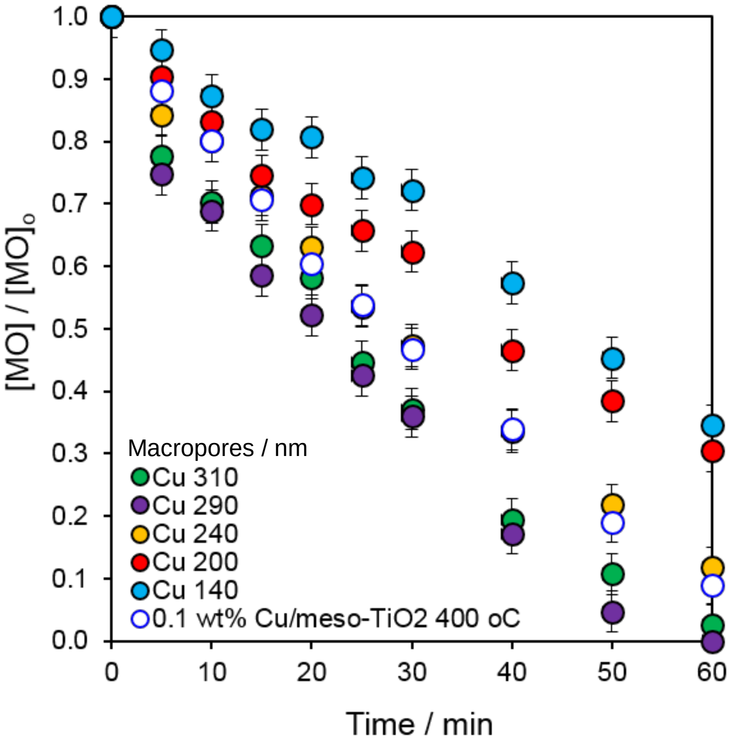

Figure 4.20 Time profiles of Methyl Orange degradation by 0.1 wt% Cu macro-meso-TiO_2 series with 140-310 nm macropores under UV-vis light.

The effect of Cu deposition on the macro-meso-TiO_2 series activity and comparison to the unpromoted supports, together with 0.1wt% Cu/meso-TiO_2-400 equivalent is introduced in **Figure 4.21.** Cu/macro-meso-TiO_2 series possess uniform 0.1 wt% Cu loading and the promoter mononuclear Cu(I) species is on average 76% across all series (**4.3.3 Inductively coupled plasma**

optical emission spectrometry and 4.3.4 X-ray absorption spectroscopy). However, this is 24% less than 0.1 wt% Cu/meso-TiO_2 counterpart, where 100% mononuclear Cu(I) species is observed. Mass normalised initial rates of Cu/macro-meso-TiO_2 were 2-5 times higher than pure the macro-mesoporous titania supports. A significant enhancement of activity upon addition of Cu promoter reflects the effect observed for Cu promoted mesoporous TiO_2 (**3.5.1 Methyl Orange decomposition**). The latter relationship is attributed to the creation of oxygen vacancies upon introducing Cu(I) species into the titania framework; these oxygen vacancies likely capture photoexcited electrons to form F-centres,[254] thereby suppressing charge carrier recombination, prolonging lifetime promoting either direct hole oxidation or indirect hydroxyl oxidation mechanisms (**1.5.1 Methyl Orange decomposition Equation 1.2 A or B-D**).[83]

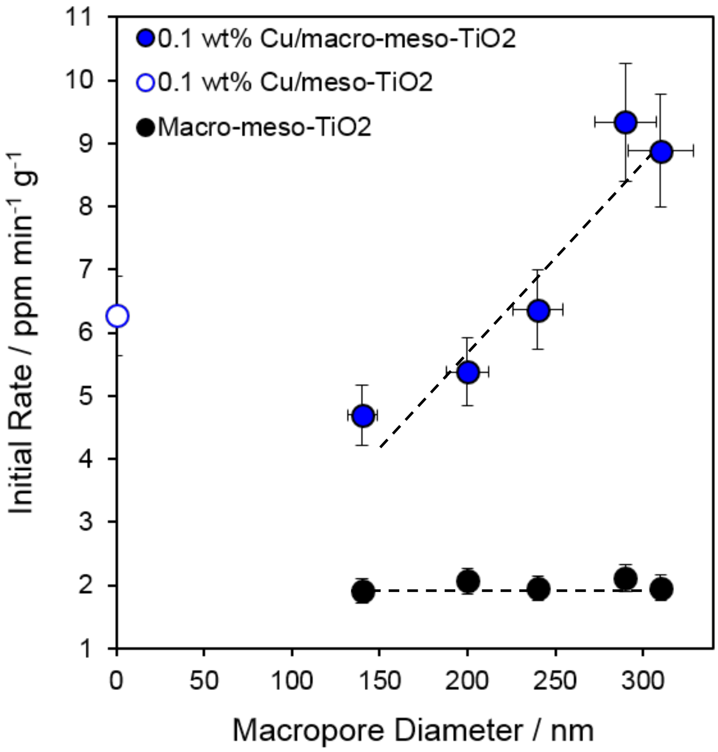

Figure 4.21 Initial rates of 0.1 wt% Cu/macro-meso-TiO_2 series together with Cu/meso-TiO_2-400 equivalent and macro-meso-TiO_2 140 – 310 nm supports under UV-vis irradiation.

The initial rates displayed a linear growth as the macropore diameter increased, starting a little below the 0.1wt% Cu/meso-TiO_2-400 counterpart. It is important to note, that addition of the macroporosity to Cu/macro-meso-TiO_2 series did not significantly reduce or increase the overall surface area. DRUVS results (**4.1.6 Diffuse reflectance UV-vis spectrophotometry**) and MO photocatalytic tests under monochromatic 365 nm wavelength (**4.2.1 Methyl Orange decomposition**) established that addition of the macroporosity did not affect the optical properties of the catalysts. In the activity data of unpromoted macro-meso-TiO_2 series, the effect of macropore diameter was not noticed probably because of the relatively slower reaction (**4.2.1 Methyl Orange decomposition**). However, in this case, the reaction rate was up to five times faster. Increase in the activity with the increase in the macropore diameter could probably arise from significantly improved overall diffusion and accessibility to the photocatalyst surface. The photocatalytic MO decomposition performance of 0.1 wt% Cu/macro-meso-TiO_2 was dominated by overall framework diffusion which improved with larger macropore diameter. Presumably, the activity would be even higher if all Cu species, present on the surface would be 100 % mononuclear Cu(I) (instead of 76 %), like it is on 0.1 wt% Cu/meso-TiO_2-400.

4.4.2 Water splitting

Mass normalised H_2 production rates of 0.1 wt% Cu/macro-meso-TiO_2 series with macropores spanning from 140 to 310 nm with a comparison to the unpromoted supports, together with 0.1wt% Cu/meso-TiO_2-400 equivalent is presented in **Figure 4.22**. Uniform 0.1 wt% Cu loading and the resulting amounts of the promoter mononuclear Cu(I) is on average 76% across all series (**4.3.3 Inductively coupled plasma optical emission spectrometry and 4.3.4 X-ray absorption spectroscopy**). However, this 24% less than 0.1 wt% Cu/meso-TiO_2 counterpart, where 100% mononuclear Cu(I) species is observed. It is also important to note, that addition of the macroporosity to Cu/macro-meso-TiO_2 series did not significantly reduce or increase the overall surface area. Based on DRUVS results (**4.1.6 Diffuse reflectance UV-vis spectrophotometry**) and MO photocatalytic tests under monochromatic 365 nm wavelength (**4.2.1 Methyl Orange decomposition**), it was established that addition of the macroporosity did not affect the optical properties of the catalysts.

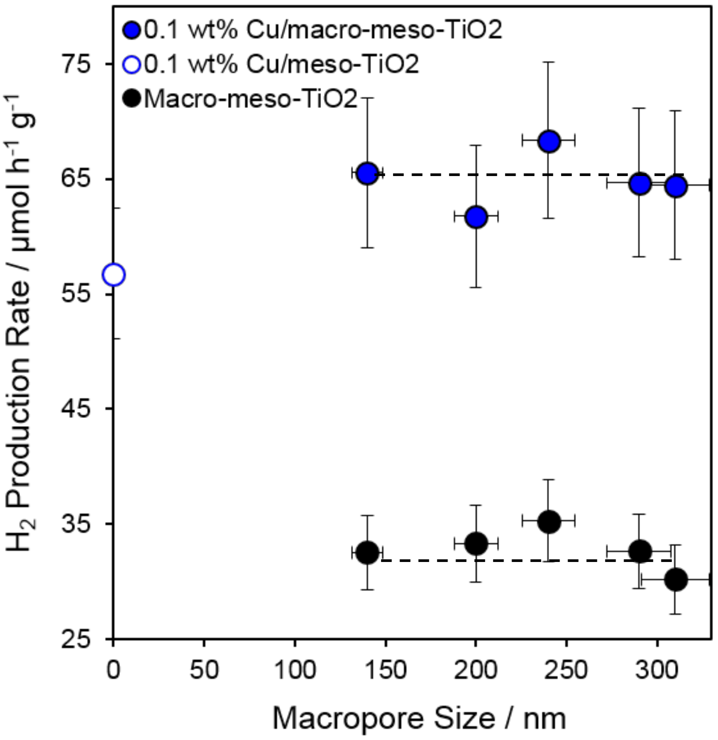

Figure 4.22 H_2 production rates of 0.1 wt% Cu/macro-meso-TiO_2 series in comparison with Cu/meso-TiO_2-400 equivalent and macro-meso-TiO_2 140 – 310 nm supports under UV-vis light.

Photocatalytic activity in H_2 production via water splitting under UV-vis irradiation of Cu/macro-meso-TiO_2 series was twice faster than the bare macro-meso-TiO_2 supports. The activity enhancement upon addition of Cu promoter species was discussed in detail in the previous sections (**3.5 Photocatalytic performance of Cu promoted mesoporous titania series, 4.4.1 Methyl Orange decomposition**). It was identified, that atomically-dispersed Cu(I) species generate oxygen vacancies in the titania framework and then these oxygen vacancies most likely capture photoexcited electrons to form F-centres,[254] thereby suppressing recombination and prolonging the lifetime of charge carriers.

The initial rates of hydrogen production were the same regardless the variation in macropore size and were ~20% more active than the 0.1 wt% Cu/meso-TiO_2-400 counterpart. The activity would be even higher if all Cu species, present on the surface would be mononuclear Cu(I), like it is on 0.1 wt% Cu/meso-TiO_2. This activity trend is the same as for the unpromoted macro-meso-TiO_2 series water splitting activity (**4.2.2 Water splitting**). It is unsurprising that the rate is independent of macropore diameter because H_2O diffusion cannot be a rate-limiting factor in an aqueous media. Moreover, the initial investigation revealed the negligible impact of mesopore diameter on water splitting reaction (**3.2.2 Water splitting**). Lastly, the results show that 140 nm macropores are sufficient.

4.5 Characterisation of Pt promoted macro-mesoporous titania series

Macro-meso-TiO_2 series with increasing macropore sizes from 140 to 310 nm examined in **4.1 Characterisation of macro-mesoporous titania series** were promoted with Pt by straightforward wet impregnation method using chloroplatinic acid ($H_2PtCl_6.6H_2O$). The newly synthesised photocatalysts have been characterised to assess retention of macro-meso-TiO_2 support qualities via a range of techniques. The active Pt promoter species, the effect on it by the different supports and the following activity have been studied and compared. In addition, Pt/macro-meso-TiO_2 series are correlated with 1.8 wt% Pt/meso-TiO_2-400 – an analogue mesoporous material, synthesised and promoted via identical processes but not containing the macropores.

4.5.1 Nitrogen porosimetry

N_2 porosimetry was employed to evaluate retention of mesopore framework of macro-meso-TiO_2 140 – 310 nm support after deposition with Pt. N_2 adsorption/desorption graphs (**Figure 4.23 (a)**) of Pt/macro-meso-TiO_2 photocatalysts feature identical isotherms to those of macro-meso-TiO_2 supports and Pt/meso-TiO_2 : type IV isotherms with H2 type hysteresis loop reveals either restricted pore entrance (ink bottle shape) or irregular channel structure of mesopore framework.[174] Specific surface area (BET), mesopore volume and mesopore size (BJH) of Pt/macro-meso-TiO_2 are compiled in **Table 4.11.** Pt/macro-meso-TiO_2 series display average 190 $m^2.g^{-1}$ surface area, 4.2 nm mesopores and 0.28 $g.cm^{-3}$ mesopore volume. When compared to unpromoted macro-meso-TiO_2 series, mesopore diameter and volume remains unchanged but there is a small increase in surface area. Overall, macro-meso-TiO_2 supports retained their characteristics after Pt deposition process. In comparison with Pt/meso-TiO_2 counterpart, no major changes are observed only pore diameter (**Figure 4.23 (b)**) and thus pore volume are slightly lower.

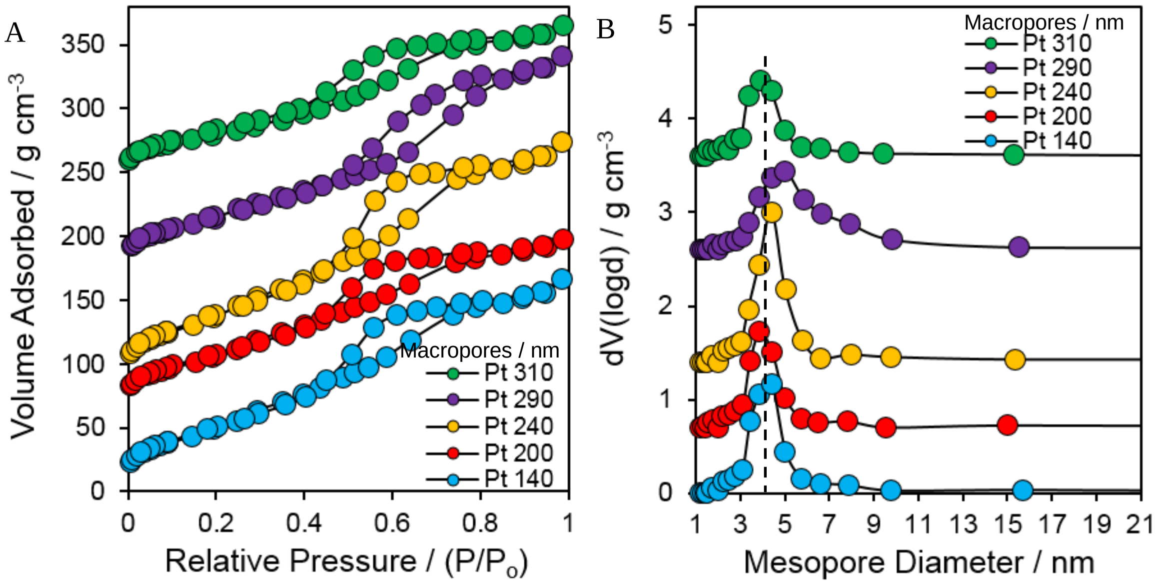

Figure 4.23 (a) Stacked isotherm plot (b) Mesopore size distribution of Pt macro-meso-TiO_2 series with 140-310 nm macropores.

Table 4.11 Summary of N_2 porosimetry results of Pt macro-meso-TiO_2 series with 140-310 nm macropores. On the right-hand side corresponding values of the macro-meso-TiO_2 supports before Pt promotion are displayed. At the bottom of the table values for Pt promoted and unpromoted meso-TiO_2 equivalents are presented.

	Pt promoted macro-meso TiO_2			macro-meso TiO_2 support		
Macropore size / nm	BET / m^{2} g^{-1}	Mesopore size / nm	Mesopore volume / g cm^{-3}	BET / m^{2} g^{-1}	Mesopore size / nm	Mesopore volume / g cm^{-3}
Pt 140	190 (±19)	4.4 (±0.4)	0.29 (±0.03)	164 (±16)	4.2 (±0.4)	0.24 (±0.02)
Pt 200	185 (±19)	3.9 (±0.4)	0.23 (±0.02)	155 (±16)	4.2 (±0.4)	0.21 (±0.02)
Pt 240	214 (±21)	4.4 (±0.4)	0.33 (±0.03)	186 (±19)	4.4 (±0.4)	0.29 (±0.03)
Pt 290	183 (±18)	4.4 (±0.4)	0.28 (±0.03)	162 (±16)	4.7 (±0.5)	0.27 (±0.03)
Pt 310	176 (±18)	3.9 (±0.4)	0.25 (±0.03)	156 (±16)	4.4 (±0.4)	0.22 (±0.02)
Average	**190 (±19)**	**4.2 (±0.4)**	**0.28 (±0.03)**	**165 (±17)**	**4.4 (±0.4)**	**0.25 (±0.03)**
Pt/meso TiO_2-400 and meso-TiO_2-400	**188 (±19)**	**5.0 (±0.5)**	**0.33 (±0.03)**	**194 (±19)**	**5.4 (±0.5)**	**0.34 (±0.03)**

4.5.2 X-ray diffraction

XRD graphs (**Figure 4.24**) of Pt/macro-meso-TiO_2 series with macropores sizes varying from 140 to 310 nm demonstrate seven well-resolved diffraction peaks indexed (101), (004), (200), (105,211), (204), (116,220), (215) matching to TiO_2 anatase crystalline phase. Based on calculations using Scherrer formula, the average size of anatase nanocrystallites is 7 nm (**Table 4.12**). In addition, a=b=3.79 Å unit cell parameter is identical to unpromoted supports and Pt/meso-TiO_2-400 counterpart. Promotion with Pt does not affect crystallinity of macro-meso-TiO_2 supports. Pt/macro-meso-TiO_2 data also mirrors the Pt/meso-TiO_2 counterpart. No Pt peaks were detected in WA XRD patterns disclosing either that Pt crystallites are smaller than 2 nm or the amounts are beyond XRD threshold.

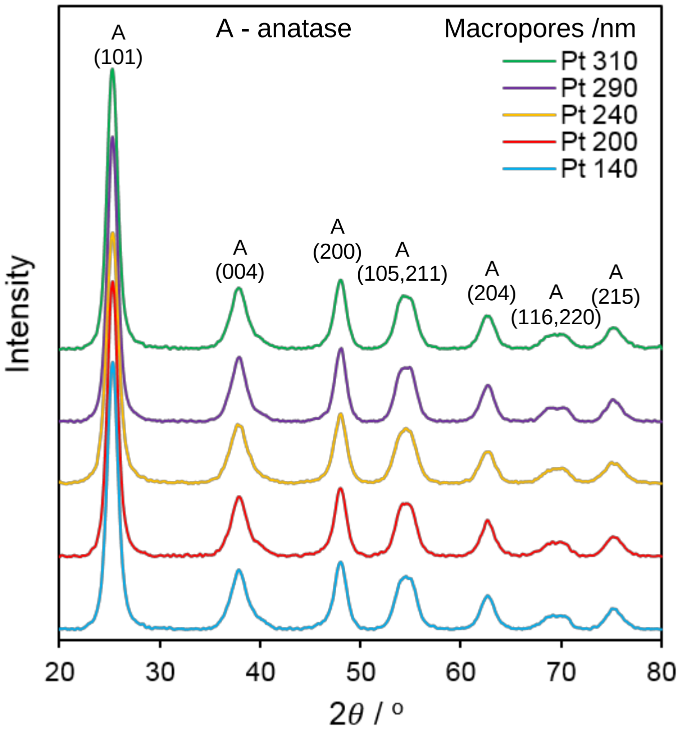

Figure 4.24 Wide angle XRD patterns of Pt macro-meso-TiO_2 series with 140-310 nm macropores.

Table 4.12 Summary of XRD results of Pt/macro-meso-TiO$_2$ series. On the right-hand side corresponding values of the macro-meso-TiO$_2$ supports before Pt promotion are displayed. At the bottom of the table values for Pt promoted and unpromoted meso-TiO$_2$ equivalents are presented.

	Pt promoted macro-meso TiO$_2$			macro-meso TiO$_2$ support		
Macropore size / nm	Crystalline phase	Crystallite size / nm	Anatase unit cell a (=b) / Å	Crystalline phase	Crystallite size / nm	Anatase unit cell a (=b) / Å
Pt 140	Anatase	7 (±0.1)	3.79 (±0.04)	Anatase	7 (±0.1)	3.79 (±0.04)
Pt 200	Anatase	7 (±0.1)	3.79 (±0.04)	Anatase	7 (±0.1)	3.79 (±0.04)
Pt 240	Anatase	7 (±0.1)	3.79 (±0.04)	Anatase	7 (±0.1)	3.79 (±0.04)
Pt 290	Anatase	7 (±0.1)	3.79 (±0.04)	Anatase	7 (±0.1)	3.79 (±0.04)
Pt 310	Anatase	7 (±0.1)	3.79 (±0.04)	Anatase	7 (±0.1)	3.79 (±0.04)
Average	**Anatase**	**7 (±0.1)**	**3.79 (±0.04)**	**Anatase**	**7 (±0.1)**	**3.79 (±0.04)**
Pt/meso TiO$_2$-400 and meso TiO$_2$-400	**Anatase**	**7 (±0.01)**	**3.79 (±0.04)**	**Anatase**	**7 (±0.1)**	**3.78 (±0.04)**

4.5.3 High-resolution scanning transmission electron microscopy

HRSTEM images of Pt/macro-meso-TiO$_2$ 140, 290, 310 nm were used to determine the size of Pt nanocrystallites which were invisible in WA XRD measurements (**4.5.2 X-ray diffraction**). In **Figure 4.25, Figure 4.26, Figure 4.27,** images **A - C** represent a snapshot of Pt distribution on macro-meso-TiO$_2$ support while graph **D** shows Pt particle size distribution. Samples Pt/macro-meso TiO$_2$ with 140, 290 and 310 nm macropore diameters all demonstrate average 2.4 nm Pt particles both in the pores and on the catalyst surface. Image **C** also features lattice fringes d$_{101}$ ~3.5 Å which correlate with the most predominant (101) anatase facet d=3.5 Å (**4.5.2 X-ray diffraction**). The difference in macropore size of the macro-meso-TiO$_2$ supports does not affect Pt particle size. Pt nanoparticle size of 2.4 nm agrees with the literature where a common 1-3 nm Pt nanoparticles are observed on porous titania.[91, 292]

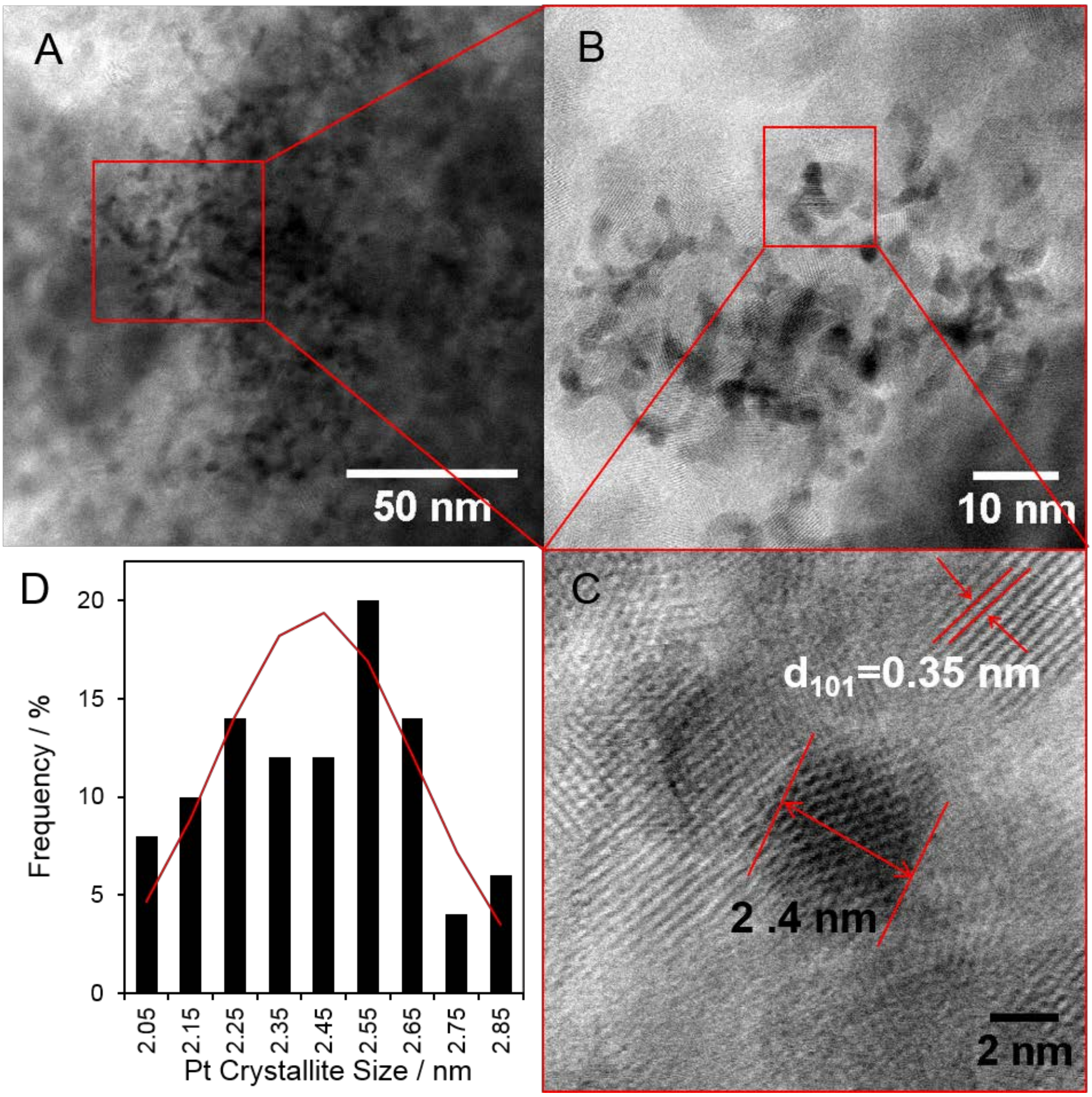

Figure 4.25 HRSTEM images and particle size distribution of 1.8 wt% Pt dispersed on macro-meso-TiO_2 with 140 nm macropores.

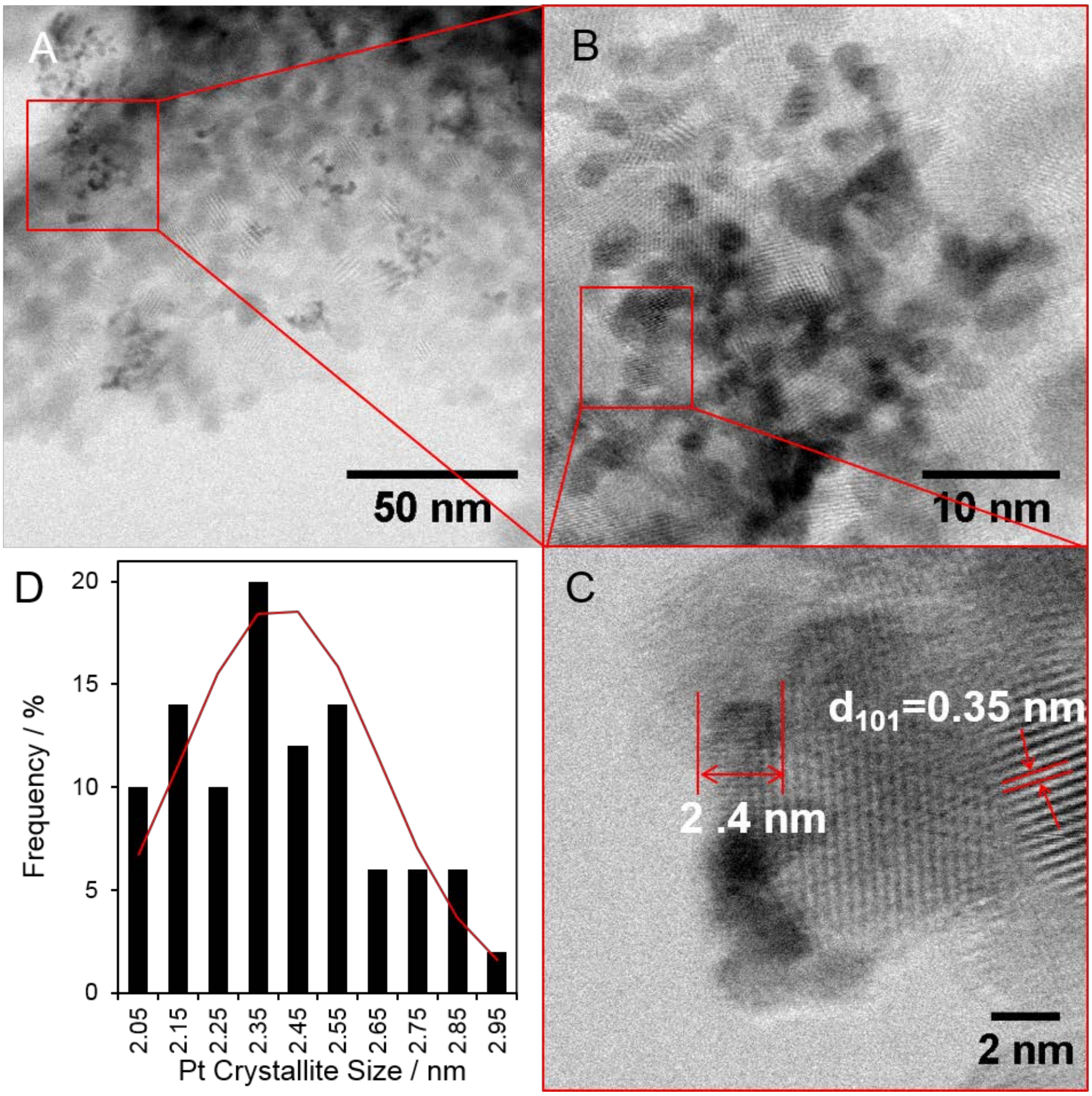

Figure 4.26 HRSTEM images and particle size distribution of 1.8 wt% Pt dispersed on macro-meso-TiO_2 with 290 nm macropores.

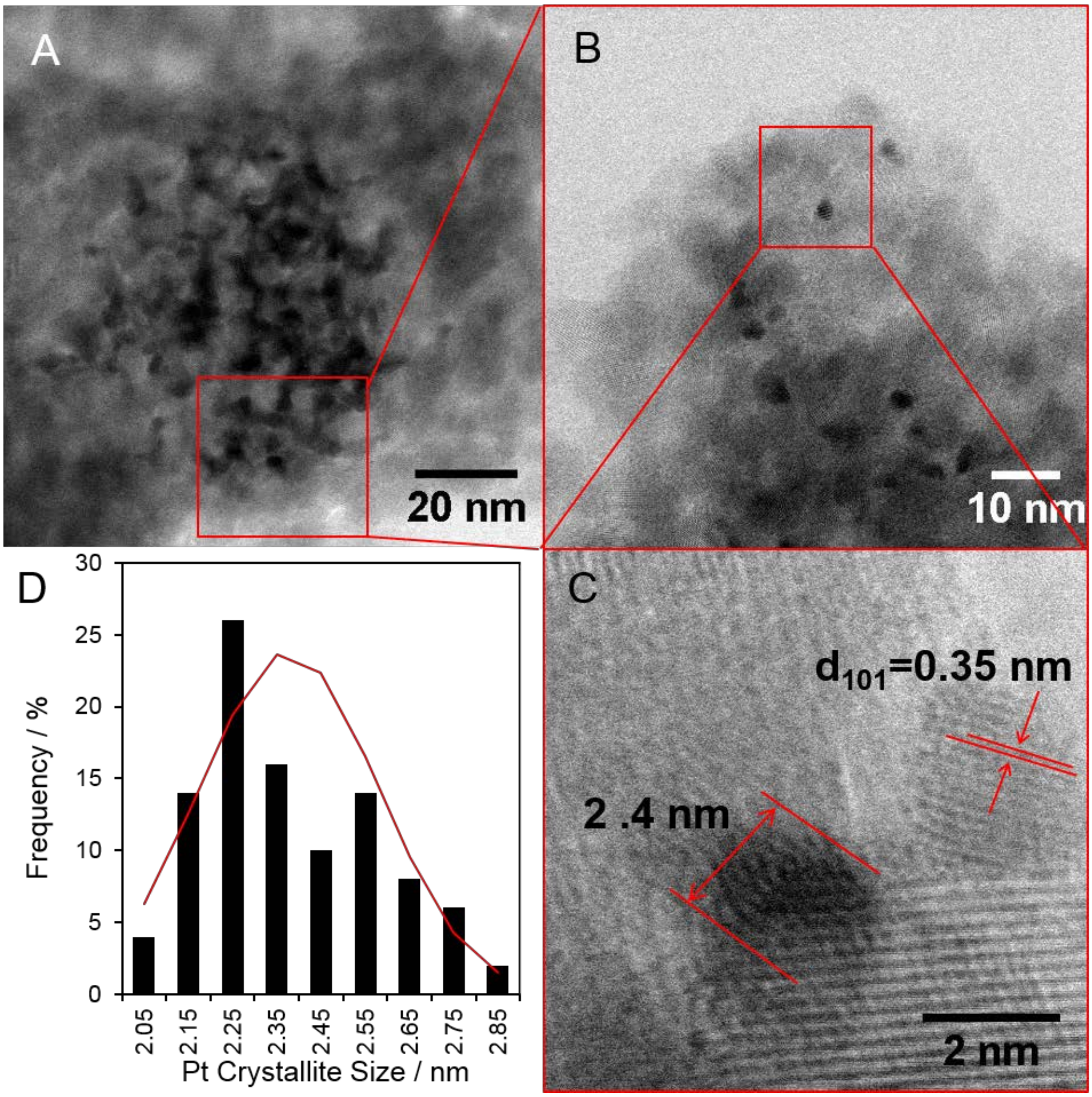

Figure 4.27 HRSTEM images and particle size distribution of 1.8 wt% Pt dispersed on macro-meso-TiO_2 with 310 nm macropores.

4.5.4 Inductively coupled plasma optical emission spectrometry

ICP – OES was used to determine experimental wt% loading of Pt on macro - mesoporous TiO_2 supports with macropores ranging from 140 to 310 nm. The average 1.3 wt% loading was measured for all the catalysts (**Table 4.13**). This 1.3 wt% loading is 0.5 wt% lower than the theoretical/expected 1.8 wt%, which was deposited on Pt/meso-TiO_2-400 counterpart. For both series of materials, identical synthesis method and the same stock solution of Pt precursor was used.

Table 4.13 ICP – OES determined Pt loadings of Pt macro-meso-TiO_2 series with 140-310 nm macropores.

Macropore size / nm	Pt loading / wt%
Pt 140	1.36 (±0.04)
Pt 200	1.34 (±0.04)
Pt 240	1.27 (±0.04)
Pt 290	1.30 (±0.04)
Pt 310	1.30 (±0.04)
Average	**1.31 (±0.04)**
Pt/meso-TiO_2-400	**1.83 (±0.05)**

4.5.5 X-ray photoelectron spectroscopy

The XPS spectra of Pt/macro-meso-TiO_2 series with macropores sizes from 140 nm to 310 nm Ti 2p region is shown in **Figure 4.28.** The binding energies for Ti 2p core levels found at 458 and 464 eV correspond to Ti $2p_{3/2}$ and Ti $2p_{1/2}$ levels respectively.[189] The Ti $2p_{3/2}$ and Ti $2p_{1/2}$ peaks are symmetric which indicates uniform chemical environment in all samples. All samples displayed 2:1 oxygen to titanium surface atomic ratio, as expected for TiO_2 structure.

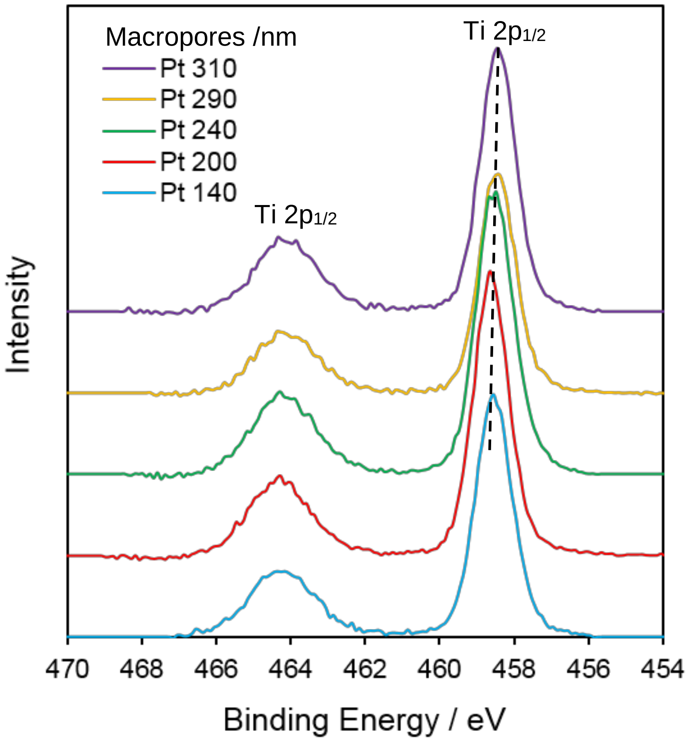

Figure 4.28 XPS spectra Ti 2p region of Pt macro-meso-TiO_2 series with 140-310 nm macropores.

The Pt region of Pt/macro-meso-TiO_2 series (**Figure 4.29**) reveals three different Pt species. The binding energies of Pt 4f found at 71.0, 72.4 and 74.9 eV corresponds to Pt metal, Pt(II) and Pt(IV). The % of each Pt species, At% and wt% of surface and Pt:Ti ratio is summarised in **Table 4.14**. The binding energies and amounts of different Pt species on the surface are consistent and it compares well with Pt/meso-TiO_2-400 counterpart. To conclude, Pt species and dispersion was similar regardless of variation in macropore diameter. The evaluation of the Pt species is challenging because of the weak signal, especially at 1.3 wt% loading, thus the standard deviations between At%, wt%, Pt(0) %, Pt(II) % and Pt(IV) % values are large.

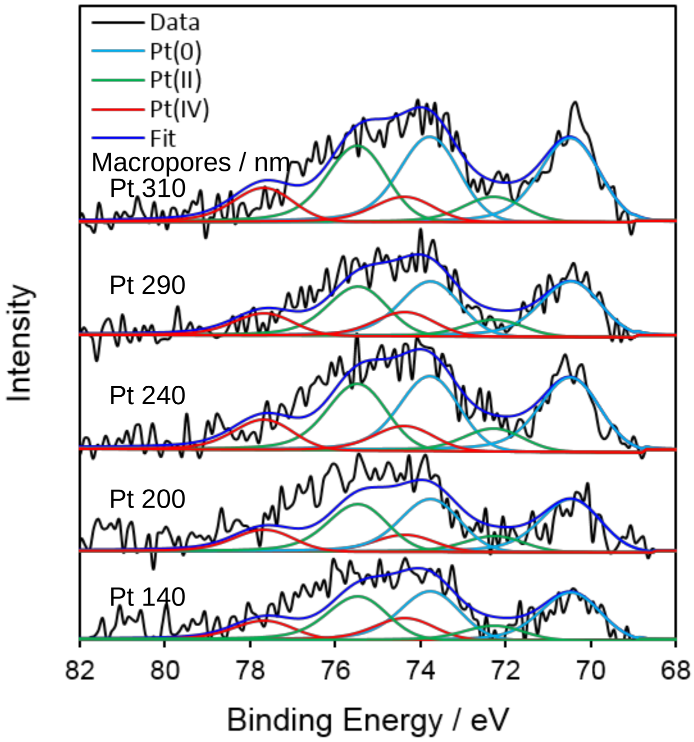

Figure 4.29 XPS spectra of Pt 4f region of Pt macro-meso-TiO$_2$ series with 140-310 nm macropores.

Table 4.14 Summary of % Pt species of Pt macro-meso-TiO$_2$ series with 140-310 nm macropores.

Macropore size / nm	Pt surface / At%	Pt surface / wt%	Pt(0) / %	Pt(II)/ %	Pt(IV)/ %	Pt:Ti
Pt 140	0.19 (±0.01)	1.55 (±0.08)	49 (±2)	30 (±2)	21 (±1)	0.007
Pt 200	0.20 (±0.01)	1.69 (±0.08)	51 (±3)	31 (±2)	18 (±1)	0.008
Pt 240	0.21 (±0.01)	1.80 (±0.09)	51 (±3)	30 (±2)	19 (±1)	0.009
Pt 290	0.20 (±0.01)	1.72 (±0.09)	49 (±2)	30 (±2)	21 (±1)	0.009
Pt 310	0.23 (±0.01)	1.92 (±0.10)	51 (±3)	31 (±2)	18 (±1)	0.010
Average	**0.21 (±0.01)**	**1.74 (±0.09)**	**50 (±3)**	**30 (±2)**	**19 (±1)**	**0.009**
Pt/meso TiO$_2$-400	**0.20 (±0.01)**	**1.61 (±0.08)**	**49 (±2)**	**26 (±1)**	**25 (±1)**	**0.008**

4.5.6 Temperature programmed oxidation

The derivative of the mass loss acquired from TPO results of Pt/macro-meso-TiO_2 with macropores sizes varying from 140 to 310 nm (**Figure 4.30**) display three types of species desorbing from the surface (**Table 4.15**). TPO of pure macro-meso-TiO_2 supports reports only two species (**4.1.5 Temperature programmed oxidation**). The decrease in mass at temperatures up to 150 °C was attributed to physisorbed atmospheric and crystalline water while the mass loss from 150 to 450 °C was combustion of carbons. The % of water and carbon losses for Pt/macro-meso-TiO_2 (**Table 4.15**) are identical to mass losses of macro-meso-TiO_2 supports (**4.1.5 Temperature programmed oxidation**). The mass decrease at >450 °C corresponds to a loss of PtO_x (**4.5.5 X-ray photoelectron spectroscopy**), which is smaller than the Pt/meso-TiO_2-400 counterpart because of the decrease in Pt wt% loading from 1.8 wt% of the Pt/meso-TiO_2-400 to 1.3 wt% of Pt/macro-meso-TiO_2 series (**4.5.4 Inductively coupled plasma optical emission spectrometry**).

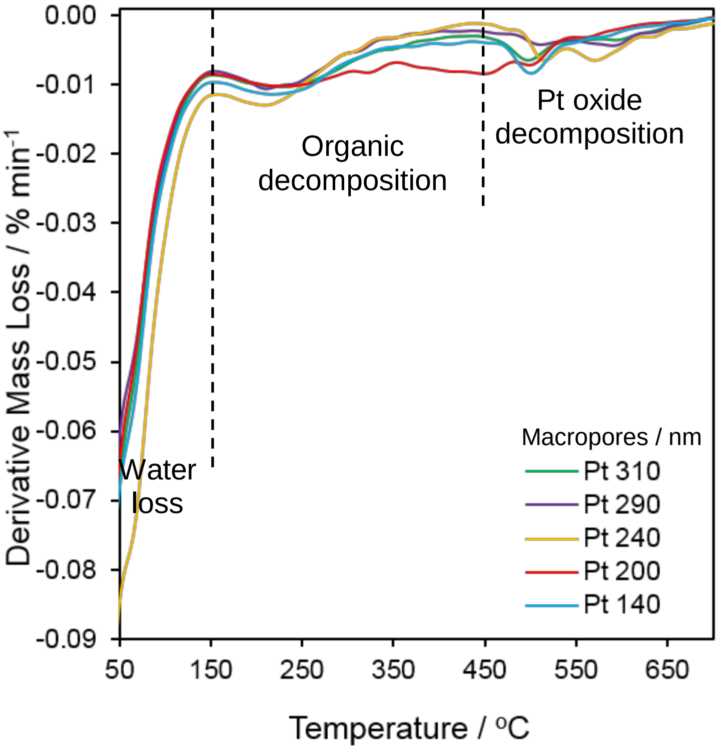

Figure 4.30 Derivative of mass loss of Pt macro-meso-TiO_2 series with 140-310 nm macropores.

Table 4.15 Summary of TPO results of Pt macro-meso-TiO$_2$ series with 140-310 nm macropores.

Macropore size / nm	Water (<150 °C) / %	Carbon (150 – 450 °C) / %	PtO$_x$ (>450 °C) / %	Total mass loss / %
Pt 140	3.5 (±0.10)	2.1 (±0.06)	0.9 (±0.03)	6.5 (±0.20)
Pt 200	3.1 (±0.09)	2.6 (±0.08)	0.9 (±0.03)	6.6 (±0.20)
Pt 240	4.6 (±0.14)	2.0 (±0.06)	1.0 (±0.03)	7.6 (±0.23)
Pt 290	3.1 (±0.09)	1.8 (±0.05)	0.8 (±0.02)	5.7 (±0.17)
Pt 310	3.3 (±0.10)	2.1 (±0.06)	0.8 (±0.02)	6.2 (±0.18)
Average	**3.5 (±0.11)**	**2.1 (±0.06)**	**0.9 (±0.03)**	**6.5 (±0.20)**
macro-meso-TiO$_2$ average	**3.5 (±0.11)**	**2.0 (±0.06)**	**-**	**5.5 (±0.17)**

4.5.7 Diffuse reflectance UV-vis spectrophotometry

Solid diffuse reflectance UV-vis optical absorption spectra and Tauc plot (**Figure 4.31**) were recorded for Pt/macro-meso-TiO$_2$ to evaluate the impact of Pt deposition on optical properties of the titania supports. Absorbance spectra (**Figure 4.31 (a)**) of the catalysts have a sharp band gap absorption edge at 325 – 380 nm. However, at wavelengths >380 nm light is still being absorbed even below the energy of the band gap absorption. Pure macro-meso-TiO$_2$ supports do not show this feature thus it is attributed to Pt species. Tauc plot (**Figure 4.31 (b))** and **Table 4.16** report an average 3.15 eV band gap of Pt/macro-meso-TiO$_2$.The band gap is notably larger than the parent macro-meso-TiO$_2$ support and closer to Pt/meso-TiO$_2$ equivalent. In both Pt/meso-TiO$_2$ and Pt/macro-meso-TiO$_2$ cases, Pt promoted titania materials exhibit a small increase in the band gaps. Based on the theory, the Kubelka-Munk function is only accurate when materials are single oxides or doped composites, where modification is within the whole structure. When KM is used for the surface modified photocatalysts, the results are less accurate, because of the band bending which in this case occurs due to the Schottky barrier. As a result, the shift of the conductance and/or valence edges is observed and this influences the band gap evaluation via KM.[257-259] This is the most probable cause of the shift of the band gap values for Pt promoted series. DRUVS results revealed that deposition of Pt increases light absorption of the Pt/macro-meso-TiO$_2$ catalysts.

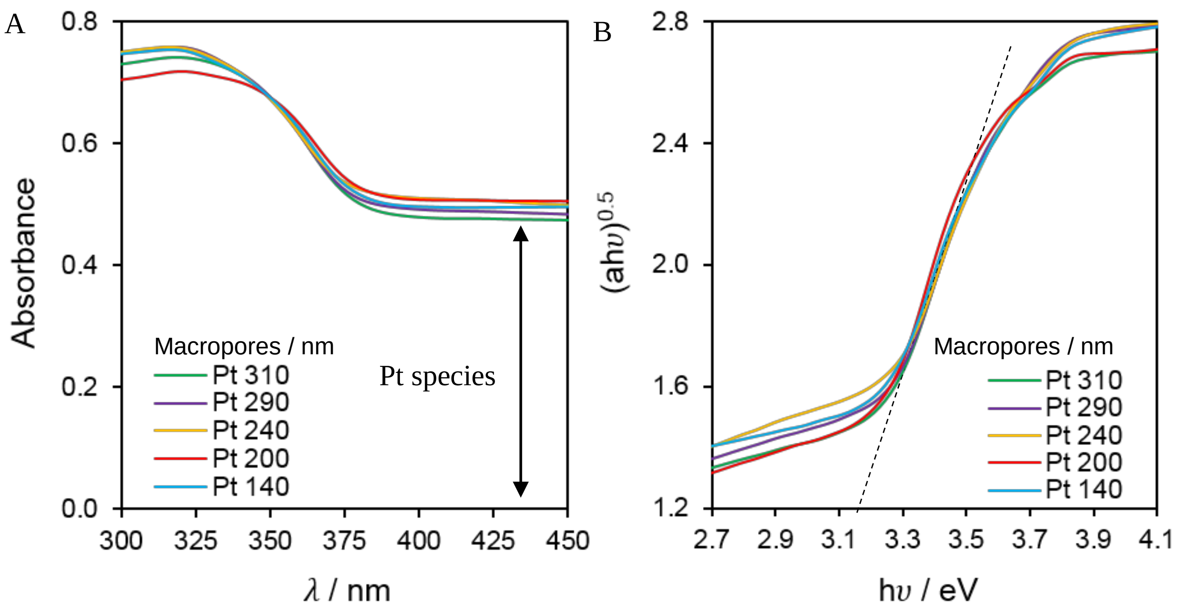

Figure 4.31 (a) UV – vis absorption spectra and (b) Tauc plot of Pt macro-meso-TiO_2 series with 140-310 nm macropores.

Table 4.16 Summary of the band gap values of Pt macro-meso-TiO_2 series with 140-310 nm macropores.

	Pt promoted macro-meso TiO_2	macro-meso TiO_2 supports
Macropore size / nm	Band Gap / eV	Band Gap / eV
Pt 140	3.15 (±0.03)	3.02 (±0.02)
Pt 200	3.13 (±0.03)	3.06 (±0.02)
Pt 240	3.16 (±0.03)	3.10 (±0.02)
Pt 290	3.16 (±0.03)	3.07 (±0.02)
Pt 310	3.16 (±0.03)	3.03 (±0.02)
Average	**3.15 (±0.03)**	**3.06 (±0.02)**
Pt/meso-TiO_2-400 and meso-TiO_2-400	**3.10 (±0.02)**	**3.07 (±0.02)**

4.5.8 Summary of the key characteristics of Pt promoted macro-mesoporous titania series

Table 4.17 Summarises the main physicochemical and electronic properties of Pt macro-meso-TiO_2 series with 140-310 nm macropores.

Sample	Pt loading / wt%(a)	SSA / $m^2.g^{-1}$ (b)	Mesopore size / nm (c)	Mesopore volume / $g.cm^{-3}$ (c)	TiO_2 Phase (XRD)	Nanocrystallite size / nm(d)	Band Gap / eV (e)	Total mass loss (H_2O) / % (f)
Pt 140	1.36 (±0.04)	190 (±19)	4.4 (±0.4)	0.29 (±0.03)	Anatase	7 (±0.1)	3.15 (±0.03)	6.5 (±0.2)
Pt 200	1.34 (±0.04)	185 (±19)	3.9 (±0.4)	0.23 (±0.02)	Anatase	7 (±0.1)	3.13 (±0.03)	6.6 (±0.2)
Pt 240	1.27 (±0.04)	214 (±21)	4.4 (±0.4)	0.33 (±0.03)	Anatase	7 (±0.1)	3.16 (±0.03)	7.6 (±0.2)
Pt 290	1.30 (±0.04)	183 (±18)	4.4 (±0.4)	0.28 (±0.03	Anatase	7 (±0.1)	3.16 (±0.03)	5.7 (±0.2)
Pt 310	1.30 (±0.04)	176 (±18)	3.9 (±0.4)	0.25 (±0.03)	Anatase	7 (±0.1)	3.16 (±0.03)	6.2 (±0.2)
Average	**1.31 (±0.04)**	**190 (±19)**	**4.2 (±0.4)**	**0.28 (±0.03)**	**Anatase**	**7 (±0.1)**	**3.15 (±0.03)**	**6.5 (±0.2)**
Pt/meso-TiO_2-400	**1.83 (±0.05)**	**188 (±19)**	**5.0 (±0.5)**	**0.33 (±0.03)**	**Anatase**	**7 (±0.1)**	**3.10 (±0.02)**	**7.4 (±0.2)**

[a]*ICP – OES;* [b]*N_2 BET;* [c]*from BJH desorption isotherm;* [d]*Mean particle diameter from XRD via Scherrer analysis;* [e]*DRUVS;* [f]*TPO;*

4.6 Photocatalytic performance of Pt promoted macro-mesoporous titania series

Photoactivity of the Pt/macro-meso-TiO_2 series with macropores ranging from 140 to 310 nm, discussed above, was investigated via photocatalytic depollution of Methyl Orange, H_2 production via water splitting and CO_2 reduction to hydrocarbons under UV-vis light irradiation. The impact of Pt deposition on photocatalyst's performance is assessed and compared to pure and Cu promoted titania series. Additionally, catalysts are correlated to the Pt/meso-TiO_2-400 counterpart which was synthesised via identical procedure without incorporation of macropores. However, Pt loading on Pt/meso-TiO_2 is 1.8 wt% while on Pt/macro-meso-TiO_2 it is lower - 1.3 wt%.

4.6.1 Methyl Orange decomposition

The time profiles of Pt/macro-meso-TiO_2 Methyl Orange degradation are presented in **Figure 4.32**. Before the illumination, catalysts were stirred in the dark for one hour to achieve MO adsorption equilibrium. Pt promoted macro-meso-TiO_2 catalysts display 30% MO adsorption. Photolysis is not observed for 20 ppm Methyl Orange dye (**Figure 3.17**).

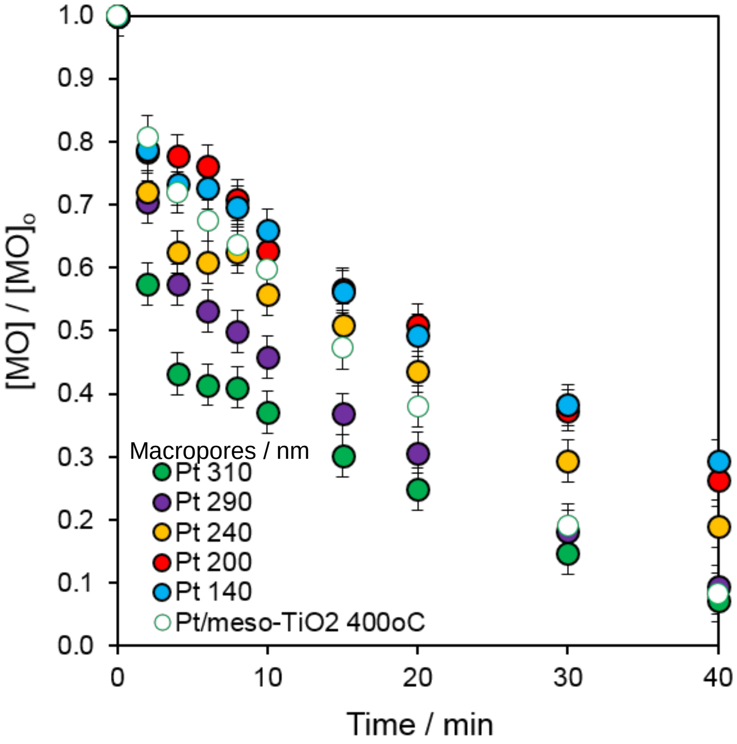

Figure 4.32 Time profiles of Methyl Orange decomposition of Pt macro-meso-TiO_2 series with 140-310 nm macropores under UV-vis irradiation.

The impact of Pt addition on macro-meso-TiO_2 series photoactivity and comparison to the Cu promoted and pure supports together with Pt/macro-meso-TiO_2-400 counterpart are summarised in **Figure 4.33**. In the Pt/macro-meso-TiO_2 series Pt loading, species and Pt:Ti ratios are uniform across the series, the only variation is in a macropore size (**4.5.4 Inductively coupled plasma optical**

emission spectrometry, 4.5.5 X-ray photoelectron spectroscopy). However, the Pt loading on macro-meso-TiO_2 series is 1.3 wt% while on Pt/meso-TiO_2 counterpart – higher, 1.8 wt%. Mass normalised initial rates of Pt/macro-meso-TiO_2 are 6-12 times higher than the bare macro-meso-TiO_2 supports and 2-3 times more active than Cu/macro-meso-TiO_2 series. A dramatic increase in the photoactivity coincides with the one observed for Pt/mesoporous TiO_2 where, in principle, Pt metal acts as an electron trap and prolongs the lifetime of the charge carriers, suppresses recombination and more holes are available to form OH radical or directly oxidise the dye (**3.7.1 Methyl Orange decomposition**). As the Fermi level of the Pt metal is lower than the conductance band of TiO_2, photo-excited electrons can be transferred from the conductance band of TiO_2 to the metal particles deposited on its surface, while photo-generated holes remain on the photocatalyst (**Schottky barrier, 1.4.1 Surface trapping**). Separated electrons on the metal particles can then carry out a reduction reaction, while holes on the TiO_2 participate in the oxidation reaction.

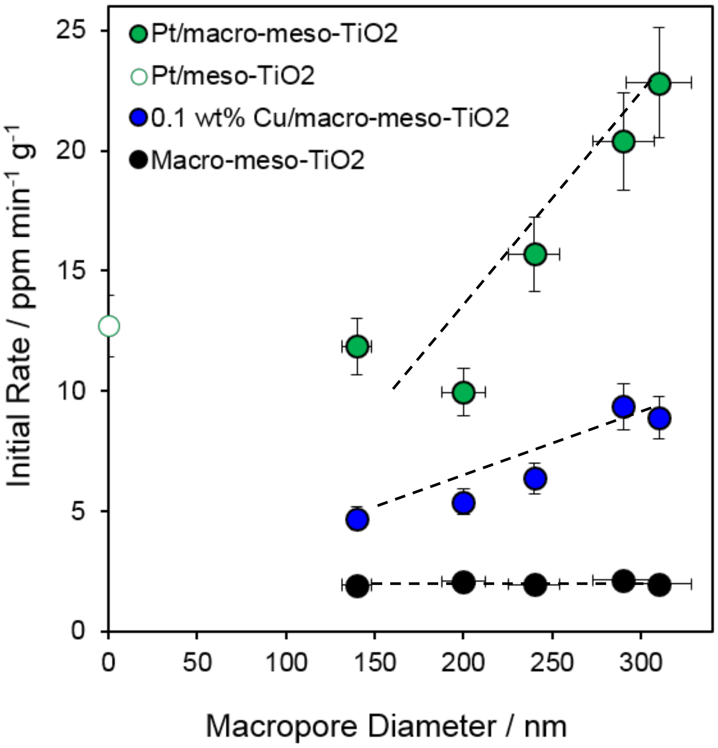

Figure 4.33 Initial rates of Pt/macro-meso-TiO_2 series together with Pt/meso-TiO_2 counterpart, 0.1 wt% Cu/macro-meso-TiO_2 series and unpromoted macro-meso-TiO_2 supports under UV-vis light.

The initial rates displayed a linear growth as macropore diameter increased, starting with the same initial rate as the Pt/meso-TiO_2-400 equivalent. It is also important to remark, that addition of the macroporosity to Pt/macro-meso-TiO_2 series did not significantly reduce or increase the overall surface area. DRUVS results (**4.1.6 Diffuse reflectance UV-vis spectrophotometry**) and MO photocatalytic tests under monochromatic 365 nm wavelength (**4.2.1 Methyl Orange decomposition**) demonstrated that addition of the macroporosity did not affect the optical properties of the catalysts. Pt/macro-meso-TiO_2 catalysts displayed an identical trend as the Cu/macro-meso-TiO_2 series, where initial rates increase as macropore size expands. In both cases, the MO degradation reaction was remarkably faster than the bare macro-meso-TiO_2, especially for Pt series (up to 12-fold). Therefore, the rate enhancement originates from the critical improvement of overall framework diffusion and accessibility to the catalyst surface with larger macropore diameter, with 310 nm macropores being the most active. Moreover, Pt/macro-meso-TiO_2 materials potentially would be even more active, if it would have 1.8 wt% Pt loading as Pt/meso-TiO_2 counterpart.

4.6.2 Water splitting

Mass normalised H_2 production rate of Pt/macro-meso-TiO_2 series with macropores spanning from 140 to 310 nm is presented in **Figure 4.34**. Pt loading, species and Pt:Ti ratios are uniform across all series, the only change is in macropore size (**4.5.4 Inductively coupled plasma optical emission spectrometry, 4.5.5 X-ray photoelectron spectroscopy**). However, the Pt loading on macro-meso-TiO_2 series is 1.3 wt% while on Pt/meso-TiO_2 counterpart – higher, 1.8 wt%. It is also important to note, that addition of the macroporosity to Pt/macro-meso-TiO_2 series did not significantly reduce or increase the overall surface area. DRUVS results (**4.1.6 Diffuse reflectance UV-vis spectrophotometry**) and MO photocatalytic tests under monochromatic 365 nm wavelength (**4.2.1 Methyl Orange decomposition**) demonstrated that addition of the macroporosity did not affect the optical properties of the catalysts.

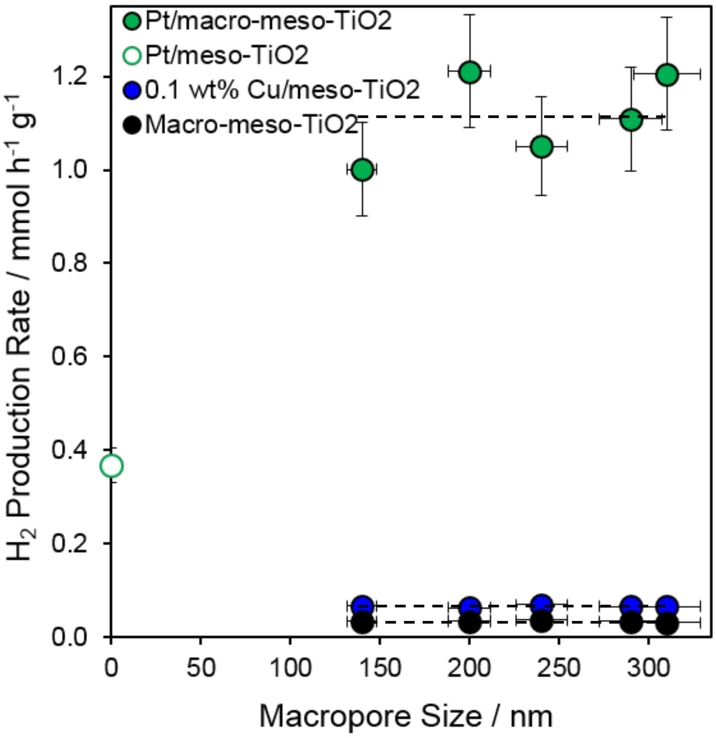

Figure 4.34 H_2 production rates of Pt/macro-meso-TiO_2 140-310 nm series in comparison with Pt/meso-TiO_2 counterpart, 0.1 wt% Cu/macro-meso-TiO_2 series and unpromoted macro-meso-TiO_2 supports under UV-vis irradiation.

Pt promotion improves the activity of macro-meso-TiO_2 supports by 33 times, while Cu - 17 times. Pt metal nanoparticles act as an electron trap suppressing recombination and prolonging charge carrier lifetime. As discussed in detail **1.4.1 Surface trapping and 3.7.1 Methyl Orange decomposition** as well as in the above paragraph of Pt/macro-meso-TiO_2 decomposition of Methyl Orange, loading with metals such as Pt, which in principle, acts as a co-catalyst on the TiO_2 surface and forms the Schottky barrier. As the Fermi level is lower than the conductance band of the titania, photo-excited electrons flow from the conductance band of TiO_2 to the metal particles deposited on its surface, while photo-generated holes remain on the photocatalyst. Separated electrons on the metal perform reduction reactions, while holes on the TiO_2 proceed with the oxidation reactions. Therefore, metals with suitable work-function prevent electron-hole recombination, leading to the higher photocatalytic activity of TiO_2.

H_2 production was the same regardless the variation in macropore size, the identical trend to the pure macro-meso-TiO_2 support and Cu/macro-meso-TiO_2, and 3 times more active than the Pt/meso-TiO_2-400 equivalent. It is expected that the rate is independent of macropore diameter because water diffusion cannot be a rate-limiting factor in the aqueous media. Initial investigation revealed the negligible impact of mesopore diameter on water splitting reaction (**Figure 3.22**). It is evident that 140 nm macropores are sufficient. Furthermore, Pt/macro-meso-TiO_2 potentially would be even more active if it would have 1.8 wt% Pt loading when compared to Pt/meso-TiO_2 counterpart.

4.6.3 Carbon dioxide reduction

Pt/macro-meso-TiO_2 with 140 – 310 nm macropores were the only macro-meso-TiO_2 series to produce significant amounts of methane to overcome GC detection limits. Macro-meso-TiO_2 and Cu/macro-meso-TiO_2 series were tested and did not produce methane or any other CO_2 reduction products. In theory, Pt metal acts as an electron trap, which separates electrons from holes and suppresses recombination and results in prolonged charge carrier lifetime and significantly improved photocatalytic activity (as discussed in detail **1.4.1 Surface trapping and 3.7.1 Methyl Orange decomposition** as well as in the two paragraphs above). It is important to note, that addition of the macroporosity to Pt/macro-meso-TiO_2 series did not significantly reduce or increase the overall surface area. Furthermore, DRUVS results (**4.1.6 Diffuse reflectance UV-vis spectrophotometry**) and MO photocatalytic tests under monochromatic 365 nm wavelength (**4.2.1 Methyl Orange decomposition**), showed that addition of the macroporosity did not affect the optical properties of the catalysts.

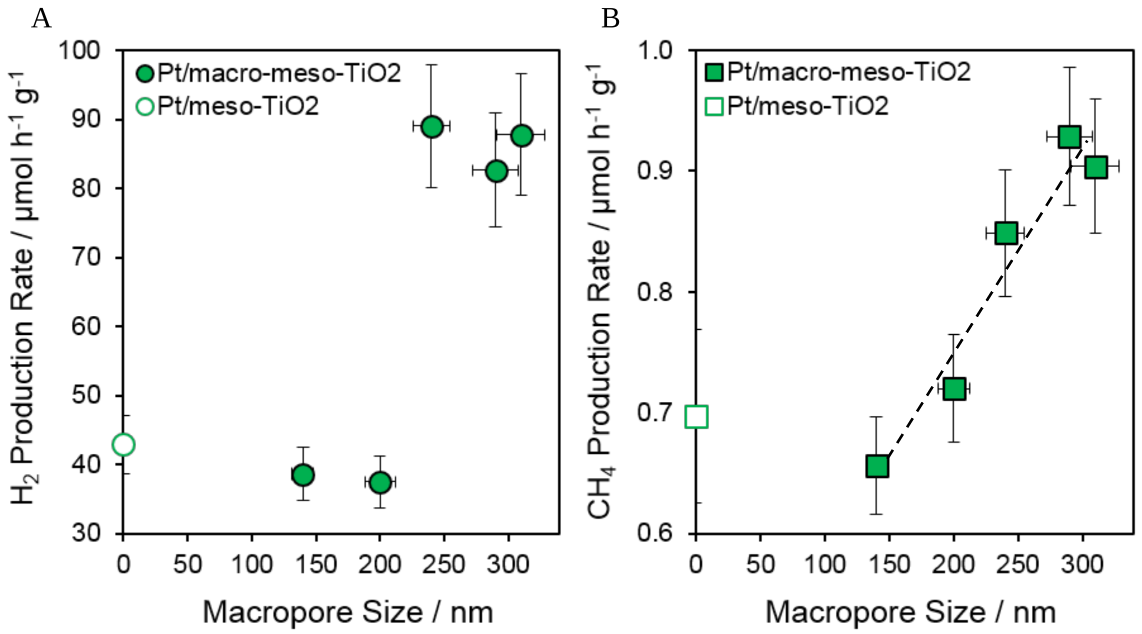

Figure 4.35 (a) H_2 (b) methane production rates via CO_2 photoreduction by Pt/macro-meso-TiO_2 series and comparison with Pt/meso-TiO_2 counterpart under UV-vis light.

Mass normalised rates of generation of CH_4 and H_2 side product are presented in **Figure 4.35 (b) Figure 4.35 (a)** respectively. CO_2 photoreduction reaction only formed methane gas and no liquid compounds, while the side water splitting reaction - hydrogen gas. The reaction was performed by saturating water and catalyst suspension with CO_2 gas, therefore, the H_2 production is detected. Methane production displays a linear increase with macropore size, starting with the same initial rate as Pt/meso-TiO_2-400 equivalent. The exact linear trend is seen in the Methyl Orange decomposition reactions of Cu and Pt promoted macro-meso-TiO_2 series (**4.4.1 and 4.6.1 Methyl Orange decomposition**). In principle, it corresponds to an enhancement in framework diffusion by macropores leading to improved performance and greater access to the photocatalyst surface, with largest 310 nm macropores being the most active. CO_2 reduction and Methyl Orange decomposition reactions are diffusionally challenging, in contrast to water splitting, where macropore diameter did not affect the activity. In CO_2 photoreduction, reactants and products (H_2O, CO_2, H_2 and CH_2) are smaller than Methyl Orange (2.6 nm), however, the CO_2 reactant is in the gas phase.

4.7 Conclusions of macro-mesoporous titania photocatalysts

Newly synthesised macro-mesoporous TiO_2 series with macropores ranging from 140 to 310 nm displayed average 165 m^2 g^{-1} surface area indicating that surface area provided by the mesoporous framework (194 m^2 g^{-1}) is preserved and is in a good agreement with literature. [167, 274] HRSTEM and SEM images confirmed successful incorporation of macropores and formation of ordered structure. Images displayed hierarchical macro-mesoporous TiO_2 structure with long-range hexagonal ordering imparted by polystyrene template and extended mesoscopic ordering resulting from the self-assembly of the F127 block copolymer. The mesopore network is perturbed by interpenetrating spherical macropores which place geometric constraints on the hexagonal configuration of mesostructure.[290] Thus, short-range mesopore order, observed in mesoporous TiO_2 equivalent (**3.1.2 X-ray diffraction** low-angle XRD data), is not retained. Moreover, this resulted in shrinkage of mesopore diameter from 5.4 nm in meso-TiO_2 to 4.4 nm in macro-meso-TiO_2. No further macroporosity effect on crystallinity or band gap was observed. Unfortunately, a stop-band feature, that is indicative of the formation of a photonic crystal in ordered macroporous structures,[277, 278] was not visible in the DRUVS measurements (**4.1.6 Diffuse reflectance UV-vis spectrophotometry**). The absence of photonic crystal properties could probably be a result of insufficient periodicity because of incorporation of disordered mesostructure or still incomplete (approx. 70%) order of the macropores. The Methyl Orange degradation tests under the monochromatic 365 nm wavelength did not show any enhancement in photocatalytic activity and when compared to the mesoporous TiO_2 counterpart, sadly confirming that photonic crystal structure was not formed and optical properties of the photocatalysts are unaffected. On the other hand, the hydrogen production rates were doubled from 18 µmol h^{-1} g^{-1} (of meso-TiO_2-400) to 34 µmol h^{-1} g^{-1}. The variation in the macropore diameter influenced neither Methyl Orange degradation nor water splitting reactions.

In the Methyl orange decomposition, Cu/macro-meso-TiO_2 series were 2-5-fold and Pt/macro-meso-TiO_2 6-12-fold more active than the parent macro-meso-TiO_2 supports. In water splitting reactions, Cu/macro-meso-TiO_2 was twice, while Pt/macro-meso-TiO_2 33 times better than the bare macro-meso-TiO_2 series. Out of all macro-meso-TiO_2 series, Pt/macro-mesoTiO_2 photocatalysts were the only ones, which demonstrated the activity in CO_2 photoreduction, with maximum methane production rate of 0.95 µmol.h^{-1}.g^{-1}. Post-modification of macro-meso-TiO_2 with Cu and Pt did not affect structural properties or crystallinity of the supports thus the resulting changes in activity can be accounted for Cu and Pt promotion effects. The exact same promoter loadings were deposited across the series of macro-mesoporous TiO_2 with macropores spanning from 140 to 310 nm – 0.1 wt% for the Cu and 1.3 wt% for the Pt species. Across all 0.1wt%, Cu/macro-meso-TiO_2 series the same mononuclear Cu(I) amounts were formed. Similarly, the variation in macropore diameter did not influence Pt species. Cu and Pt mode of action was discussed in detail in chapter **3 Mesoporous titania photocatalysts**; 0.1 wt% Cu contains mononuclear Cu(I) species which creates oxygen vacancies that trap electrons on TiO_2 surface, in that way suppressing the recombination of holes and electrons; in a similar manner Pt metallic species formed on the titania surface, in theory, develops the Schottky barrier which also helps to trap electrons and prolong the lifetime of the charge carriers. The Methyl Orange degradation and CO_2 reduction reactions showed that increase in macropore diameter led to an increase in the activity, while the water splitting tests displayed no change in hydrogen production rate across different macropore sizes. The macropore diameter becomes significant in the reactions involving bulky or gas reactants or products indicating that improved diffusion and accessibility to the catalyst increases the activity. This effect is more pronounced when macro-mesoporous TiO_2 series are promoted with Cu or Pt because the rates of the reactions are faster and diffusion limitations become more significant. Most importantly, in all reactions (Methyl Orange depollution, water splitting, CO_2 photoreduction) Cu and Pt/macro-meso-TiO_2 series were significantly better than their Cu and Pt/meso-TiO_2 counterparts. The key factor dominating the activities of Methyl Orange degradation and CO_2 photoreduction reactions is the diameter of macropores and for the CO_2 reduction reaction to take place, the presence of Pt(0) promoter species is required. On the other hand, for the water splitting reaction, the photoactivity is still significantly improved by the incorporation of macropores but the variation in their size has no affect.

Comparison of the activity results with the literature is challenging because of the broad spectrum of operating conditions used in the publications, such as light intensity and distribution, change in stock solution concentrations, etc. As a result, the activity of the synthesized materials has been compared with the meso-TiO_2 equivalent and within the series, to understand the effect of the macroporosity and metal promotion. However, since Pt/macro-meso-TiO_2 is the only macro-meso-TiO_2 series, which displayed photoactivity in CO_2 reduction reactions, in this case, the activity will be parallelised with the literature. In the publications, most frequently observed selectivity is to entirely or a majority of the methane product, which correlates well with Pt/macro-meso-TiO_2 results.[286] [293] Since the reaction takes place in aqueous media, the side water splitting reaction forms H_2 product. Fang et al.[294] synthesised 3.5 $\mu mol.h^{-1}.g^{-1}$ of methane (254 nm, 20 $mW.cm^{-2}$, 3.5 bar) by using 0.6 wt% Pt/hierarchical TiO_2 microspheres. The photoactivity of 1.3 wt% Pt/macro-meso-TiO_2 produced in this thesis displayed 0.95 $\mu mol.h^{-1}.g^{-1}$ methane production rate and it is in a range with the literature, especially taking into account that Fang and co-workers performed the reaction under nearly four times higher pressure. As a rule, the higher reaction pressure increases CO_2 solubility resulting in improved production rates.

Chapter 5

Conclusions and Future Work

5 Overall conclusions and future work

The main aims of this PhD research project were to investigate the impact of nanostructures, in this case mesopore and macropore frameworks, on the activity of TiO_2 photocatalysts in various reactions such as Methyl Orange degradation, water splitting and CO_2 photoreduction, and to establish the effect of porous architectures on the Cu and Pt promoter species. The research was divided into two main subtasks: Chapter 3 Mesoporous TiO_2 and Chapter 4 Macro-mesoporous TiO_2. These two areas have been investigated and demonstrated in this thesis and all measurable aims were achieved.

Chapter 3 presented a facile route to a series of high area mesoporous TiO_2 materials synthesised by a one-pot surfactant templating method and thermal processing at temperatures spanning from 300 to 900 ^{o}C. The mesoporous TiO_2 series demonstrated tunable structural and photophysical properties and the resulting impact on photocatalytic activity. Increasing calcination temperature induced continuous expansion of uniform mesopores accompanied by the decrease in the surface area leading to the absolute collapse of mesopore framework at 800 ^{o}C. Furthermore, the rutile crystalline phase was promoted by the increase of thermal processing temperature, which narrowed the band gap. Methyl Orange degradation under UV-vis irradiation displayed a weak direct correlation with mesopore diameter and strong direct correlation with rutile %, imparting a two-fold rate improvement. While MO decomposition was influenced by both structural and electronic effects, photocatalytic H_2 production via water splitting is more sensitive to rutile formation, inducing a 25-fold increase in productivity. The enhanced activity could be attributed to anatase/rutile heterojunction formation which improved charge separation and reduced recombination. All meso-TiO_2 samples displayed prolonged charge carrier lifetime compared to that of the commercial P25 sample with the most active meso-TiO_2-700 sample having 7 times that of P25. The impact of surface area to photoactivity was negligible.

Post-modification of mesoporous TiO_2 by wet-impregnation with ultra-low ($\leq$0.1 wt%) concentrations of Cu formed undercoordinated atomically-dispersed Cu(I) species, which, as extra-framework, decorated the surface of titania. The formation of atomically-dispersed Cu(I) was strongly controlled by the copper loading and mesoporous TiO_2 support. Mass normalised initial rates of MO dye degradation were inversely proportional to copper loading but directly proportional to the concentration of mononuclear Cu(I) and were six-times faster, relatively to the unmodified meso-TiO_2-500 support. Moreover, a synergy between Cu(I) and CuO in 0.81 wt% Cu/meso-500 sample enhanced H_2 production by four-fold in comparison to the mesoporous scaffold. The promotion of the activity could be ascribed to the creation of oxygen vacancies by mononuclear Cu(I) species into the titania framework, which capture photoexcited electrons and suppress charge carrier recombination. Three consecutive reactions confirmed the retention and stability of mononuclear

Cu(I) species. The most suitable support for promoting 100% atomically-dispersed Cu(I) was meso-TiO_2-500, while the worst – meso-TiO_2-800.

Post-functionalisation of mesoporous TiO_2 by wet-impregnation with the optimum 1.8 wt% Pt loading formed metallic platinum species, which, in theory, creates a Schottky barrier. Multiple characterisation techniques confirmed the retention of mesoporous TiO_2 structure and crystallinity. According to the values of mass normalised initial rates, the Pt promoted series were five times more active than the bare supports, and twice better than Cu promoted series, for the methyl orange decomposition. Furthermore, H_2 production via water splitting showed ten-fold increase in comparison to the unpromoted meso-TiO_2 photocatalysts and eight-fold enhancement to Cu/meso-TiO_2 series. Only promotion with Pt produced the CO_2 reduction product – methane, at a comparable to literature rate (1.3 μmol.h^{-1} .g^{-1}). The considerably improved activity arose from the formation of the Schottky barrier which, in principle, channels electrons to populate on the metal and creates electron trap sites. This results in increased lifetimes and lower recombination of charge carriers. The activity of Pt promoted series were significantly conditioned by on the mesoporous TiO_2 support used, which dictated nanoparticle size of Pt species.

Chapter 4 introduced a straightforward route to a series of high surface area macro-mesoporous TiO_2 materials with macropore diameters ranging from 140 to 310 nm, synthesised by a one-pot soft-hard templating technique involving polystyrene as a hard template. The impact of incorporation of macropores into the mesopore framework discussed in Chapter 3 was investigated. Successful production of hierarchical macro-mesoporous TiO_2 architecture with ordered long-range hexagonal macropore structure and extended mesoscopic ordering was confirmed. The addition of macropores to the meso-TiO_2 structure can influence the framework diffusion and/or improve light absorption by the formation of the photonic crystal. Sadly, a stop-band feature, indicative of the formation of a photonic crystal in ordered macroporous structures,[277, 278] was not visible in the DRUVS measurements. Furthermore, Methyl Orange degradation tests under the monochromatic 365 nm wavelength did not show any enhancement in photocatalytic activity, confirming that optical properties of the macro-meso-TiO_2 photocatalysts were unaffected. The absence of photonic crystal properties could probably be the result of insufficient periodicity because of incorporation of disordered mesostructure or still incomplete (approx. 70%) order of the macropores. Despite that, the hydrogen production rates were doubled from 18 μmol h^{-1} g^{-1} (of meso-TiO_2-400 counterpart) to 34 μmol h^{-1} g^{-1}.

Post-modification of macro-meso-TiO_2 series with 0.1 wt% mononuclear Cu(I) or 1.3 wt% metallic Pt significantly (in some cases up to 33 times) promoted photocatalytic activity in Methyl Orange, water splitting and CO_2 reduction reactions. The identical modes of Cu and Pt promotion, as for Cu/meso-TiO_2 and Pt/meso-TiO_2 described above, were identified. Ultimately, in all cases, Cu and

Pt/macro-meso-TiO_2 series were significantly better than their Cu and Pt/meso-TiO_2 counterparts. Regardless of the absence of enhancement of optical properties, the incorporation of macropores notably improved meso-TiO_2 performance. Moreover, Methyl Orange degradation and CO_2 reduction reactions displayed that the increase in macropore diameter led to an increase in the activity, with 310 nm macropores being the most active. On the other hand, water splitting tests displayed no change in hydrogen production rate across different macropore sizes, revealing that 140 nm macropores are sufficient. The macropore diameter becomes significant in the reactions involving bulky or gas reactants or products indicating improved diffusion and accessibility to the catalyst.

To conclude, the outcome of this research project in combination with the recommendations below should provide an insight into the impact of mesoporosity and macroporosity, together with Cu and Pt promoter species. The photocatalysts demonstrated good performance for depollution of water and capability of producing CH_4 and H_2 in a competitive to literature ways. The leading factors influencing the activities of the photocatalysts were titania crystalline phase, Cu and Pt promoter species and their distribution on the surface as well as macropore diameters and their incorporation to the mesoporous framework. Furthermore, Cu/meso-TiO_2 series did not deactivate and could be used in a flow type reactor, which would make the reactions even more economically and environmentally friendly. Even though the photocatalysts were mostly active in the UV light, the reactions were performed at room temperature and under atmospheric pressure, while using water as a reaction medium. The synthetic protocol of manufacturing the photocatalysts described in this thesis can be replicated in the larger scale (100 of grams).

Even the photocatalysts, synthesised during this project were very active under UV light, they were less economically efficient since UV radiation is only 3-4% of the solar light spectrum.[12] Initially, the idea of promoting titania photocatalysts with Cu was to produce a catalyst, which is able to efficiently absorb solar spectrum and would not require an artificial light source. This still remains an important goal, and in a future work, a co-catalyst to Cu/TiO_2 or Pt/TiO_2 could be introduced. Formation of TiO_2 heterojunction with the narrower band-gap semiconductor such as $BiVO_4$, would absorb visible light and would channel electrons to the conductance band of titania whilst improving charge separation (**Figure 5.1**).[295-297] Various semiconductors with the narrow band gaps like WO_3 or other materials like g-C_3N_4 and CoP could be employed.

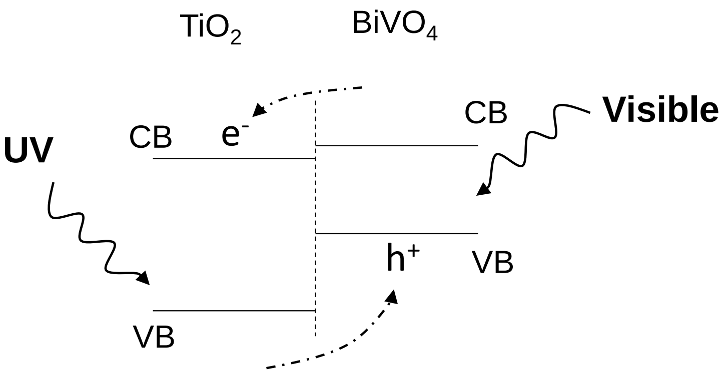

Figure 5.1 A schematic representation of a heterojunction between TiO_2 and narrow band gap semiconductor allowing efficient solar spectrum absorption.

In the characterisation and testing of macro-mesoporous TiO_2, it was identified that the materials did not display photonic crystal properties, which were greatly desired. Further research on developing macro-meso-TiO_2 materials with enhanced optical properties, should focus on preserving ordered hexagonal arrays of mesopores. In addition, 100% periodicity and incorporation of macropores should be achieved. Only highly periodically ordered macropore structure can form the photonic crystal and achieve the slow-light effect leading to enhanced absorption efficiency. The optimum photocatalyst would be achieved by combining the best photocatalyst, synthesised during this thesis, with co-doping (discussed above) and absolute periodicity of the macropores.

6 List of References

1. N. Armaroli and V. Balzani, *Angewandte Chemie-International Edition*, 2007, **46**, 52-66.
2. T. Faunce, S. Styring, M. R. Wasielewski, G. W. Brudvig, A. W. Rutherford, J. Messinger, A. F. Lee, C. L. Hill, H. deGroot, M. Fontecave, D. R. MacFarlane, B. Hankamer, D. G. Nocera, D. M. Tiede, H. Dau, W. Hillier, L. Z. Wang and R. Amal, *Energy & Environmental Science*, 2013, **6**, 1074-1076.
3. X. B. Chen, S. H. Shen, L. J. Guo and S. S. Mao, *Chemical Reviews*, 2010, **110**, 6503-6570.
4. S. Malato, P. Fernández-Ibáñez, M. I. Maldonado, J. Blanco and W. Gernjak, *Catalysis Today*, 2009, **147**, 1-59.
5. S. C. Roy, O. K. Varghese, M. Paulose and C. A. Grimes, *Acs Nano*, 2010, **4**, 1259-1278.
6. D. Chen, X. G. Zhang and A. F. Lee, *Journal of Materials Chemistry A*, 2015, **3**, 14487-14516.
7. A. Kudo and Y. Miseki, *Chemical Society Reviews*, 2009, **38**, 253-278.
8. M. R. Hoffmann, S. T. Martin, W. Choi and D. W. Bahnemann, *Chemical Reviews*, 1995, **95**, 69-96.
9. A. L. Linsebigler, G. Q. Lu and J. T. Yates, *Chemical Reviews*, 1995, **95**, 735-758.
10. H. Kisch, *Angewandte Chemie-International Edition*, 2013, **52**, 812-847.
11. A. Fujishima, X. Zhang and D. A. Tryk, *International Journal of Hydrogen Energy*, 2007, **32**, 2664-2672.
12. J. R. Holton, J. A. Curry and J. A. Pyle, *Journal*, 2003, **3**.
13. A. J. Cowan, J. W. Tang, W. H. Leng, J. R. Durrant and D. R. Klug, *Journal of Physical Chemistry C*, 2010, **114**, 4208-4214.
14. S. Fukahori, H. Ichiura, T. Kitaoka and H. Tanaka, *Environmental Science & Technology*, 2003, **37**, 1048-1051.
15. M. Anpo and M. Takeuchi, *Journal of Catalysis*, 2003, **216**, 505-516.
16. S. Y. Dong, J. L. Feng, M. H. Fan, Y. Q. Pi, L. M. Hu, X. Han, M. L. Liu, J. Y. Sun and J. H. Sun, *Rsc Advances*, 2015, **5**, 14610-14630.
17. M. Tahir and N. S. Amin, *Renewable & Sustainable Energy Reviews*, 2013, **25**, 560-579.
18. X. Chen and S. S. Mao, *Chemical Reviews*, 2007, **107**, 2891-2959.
19. U. I. Gaya and A. H. Abdullah, *Journal of Photochemistry and Photobiology C-Photochemistry Reviews*, 2008, **9**, 1-12.
20. J. Schneider, M. Matsuoka, M. Takeuchi, J. L. Zhang, Y. Horiuchi, M. Anpo and D. W. Bahnemann, *Chemical Reviews*, 2014, **114**, 9919-9986.
21. A. Selloni, *Nat Mater*, 2008, **7**, 613-615.
22. J. F. Zhang, P. Zhou, J. J. Liu and J. G. Yu, *Physical Chemistry Chemical Physics*, 2014, **16**, 20382-20386.
23. U. Diebold, *Surface Science Reports*, 2003, **48**, 53-229.
24. A. Sclafani and J. M. Herrmann, *Journal of Physical Chemistry*, 1996, **100**, 13655-13661.
25. M. C. Yan, F. Chen, J. L. Zhang and M. Anpo, *Journal of Physical Chemistry B*, 2005, **109**, 8673-8678.
26. D. C. Hurum, A. G. Agrios, K. A. Gray, T. Rajh and M. C. Thurnauer, *Journal of Physical Chemistry B*, 2003, **107**, 4545-4549.
27. S. N. Habisreutinger, L. Schmidt-Mende and J. K. Stolarczyk, *Angewandte Chemie-International Edition*, 2013, **52**, 7372-7408.
28. R. I. Bickley, T. Gonzalez-Carreno, J. S. Lees, L. Palmisano and R. J. D. Tilley, *Journal of Solid State Chemistry*, 1991, **92**, 178-190.
29. D. C. Hurum, A. G. Agrios, K. A. Gray, T. Rajh and M. C. Thurnauer, *The Journal of Physical Chemistry B*, 2003, **107**, 4545-4549.
30. J. Zhang, Q. Xu, Z. Feng, M. Li and C. Li, *Angewandte Chemie-International Edition*, 2008, **47**, 1766-1769.
31. G. Li, L. Chen, M. E. Graham and K. A. Gray, *Journal of Molecular Catalysis A: Chemical*, 2007, **275**, 30-35.
32. M. A. Grela and A. J. Colussi, *The Journal of Physical Chemistry B*, 1999, **103**, 2614-2619.

33. I. Martini, J. H. Hodak and G. V. Hartland, *The Journal of Physical Chemistry B*, 1998, **102**, 9508-9517.
34. M. A. Henderson, *Surface Science Reports*, 2011, **66**, 185-297.
35. P. Atkins and J. de Paula, *Atkins' Physical Chemistry*, OUP Oxford, 10th edn., 2014.
36. N. Serpone, *Journal of Physical Chemistry B*, 2006, **110**, 24287-24293.
37. G. Rothenberger, D. Fitzmaurice and M. Graetzel, *The Journal of Physical Chemistry*, 1992, **96**, 5983-5986.
38. N. Serpone, D. Lawless and R. Khairutdinov, *The Journal of Physical Chemistry*, 1995, **99**, 16646-16654.
39. P. V. Kamat, *Journal of Physical Chemistry C*, 2007, **111**, 2834-2860.
40. N. Satoh, T. Nakashima, K. Kamikura and K. Yamamoto, *Nature Nanotechnology*, 2008, **3**, 106-111.
41. C. B. Almquist and P. Biswas, *Journal of Catalysis*, 2002, **212**, 145-156.
42. K. Koci, L. Obalova, L. Matejova, D. Placha, Z. Lacny, J. Jirkovsky and O. Solcova, *Applied Catalysis B-Environmental*, 2009, **89**, 494-502.
43. L. J. Liu, H. L. Zhao, J. M. Andino and Y. Li, *Acs Catalysis*, 2012, **2**, 1817-1828.
44. C. M. Yim, C. L. Pang and G. Thornton, *Physical Review Letters*, 2010, **104**.
45. R. Schaub, P. Thostrup, N. Lopez, E. Laegsgaard, I. Stensgaard, J. K. Norskov and F. Besenbacher, *Physical Review Letters*, 2001, **87**.
46. K. Fukui, H. Onishi and Y. Iwasawa, *Physical Review Letters*, 1997, **79**, 4202-4205.
47. S. Wendt, R. Schaub, J. Matthiesen, E. K. Vestergaard, E. Wahlstrom, M. D. Rasmussen, P. Thostrup, L. M. Molina, E. Laegsgaard, I. Stensgaard, B. Hammer and F. Besenbacher, *Surface Science*, 2005, **598**, 226-245.
48. X. Q. Gong and A. Selloni, *Journal of Physical Chemistry B*, 2005, **109**, 19560-19562.
49. A. Vittadini, A. Selloni, F. P. Rotzinger and M. Gratzel, *Physical Review Letters*, 1998, **81**, 2954-2957.
50. J. G. Yu, J. X. Low, W. Xiao, P. Zhou and M. Jaroniec, *Journal of the American Chemical Society*, 2014, **136**, 8839-8842.
51. J. G. Yu, L. F. Qi and M. Jaroniec, *Journal of Physical Chemistry C*, 2010, **114**, 13118-13125.
52. B. H. Wu, C. Y. Guo, N. F. Zheng, Z. X. Xie and G. D. Stucky, *Journal of the American Chemical Society*, 2008, **130**, 17563-17567.
53. G. Liu, H. G. Yang, X. W. Wang, L. N. Cheng, J. Pan, G. Q. Lu and H. M. Cheng, *Journal of the American Chemical Society*, 2009, **131**, 12868-12869.
54. W.-S. Wang, D.-H. Wang, W.-G. Qu, L.-Q. Lu and A.-W. Xu, *The Journal of Physical Chemistry C*, 2012, **116**, 19893-19901.
55. R. Liu, J. Duay and S. B. Lee, *Chemical Communications*, 2011, **47**, 1384-1404.
56. R. A. Andrievskii, *Uspekhi Khimii*, 2002, **71**, 967-981.
57. D. Grosso, G. Soler-Illia, F. Babonneau, C. Sanchez, P. A. Albouy, A. Brunet-Bruneau and A. R. Balkenende, *Advanced Materials*, 2001, **13**, 1085-1090.
58. E. L. Crepaldi, G. J. d. A. A. Soler-Illia, D. Grosso, F. Cagnol, F. Ribot and C. Sanchez, *Journal of the American Chemical Society*, 2003, **125**, 9770-9786.
59. C.-W. Wu, T. Ohsuna, M. Kuwabara and K. Kuroda, *Journal of the American Chemical Society*, 2006, **128**, 4544-4545.
60. K. Shankar, J. Bandara, M. Paulose, H. Wietasch, O. K. Varghese, G. K. Mor, T. J. LaTempa, M. Thelakkat and C. A. Grimes, *Nano Letters*, 2008, **8**, 1654-1659.
61. K. Zhu, N. R. Neale, A. Miedaner and A. J. Frank, *Nano Letters*, 2007, **7**, 69-74.
62. O. K. Varghese, M. Paulose and C. A. Grimes, *Nat Nano*, 2009, **4**, 592-597.
63. R. S. Devan, R. A. Patil, J. H. Lin and Y. R. Ma, *Advanced Functional Materials*, 2012, **22**, 3326-3370.
64. D. Chen, L. Cao, F. Huang, P. Imperia, Y.-B. Cheng and R. A. Caruso, *Journal of the American Chemical Society*, 2010, **132**, 4438-4444.
65. J. F. Chen, Z. J. Hua, Y. S. Yan, A. A. Zakhidov, R. H. Baughman and L. B. Xu, *Chemical Communications*, 2010, **46**, 1872-1874.
66. M. E. Davis, *Nature*, 2002, **417**, 813-821.
67. D. H. Chen, F. Z. Huang, Y. B. Cheng and R. A. Caruso, *Advanced Materials*, 2009, **21**, 2206-2210.

68. N. Lakshminarasimhan, E. Bae and W. Choi, *The Journal of Physical Chemistry C*, 2007, **111**, 15244-15250.
69. C. M. A. Parlett, K. Wilson and A. F. Lee, *Chemical Society Reviews*, 2013, **42**, 3876-3893.
70. M. M. Ren, R. Ravikrishna and K. T. Valsaraj, *Environmental Science & Technology*, 2006, **40**, 7029-7033.
71. J. I. L. Chen and G. A. Ozin, *Journal of Materials Chemistry*, 2009, **19**, 2675-2678.
72. J. I. L. Chen, G. von Freymann, V. Kitaev and G. A. Ozin, *Journal of the American Chemical Society*, 2007, **129**, 1196-1202.
73. S. H. Ko, D. Lee, H. W. Kang, K. H. Nam, J. Y. Yeo, S. J. Hong, C. P. Grigoropoulos and H. J. Sung, *Nano Letters*, 2011, **11**, 666-671.
74. J. G. Yu, J. J. Fan and L. Zhao, *Electrochimica Acta*, 2010, **55**, 597-602.
75. F. Dong, Y. Sun, M. Fu, W.-K. Ho, S. C. Lee and Z. Wu, *Langmuir*, 2012, **28**, 766-773.
76. P. V. Kamat, *Journal of Physical Chemistry Letters*, 2012, **3**, 663-672.
77. Y. Cong, J. L. Zhang, F. Chen and M. Anpo, *Journal of Physical Chemistry C*, 2007, **111**, 6976-6982.
78. L. X. Yang, S. L. Luo, Y. Li, Y. Xiao, Q. Kang and Q. Y. Cai, *Environmental Science & Technology*, 2010, **44**, 7641-7646.
79. N. P. Xu, Z. F. Shi, Y. Q. Fan, J. H. Dong, J. Shi and M. Z. C. Hu, *Industrial & Engineering Chemistry Research*, 1999, **38**, 373-379.
80. M. Kong, Y. Z. Li, X. Chen, T. T. Tian, P. F. Fang, F. Zheng and X. J. Zhao, *Journal of the American Chemical Society*, 2011, **133**, 16414-16417.
81. W. J. Ong, L. L. Tan, S. P. Chai, S. T. Yong and A. R. Mohamed, *Chemsuschem*, 2014, **7**, 690-719.
82. Y. L. Yu, P. Zhang, L. M. Guo, Z. D. Chen, Q. Wu, Y. H. Ding, W. J. Zheng and Y. Cao, *Journal of Physical Chemistry C*, 2014, **118**, 12727-12733.
83. P. J. Whitham, K. E. Knowles, P. J. Reid and D. R. Gamelin, *Nano Letters*, 2015, **15**, 4045-4051.
84. Y. J. Wang, Q. S. Wang, X. Y. Zhan, F. M. Wang, M. Safdar and J. He, *Nanoscale*, 2013, **5**, 8326-8339.
85. P. Sangpour, F. Hashemi and A. Z. Moshfegh, *Journal of Physical Chemistry C*, 2010, **114**, 13955-13961.
86. X. Q. Qiu, M. Miyauchi, K. Sunada, M. Minoshima, M. Liu, Y. Lu, D. Li, Y. Shimodaira, Y. Hosogi, Y. Kuroda and K. Hashimoto, *Acs Nano*, 2012, **6**, 1609-1618.
87. G. Colon, M. Maicu, M. C. Hidalgo and J. A. Navio, *Applied Catalysis B-Environmental*, 2006, **67**, 41-51.
88. D. Liu, Y. Fernández, O. Ola, S. Mackintosh, M. Maroto-Valer, C. M. A. Parlett, A. F. Lee and J. C. S. Wu, *Catalysis Communications*, 2012, **25**, 78-82.
89. J. G. Yu and J. R. Ran, *Energy & Environmental Science*, 2011, **4**, 1364-1371.
90. Y. Liu, B. Zhang, L. Luo, X. Chen, Z. Wang, E. Wu, D. Su and W. Huang, *Angewandte Chemie International Edition*, 2015, **54**, 15260-15265.
91. A. A. Ismail and D. W. Bahnemann, *Journal of Physical Chemistry C*, 2011, **115**, 5784-5791.
92. F. B. Li and X. Z. Li, *Chemosphere*, 2002, **48**, 1103-1111.
93. T. Bak, J. Nowotny, M. Rekas and C. C. Sorrell, *International Journal of Hydrogen Energy*, 2002, **27**, 991-1022.
94. Z. Jiang, Z. Y. Zhang, W. F. Shangguan, M. A. Isaacs, L. J. Durndell, C. M. A. Parlett and A. F. Lee, *Catalysis Science & Technology*, 2016, **6**, 81-88.
95. S. Sakthivel, M. V. Shankar, M. Palanichamy, B. Arabindoo, D. W. Bahnemann and V. Murugesan, *Water Research*, 2004, **38**, 3001-3008.
96. M. Murdoch, G. I. N. Waterhouse, M. A. Nadeem, J. B. Metson, M. A. Keane, R. F. Howe, J. Llorca and H. Idriss, *Nature Chemistry*, 2011, **3**, 489-492.
97. Y. Tian and T. Tatsuma, *Journal of the American Chemical Society*, 2005, **127**, 7632-7637.
98. W. B. Hou and S. B. Cronin, *Advanced Functional Materials*, 2013, **23**, 1612-1619.
99. N. Zhang, C. Han, Y.-J. Xu, J. J. Foley Iv, D. Zhang, J. Codrington, S. K. Gray and Y. Sun, *Nat Photon*, 2016, **10**, 473-482.
100. G. L. Li and Z. Yin, *Physical Chemistry Chemical Physics*, 2011, **13**, 2824-2833.

101. H. Tong, N. Umezawa and J. H. Ye, *Chemical Communications*, 2011, **47**, 4219-4221.
102. S. G. Kumar and L. G. Devi, *Journal of Physical Chemistry A*, 2011, **115**, 13211-13241.
103. H. Tong, S. X. Ouyang, Y. P. Bi, N. Umezawa, M. Oshikiri and J. H. Ye, *Advanced Materials*, 2012, **24**, 229-251.
104. S. Rehman, R. Ullah, A. M. Butt and N. D. Gohar, *Journal of Hazardous Materials*, 2009, **170**, 560-569.
105. S. Bagwasi, B. Z. Tian, J. L. Zhang and M. Nasir, *Chemical Engineering Journal*, 2013, **217**, 108-118.
106. R. Jaiswal, N. Patel, A. Dashora, R. Fernandes, M. Yadav, R. Edla, R. S. Varma, D. C. Kothari, B. L. Ahuja and A. Miotello, *Applied Catalysis B-Environmental*, 2016, **183**, 242-253.
107. W. M. Campbell, A. K. Burrell, D. L. Officer and K. W. Jolley, *Coordination Chemistry Reviews*, 2004, **248**, 1363-1379.
108. D. Chatterjee and S. Dasgupta, *Journal of Photochemistry and Photobiology C-Photochemistry Reviews*, 2005, **6**, 186-205.
109. E. Lestini, K. Nikitin, J. K. Stolarczyk and D. Fitzmaurice, *Chemphyschem*, 2012, **13**, 797-810.
110. H. Imahori, S. Kang, H. Hayashi, M. Haruta, H. Kurata, S. Isoda, S. E. Canton, Y. Infahsaeng, A. Kathiravan, T. Pascher, P. Chabera, A. P. Yartsev and V. Sundstrom, *Journal of Physical Chemistry A*, 2011, **115**, 3679-3690.
111. L. Spanhel, H. Weller and A. Henglein, *Journal of the American Chemical Society*, 1987, **109**, 6632-6635.
112. A. Hagfeldt, G. Boschloo, L. C. Sun, L. Kloo and H. Pettersson, *Chemical Reviews*, 2010, **110**, 6595-6663.
113. M. Gratzel, *Journal of Photochemistry and Photobiology C-Photochemistry Reviews*, 2003, **4**, 145-153.
114. N. Barbero and D. Vione, *Environmental Science & Technology*, 2016, **50**, 2130-2131.
115. World Health Organization WHO (2017), Global Health Observatory Data Repository, http://www.who.int/mediacentre/factsheets/fs391/en/, DOI: /entity/mediacentre/factsheets/fs391/en/index.html).
116. S. D. Richardson and T. A. Ternes, *Analytical Chemistry*, 2014, **86**, 2813-2848.
117. N. Bolong, A. F. Ismail, M. R. Salim and T. Matsuura, *Desalination*, 2009, **239**, 229-246.
118. A. Jurado, E. Vàzquez-Suñé, J. Carrera, M. López de Alda, E. Pujades and D. Barceló, *Science of The Total Environment*, 2012, **440**, 82-94.
119. M. Stuart, D. Lapworth, E. Crane and A. Hart, *Science of The Total Environment*, 2012, **416**, 1-21.
120. T. Deblonde, C. Cossu-Leguille and P. Hartemann, *International Journal of Hygiene and Environmental Health*, 2011, **214**, 442-448.
121. Y. J. Chan, M. F. Chong, C. L. Law and D. G. Hassell, *Chemical Engineering Journal*, 2009, **155**, 1-18.
122. X. P. Huang, X. J. Hou, J. C. Zhao and L. Z. Zhang, *Applied Catalysis B-Environmental*, 2016, **181**, 127-137.
123. F. Persico, M. Sansotera, C. L. Bianchi, C. Cavallotti and W. Navarrini, *Applied Catalysis B-Environmental*, 2015, **170**, 83-89.
124. F. F. Dias, A. A. S. Oliveira, A. P. Arcanjo, F. C. C. Moura and J. G. A. Pacheco, *Applied Catalysis B-Environmental*, 2016, **186**, 136-142.
125. G. Ovejero, A. Rodriguez, A. Vallet and J. Garcia, *Chemical Engineering Journal*, 2013, **215**, 168-173.
126. Y. M. Liu, S. Chen, X. Quan, H. T. Yu, H. M. Zhao and Y. B. Zhang, *Environmental Science & Technology*, 2015, **49**, 13528-13533.
127. P. V. Nidheesh and R. Gandhimathi, *Desalination*, 2012, **299**, 1-15.
128. P. V. Nidheesh, R. Gandhimathi, S. Velmathi and N. S. Sanjini, *Rsc Advances*, 2014, **4**, 5698-5708.
129. P. V. Nidheesh and R. Gandhimathi, *Clean-Soil Air Water*, 2014, **42**, 779-784.
130. S. Karthikeyana, M. P. Pachamuthu, M. A. Isaacs, S. Kumar, A. F. Lee and G. Sekaran, *Applied Catalysis B-Environmental*, 2016, **199**, 323-330.

131. C. A. Cole, L. D. Ochs and F. C. Funnell, *Journal (Water Pollution Control Federation)*, 1974, **46**, 2579-2592.
132. Q. Yang, H. Choi, S. R. Al-Abed and D. D. Dionysiou, *Applied Catalysis B-Environmental*, 2009, **88**, 462-469.
133. J. Song, X. Wang, J. Yan, J. Yu, G. Sun and B. Ding, *Scientific Reports*, 2017, **7**, 1636.
134. F. M. D. Chequer, G. A. R. d. Oliveira, E. R. A. c. Ferraz, J. C. Cardoso, M. V. B. Zanoni and D. P. d. Oliveira, in *Eco-Friendly Textile Dyeing and Finishing*, ed. M. Günay, InTech, Rijeka, 2013, DOI: 10.5772/53659, p. Ch. 06.
135. M. Rochkind, S. Pasternak and Y. Paz, *Molecules*, 2015, **20**, 88.
136. D. Lawless, N. Serpone and D. Meisel, *Journal of Physical Chemistry*, 1991, **95**, 5166-5170.
137. E. Neyens and J. Baeyens, *Journal of Hazardous Materials*, 2003, **98**, 33-50.
138. L. H. Yu, J. Y. Xi, M. D. Li, H. T. Chan, T. Su, D. L. Phillips and W. K. Chan, *Physical Chemistry Chemical Physics*, 2012, **14**, 3589-3595.
139. S. K. Kansal, M. Singh and D. Sud, *Journal of Hazardous Materials*, 2007, **141**, 581-590.
140. S. Kumar, C. M. A. Parlett, M. A. Isaacs, D. V. Jowett, R. E. Douthwaite, M. C. R. Cockett and A. F. Lee, *Applied Catalysis B-Environmental*, 2016, **189**, 226-232.
141. B. A. Pinaud, J. D. Benck, L. C. Seitz, A. J. Forman, Z. B. Chen, T. G. Deutsch, B. D. James, K. N. Baum, G. N. Baum, S. Ardo, H. L. Wang, E. Miller and T. F. Jaramillo, *Energy & Environmental Science*, 2013, **6**, 1983-2002.
142. Hydrogen Production: Natural Gas Reforming, https://energy.gov/eere/fuelcells/hydrogen-production-natural-gas-reforming).
143. I. Roger, M. A. Shipman and M. D. Symes, *Nature Reviews Chemistry*, 2017, **1**.
144. G. M. Wang, H. Y. Wang, Y. C. Ling, Y. C. Tang, X. Y. Yang, R. C. Fitzmorris, C. C. Wang, J. Z. Zhang and Y. Li, *Nano Letters*, 2011, **11**, 3026-3033.
145. M. L. Ghirardi, M. C. Posewitz, P. C. Maness, A. Dubini, J. P. Yu and M. Seibert, *Annual Review of Plant Biology*, 2007, **58**, 71-91.
146. S. H. Liu, Z. H. Zhao and Z. Z. Wang, *Photochemical & Photobiological Sciences*, 2007, **6**, 695-700.
147. Z. H. Pu, Y. L. Luo, A. M. Asiri and X. P. Sun, *Acs Applied Materials & Interfaces*, 2016, **8**, 4718-4723.
148. X. X. Chang, T. Wang and J. L. Gong, *Energy & Environmental Science*, 2016, **9**, 2177-2196.
149. V. P. Indrakanti, J. D. Kubicki and H. H. Schobert, *Energy & Environmental Science*, 2009, **2**, 745-758.
150. W. H. Koppenol and J. D. Rush, *The Journal of Physical Chemistry*, 1987, **91**, 4429-4430.
151. T. Inoue, A. Fujishima, S. Konishi and K. Honda, *Nature*, 1979, **277**, 637-638.
152. N. M. Dimitrijevic, B. K. Vijayan, O. G. Poluektov, T. Rajh, K. A. Gray, H. Y. He and P. Zapol, *Journal of the American Chemical Society*, 2011, **133**, 3964-3971.
153. M. Gattrell, N. Gupta and A. Co, *Journal of Electroanalytical Chemistry*, 2006, **594**, 1-19.
154. H. J. Freund and M. W. Roberts, *Surface Science Reports*, 1996, **25**, 225-273.
155. G. H. Liu, N. Hoivik, K. Y. Wang and H. Jakobsen, *Solar Energy Materials and Solar Cells*, 2012, **105**, 53-68.
156. J. Qiao, Y. Liu and J. Zhang, *Electrochemical Reduction of Carbon Dioxide: Fundamentals and Technologies*, CRC Press, 2016.
157. M. Anpo, H. Yamashita, Y. Ichihashi and S. Ehara, *Journal of Electroanalytical Chemistry*, 1995, **396**, 21-26.
158. M. Subrahmanyam, S. Kaneco and N. Alonso-Vante, *Applied Catalysis B-Environmental*, 1999, **23**, 169-174.
159. N. Sasirekha, S. J. S. Basha and K. Shanthi, *Applied Catalysis B-Environmental*, 2006, **62**, 169-180.
160. K. Koci, L. Obalova and O. Solcova, *Chemical and Process Engineering-Inzynieria Chemiczna I Procesowa*, 2010, **31**, 395-407.
161. O. K. Varghese, M. Paulose, T. J. LaTempa and C. A. Grimes, *Nano Letters*, 2009, **9**, 731-737.
162. K. Ikeue, H. Yamashita, M. Anpo and T. Takewaki, *Journal of Physical Chemistry B*, 2001, **105**, 8350-8355.

163. S. S. Tan, L. Zou and E. Hu, *Catalysis Today*, 2008, **131**, 125-129.
164. I. A. Shkrob, N. M. Dimitrijevic, T. W. Marin, H. Y. He and P. Zapol, *Journal of Physical Chemistry C*, 2012, **116**, 9461-9471.
165. W. G. Tu, Y. Zhou, Q. Liu, Z. P. Tian, J. Gao, X. Y. Chen, H. T. Zhang, J. G. Liu and Z. G. Zou, *Advanced Functional Materials*, 2012, **22**, 1215-1221.
166. T. W. Woolerton, S. Sheard, E. Reisner, E. Pierce, S. W. Ragsdale and F. A. Armstrong, *Journal of the American Chemical Society*, 2010, **132**, 2132-2133.
167. J. Jin, S. Z. Huang, J. Liu, Y. Li, D. S. Chen, H. E. Wang, Y. Yu, L. H. Chen and B. L. Su, *Journal of Materials Chemistry A*, 2014, **2**, 9699-9708.
168. B. T. Holland, C. F. Blanford and A. Stein, *Science*, 1998, **281**, 538-540.
169. S. H. Im, G. E. Khalil, J. Callis, B. H. Ahn, M. Gouterman and Y. N. Xia, *Talanta*, 2005, **67**, 492-497.
170. G. A. Somorjai and Y. Li, *Introduction to surface chemistry and catalysis*, John Wiley & Sons, 2010.
171. R. P. H. Gasser and G. Ehrlich, *Physics Today*, 2008, **40**, 128-129.
172. P. A. Webb and C. Orr, *Analytical methods in fine particle technology*, Micromeritics Instrument Corp, 1997.
173. K. S. W. Sing, D. H. Everett, R. A. W. Haul, L. Moscou, R. A. Pierotti, J. Rouquerol and T. Siemieniewska, *Pure and Applied Chemistry*, 1985, **57**, 603-619.
174. F. Rouquerol, J. Rouquerol and K. S. W. Sing, *Adsorption by Powders and Porous Solids: Principles, Methodology and Applications*, Academic Press, 1999.
175. J. Rouquerol, F. Rouquerol and K. S. Sing, *Adsorption by powders and porous solids*, Academic press, 1998.
176. S. Brunauer, P. H. Emmett and E. Teller, *Journal of the American Chemical Society*, 1938, **60**, 309-319.
177. P. Scherrer, *Nachrichten von der Gesellschaft der Wissenschaften zu Göttingen, mathematisch-physikalische Klasse*, 1918, **1918**, 98-100.
178. N. Pernicone, *CATTECH*, 2003, **7**, 196-204.
179. J. W. Niemantsverdriet, *Spectroscopy in catalysis*, John Wiley & Sons, 2007.
180. R. A. Spurr and H. Myers, *Analytical Chemistry*, 1957, **29**, 760-762.
181. M. T. Weller, *Inorganic materials chemistry*, Oxford University Press Oxford, 1994.
182. R. Jenkins and R. Snyder, *Introduction to X-ray powder diffractometry*, John Wiley & Sons, 2012.
183. B. D. Cullity and S. R. Stock, *Elements of X-ray Diffraction*, Prentice hall Upper Saddle River, NJ, 2001.
184. T. G. Rochow and P. A. Tucker, *Introduction to microscopy by means of light, electrons, X rays, or acoustics*, Springer, New York, 2nd edn., 1994.
185. M. Isaacs, DOI: http://orca.cf.ac.uk/69607/Doctoral, 2014.
186. R. J. Keyse, *Introduction to Scanning Transmission Electron Microscopy*, BIOS Scientific Publishers, 1998.
187. R. Richards, *Surface and Nanomolecular Catalysis*, Taylor & Francis, 2006.
188. I. Chorkendorff and J. W. Niemantsverdriet, *Concepts of Modern Catalysis and Kinetics*, Wiley, 2003.
189. NIST X-ray Photoelectron Spectroscopy (XPS) Database, Version 3.5, https://srdata.nist.gov/xps/Default.aspx).
190. M. A. Newton and W. van Beek, *Chemical Society Reviews*, 2010, **39**, 4845-4863.
191. H. H. Perkampus, H. C. Grinter and T. L. Threlfall, *UV-VIS Spectroscopy and Its Applications*, Springer Berlin Heidelberg, 2013.
192. S. M. Sze and K. K. Ng, *Physics of semiconductor devices*, Hoboken, 3rd ed. / S.M. Sze and Kwok K Ng. edn.
193. R. Sanjines, H. Tang, H. Berger, F. Gozzo, G. Margaritondo and F. Levy, *Journal of Applied Physics*, 1994, **75**, 2945-2951.
194. K. Zaghib, A. Mauger, J. B. Goodenough, F. Gendron and C. M. Julien, *Chemistry of Materials*, 2007, **19**, 3740-3747.
195. R. Lopez and R. Gomez, *Journal of Sol-Gel Science and Technology*, 2012, **61**, 1-7.
196. J. R. Lakowicz, *Principles of Fluorescence Spectroscopy*, Springer US, 2007.

197. R. Daghrir, P. Drogui and D. Robert, *Industrial & Engineering Chemistry Research*, 2013, **52**, 3581-3599.
198. E. J. W. Crossland, N. Noel, V. Sivaram, T. Leijtens, J. A. Alexander-Webber and H. J. Snaith, *Nature*, 2013, **495**, 215-219.
199. R. Zhang, A. A. Elzatahry, S. S. Al-Deyab and D. Zhao, *Nano Today*, 2012, **7**, 344-366.
200. J. Tang, Y. Wu, E. W. McFarland and G. D. Stucky, *Chemical Communications*, 2004, DOI: 10.1039/B403690E, 1670-1671.
201. W. Li, Z. X. Wu, J. X. Wang, A. A. Elzatahry and D. Y. Zhao, *Chemistry of Materials*, 2014, **26**, 287-298.
202. A. A. Ismail and D. W. Bahnemann, *Journal of Materials Chemistry*, 2011, **21**, 11686-11707.
203. A. S. Poyraz, C. H. Kuo, S. Biswas, C. K. King'ondu and S. L. Suib, *Nat. Commun.*, 2013, **4**.
204. D. S. Kim and S. Y. Kwak, *Appl. Catal. A-Gen.*, 2007, **323**, 110-118.
205. F. He, J. L. Li, T. Li and G. X. Li, *Chemical Engineering Journal*, 2014, **237**, 312-321.
206. P. Periyat, N. Leyland, D. E. McCormack, J. Colreavy, D. Corr and S. C. Pillai, *Journal of Materials Chemistry*, 2010, **20**, 3650-3655.
207. J. C. Yu, L. Z. Zhang and J. G. Yu, *Chemistry of Materials*, 2002, **14**, 4647-4653.
208. S. Y. Choi, M. Mamak, N. Coombs, N. Chopra and G. A. Ozin, *Advanced Functional Materials*, 2004, **14**, 335-344.
209. E. L. Crepaldi, G. Soler-Illia, D. Grosso, F. Cagnol, F. Ribot and C. Sanchez, *Journal of the American Chemical Society*, 2003, **125**, 9770-9786.
210. J. B. Joo, Q. Zhang, I. Lee, M. Dahl, F. Zaera and Y. D. Yin, *Advanced Functional Materials*, 2012, **22**, 166-174.
211. L. Kesong, Z. Wei, S. Keying, L. Li, Z. Lili, Z. Milin and F. Honggang, *Nanotechnology*, 2006, **17**, 1363.
212. D. H. Chen, L. Cao, F. Z. Huang, P. Imperia, Y. B. Cheng and R. A. Caruso, *Journal of the American Chemical Society*, 2010, **132**, 4438-4444.
213. D. M. Antonelli and J. Y. Ying, *Angewandte Chemie International Edition in English*, 1995, **34**, 2014-2017.
214. C. K. Tsung, J. Fan, N. F. Zheng, Q. H. Shi, A. J. Forman, J. F. Wang and G. D. Stucky, *Angewandte Chemie-International Edition*, 2008, **47**, 8682-8686.
215. P. D. Yang, D. Y. Zhao, D. I. Margolese, B. F. Chmelka and G. D. Stucky, *Nature*, 1998, **396**, 152-155.
216. NIST Chemistry WebBook, SRD 69, Titanium tetrachloride, http://webbook.nist.gov/cgi/cbook.cgi?ID=C7550450&Mask=8).
217. W. Zhou, F. F. Sun, K. Pan, G. H. Tian, B. J. Jiang, Z. Y. Ren, C. G. Tian and H. G. Fu, *Advanced Functional Materials*, 2011, **21**, 1922-1930.
218. M. F. Atitar, A. A. Ismail, S. A. Al-Sayari, D. Bahnemann, D. Afanasev and A. V. Emeline, *Chemical Engineering Journal*, 2015, **264**, 417-424.
219. C.-C. Wang, Z. Zhang and J. Y. Ying, *Nanostructured Materials*, 1997, **9**, 583-586.
220. A. Alagarasi, P. U. Rajalakshmi, K. Shanthi and P. Selvam, *Catalysis Today*, 2017, DOI: http://dx.doi.org/10.1016/j.cattod.2017.08.001.
221. G. Liu, L. Z. Wang, H. G. Yang, H. M. Cheng and G. Q. Lu, *Journal of Materials Chemistry*, 2010, **20**, 831-843.
222. S. Sajjad, S. A. K. Leghari and J. L. Zhang, *RSC Advances*, 2013, **3**, 12678-12687.
223. I. H. Tseng, W. C. Chang and J. C. S. Wu, *Applied Catalysis B-Environmental*, 2002, **37**, 37-48.
224. X. J. Feng, J. D. Sloppy, T. J. LaTemp, M. Paulose, S. Komarneni, N. Z. Bao and C. A. Grimes, *Journal of Materials Chemistry*, 2011, **21**, 13429-13433.
225. R. M. Navarro, J. Arenales, F. Vaquero, I. D. González and J. L. G. Fierro, *Catalysis Today*, 2013, **210**, 33-38.
226. T. A. Kandiel, A. A. Ismail and D. W. Bahnemann, *Physical Chemistry Chemical Physics*, 2011, **13**, 20155-20161.
227. Anatase mineral information and data, http://www.mindat.org/min-213.html).
228. Rutile mineral information and database, https://www.mindat.org/min-3486.html).
229. T. Ohsaka, F. Izumi and Y. Fujiki, *Journal of Raman Spectroscopy*, 1978, **7**, 321-324.

230. R. Radnik, C. Mohr and P. Claus, *Physical Chemistry Chemical Physics*, 2003, **5**, 172-177.
231. A. Kubacka, M. Fernández-García and G. Colón, *Chemical Reviews*, 2012, **112**, 1555-1614.
232. R. C. Pawar, S. Kang, J. H. Park, J.-h. Kim, S. Ahn and C. S. Lee, 2016, **6**, 31147.
233. B. Vijayan, N. M. Dimitrijevic, T. Rajh and K. Gray, *The Journal of Physical Chemistry C*, 2010, **114**, 12994-13002.
234. D. O. Scanlon, C. W. Dunnill, J. Buckeridge, S. A. Shevlin, A. J. Logsdail, S. M. Woodley, C. R. A. Catlow, M. J. Powell, R. G. Palgrave, I. P. Parkin, G. W. Watson, T. W. Keal, P. Sherwood, A. Walsh and A. A. Sokol, *Nature Materials*, 2013, **12**, 798-801.
235. Y. J. Li, X. D. Li, J. W. Li and J. Yin, *Water Research*, 2006, **40**, 1119-1126.
236. D. S. Tsoukleris, A. I. Kontos, P. Aloupogiannis and P. Falaras, *Catalysis Today*, 2007, **124**, 110-117.
237. G. Rothenberg, *Catalysis: Concepts and Green Applications*, Wiley, 2008.
238. P. T. Landsberg, *Recombination in Semiconductors*, Cambridge University Press, 2003.
239. J. Goscianska, M. Marciniak and R. Pietrzak, *Chemical Engineering Journal*, 2014, **247**, 258-264.
240. F. Gritti and G. Guiochon, *Journal of Chromatography A*, 2015, **1384**, 76-87.
241. D. S. Kim and S.-Y. Kwak, *Environmental Science & Technology*, 2009, **43**, 148-151.
242. A. Fujishima, T. N. Rao and D. A. Tryk, *Journal of Photochemistry and Photobiology C: Photochemistry Reviews*, 2000, **1**, 1-21.
243. M. Heinemann, B. Eifert and C. Heiliger, *Physical Review B*, 2013, **87**.
244. J. Z. Y. Tan, Y. Fernández, D. Liu, M. Maroto-Valer, J. Bian and X. Zhang, *Chemical Physics Letters*, 2012, **531**, 149-154.
245. S. Zhang, B. Peng, S. Yang, H. Wang, H. Yu, Y. Fang and F. Peng, *International Journal of Hydrogen Energy*, 2015, **40**, 303-310.
246. L. S. Yoong, F. K. Chong and B. K. Dutta, *Energy*, 2009, **34**, 1652-1661.
247. S. Xu, A. J. Du, J. Liu, J. Ng and D. D. Sun, *International Journal of Hydrogen Energy*, 2011, **36**, 6560-6568.
248. S. Qin, F. Xin, Y. Liu, X. Yin and W. Ma, *Journal of Colloid and Interface Science*, 2011, **356**, 257-261.
249. Y. Lee, S. Kim, J. K. Kang and S. M. Cohen, *Chemical Communications*, 2015, **51**, 5735-5738.
250. A. Dhakshinamoorthy, A. M. Asiri and H. Garcia, *Angewandte Chemie-International Edition*, 2016, **55**, 5414-5445.
251. Y. Q. Wang, T. T. Jiang, D. W. Meng, J. H. Kong, H. X. Jia and M. H. Yu, *Rsc Advances*, 2015, **5**, 16277-16283.
252. B. Bhushan, *Handbook of nanomaterials properties*, 2014.
253. V. J. Babu, S. Vempati, T. Uyar and S. Ramakrishna, *Physical Chemistry Chemical Physics*, 2015, **17**, 2960-2986.
254. B. Choudhury, M. Dey and A. Choudhury, *Applied Nanoscience*, 2014, **4**, 499-506.
255. V. Jovic, Z. Al-Azri, W. T. Chen, D. Sun-Waterhouse, H. Idriss and G. Waterhouse, *Topics in Catalysis*, 2013, **56**, 1139-1151.
256. X. Yin, D. He, P. Jiang, G. Zhou, H. Chen and Y. Deng, *Applied Catalysis A: General*, 2016, **509**, 38-44.
257. P. Kubelka and F. Munk, *Zeitschrift fur Technische Physik*, 1931, 593-601.
258. P. Kubelka, *J. Opt. Soc. Am.*, 1954, **44**, 330-335.
259. B. D. Viezbicke, S. Patel, B. E. Davis and D. P. Birnie, *Physica Status Solidi B-Basic Solid State Physics*, 2015, **252**, 1700-1710.
260. S. Sato and J. M. White, *Chemical Physics Letters*, 1980, **72**, 83-86.
261. D. Y. C. Leung, X. L. Fu, C. F. Wang, M. Ni, M. K. H. Leung, X. X. Wang and X. Z. Fu, *Chemsuschem*, 2010, **3**, 681-694.
262. H. J. Choi and M. Kang, *International Journal of Hydrogen Energy*, 2007, **32**, 3841-3848.
263. Q. H. Zhang, W. D. Han, Y. J. Hong and J. G. Yu, *Catalysis Today*, 2009, **148**, 335-340.
264. J. Pan, X. Wu, L. Z. Wang, G. Liu, G. Q. Lu and H. M. Cheng, *Chemical Communications*, 2011, **47**, 8361-8363.
265. O. Ozcan, F. Yukruk, E. U. Akkaya and D. Uner, *Topics in Catalysis*, 2007, **44**, 523-528.

266. L. H. Chen, X. Y. Li, G. Tian, Y. Li, J. C. Rooke, G. S. Zhu, S. L. Qiu, X. Y. Yang and B. L. Su, *Angewandte Chemie-International Edition*, 2011, **50**, 11156-11161.
267. J. Du, X. Y. Lai, N. L. Yang, J. Zhai, D. Kisailus, F. B. Su, D. Wang and L. Jiang, *ACS Nano*, 2011, **5**, 590-596.
268. J. P. Dacquin, J. Dhainaut, D. Duprez, S. Royer, A. F. Lee and K. Wilson, *Journal of the American Chemical Society*, 2009, **131**, 12896-12897.
269. M. H. Sun, S. Z. Huang, L. H. Chen, Y. Li, X. Y. Yang, Z. Y. Yuan and B. L. Su, *Chemical Society Reviews*, 2016, **45**, 3479-3563.
270. P. D. Yang, T. Deng, D. Y. Zhao, P. Y. Feng, D. Pine, B. F. Chmelka, G. M. Whitesides and G. D. Stucky, *Science*, 1998, **282**, 2244-2246.
271. J. Xiao, D. H. Mei, X. L. Li, W. Xu, D. Y. Wang, G. L. Graff, W. D. Bennett, Z. M. Nie, L. V. Saraf, I. A. Aksay, J. Liu and J. G. Zhang, *Nano Letters*, 2011, **11**, 5071-5078.
272. P. Trogadas, V. Ramani, P. Strasser, T. F. Fuller and M. O. Coppens, *Angewandte Chemie-International Edition*, 2016, **55**, 122-148.
273. Z. Y. Yuan and B. L. Su, *Journal of Materials Chemistry*, 2006, **16**, 663-677.
274. W. Sun, S. X. Zhou, B. You and L. M. Wu, *Chemistry of Materials*, 2012, **24**, 3800-3810.
275. F. Bosc, P. Lacroix-Desmazes and A. Ayral, *Journal of Colloid and Interface Science*, 2006, **304**, 545-548.
276. M. Wu, Y. Li, Z. Deng and B. L. Su, *Chemsuschem*, 2011, **4**, 1481-1488.
277. E. Yablonovitch, *Physical Review Letters*, 1987, **58**, 2059-2062.
278. S. John, *Physical Review Letters*, 1987, **58**, 2486-2489.
279. R. C. Schroden, M. Al-Daous, C. F. Blanford and A. Stein, *Chemistry of Materials*, 2002, **14**, 3305-3315.
280. C. Lopez, *Advanced Materials*, 2003, **15**, 1679-1704.
281. J. I. L. Chen, G. von Freymann, S. Y. Choi, V. Kitaev and G. A. Ozin, *Advanced Materials*, 2006, **18**, 1915-1919.
282. Y. Z. Li, T. Kunitake and S. Fujikawa, *Journal of Physical Chemistry B*, 2006, **110**, 13000-13004.
283. M. Srinivasan and T. White, *Environmental Science & Technology*, 2007, **41**, 4405-4409.
284. X. Z. Zheng, S. G. Meng, J. Chen, J. X. Wang, J. J. Xian, Y. Shao, X. Z. Fu and D. Z. Li, *Journal of Physical Chemistry C*, 2013, **117**, 21263-21273.
285. M. M. Ren and K. Valsaraj, *International Journal of Chemical Reactor Engineering*, 2009, **7**.
286. F. Wang, Y. Zhou, P. Li, H. J. Li, W. G. Tu, S. C. Yan and Z. G. Zou, *RSC Advances*, 2014, **4**, 43172-43177.
287. J. I. L. Chen, E. Loso, N. Ebrahim and G. A. Ozin, *Journal of the American Chemical Society*, 2008, **130**, 5420-5421.
288. H. A. Chen, S. Chen, X. Quan and Y. B. Zhang, *Environmental Science & Technology*, 2010, **44**, 451-455.
289. Y. Lu, H. T. Yu, S. Chen, X. Quan and H. M. Zhao, *Environmental Science & Technology*, 2012, **46**, 1724-1730.
290. O. Sel, D. Kuang, M. Thommes and B. Smarsly, *Langmuir*, 2006, **22**, 2311-2322.
291. J. D. Joannopoulos, S. G. Johnson, J. N. Winn and R. D. Meade, *Photonic Crystals: Molding the Flow of Light*, Princeton University Press, 2011.
292. L. F. Qi, W. K. Ho, J. L. Wang, P. Y. Zhang and J. G. Yu, *Catalysis Science & Technology*, 2015, **5**, 2366-2377.
293. S. Xie, Y. Wang, Q. Zhang, W. Deng and Y. Wang, *ACS Catalysis*, 2014, **4**, 3644-3653.
294. B. Z. Fang, A. Bonakdarpour, K. Reilly, Y. L. Xing, F. Taghipour and D. P. Wilkinson, *Acs Applied Materials & Interfaces*, 2014, **6**, 15488-15498.
295. X. Zhu, F. Zhang, M. Wang, X. Gao, Y. Luo, J. Xue, Y. Zhang, J. Ding, S. Sun, J. Bao and C. Gao, *Applied Catalysis A: General*, 2016, **521**, 42-49.
296. J. Resasco, H. Zhang, N. Kornienko, N. Becknell, H. Lee, J. Guo, A. L. Briseno and P. Yang, *ACS Central Science*, 2016, **2**, 80-88.
297. S. Wang, W. Li, F. Chen, S. Gu and Z. Chang, *Australian Journal of Chemistry*, 2015, **68**, 1268-1275.